AD-775 992

EXPLOSIVE ELECTRON EMISSION AND THE
CHARACTERISTICS OF HIGH-CURRENT
ELECTRON FLOW

Robert K. Parker

Air Force Weapons Laboratory
Kirtland Air Force Base, New Mexico

February 1974

AFWL.-TR-73-92

AIR FORCE WEAPONS LABORATORY
Air Force Systems Command
Kirtland Air Force Base
New Mexico 87117

DISCLAIMER NOTICE

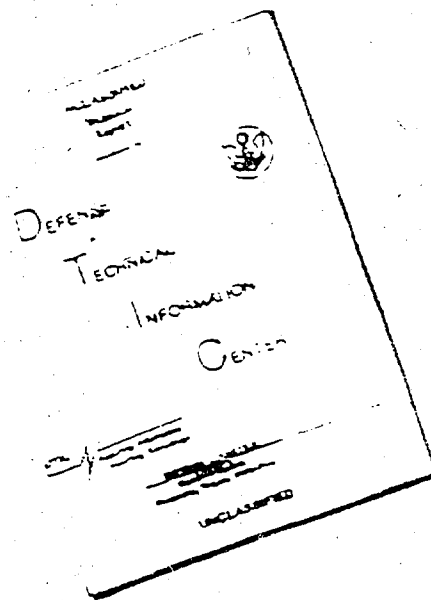THIS DOCUMENT IS BEST QUALITY AVAILABLE. THE COPY FURNISHED TO DTIC CONTAINED A SIGNIFICANT NUMBER OF PAGES WHICH DO NOT REPRODUCE LEGIBLY.

EXPLOSIVE ELECTRON EMISSION AND THE

CHARACTERISTICS OF HIGH-CURRENT ELECTRON FLOW

Robert K. Parker

TECHNICAL REPORT NO. AFWL-TR-73-92

Approved for public release; distribution unlimited.

Final Report for Period October 1970 through January 1973

iⁿ

FOREWORD

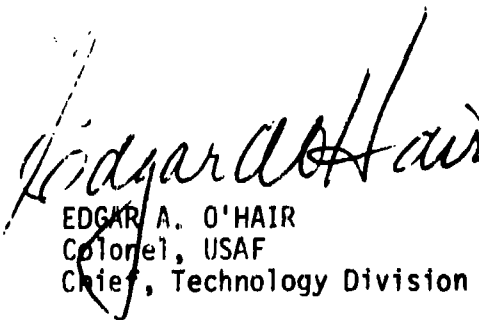This technical report has been reviewed and is approved.

CHARLES V. DUNCAN III
Captain, USAF
Project Officer

THOMAS C. MAY
Major, USAF
Chief, Simulation Branch

EDGAR A. O'HAIR
Colonel, USAF
Chief, Technology Division

AD-775 992

DOCUMENT CONTROL DATA · R & D

(Security classification of title, body of abstract and indexing annotation must be entered when the overall report is classified)

1 ORIGINATING ACTIVITY (Corporate author)	2a. REPORT SECURITY CLASSIFICATION
Air Force Weapons Laboratory (DYS) Kirtland Air Force Base, New Mexico 87117	UNCLASSIFIED
	2b. GROUP

3. REPORT TITLE

EXPLOSIVE ELECTRON EMISSION AND THE CHARACTERISTICS OF HIGH-CURRENT ELECTRON FLOW

4. DESCRIPTIVE NOTES *(Type of report and inclusive dates)*
October 1970-January 1973; Final Report

5. AUTHOR(S) *(First name, middle initial, last name)*

Robert K. Parker

6 REPORT DATE	7a. TOTAL NO. OF PAGES	7b. NO. OF REFS
February 1974	298	78

8a. CONTRACT OR GRANT NO.	9a. ORIGINATOR'S REPORT NUMBER(S)
b. PROJECT NO. 8809	AFWL-TR-73-92
c. Task No. 17	9b. OTHER REPORT NO(S) *(Any other numbers that may be assigned this report)*
d.	

10 DISTRIBUTION STATEMENT

Approved for public release; distribution unlimited.

11 SUPPLEMENTARY NOTES	12 SPONSORING MILITARY ACTIVITY
	AFWL (DYS) Kirtland AFB, NM 87117

13 ABSTRACT

(Distribution Limitation Statement A)

Within the past several years, an increasing effort has been concentrated on the development of high-current, relativistic electron beams. Initially, this effort had been impeded by limitations in the high-voltage and pulsed-power technology required to develop pulsed, high-power electron accelerators. These technologies have been developed to a level where powers on the order of 10^{13} watts are now available for time durations of approximately 100 nanoseconds. Emphasis has more recently been centered on controlling and concentrating these beams. The initial behavior of the beam within the diode region of the accelerator becomes an extremely critical element. The high-current, cold-cathode diode which is distinguished by non-self-convergent electron flow has been studied to define operative electron emission mechanisms, to determine the dominant plasma phenomena within the interelectrode volume, to classify the modes of electron flow, and to verify the Friedlander beam convergence criterion. The results of this diode study provide a complete and self-consistent description of the dominant processes acting within a high-current, cold-cathode diode.

NATIONAL TECHNICAL
INFORMATION SERVICE

i

14 KEY WORDS	LINK A		LINK B		LINK C	
	ROLE	WT	ROLE	WT	ROLE	WT
Electron emission High-current diodes Electron beam sources Field emission Pulsed power Flash X ray						

i a

ABSTRACT

(Distribution Limitation Statement A)

Within the past several years, an increasing effort has been concentrated on the development of high-current, relativistic electron beams. Initially, this effort had been impeded by limitations in the high-voltage and pulsed-power technology required to develop pulsed, high-power electron accelerators. These technologies have been developed to a level where powers on the order of 10^{13} watts are now available for time durations of approximately 100 nanoseconds. Emphasis has more recently been centered on controlling and concentrating these beams. The initial behavior of the beam within the diode region of the accelerator becomes an extremely critical element. The high-current, cold-cathode diode which is distinguished by non-self-convergent electron flow has been studied to define operative electron emission mechanisms, to determine the dominant plasma phenomena within the interelectrode volume, to classify the modes of electron flow, and to verify the Friedlander beam convergence criterion. The results of this diode study provide a complete and self-consistent description of the dominant processes acting within a high-current, cold-cathode diode.

CONTENTS

CONTENTS (cont'd)

CONTENTS (cont'd)

ILLUSTRATIONS

ILLUSTRATIONS (cont'd)

ILLUSTRATIONS (cont'd)

ILLUSTRATIONS (cont'd)

ILLUSTRATIONS (cont'd)

ILLUSTRATIONS (cont'd)

TABLES

SECTION I

INTRODUCTION

1. GENERAL COMMENTS

During the early 1960s rapid advances in high-voltage and pulsed-power technologies led to the development of pulsed-power systems which by now are capable of generating electromagnetic power levels in excess of 10^{13} watts for times less than 10^{-7} seconds. The predominant application of this technology has been the development of electron accelerators which generate pulsed, high-current, relativistic electron beams. Much of the early work in this field must be credited to the group at the Atomic Weapons Research Establishment, Aldermaston, England, headed by J. C. Martin. More recently, several government and private laboratories* have become active in the development of these pulsed, high-power electron accelerators; and many systems offering a wide variety of electron beam parameters are now available. The range of available beam parameters is illustrated in table I.

These high-power electron accelerators typically incorporate four major components: an energy storage circuit, a pulse-forming network, a low-inductance switch, and a cold-cathode diode structure. Although

---

*These laboratories include the Air Force Weapons Laboratory, Field Emission Corporation, Ion Physics Corporation, Maxwell Laboratories Incorporated, Naval Research Laboratory, Physics International Company, Sandia Laboratories, and Simulation Physics Incorporated.

Table I

CAPABILITIES OF PULSED, HIGH-CURRENT ELECTRON ACCELERATORS

Electron kinetic energy	50 keV - 10 MeV
Beam current	5 kA - 1 MA
Pulse duration	10 nsec - 100 nsec
Total beam energy	100 J - 1 MJ
Accelerator impedance	1.0 ohm - 100 ohm

all electron accelerators of this type have components which perform these functions, their design concepts have evolved from two distinctly different apprcaches: those systems which rely on a pulse-charging technique to apply the high voltage to the pulse-forming network, and those which use a direct current charge. Most high-current electron accelerators are of the pulse-charged variety. The only exceptions are the Van de Graaff generator-charged accelerators, developed by the Ion Physics Corporation, and the fast Marx generator systems, developed by the Field Emission Corporation.

As an introduction to later discussions, a simplified schematic of a pulse-charged electron accelerator is shown in figure 1. The initial storage is in the capacitors of the Marx generator (named after Erwin Marx, the Briton who invented the circuit in the 1930s), an energy storage circuit in which the capacitive elements are charged in parallel but discharged in series. Such a circuit has the dual advantage of increasing the voltage at which the energy is delivered and decreasing the time constant which limits the rate of delivery. After being discharged, the Marx generator is switched to pulse charge a pulse-forming line which may

2
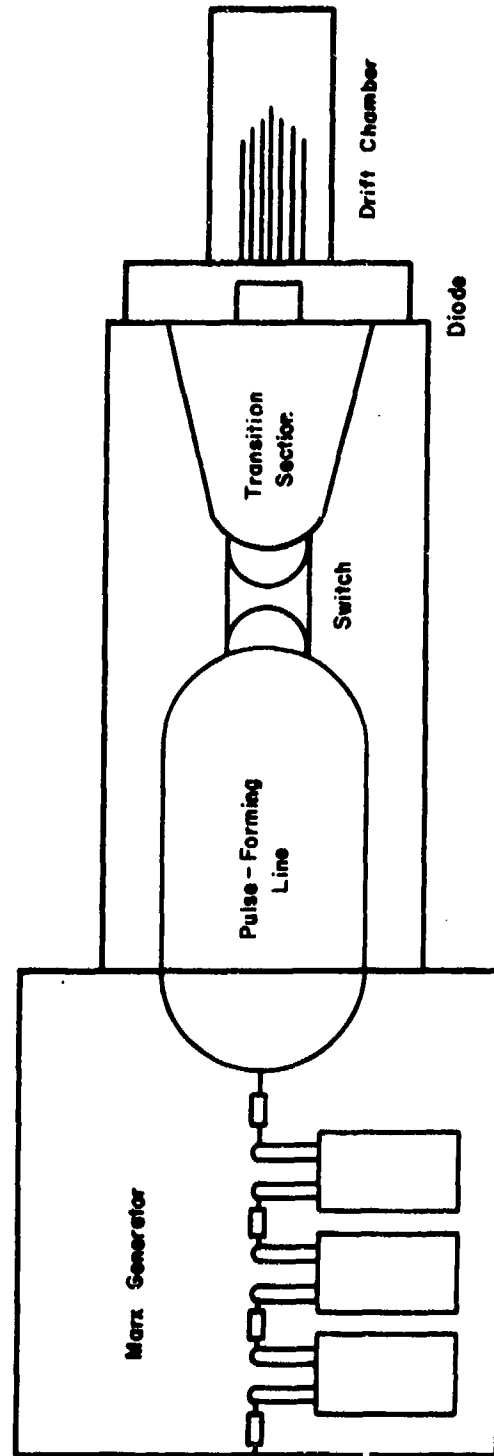
Figure 1. Schematic of Pulsed, High-Current Electron Accelerator

Marx Generator

Pulse-Forming Line

Switch

Transition Section

Drift Chamber

Diode

3

take the form of either a conventional transmission line or a Blumlein (a folded transmission line originally devised in the 1930s by Alan Blumlein). The use of a Blumlein has the advantage of doubling the voltage at which the energy is delivered to the load. These pulse-forming lines may be configured in either a planar or a coaxial geometry.

The low-inductance switch which connects the pulse-forming line to the diode may be either over-volted or command triggered. When the switch is closed, a square voltage pulse of short duration is applied to the cold-cathode diode. The diode responds to the application of this pulse by accelerating an intense, high-current electron beam to relativistic kinetic energies. Since the anode plane of the diode is formed by a very thin conducting film, the electron beam easily penetrates the anode and enters the drift chamber. Propagation and concentration of the electron beam are then possible within the partially evacuated drift chamber.

2. APPLICATIONS OF INTENSE, RELATIVISTIC ELECTRON BEAMS

The initial incentive to develop high-current, relativistic electron accelerators was provided by a desire to study the response of materials exposed to in-depth energy deposition at very high dose rates (Refs. 1, 2, 3). The required dose rates were achieved by operating the electron accelerators in either a bremsstrahlung or an electron beam mode. In the bremsstrahlung or flash X-ray mode the electron beam is stopped in a "thick" anode of high atomic number. The resultant X-ray flux can then be used to irradiate a target of interest. To achieve even higher dose rates, the electron beam can be extracted from the accelerator and allowed to strike the target directly.

4

As the capabilities of these accelerators increased, additional applications have been recognized. Perhaps the most intriguing of these applications has the intense, relativistic electron beam being used to investigate new approaches to the twofold problem of producing useful electrical power from controlled thermonuclear fusion reactions. For controlled fusion to be a viable concept, techniques have had to be developed to produce the ultra-high plasma temperatures required to maintain fusion reactions under controlled conditions. Once formed, the hot plasma must be confined for a sufficient interval that more energy is released through fusion than has been expended in the ignition process. Although ignition has been obtained, attempts to confine the resultant plasma by means of intense magnetic field configurations have so far not yielded a workable solution.

The very high power densities and substantial total energies associated with intense electron beams provided the initial incentive for evaluating the application of these beams to the problems of controlled fusion. These beams also have the more subtle, but equally advantageous, feature of a large azimuthal self-magnetic field which is associated with the current flow. Such fields can account for a significant fraction of the total beam energy, and may prove to be extremely useful for plasma containment. Electron beams can interact with self-generated plasma turbulance and thus add energy to the system. Such heating may potentially be more efficient than classical resistive mechanisma. Finally, the large space charge inherent in high-current beams produces a deep electrostatic potential well which can trap and accelerate ions.

5

These features have led to a wide variety of schemes for using intense, relativistic electron beams to achieve controlled fusion. In their August 1971 article describing the application of pulsed-power technology to controlled thermonuclear fusion (Ref. 4), L. S. Levine and I. M. Vitkovitsky reviewed many of these schemes and concluded that published evaluations are preliminary and speculative. Nevertheless, they did consider several of these approaches to have promise.

The first approach to appear in the open literature was that suggested by Winterberg (Ref. 5). He proposed that an intense electron pulse be concentrated on a small solid pellet of a deuterium-tritium mixture. Although detailed calculations of the interaction between the beam and the target have not been published, Winterberg's preliminary calculations indicated that an energy input of 5×10^6 joules was required to generate an inertially confined plasma of thermonuclear temperature and density. Even with the confining effects of a solid heavy tamper included, Eden and Saunders (Ref. 6) predicted a much higher energy requirement. They estimated that approximately 10^9 joules would be necessary to achieve a useful energy return. More recent calculations by Babykin et al. (Ref. 7) included not only the effects of a tamper, but also acknowledged the confinement resulting from the large self-magnetic field. If the energy can be delivered in a nanosecond, they estimated that only 10^5 joules would be required. Regrettably, no experimental evidence is available as yet to substantiate these predictions.

The astron concept developed by N. C. Christofilos is the most prominent example of plasma confinement using the self-magnetic field of a

6

relativistic electron beam (Ref. 8). The basic idea of the astron concept is to inject an intense relativistic electron beam into the field of a large conventional solenoid wound around a cylindrical vacuum chamber. Entering the field off-axis, the beam is wrapped into a cylindrical layer about 1 meter in diameter, and centered within the vacuum chamber. If enough electrons can be added to the layer, the electron current will be sufficient to cancel and then reverse the magnetic field along the axis. With field reversal, closed field lines are established around the electron sheet and the confining magnetic bottle is complete. In the full-scale experiment at the Lawrence Livermore Laboratory of the University of California, the electron current must be increased by a factor of 10 before field reversal can be completed. Complete field reversal in a small system has been achieved at Cornell University, however (Ref. 9).

The use of an electron beam to turbulently heat a fusion plasma is attractive since it represents an extension of a well-established area in which considerable research has already been completed. Because the parameters of these intense beams differ so greatly from those which have previously been used in plasma heating experiments, much of the theoretical analysis of such interactions will have to be reevaluated and perhaps modified. Considerable interest has been stimulated in this area within the past several years and the preliminary results of a number of experiments have already been reported (Refs. 10, 11, 12, 13, 14). The results of these experiments are being evaluated with considerable interest.

3. SIGNIFICANCE OF DIODE PHENOMENOLOGY

Early in the development of these accelerators, the most significant problems arose from limitations in high-voltage and pulsed-power technology. Nevertheless, some effort was made to assess the basic physics underlying observed diode phenomena. More recently, with an enhanced understanding of the technological problems, the availability of more sophisticated beam diagnostic techniques, and an increased emphasis on the propagation of low-impedance beams, several more detailed diode studies have been initiated. In spite of these efforts, a complete or self-consistent description of diode phenomena is not yet available. Hence, the lack of a comprehensive diode model remains as one of the more-critical restrictions limiting the expanded application of available pulsed accelerator technology.

The diode is an extremely critical link in coupling the tremendous power levels available through pulsed-power technology to the application of interest. Several factors contribute to this situation. First, the ability to propagate an electron beam within the drift space is largely determined by the beam initial conditions as it enters the drift region. These initial conditions are in turn determined predominantly by the dynamics of electron flow within the diode. Secondly, the maximum current which can be accelerated by a given applied voltage is limited by beam convergence and space-charge effects within the diode. Furthermore, the duration of the electron beam can be limited by plasma effects which cause the diode to transition to a vacuum arc on a time scale comparable to the pulse duration. Finally, the maximum energy transfer from the

8

pulse-forming line to the electron beam is achieved if the load (diode) resistance is matched to the impedance of the line. Efficient transfer is therefore complicated by the fact that the observed diode resistance is not constant in time. Unless the diode resistance can be held at some finite value which can be matched to the line impedance, the overall efficiency of the accelerator would be limited by the varying resistance.

Several inconsistencies persist in present understanding of cold-cathode diode behavior. Although these points will be discussed in greater detail in later sections of this report, a brief enumeration of some of the more prominent features of observed diode phenomenology will serve to emphasize specific problem areas, and aid in defining the objectives of the present investigation.

The initial electron emission from the cold cathodes used in these diodes is generally agreed to be field emission. Although a theoretical understanding of such emission has been available for many decades, the application of the Fowler-Nordheim equation to predict the observed current densities would require the existence of local surface fields two orders of magnitude higher than the applied field. This discrepancy becomes even worse if the depression of the electric field at the cathode surface caused by the electron space charge is considered.

One possible explanation for this discrepancy requires the existence of surface roughness or whisker-like projections which produce substantial field enhancement at the cathode surface. With the intense current densities observed in operational diodes, however, ohmic skin heating ensures that even small surface irregularities would be destroyed within a few

9

nanoseconds. Friedlander et al. (Ref. 15) have speculated that the source of electron emission for the remainder of the pulse must therefore be a dense plasma cloud close to the cathode surface. The precise nature of this plasma cloud and its relation to other diode phenomena were not specified and remain undetermined.

Although high-current electron flow is generally space-charge limited, there has been some debate as to whether the electron flow in low-resistance diodes is similarly limited. The simple Child-Langmuir equation for the resistance R (ohms) of a planar diode is as follows:

$$R = 136 \left(d/r_0\right)^2 V^{-1/2} \tag{1}$$

where d is the anode-cathode separation, r_0 is the cathode radius, and V is the applied voltage in megavolts. In several experiments, the dependence of resistance on diode geometry and applied voltage has agreed with the predictions of Child-Langmuir space-charge theory (Refs. 16, 17, 18). In conflict with these results, another group (Ref. 19) observed a very nonlinear variation of diode resistance, with anode-cathode spacing. At relatively large separations, the resistance followed Child-Langmuir scaling, but as the separation was decreased, a point was reached beyond which the resistance fell sharply. More significantly, all investigators have found that the measured resistance of such diodes was considerably below the predicted Child-Langmuir value. Specifically, observed diode currents for a given applied voltage have exceeded that predicted by elementary, planar, space-charge theory by factors of from two to three.

The anomalously high diode currents and the time variation in the diode resistance are generally ascribed to the presence of ions and/or

plasma in the anode-cathode region. Several ionization mechanisms have been suggested. With the diode normally being operated in an ambient pressure ranging from 10^{-3} to 10^{-5} torr, the probability of ionizing the background gas by electron bombardment can be significant. Ions produced in the region immediately adjacent to the cathode surface would be especially effective in neutralizing the electron space charge. At the high power densities generated by these accelerators (10^8 to 10^{12} watts/cm^2), vaporization of the anode becomes a second probable source of ions. Toward the upper end of this range, the power densities are more than sufficient to quickly destroy any material object in the path of the electron beam. A third possibility arises from the explosive nature of the probable electron emission mechanism. This process makes the cathode surface an equally plausible source of plasma. Any quantitative analysis of either cathode or anode plasma formation must be complicated by the presence of adsorbed and absorbed gases. With an ambient pressure of 10^{-5} torr, the monolayer deposition time is only 0.23 second.

The effects of the ions produced by any of these mechanisms is dependent on the properties of the resultant plasma. If the plasma conductivity is low, the ions may act to neutralize the electron space charge. Alternatively, if the conductivity is sufficiently high, the plasma could result in a deformation of the effective electrode surface, and thus modify the diode geometry. Quantitative analysis of these effects has not been attempted and existing discussions are based primarily on conjecture.

With pulse-charged accelerators, an analysis of diode plasma phenomena can sometimes be complicated by the presence of a "prepulse," a pulsed

11

voltage which appears across the diode prior to the discharge of the main accelerating pulse. A prepulse results from a capacitive coupling of the charging voltage on the pulse-forming line across the output switch to the diode. On some accelerators the prepulse is an appreciable fraction of the main pulse amplitude, and can reach magnitudes ranging to hundreds of kilovolts. The resulting prepulse currents are more than sufficient to pre-ionize or precondition the diode region.

The dynamics of electron flow in a low-resistance diode are further complicated by the presence of a large self-magnetic field. At the very high currents characteristic of these diodes, the azimuthal magnetic field can lead to a severe convergence of the electron beam within the diode. Hence, the presence of the self-magnetic field establishes a limiting criterion for space-charge limited flow in the diode. Currents in excess of this limiting value generate sufficiently intense self-fields that the magnetic gyroradius of electrons emitted from the periphery of the cathode is less than the diode separation. Once this occurs, these electrons cannot reach the anode in their initial traversal of the gap. Although current flow ostensibly in excess of the limiting current has been experimentally observed, preliminary theoretical descriptions of electron flow dominated by self-magnetic fields have not completely removed this contradiction. Quantitative correlation between observed and theoretical flow under these conditions is not yet available.

4. OBJECTIVES

Having successfully demonstrated the exceptional capabilities of an intense, relativistic electron beam as a pulsed energy source, the obvious

12

extension has been to develop accelerators capable of generating electron beams of even greater total energy. For most applications, the accelerating voltage and the pulse duration are restricted. Moreover, the electron beam must be extracted from the accelerator, propagated some distance, and then concentrated to increase the power density of the delivered energy pulse.

To increase the total beam energy under these constraints, the beam current must be increased. For the beam current to be increased, however, the characteristic impedance of the pulse-forming line and the diode structure must be proportionally reduced. Similarly, to match the line impedance, the diode resistance must also be reduced. But as the diode resistance is decreased, the dynamics of electron flow within the diode become increasingly affected by plasma and self-magnetic effects. As the beam impedance is decreased, the effects of initial conditions on the beam propagation characteristics become more substantial. These trends emphasize the need to understand the response of low-impedance diodes.

A comprehensive and self-consistent description of the electron flow within a low-resistance diode is not yet available. In an attempt to satisfy this requirement, the objectives of this study are as follows:

a. Develop the experimental techniques necessary to follow the evolution of diode processes throughout the applied voltage pulse.

b. Analyze the resultant data in an effort to quantify the following aspects of observed diode behavior:

    (1) Electron emission processes

    (2) Space-charge limitation to electron flow

13

      (3) Plasma production and effects on electron flow

      (4) Beam convergence criterion

   c. From a careful evaluation of these phenomena, provide a basis for predicting the characteristics of electron flow in a planar, low-resistance diode.

SECTION II

DIODE PHYSICS

1. INTRODUCTION

Such factors as the electron emission processes, the dynamics of electron flow, and possible plasma effects on both the emission and acceleration of the electrons must be carefully considered before analyzing observed diode behavior. Although the theory of electron emission from a conducting surface is well known and widely accepted, correlating predicted emission with observed current densities has required several extensions of the basic theory to account for actual surface conditions. A brief review of pertinent electron-emission mechanisms and a description of applicable surface effects will provide the background for later discussions of explosive electron emission and plasma effects in the diode.

The observed reduction in the diode resistance with time can be compared to the transition of an initially nonconducting, evacuated gap to a vacuum arc. Fortunately, considerable effort has been expended during the past several decades in studying the high-voltage breakdown of vacuum gaps under steady-state or long-pulse conditions. Although these studies were directed toward improvement of the high-voltage insulation properties of vacuum gaps, many of the results are pertinent to a study of high-current diode phenomenology. Within the past several years, a series of Soviet studies has extended this early work to nanosecond pulse durations and demonstrated the explosive effect of very powerful field emission. The

15

results of these studies have confirmed and extended several of the concepts developed from the earlier work and are extremely important to a proper interpretation of plasma effects in the diode. An in-depth development of these topics is therefore required.

Three distinct modes can be identified for the electron flow within a diode, depending on the emitted current density and the magnitude of the applied voltage: (1) source limited; (2) space-charge limited; (3) self-magnetic field limited. At low electron emission densities, the current flow is source limited. More electrons can traverse the diode than are emitted. As the emission rate is increased, the electrons accumulating in the diode constitute a space charge that exerts a retarding field at the cathode. With higher emission rates, the electron density and hence the retarding component of the field must also increase. When the retarding component at the cathode equals the applied field, the electron flow becomes space-charge limited. Any further increase in the emission rate will depress the potential in the vicinity of the cathode to a level below that of the cathode itself. Consequently, only electrons emitted with a finite velocity are energetically able to pass the potential minimum and reach the anode. The remaining electrons are returned to the cathode by the opossing field.

In the space-charge limited mode, the current scales with the anode voltage to the 3/2 power. Since the azimuthal, self-magnetic field produced by electron flow within the diode is proportional to the total current, increased accelerating voltages result in rapidly increasing currents, which in turn generate stronger magnetic fields. The trajectory of an electron accelerated by the crossed electric and magnetic fields within the

16

results of these studies have confirmed and extended several of the concepts developed from the earlier work and are extremely important to a proper interpretation of plasma effects in the diode. An in-depth development of these topics is therefore required.

Three distinct modes can be identified for the electron flow within a diode, depending on the emitted current density and the magnitude of the applied voltage: (1) source limited; (2) space-charge limited; (3) self-magnetic field limited. At low electron emission densities, the current flow is source limited. More electrons can traverse the diode than are emitted. As the emission rate is increased, the electrons accumulating in the diode constitute a space charge that exerts a retarding field at the cathode. With higher emission rates, the electron density and hence the retarding component of the field must also increase. When the retarding component at the cathode equals the applied field, the electron flow becomes space-charge limited. Any further increase in the emission rate will depress the potential in the vicinity of the cathode to a level below that of the cathode itself. Consequently, only electrons emitted with a finite velocity are energetically able to pass the potential minimum and reach the anode. The remaining electrons are returned to the cathode by the opossing field.

In the space-charge limited mode, the current scales with the anode voltage to the 3/2 power. Since the azimuthal, self-magnetic field produced by electron flow within the diode is proportional to the total current, increased accelerating voltages result in rapidly increasing currents, which in turn generate stronger magnetic fields. The trajectory of an electron accelerated by the crossed electric and magnetic fields within the

16

diode is quasi-cycloidal. As the applied voltage is increased for a given

diode configuration, a point is reached at which the self-magnetic field

is sufficient to reduce the gyro-radius of an electron emitted from the

perimeter of the cathode to less than the anode-cathode separation. The

critical current causing this condition is recognized as the upper limit

to classical space-charge limited flow. Current flow beyond this limiting

value is dominated by the self-magnetic field and is distinguished by a

severe convergence of the electron beam within the diode. In view of past

debates concerning the nature of space-charge limited flow in pulse, high-

current diodes and the present limitations to understanding electron flow

dominated by the self-magnetic field, these topics will also be developed

with care.

2. ELECTRON EMISSION MECHANISMS

The emission of electrons from a conducting surface affected by the

presence of a strong external electric field is highly dependent on the

magnitude of the field and the temperature of the emitting surface. With

the potential barrier of the metal-vacuum boundary lowered by the applied

electric field, two distinct emission mechanisms are recognized. The

electrons may either possess sufficient kinetic energy to surmount the

barrier, or quantum-mechanically "tunnel" through the lowered potential

distribution. If the conductor is heated, a significant fraction of the

free electrons may gain sufficient kinetic energy to escape over the

lowered barrier. Such emission has been described as field-enhanced

thermionic or Schottky emission. Alternatively, when the external electric

field is increased to approximately 10^7 volts/cm, the probability of

electrons in the vicinity of the Fermi level tunneling through the lowered potential barrier becomes appreciable. Electron emission from a cold surface ($T \approx 0°K$) by tunneling is defined as field emission while similar emission at elevated temperatures is described as T-F emission.

Defining the applied surface field as F(volts/cm) and the surface temperature as T(°K), tunneling becomes the dominant emission mechanism if

$$kT < (he^{1/4}/\pi^2 \, m^{1/2}) \, F^{3/4} \qquad (2)$$

where k is the Boltzmann constant, h is Planck's constant, and e and m are, respectively, the charge and mass of an electron. After substituting the appropriate values for the physical constants and rearranging, the criterion for tunneling becomes

$$F > 439 \, T^{4/3} \qquad (3)$$

To illustrate the relative magnitudes of the two emission mechanisms, the total emission current density j(amperes/cm^2) as a function of applied field at various values of surface temperature is shown in figure 2. For this example, the emitter work function ϕ(eV) was chosen to be 4.5 eV. The dotted line represents the criterion for equal thermionic and tunneling contributions to the total emitted current density. Emission in the region to the left of this line results predominantly from field-enhanced thermionic emission, while emission in the region to the right is dominated by tunneling. Pure field emission applies only to the special case of zero surface temperature. When the surface temperature is zero, only emission by tunneling is possible.

Using the one-dimensional, surface-potential model shown in figure 3, Fowler and Nordheim developed the theory of electron field-emission from a cold metal (Ref. 20). The emitted current density, $j(T,F)$, (amperes/cm^2)
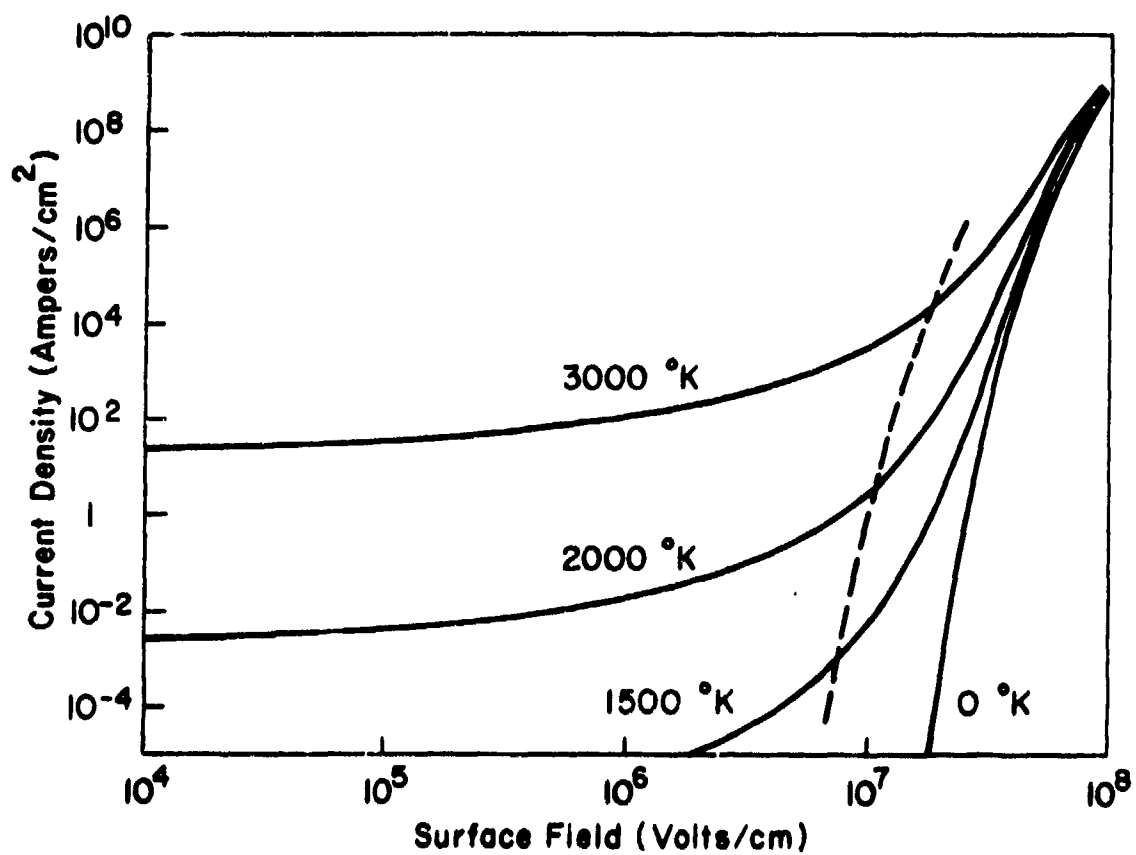
Figure 2. Emitted Current Density as a Function of Temperature
and Surface Field
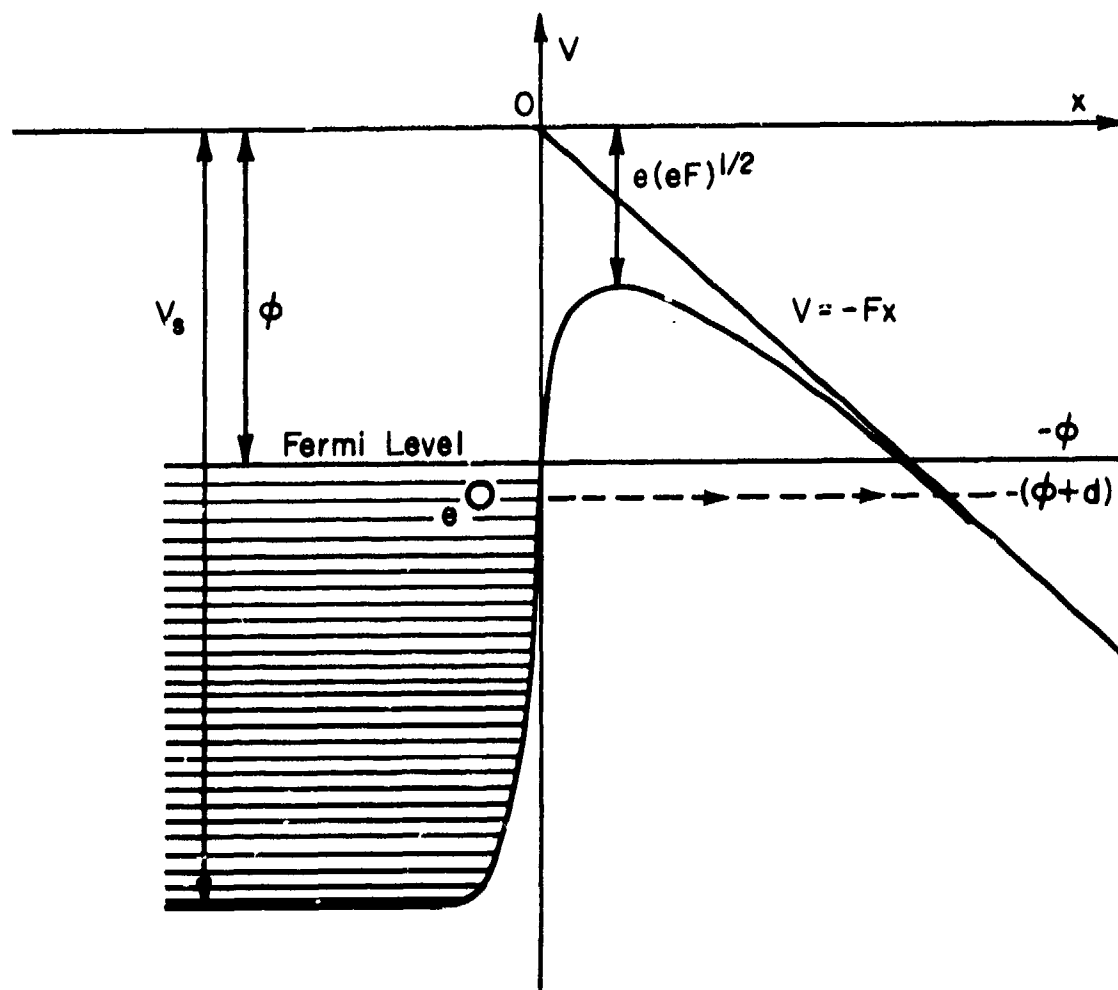
Figure 3. Field-Distorted Surface Potential Barrier

20

may be written in the following simplified form for field emission:

$$j(0,F) = (1.54 \times 10^{-6} \ F^2/\phi) \ exp \left[-6.83 \times 10^7 \ \phi^{3/2} \ f(y)/F\right] \quad (4)$$

where $f(y)$ is a slowly varying function (Nordheim elliptic function) which, over the useful range of the equation, is almost constant and generally varies between 0.7 and 0.95. Taking advantage of this fact, the Fowler-Nordheim equation can be further simplified to the following form:

$$j(0,F) = (1.54 \times 10^{-6} \ F^2/\phi) \ exp \ (-6.42 \times 10^7 \ \phi^{3/2}/F) \quad (5)$$

The emitted current densities predicted by the Fowler-Nordheim equation are shown in figure 4 for a variety of work functions over the pertinent range in F.

The field-emitted current density at elevated temperature (T-F emission) has been related to pure field emission through the following relation (Ref. 21):

$$j(T,F) = j(0,F) \ \pi \ p/\sin \pi \ p \quad (6)$$

where $p \approx kT/d$. The parameter d has the dimensions of energy (eV) and is given by

$$d \approx 9.25 \times 10^{-9} \ F/\phi^{1/2} \quad (7)$$

The equation for T-F emission is quite accurate provided p remains less than about 2/3.

3. CATHODE PROCESSES

a. Cathode Protrusions or Whiskers

Boyle, Kisluik and Germer were the first to demonstrate that the electron emission from a "broad" area cathode prior to breakdown could be
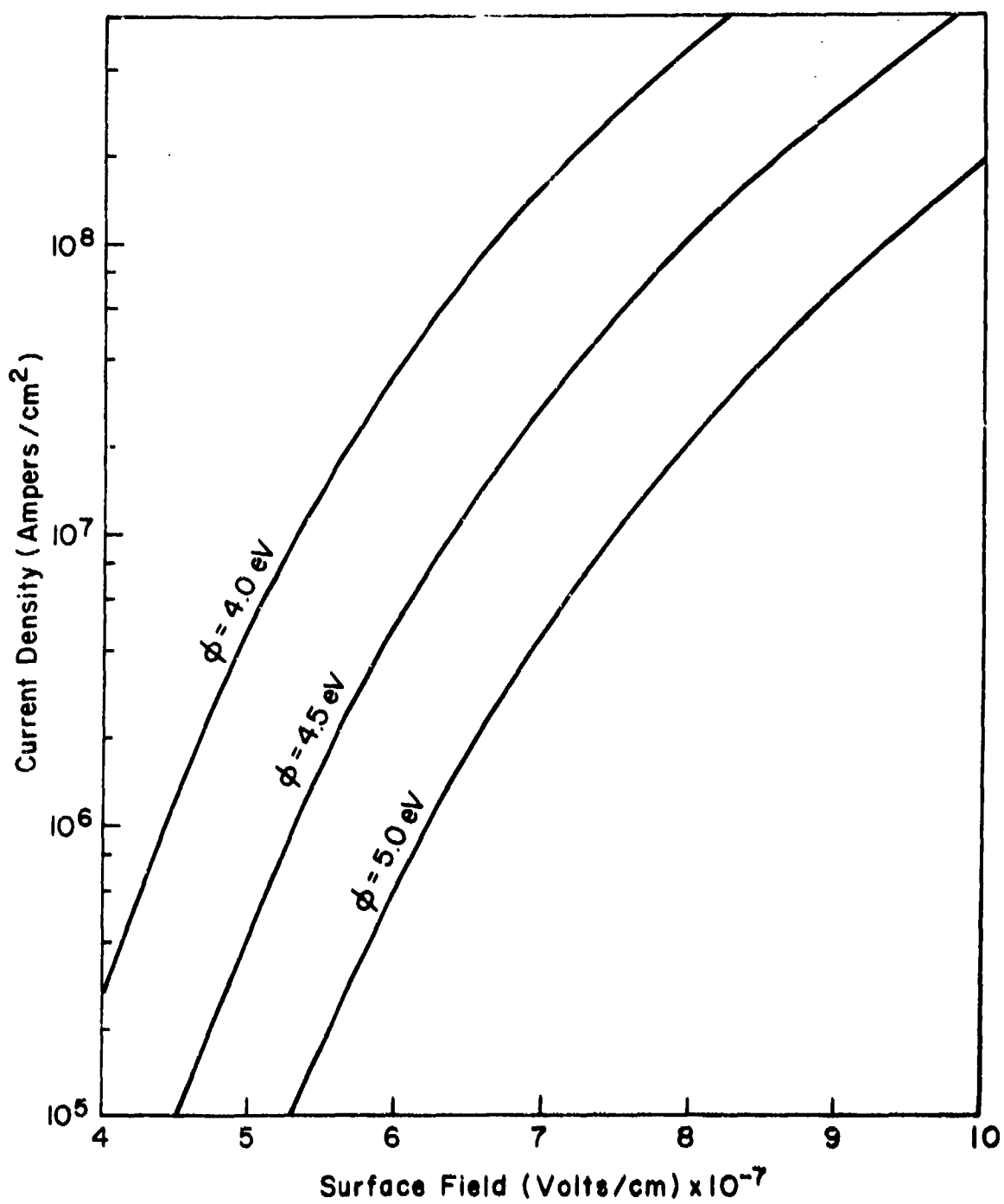
Figure 4.   Field-Emitted Current Density as a Function of Surface Field
and Work Function

22

made to agree with that predicted by the Fowler-Nordheim theory if they assumed that the emission occurred from a small emission site or point on the otherwise flat surface (Ref. 22). The existence of such a point means that the field at the tip of the emitter is substantially enhanced relative to the average electric field between the electrodes.

The field at the tip of the emission site F can be related to the average interelectrode field, $E = V/d$, through the field enhancement factor m, where V is the total voltage applied across the electrode gap d.

$$F = mE \qquad (8)$$

The enhancement factor is therefore defined as the ratio of microscopic or local field at the tip of the emitter to the average field in the diode.

Measurement of the emitting area $A(cm^2)$ and the field enhancement factor is then obtained by rewriting the Fowler-Nordheim equation in the following form:

$$\ell n(I/E^2) = \ell n(1.54 \times 10^{-6}/\phi) + \ell n\, A + 2\ell n\, m - 6.42 \times 10^7\, \phi^{3/2}/(mE)$$
$$(9)$$

where I is the total emission current (amperes). The characteristics of the emission sites can now be determined by plotting $\ell n(I/E^2)$ versus $1/E$. If the observed current has been field emitted, the resulting Fowler-Nordheim plot should be a straight line with an intercept on the logarithmic axis of

$$\ell n(1.54 \times 10^{-6}/\phi) + \ell n\, A + 2\ell n\, m \qquad (10)$$

and a slope

$$-6.42 \times 10^7\, \phi^{3/2}/(mE) \qquad (11)$$

23

Values of m and A obtained from such an analysis must be interpreted with care if the emission is from a large-area cathode. If the emission source were a single point, these values could be used directly to determine the appropriate configuration of the emitting point. Several experimental observations, however, have established that the emission from broad-area cathodes originated from a number of point emitters (Refs. 23, 24, 25). Observations of the emitter concentration on the cathode surface have ranged from 10 to 10^4 per square centimeter. In spite of this complication, analysis of multiple-point emission has shown that the combined currents from many emitters will still produce a straight-line Fowler-Nordheim plot (Ref. 26). The field enhancement factor derived from the plot is now weighted toward the larger enhancement factors of the set. Similarly, the derived emission area is not the total emission area, but rather a qualitative measure of the magnitude of the actual area.

Other than their existence and some knowledge regarding their physical size and shape, little is known about the point emitters which appear on the surface of even the most highly polished electrode surfaces. Several experimenters have been able to take electron microphotographs of observed emission sites (Refs. 23, 24, 25). From these photographs, the emitting points were seen to have a whisker-like appearance. The observed electrode projections ranged from 10^{-4} to 10^{-3} cm in length, and the sharper projections had a height-to-base ratio of approximately five. Beyond this, little else is known. The role of the electric field at the cathode surface or perhaps possible surface contaminants on the formation and growth of these microprojections is not completely understood.

24

Although many of the critical whisker parameters remain unknown, the size and shape of the field-emitting projections have been correlated with observed enhancement factors. The observed variation of the enhancement factor with electrode separation is shown in figure 5 (Refs. 22, 27, 28). The enhancement factor in very small gaps was observed to increase rapidly with gap spacing from unity to perhaps 40 or 50. In larger gaps there was a slow variation with gap spacing. Qualitative agreement between experimental and calculated enhancement factors for the case of broad-area chathodes was achieved by interpreting the overall enhancement factor m as the product of an enhancement factor m_1, associated with the microscopic protrusions; and an enhancement factor m_2, associated with the macroscopic changes in the electric field which result from the shape of the cathode edge (Ref. 27).

The microscopic enhancement factor of a projection is dependent on the ratio h/r_t, where h is the projection height (cm), and r_t is the radius of curvature of the tip (cm). The variation of m_1 with h/r_t has been calculated for two ideal protrusion shapes: a prolate hemispheroid and a cylindrical rod terminated by a hemispherical tip (Ref. 29). The results of these calculations are shown in figure 6. The equation for the cylindrical protrusion has been given by Vibrans (Ref. 30) as

$$m_1 = h/r_t + 2 \qquad (12)$$

The anticipated variation of m_2 with electrode geometry was calculated by using a pair of semi-infinite slab electrodes with rounded corners as a model (Ref. 27). The curve shown in figure 7 represents the ratio of the maximum value of the electric field in the region of the rounded portion of the slab electrode to the average field in the gap.

25
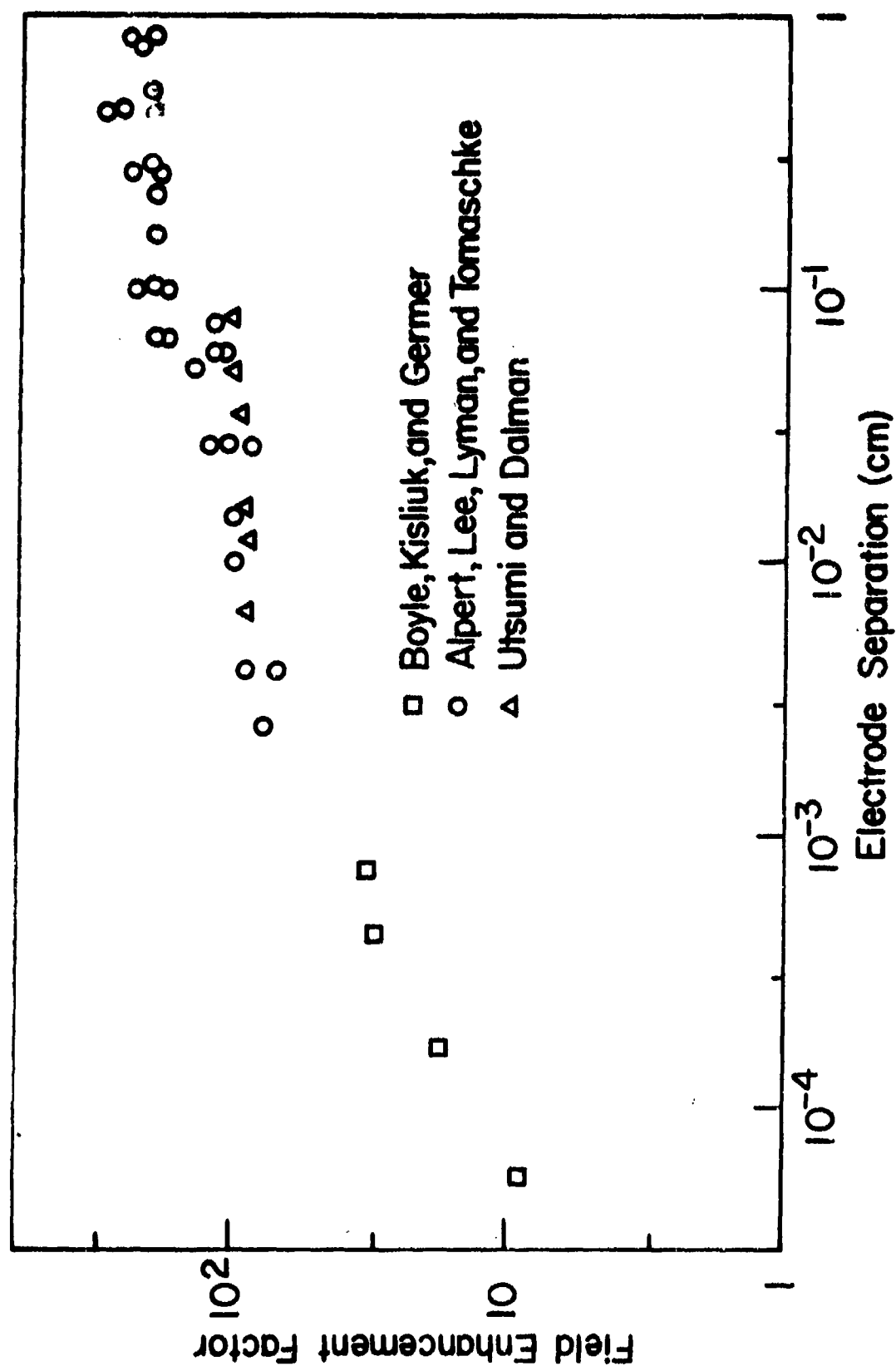
Figure 5. Variation in Field Enhancement Factor with Electrode Separation
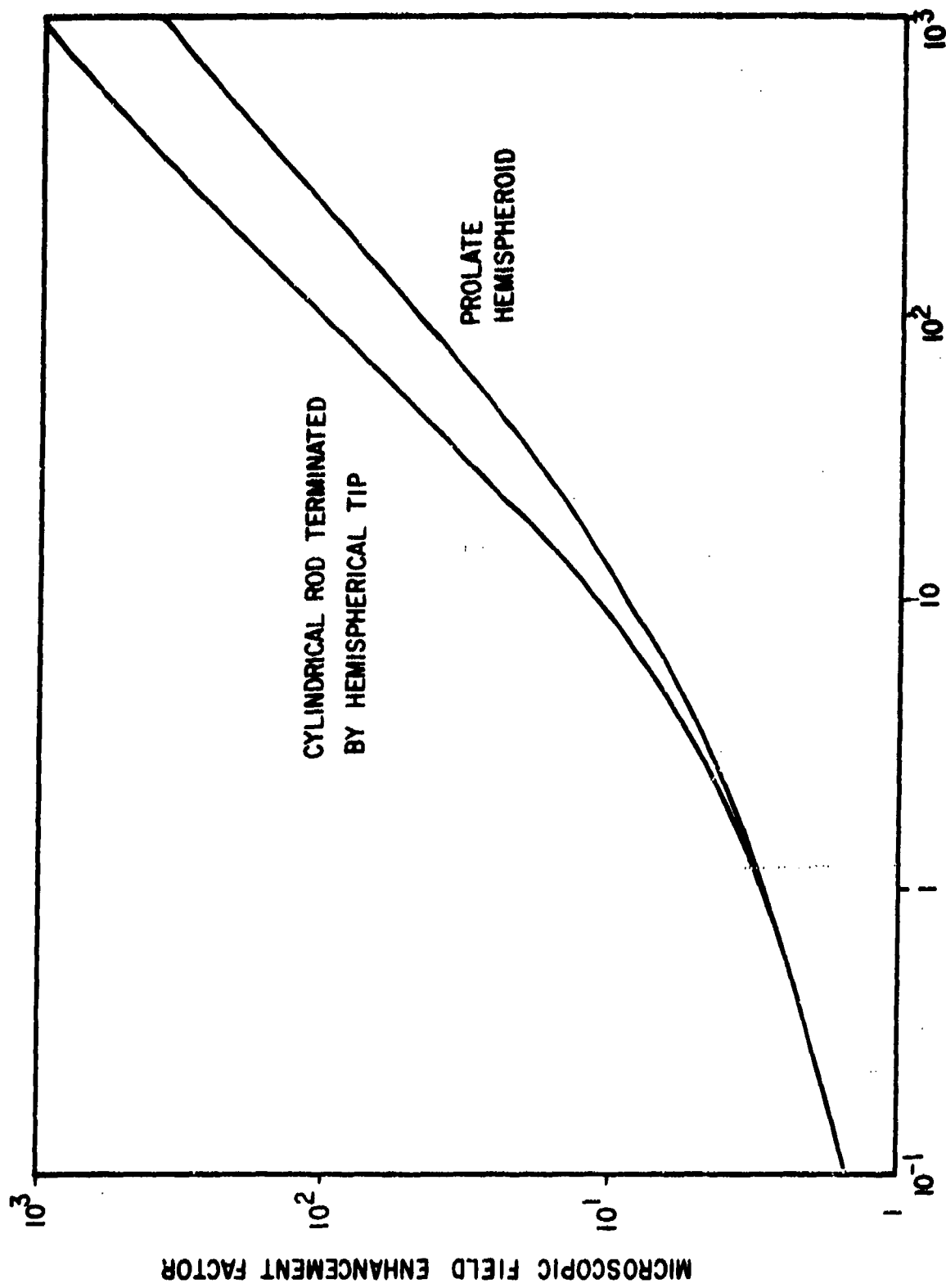
Figure 6. Field Enhancement for Two Ideal Protrusion Shapes

27
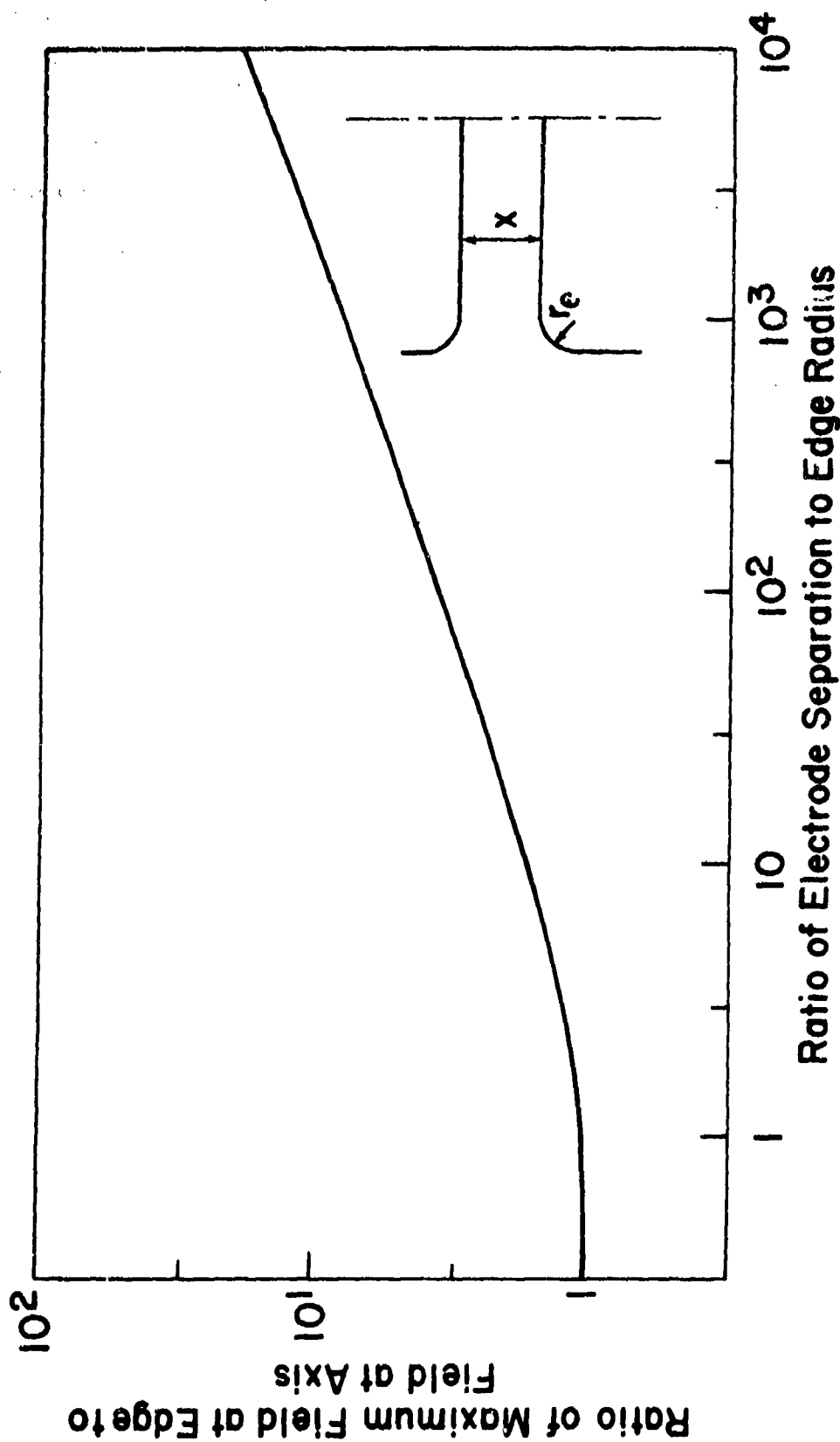
Figure 7. Edge Enhancement as a Function of Electrode Geometry

b. Space-Charge Effects on Field Emission

Space-charge effects further complicate the proper interpretation of a Fowler-Nordheim plot. When the field-emitted electron current densities exceed 10^6 amperes/cm^2, Dyke et al. (Ref. 31) have shown that the electron space-charge in the vicinity of the emitter surface is sufficient to appreciably reduce the applied field. While the space-charge effects do not invalidate the Fowler-Nordheim equation, they do cause an apparent departure from this equation if the current density is plotted as a function of the applied microscopic field F rather than the true surface field F_s. The true surface field is equal to the applied field less the space-charge component. Calculations of the electrostatic potential and the current density distribution have been performed for the case of a point-to-plane, field-emission diode (Ref. 29). The results are shown in figure 8 for two typical values of the emitter work function. Since F_s is the actual field at the cathode surface, the dashed curves $j(0,F_s)$ simply represent the Fowler-Nordheim equation for ϕ = 3 and 4.5 eV. The straight line $j_s(F)$ represents the upper limit which corresponds to fully space-charge limited electron flow. The space-charge limited current density j_s must be independent of the cathode work function and is relatively insensitive to the protrusion radius and the electrode separation. The curves $j(0,F)$ then represent the calculated dependence of the actual emission density on the applied field.

c. Energy Exchange Processes

Electron emission at the extremely high-current densities distinctive of field emission produces substantial ohmic heating of the emitter.

29
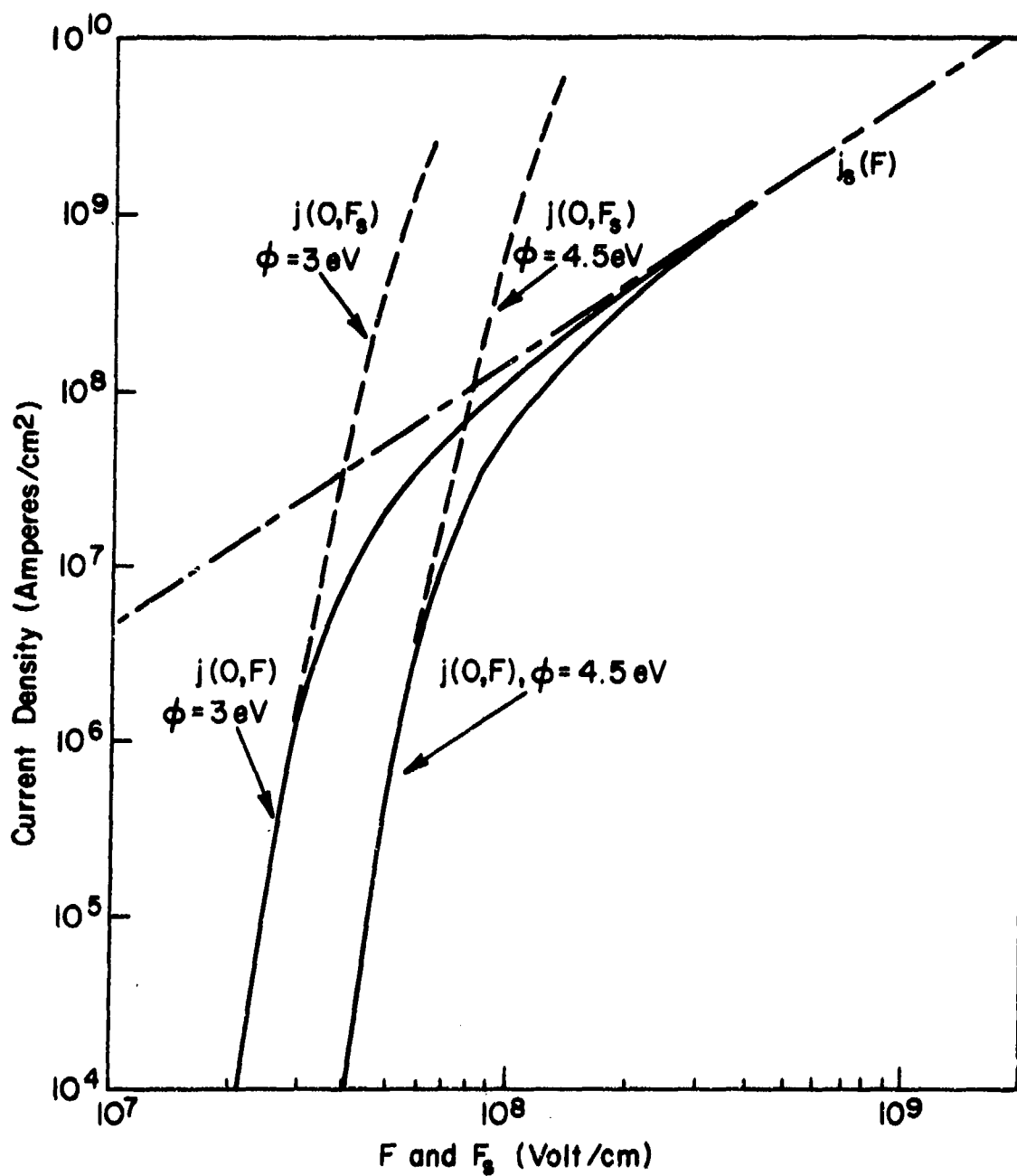
Figure 8. Space-Charge Effects on Field Emission from a Point to Plane Diode

The presence of high cathode temperature at the tip of an initially cool single-point emitter was first inferred by Dyke (Ref. 31) from several observed effects which require the existence of T-F rather than field emission. Several later experiments, however, could not be explained by appealing to the resistive heating theory. In this regard, the rapid heating of supercooled field-emission tips and the long-term emission stability which can be achieved at emitted current densities just below the threshold for vacuum breakdown are of particular note. Further analysis of the physical situation led to the recognition of a second energy exchange process, the Nottingham effect, which accompanies field and T-F emission.

Nottingham (Ref. 32) recognized that when the emitted electrons are replaced in the internal distribution that an energy exchange process develops between the crystal lattice and the electron distribution. Applying the Sommerfeld free-electron model for metals, he proposed that the emitted electrons are replaced from the Fermi level. Thus, if an electron is emitted from a position within the internal distribution located below the Fermi level, the replacement electron must give up a certain amount of energy to the crystal lattice. The amount of energy lost is equal to the energy difference between the Fermi level and the energy level of the emitted electron. The energy lost by the replacement electron is then gained by the crystal lattice. Similarly, if an electron is emitted from a position above the Fermi level, the replacement electron must extract the required energy differential from the crystal lattice. The latter sequence corresponds to cooling the emission surface while the former results in heating.

Referring to the energy diagram shown in figure 9, the average energy $\bar{U}'$ of the charge carriers which replace the emitted electrons is equal to $-\phi$ if the zero reference energy is that of an electron at rest outside the metal. In thermionic emission, the average energy of the emitted electrons $\bar{U}$ is 2 kT. Consequently, the Nottingham effect leads to a cooling of the cathode surface by an amount $\bar{U} - \bar{U}' = \phi + 2$ kt per emitted electron. For typical thermionic current densities, the net rate of energy loss by the cathode is a few watts/cm^2.

In the limiting case of field emission (T = 0°K), there are no conduction electrons above the Fermi level. As illustrated in figure 9, the energy distribution of the field-emitted electrons is exponential and the average energy of the emitted electrons is $-(\phi + d)$. The amount of energy added to the crystal lattice is therefore equal to d, which is given by equation (7). The Nottingham effect therefore produces heating of the cathode by an amount which may vary from 0.1 to 0.3 eV per emitted electron, depending on the applied field and the cathode work function. Although the amount of energy exchange per electron is much smaller than in the case of thermionic emission, the effect on tip temperature is much greater because field emission current densities can readily exceed 10^7 amperes/cm^2. Typically, Nottingham power inputs at the emitting surface are on the order of 10^8 watts/cm^2.

At high current densities, emission-induced heating raises the average energy of the conduction electrons and hence, the average energy $\bar{U}$ of the emitted electrons. As a result, the energy input from the Nottingham effect decreases in magnitude and eventually reverses direction at high

32
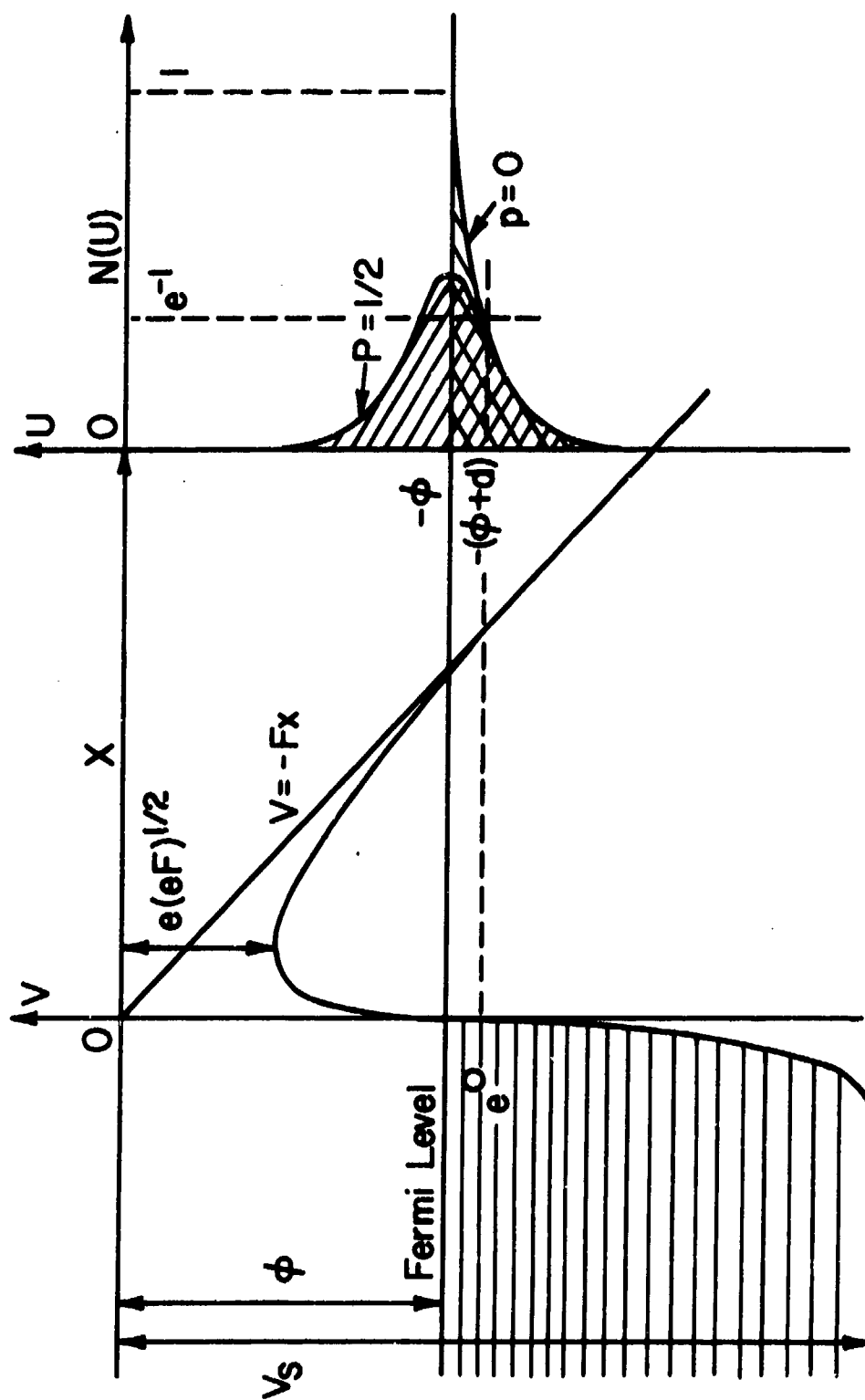
Figure 9. Energy Distribution for Field or T-F Emitted Electrons

temperatures. Above this inversion temperature, the Nottingham effect removes energy from the lattice and opposes the resistive heating. As a source of cooling, the Nottingham effect has a moderating influence on the tip temperature. The simple theory yields an approximate relation between the applied electric field F(volts/cm) at the protrusion tip, the cathode work function ϕ(eV), and the inversion temperature T_i(°K).

$$T_i = d/2k$$
$$\approx 5.35 \times 10^{-5} \, F/\phi^{1/2} \tag{13}$$

4. FIELD-EMISSION INITIATED VACUUM ARC

a. Field-Emission Hypothesis

Electrical breakdown between metallic electrodes has been a long-standing problem in the electronics industry, particularly in the design of high-energy particle accelerators. Over the years many theories have been proposed to explain the initiation of vacuum breakdown. For convenience, these theories have been grouped into three categories.

(1) Field-emission hypothesis--first proposed by Ahearn in 1936 (Ref. 33) and later refined and experimentally verified by Dyke (Ref. 34) in 1953.

(2) Clump hypothesis--described by Cranberg in 1952 (Ref. 35).

(3) Particle exchange hypothesis--the basic model first proposed by Van Atta et al. in 1953 (Ref. 36).

The diversity of theory reflects the complexity of the physical processes which may be involved. Prior to the 1950s, quantitative verification of the various proposed breakdown initiation mechanisms had been difficult.

34

However, with an increased ability to achieve high vacuum and the development of techniques to determine both the degree of surface contamination and the microscopic condition of the electrode surfaces, the more recent studies provide excellent detail and cover a wide range of pertinent parameters and experimental configurations.

In a recent paper, Charbonnier reviewed the processes associated with the initiation of vacuum breakdown (Ref. 21). When limited to the range of applied electric field and pulse duration experienced in the diodes of pulsed, high-current electron accelerators, the dominant processes which initiate the transition to a vacuum arc must be described by the field-emission hypothesis. The particle exchange and clump theories, which involve substantial transit times across the gap, are not likely to cause breakdown under impulse conditions.

According to the field emission hypothesis, vacuum breakdown proceeds as follows. The field-emission from microprotrusions on the cathode surface occurs at comparatively low applied fields. As the gap voltage is increased, the field-emitted current density increases exponentially. Excessive emission then results in protrusion heating. The accelerated electron streams emitted from multiple-cathode protrusions may also cause localized heating at the anode surface. When the applied voltage reaches a critical value, regenerative thermal instabilities will develop at either the cathode or anode. Once these instabilities have been initiated, breakdown by evaportation and subsequent ionization of the electrode material follows immediately. Such factors as the electrode geometry, the field enhancement factor, the relative electrode material, and the pulse duration

35

of the gap voltage determine whether this critical condition first occurs at the cathode or anode.

b. Cathode-Initiated Vacuum Breakdown

Quantitative investigations first by Dyke (Ref. 34) and than later by Charbonnier (Ref. 21) and Fursei (Ref. 37) have led to a consistent description of the critical conditions which result in cathode-initiated vacuum breakdown. They argue that cathode-initiated breakdown occurs in the following manner. Emission at the high-current densities character-istic of field-emission produces substantial ohmic and Nottingham heating of the microscopic emission sites. While the Nottingham effect is the primary energy exchange process in the initially cold emitter, ohmic heating takes over as the resistance increases at elevated temperatures. The heat-ing continues until a critical tip temperature is achieved. Experimental studies of cathode-initiated breakdown have shown that the onset of a rapid thermal instability occurs when the tip temperature reaches a critical value which corresponds to a vapor pressure of the protrusion material on the order of 10^{-4} torr.

The unstable condition which triggers the breakdown has its basis in the space-charge limited character of high-current density emission. The calculated current densities required to raise the steady-state tip temperature of a typical protrusion to the critical value are on the order 10^7 amperes/cm^3. Emitted current densities of this magnitude are more than sufficient to space-charge limit the current flow in the vicinity of the protrusion tip. The emitted current density is consequently reduced to a small fraction of what it would be if space-charge effects were absent.

As the tip temperature increases, cathode material is evaporated into the region immediately beyond the whisker tip. Evaporation into this region maximizes not only the probability of cathode vapor being ionized by electron collision but also the effect of the resultant ions in neutralizing the electron space charge. With the space-charge limitation thereby reduced, extremely rapid increases in the emitted current density and the subsequent resistive heating follow immediately. The regenerative nature of this cycle will therefore result in the rapid destruction of the emission site once the critical tip temperature has been attained.

Since the critical tip temperature in refractory metals is slightly greater than the Nottingham inversion temperature, the Nottingham effect has a stabilizing influence on the tip temperature for these metals. This relationship explains the stability of emitted current densities close to the critical breakdown value. Consideration of the Nottingham effect may affect the timing of the breakdown sequence, but does not cause much change in the critical breakdown conditions.

The arguments given above imply that for a given set of experimental parameters, cathode-initiated field-emission breakdown should occur at a well-defined, critical current density. In a well-controlled experiment, the effects of such parameters as cathode material (work function, evaporation characteristics, thermal and electrical properties), protrusion geometry (thermal coupling to cathode base), and voltage pulse duration can be predicted. Without careful control, the critical current density may vary over a rather wide range, typically from 10^4 to 10^9 amperes/cm^2. Nevertheless, since the emitted current density is such a strong function of the

37

applied field, the corresponding breakdown fields fall in a fairly narrow
range. For long pulse or steady voltages and cathode work functions of
approximately 5 eV, the critical breakdown fields range from 5 to 8 x 10^7
volts/cm.

Experimental confirmation of the existence of a critical breakdown
field is available from several sources. Although Dyke (Ref. 34) is credited
with the initial quantitative confirmation, there was some doubt as to the
general application of his explanation because of the very special conditions
(ultra-high vacuum; smooth, single-crystal, needle-shaped cathode) of his
experiment. The most extensive and conclusive confirmation is that of
Alpert et al. (Ref. 27). Using broad-area, tungsten electrodes, the
authors investigated ultra-high-vacuum breakdown for applied voltages up
to 250 kV. They concluded that in all cases breakdown occurred at an average
field of approximately 6 x 10^7 volts/cm, in agreement with Dyke. A compar-
ison of their breakdown data with that of Dyke, Boyle, et al. (Ref. 22)
and Gofman (Ref. 38) is shown in figure 10. The critical breakdown field
was found to be constant and independent of gap spacing for a range of over
five orders of magnitude regardless of geometry.

The description of cathode initiated breakdown given above is predi-
cated on an assumption of thermal steady-state, and is strictly valid only
if the duration of the voltage pulse is long compared to the time constant
for thermal equilibrium within the emitting protrusion. In general, this
is not a significant restriction in that the very small dimensions of prac-
tical protrusions result in extremely short thermal equilibrium times. For
example, calculations which included both Joule and Nottingham heating have
shown that protrusions with a 0.1-micron tip radius approach steady-state

Figure 10. Variation in Critical Steady-State Breakdown Field with Electrode Separation

39

temperatures in times of the order 10^{-8} to 10^{-7} seconds (Ref. 39).

When the voltage pulse duration becomes less than the thermal equi-
librium time, the critical breakdown field will begin to increase. To
estimate the relationship between the critical breakdown field and the
pulse duration, consider the situation when the voltage pulse duration t_p
is less than $\rho c h^2/\lambda$, where ρ, c, and λ are the density, specific heat, and
thermal conductivity of the tip material, and h is the emitter height. The
pulse length is now sufficiently short that thermal diffusion does not
appreciably affect the temperature profile along the protrusion, and the
tip temperature is governed by the local generation of heat. Neglecting
the Nottingham effect and the temperature variation of resistivity, the
adiabatic heat flow equation can be integrated to yield the following
expression

$$j^2 t_p = (\rho c/\Omega) \, T_{max} \qquad (14)$$

where Ω is the resistivity of the protrusion material (ohm $\cdot$ cm), and T_{max}
($^\circ$K) is the critical tip temperature which corresponds to a vapor pressure
of 10^{-4} torr. For tungsten, the product of $j^2 t_p$ is limited to approximately
2.6×10^8 (amperes^2/cm^4 $\cdot$ sec) which corresponds to an emitted current
density of $1.6 \times 10^4 \, t_p^{-1/2}$ (amperes/cm^2) (Ref. 29). Taking t_p to be on the
order of the minimum thermal equilibrium time or approximately 10 nanoseconds
yields a current density on the order of 10^8 amperes/cm^2. Noting from
figure 8 that j is roughly proportional to V^3 in this range of current
densities, the critical breakdown field must increase approximately as $t_p^{-1/6}$.
At current densities in excess of 10^8 amperes/cm^2, the emission is fully
space-charge limited. The strongest dependence of the breakdown field on

40

pulse width must therefore be $F \propto t_p^{-1/3}$. Pulse durations in the nanosecond range thus result in breakdown fields somewhat in excess of the long pulse or steady-field value.

c. Cathode- versus Anode-Initiated Breakdown

To determine whether the breakdown process will be initiated at the anode or cathode, Charbonnier derived a boundary value for the protrusion field enhancement factor which is dependent on the relative electrode materials, the gap geometry, and the duration of the voltage pulse. The boundary value m_0 was chosen such that the existence of cathode protrusions with an enhancement factor m greater than m_0 will result in excessive heating of these protrusions before a critical power loading can be achieved at the anode. Alternatively, if all cathode protrusions have enhancement factors less than m_0, field emission from the sharper protrusions will lead to excessive heating at the anode. The subsequent evaporation and ionization of anode material results in breakdown before the current density at the protrusion reaches a critical value.

Using plane, parallel electrodes and a hemispherically-capped, cylindrical, cathode protrusion as a model (see figure 11), Charbonnier (Ref. 21) examined the critical conditions at anode and cathode which result in breakdown. The processes leading to cathode-initiated breakdown were described in the preceding paragraphs. The maximum power density which can be sustained at the anode is dependent on the anode material, the duration of the voltage pulse, and, for very short pulses, the magnitude of the applied voltage.

To determine the power density at the anode, it is necessary to know the expansion of the electron beam as it traverses the gap. The radial

41
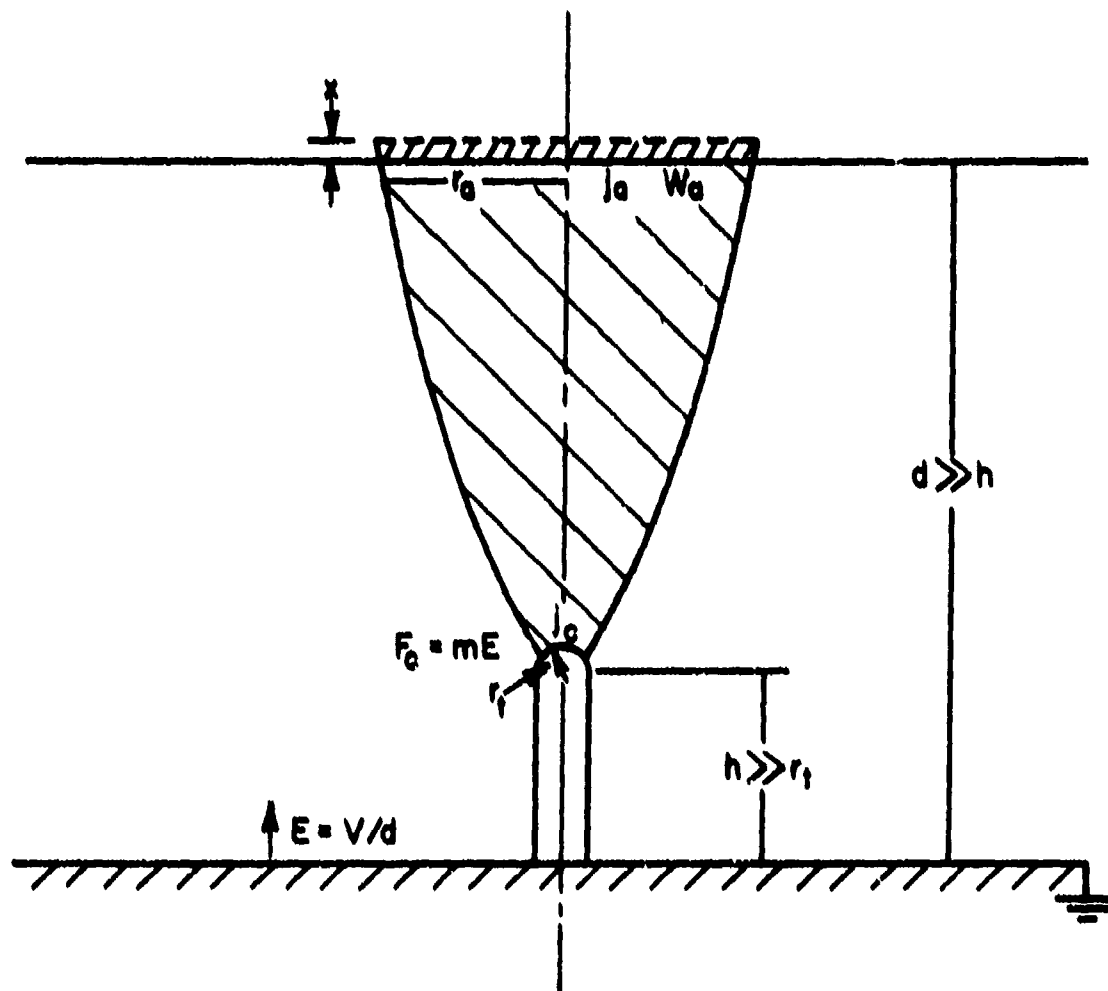
Figure 11. Field Emission from a Whisker-Like Cathode Protrusion
in a Plane Parallel Gap

expansion of the beam is dependent on the initial electron velocity result-
ing from its field emission, the shape of the field lines near the tip of
the emitting protrusion, and, at high-current densities, space-charge
effects. Normally the accelerating voltages greatly exceed the internal
potential barrier within the cathode material (eV $>>$ ϕ) and the initial
velocity of the electron is negligible. The field distortion in the
vicinity of the protrusion tip is substantial, however. The electrons are
strongly accelerated in this region, and acquire essentially all of their
transverse velocity within a distance equivalent to a few tip radii.
Vibrans (Ref. 31) has shown that nonuniform field effects are the predom-
inant cause of beam spreading. Space-charge effects can therefore be
neglected.

After entering the parallel field in the gap, the electrons follow
a parabolic trajection. Utsumi (Ref. 28) has incorporated the effects of
the nonuniform field by revising the parabolic trajectory as follows:

$$z = hr^2/4\eta \tag{15}$$

where r is the radial coordinate and η is the spreading factor. Calculated
values for the spreading factor as a function of h/r_t for cylindrical and
semispheroid protrusions are shown in figure 12. For cylindrical protru-
sions with h/r_t greater than about 3, the spreading factor is equal to 0.5.

The radius of the anode spot r_a can be related to the protrusion
field enhancement factor by using the equation for the enhancement factor
of a cylindrical protrusion derived by Vibrans given in equation (12).
Assuming that $r_t << h << d$, the beam radius at the anode, r_a, and the anode
power density, W_a, can be written as
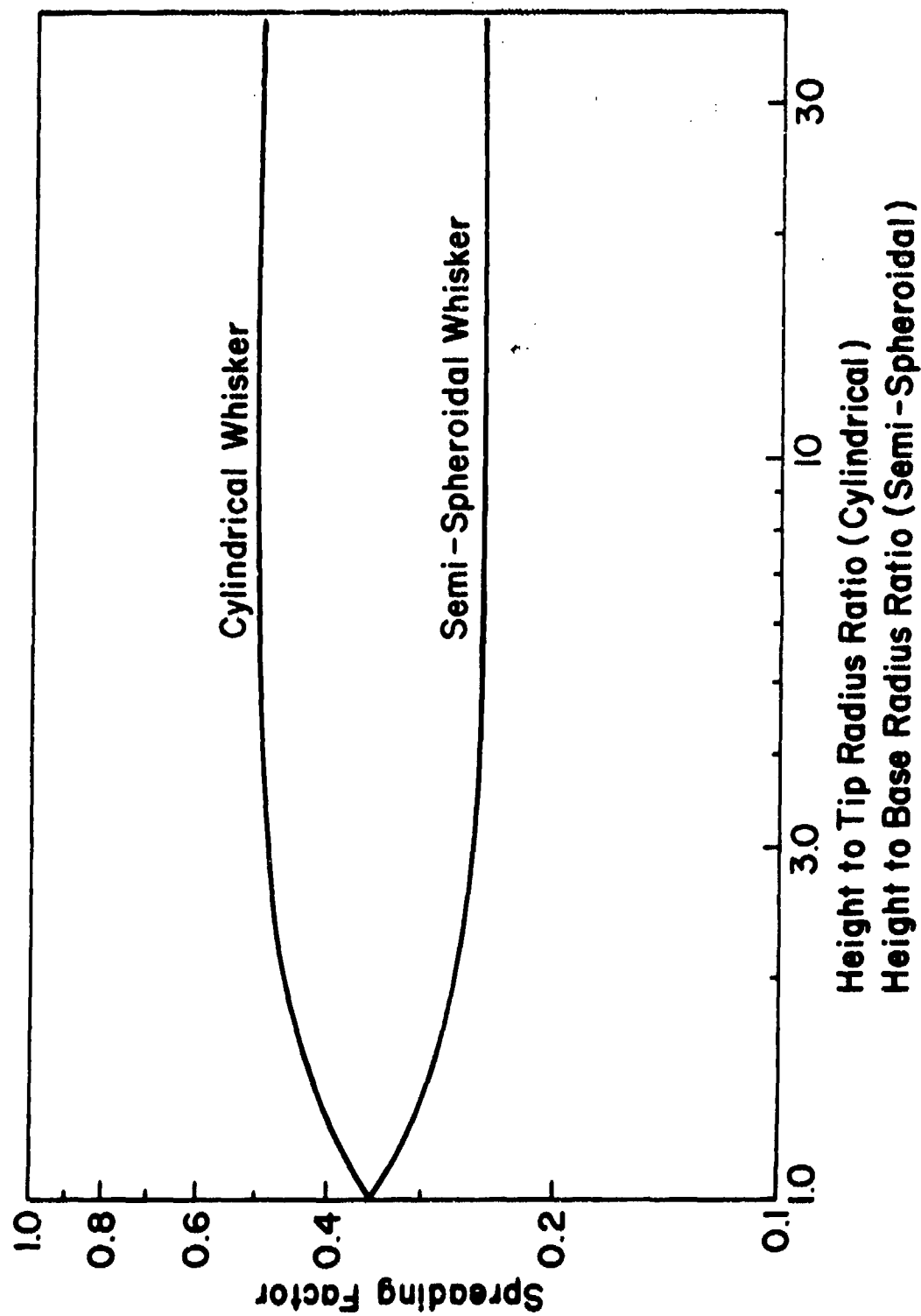
Figure 12. Variation in Electron Beam Spreading Factor with Whisker Geometry

44

$$r_a = \left(2 \, mr_t d\right)^{1/2} \qquad (16)$$

and

$$W_z = IV/\pi \, r_a^2 = hjF/(2m^3) \qquad (17)$$

or

$$m = \left(hj_c F/2W_a\right)^{1/3} \qquad (18)$$

In this expression for the field enhancement factor, the numerator depends only on conditions at the protrusion tip, and the denominator only on conditions at the anode. Field emission at a current density above a critical value j_c causes excessive emission-induced heating at the protrusion tip. The critical current density can, in turn, be related to a critical value of the field F_c at the protrusion tip through the Fowler-Nordheim equation. Similarly, there is a maximum power density which can be sustained at the anode above which evaporation, ionization, and subsequently, breakdown result. A boundary value for the field enhancement factor can, therefore, be defined as

$$m_0 = \left(hj_c F_c/2W_{am}\right)^{1/3} \qquad (19)$$

where W_{am} is the maximum anode power density.

For the present situation, where the gap spacing and the radius of the anode spot are usually small, the critical beam power density at the anode is determined by heat absorption and diffusion into the bulk of the anode, rather than by radiation. Three possible cases are recognized, depending on the voltage pulse duration relative to two characteristic anode thermal time constants. The time constants t_{c1} and t_{c2} are defined by setting the thermal diffusion length $(2\lambda \, t/c\rho)^{1/2}$ equal to first the

45

effective electron penetration depth x and then the beam radius at the anode r_a. Thus,

$$t_{c_1} = c\rho x^2/2\lambda \qquad (20)$$

and

$$t_{c_2} = c\rho r_a^2/2\lambda \qquad (21)$$

where c, ρ, and λ are the specific heat, density, and thermal conductivity of the anode material. In practice, x is usually much smaller than r_a, so that $t_{c_1} \ll t_{c_2}$.

The duration of the voltage pulse applied across the diodes of pulsed high-current accelerators are typically less than 100 nanoseconds. Depending on the anode material and the accelerating voltage, the pulse length is therefore comparable to or less than t_{c_1}. In this situation, the pulse duration is too short for significant heat diffusion beyond the depth x. Assuming the temperature distribution to be approximately uniform to the depth x, the temperature rise at the end of the pulse is approximately

$$\Delta T = W\, t_p/xcp \qquad (22)$$

and

$$m_0 = \left(\frac{hj_c\, F_c\, t_p}{2\, xcp\, \Delta T_m}\right) \qquad (23)$$

The probable magnitude of m_0 can be estimated from the following argument. Levine (Ref. 40) demonstrated that resistive heating causes a long cylindrical protrusion made of tungsten (or other materials for which the resistivity increases at least linearly with the temperature) to heat

46

without limit if the product of current density by protrusion height $j_c h$ exceeds a critical value, which for tungsten is 1.4×10^4 amperes/cm. This corresponds to a critical field of approximately 6×10^7 volt/cm. Substituting these values into equation (23) yields

$$m_0 = 7500 \ W_{am}^{-1/3} \qquad (24)$$

Assuming the use of a tungsten anode, ΔT_m is $2500°K$ and $x \approx 2 \times 10^{-2} \ V^{3/2}$ where x is in centimeters and V is in megavolts. Equation (24) then becomes

$$m_0 \approx 20 \ t_p^{1/3} \ V^{-1/2} \qquad (25)$$

where t_p is in microseconds. Setting $t_p = 0.1 \ \mu sec$ and $V = 1 \ MV$ yields $m_0 \approx 9$. Since large surfaces with maximum local field enhancement factors less than 20 are seldom achieved, cathode-initiated breakdown is virtually certain in the diodes of pulsed electron accelerators.

The distinction made here concerns only the initial phase of the breakdown. Substantial evaporation and subsequent ionization at one electrode results in a strong increase in electron beam current and power, which rapidly pushes the other electrode beyond the thermal limit. Both electrodes will therefore participate eventually in the development of a vacuum arc.

5. HIGH-SPEED BREAKDOWN PROCESSES

a. Nanosecond Bre-'down and the Formation of Cathode Flares

Within the past several years, a continuing series of Soviet studies have been reported which describe the phenomena of explosive field emission. These studies are particularly pertinent to diode phenomenology since they

47

extend the earlier work on field-emission breakdown to the range of nano-second pulse durations and emphatically demonstrate the processes associated with the transition to a vacuum arc. Prominent articles related to this subject include those of Mesyats et al. (Refs. 41, 42), Bugayev et al. (Refs. 43, 44), Kartsev et al. (Ref. 45), and Fursey et al. (Refs. 37, 46, 47).

A general summary of the discharge phenomena in question has been given by Mesyats and Proskurovsky (Refs. 41, 48). Of particular interest to a study of diode phenomenology are two experimental studies in which the authors investigated the high-speed processes which occur during pulsed breakdown of vacuum gaps. In the first set of experiments, flat, broad-area electrodes of molybdenum, copper, aluminum, lead, and graphite were subjected to square pulse voltages of 20 to 50 kV having rise times of approximately 1 nanosecond and pulse durations which varied from about 10 to 100 nanoseconds. The electrodes were placed in a vacuum (10^{-8} torr) and separated by from 0.1 to 0.5 mm. The evolution of high-speed break-down processes initiated at the electrode surfaces was then observed using electro-optical photography of plasma motion in gap, and by monitoring the current flow in the diode.

The results of these tests have provided the first direct evidence of the dominant role of cathode processes in the initiation of pulsed break-down. The observations of Bugayev et al. are best illustrated by considering a schematic of the observed plasma phenomena, time correlated with the resultant current pulse (Refs. 43, 44, 49). The schematic (figure 13) shows the photographed plasma motion which developed during the breakdown

48
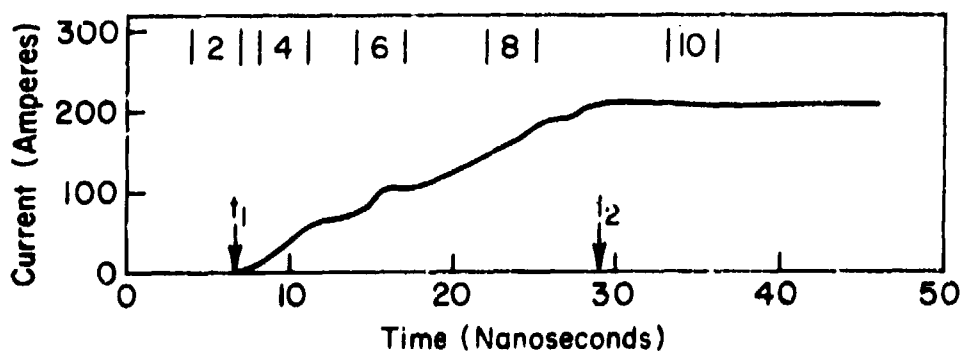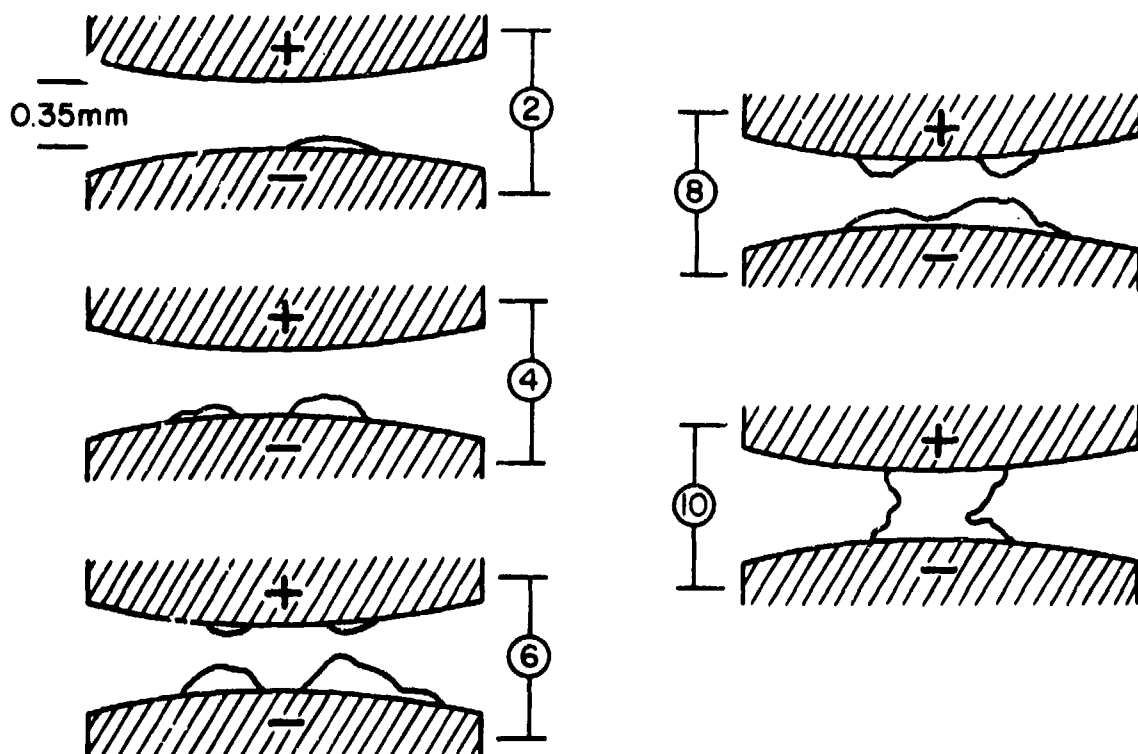
Figure 13. Observed Plasma Motion During the Breakdown of Vacuum Gap

49

of copper electrodes separated by 0.36 mm. The voltage pulse was applied at t_0, followed by the emission of the first measurable current at t_1. By t_1, a vacuum arc had been established and the current had risen to a value limited by the circuit parameters. From the photographs, localized plasma flares were observed on the cathode 4 to 6 nanoseconds after the application of the voltage to the gap. Moreover, the appearance of the cathode flares was coincident to the initial observation of measurable current. Following its formation, the cathode flare plasma expanded at a velocity of approximately 2×10^6 cm/sec.

The initiation of the breakdown was as predicted by the field-emission hypothesis. Phenomena associated with the explosive nature of the protrusion destruction and the formation and expansion of cathode flares are, however, beyond the scope of the field-emission hypothesis. Note that the total current following the flare formation was substantially higher than the stable field-emission current. Moreover, current emission after t_1 was space-charge limited and therefore dependent on the expansion of flare plasmas.

The observed dependence of the time interval $t_1 - t_0 = t_b$ on applied field, cathode material, and electrode separation is shown in figure 14 (Refs. 44, 49). The time to breakdown t_b was found to be independent of electrode separation but strongly dependent on the magnitude of the applied field. A moderate dependence on cathode material was also observed. The range of applied field producing a sharp increase in the breakdown delay, t_b, corresponded to the fields required for steady-state breakdown.

50
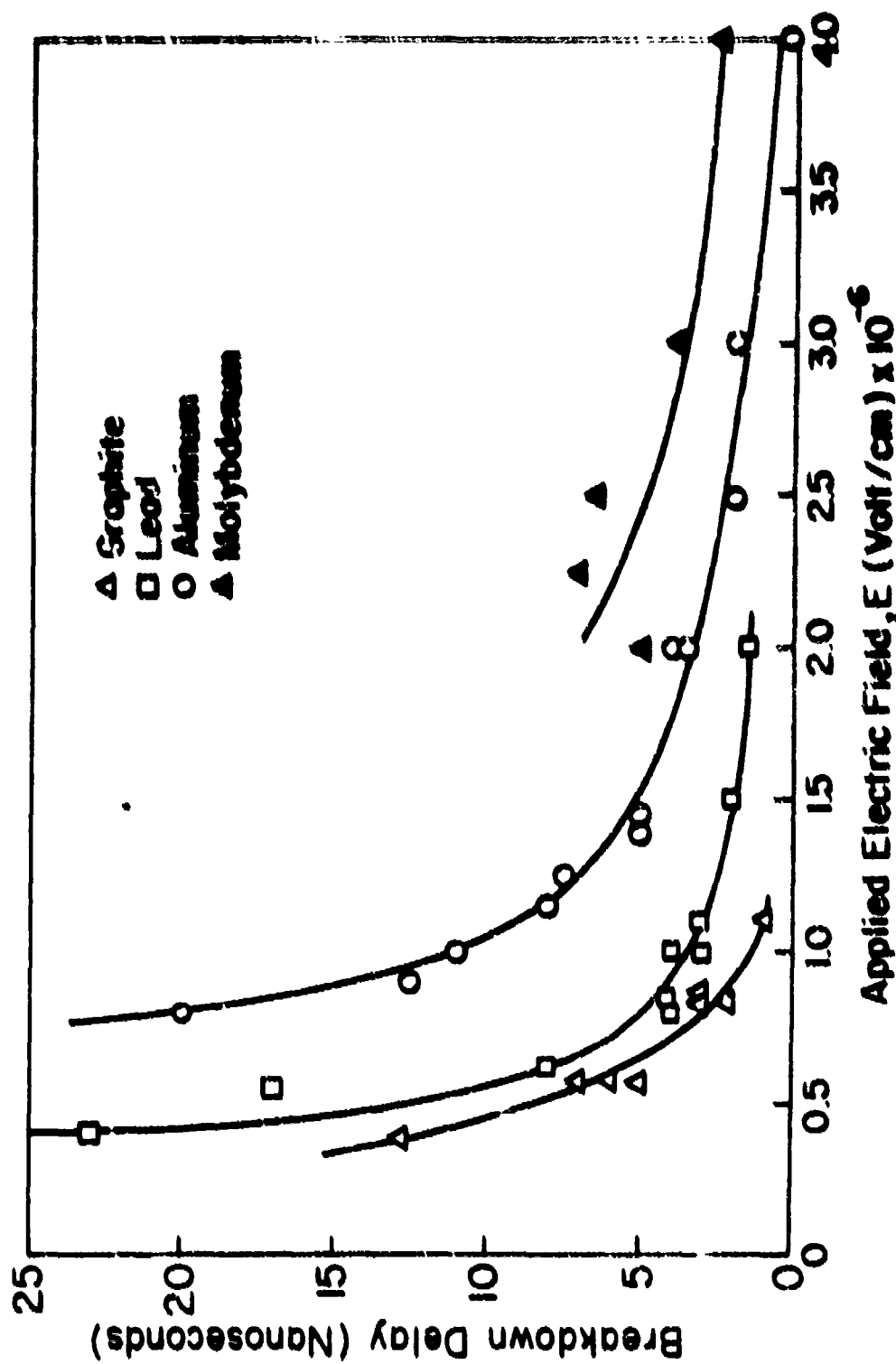
Figure 14. Breakdown Delay as a Function of Applied Field and Electrode Materials

51

Although these initial experiments posed several intriguing questions concerning the basic nature of the explosion process and subsequent electron emission, quantitative measurement of such factors as the critical breakdown conditions and the flare plasma parameters was not possible under the constraints of their initial experiment. To remove these difficulties, Mesyats et al, switched to an electrode configuration similar to that used by Dyke; i.e., they replaced the broad-area cathode with a microscopic, single-point emitter. By using a single-point emitter of 1- to 10-micron diameter, the precise electrode geometry and surface conditions were known. Throughout the second series of experiments, needle cathodes of tungsten, molybdenum, and copper were placed in vacuo 0.05 to 1 cm from a planar anode and subjected to square pulses of 10 to 500 kV. As in the initial experiments, the voltage rise time was approximately 1 nanosecond. Pulse widths varied from 5 to 50 nanoseconds, but in all cases were less than the time required to evaporate anode material. The objectives of the experiment were to evaluate protrusion heating under transient conditions, to investigate the protrusion explosion process, and to determine the electron emission mechanism following the protrusion explosion.

b. Time-Dependent Heating of Cathode Protrusion

As stated earlier, the thermal equilibrium time for protrusions with 0.1-micron tip radii are of the order 10^{-7} to 10^{-8} nanoseconds. When the pulse duration is less than the protrusion equilibrium time, steady-state analysis is no longer appropriate. Mesyats extended the previous protrusion heating calculations by considering the time-dependent problem. If the time to breakdown is greater than $(\rho c r_t/\lambda)^2$ but less than $(\rho ch/\lambda)^2$,

the calculation reduces to solving the following one-dimensional, semi-infinite boundary value problem.

$$\frac{\rho c}{\lambda} \frac{\partial T(z,t)}{\partial t} = \frac{\partial^2 T(z,t)}{\partial z^2} + \frac{Q(T)}{\lambda}$$

$$T(z,0) = T_0$$

$$\lambda \frac{\partial T(0,t)}{\partial z} = -H(T) \tag{26}$$

where r_t and h are the protrusion tip radius and height, respectively; ρ, λ, and c are the density, thermal conductivity, and specific heat of the protrusion material; and $Q(T)$ and $H(T)$ are the volumetric source and heat flux vector (rate of energy transfer per unit area). For the case of emission-induced heating, the volumetric heat source results from resistive heating while the Nottingham effect determines the heating or cooling at the surface. The appropriate expressions for $Q(T)$ and $H(T)$ are, therefore,

$$Q(T) = j_{TF}(T)^2 \, \Omega(T) \tag{27}$$

$$H(T) = \frac{\pi k T}{e} \, j_{TF}(T) \cot \pi \, p(T) \tag{28}$$

where k is the Boltzmann constant, e is the electronic charge, $j_{TF}(T)$ is the T-F emission current density, Ω is the resistivity, and p is the dimensionless parameter introduced in equation (6). By incorporating equation (13), p can be written as being equal to $T/(2/T_i)$, where T_i is

53

the Nottingham inversion temperature.. If the change in resistivity with temperature is included by defining $\Omega = \Omega_0 T$, three dimensionless coordinates can be defined as follows:

$$X = j_F\left(\Omega_0/\lambda\right)^{1/2} z$$

$$\tau = \left(j_F^2 \, \Omega_0/\rho c\right) t$$

$$Y = \left(\pi T/2T_i\right) \tag{29}$$

where j_F is the field emission current density, which is independent of the temperature. Since the T-F emission current is determined by the surface temperature of the emitter, the boundary condition is defined as $Y_E = Y(0,\tau)$. By substituting equations (27), (28), and (29) into equation (26), the boundary value problem can be rewritten as

$$\frac{\partial Y}{\partial \tau} = \frac{\partial^2 Y}{\partial X^2} + Y \left(\frac{Y_E}{\sin Y_E}\right)^2$$

$$Y\big|_{\tau=0} = Y_0$$

$$\frac{\partial Y}{\partial X}\bigg|_{X=0} = - \frac{\pi k}{e\left(\Omega_0\lambda\right)^{1/2}} \left(\frac{Y_E}{\sin Y_E}\right)^2 \tag{30}$$

where $Y_E = Y(0,\tau)$. The Wiedmann-Franz law gives $\pi k/e(\Omega_0\lambda)^{1/2}$ as being equal to $\sqrt{3}$. Mesyats et al. have solved the boundary value problem numerically using the physical constants of tungsten (Ref. 47). The calculated dependence of the surface temperature with time is shown in figure 15, which gives values of j_{TF}/j_F as a function of τ. The ratio of j_{TF}/j_F is

54
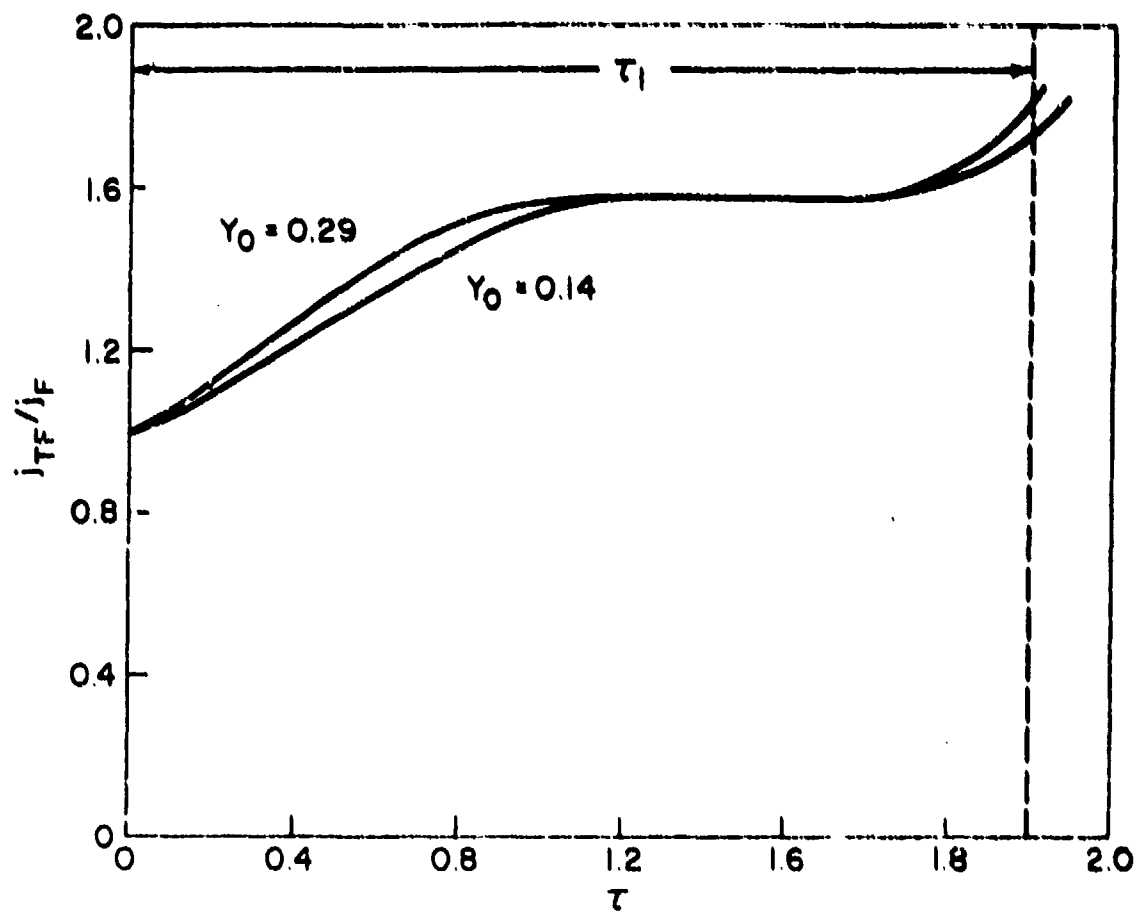
Figure 15. Solution to One-Dimensional, Transient Heating Problem

given by

$$J_{TF}/J_F = \pi p/\sin \pi p \qquad (31)$$

where $p = T/2T_i$ and $T_i \approx 5.35 \times 10^{-5} F/\phi^{1/2}$. T_i is in °K, F in volt/cm, and ϕ in eV. For a fixed value of F, J_{TF}/J_F is, therefore, a measure of the surface temperature. The plateau on the curve when $J_{TF} = (\pi/2)J_F$ results from the effects of Nottingham cooling. At later time when J_{TF} exceeds $(\pi/2)J_F$, unrestricted heating results and the emitted current density rapidly increases. For this analysis, breakdown was said to occur at the instant when J_{TF} exceeded $(\pi/2)J_F$ by 10 percent. The breakdown delay interval τ_i was seen to be unchanged by variation in the initial condition Y_0. In this case, the values of Y_0 correspond to the magnitude of applied field. For initial surface temperatures on the order of room temperature, the values of Y_0 used in the calculation correspond to the following approximate values of applied field and initial field-emission current density (table II).

Table II

INITIAL CONDITIONS FOR TRANSIENT HEATING CALCULATION

Y_0	F_0(volt/cm)	J_F(ampere/cm^2)
0.14	6×10^7	5×10^7
0.29	1.2×10^8	2×10^8

If τ_i is independent of the initial applied field over the range listed above, the following approximate relation is valid:

$$J_F^2 \, t_b \approx 2.2 \, \rho c/\Omega_0 \qquad (32)$$

56

where t_b is the breakdown delay interval. Such a relation is not unexpected (see equation (14)). By assuming that the critical current density j_c was equal to i_{TF}/r_t^2, where i_{TF} is the T-F emission current, and r_t is the emitted tip radius, Mesyats reduced equation (32) to

$$j_c^2 \, t_b = 0.55 \, \frac{\pi^4 pc}{\Omega_o} \qquad (33)$$

Using the physical constants of tungsten, $j_c^2 \, t_b = 4.5 \times 10^9$ ampere · sec/cm⁴ which was in good agreement with the experimental value of 4×10^9 ampere · sec/cm⁴.

As shown in figure 8, emitted current densities in excess of approximately 10^6 ampere/cm² result in an apparent departure from the Fowler-Nordheim relation because of space-charge effects. The emission of transiently stable current densities of the order 10^9 amperes/cm² is, therefore, definitely space-charge limited. The space-charge limited current density can be estimated from the infinite-planar Child-Langmuir equation

$$j_c \approx \frac{4}{9\mu} \, \frac{V_c^{3/2}}{Z^2} \qquad (34)$$

In this equation, μ is equal to $2\pi \, (2m/e)^{1/2}$ where m and e are the electron mass and charge, respectively. V_c can be estimated by assuming that $V_c = F_c Z$, where F_c is the field at the tip of the emitter ($F_c = mE$) and Z is a characteristic length of the field distortion around the emitter tip. By assuming that Z is of the order of the emitter tip radius, equation (34) can be rewritten as

$$j_c \approx \frac{4}{9\mu} \frac{(mE)^{3/2}}{r_t^{1/2}} \tag{35}$$

Combining equations (33) and (35) results in

$$t_b = \frac{280 \; \mu^2 \; \rho c \; r_t}{\Omega_0 \; m^3 \; E^3} \tag{36}$$

When using broad-area cathodes, the parameters r_t and m are generally unknown unless the stable field-emission current can be measured. Experimental results have shown, however, that for a given range of F, t_b does not vary much. In view of equation (36), this would imply that the enhancement factor and tip radius characteristic of the sharpest protrusions vary within a limited range. Equation (36) can therefore be reduced to

$$t_b \; \alpha \; E^{-1/3} \tag{37}$$

This relation is verified by the data shown in figure 16 which shows the dependence of the breakdown delay time for aluminum electrodes on the magnitude of the applied field. The data is plotted a $\log_{10} t_b$ versus $\log_{10} E$ to show the linear dependence and slope of approximately 3 with respect to the abscissa.

c. Protrusion Explosion

The explosive nature of the destruction of a protrusion has been compared to the explosion of thin wires by electric current in vacuo. The expansion of exploding wire plasma into vacuum has been described as the sudden adiabatic expansion of a spherical gas cloud (Ref. 50). Since the
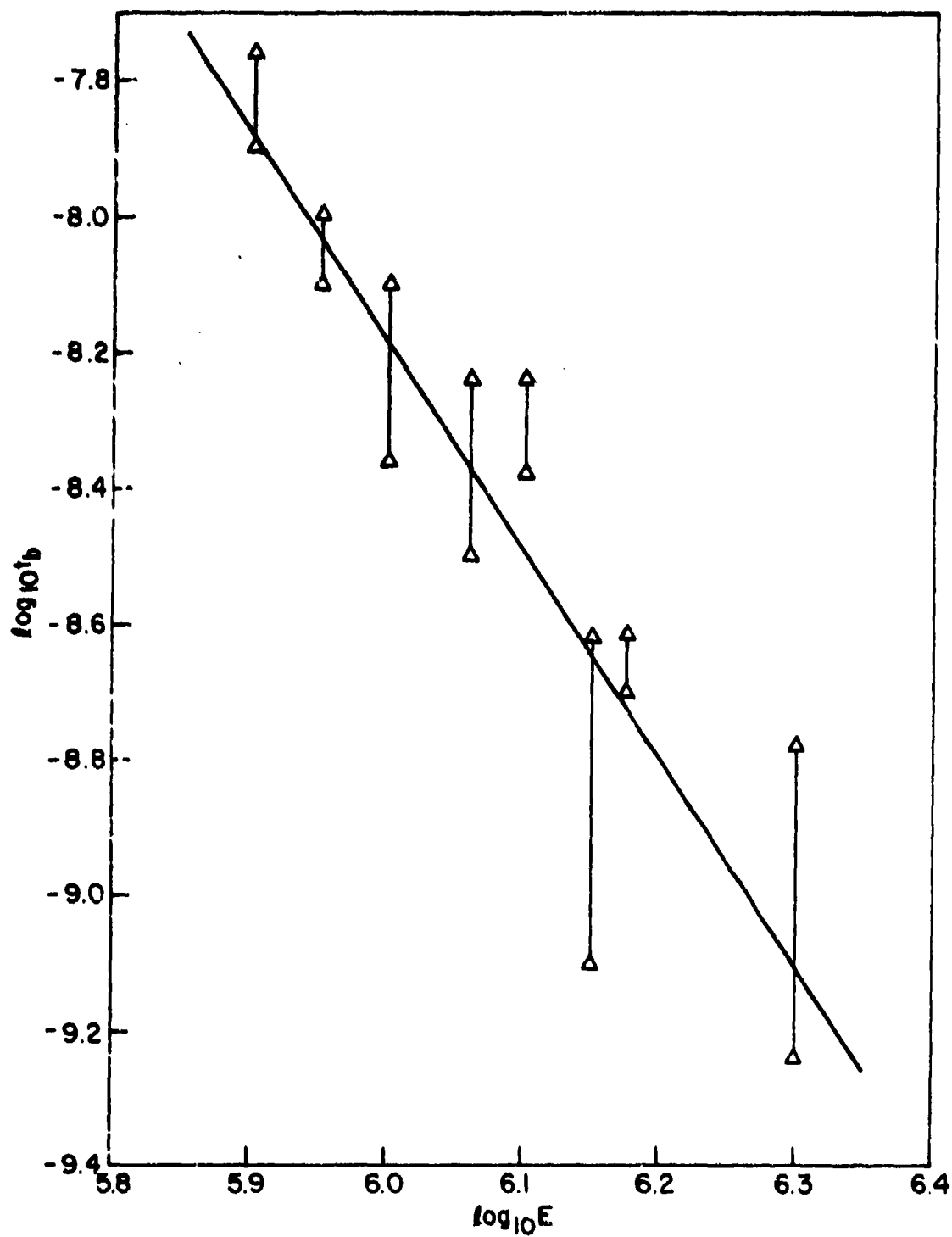
Figure 16.   Breakdown Delay as a Function of Applied Field

59

flare plasma becomes collision-free for inelastic processes in times on the order of 10^{-8} seconds and subsequent plasma heating by electron flow becomes negligible, Mesyats et al. (Ref. 48) have applied the gas dynamic solution for adiabatic expansion to the cathode flare. From gas dynamics the boundary velocity v_{max} can be related to the late-time inertial expansion velocity v_∞ in the following manner

$$v_{max} = \left(\frac{2\gamma}{\gamma-1}\right)^{1/2} v_\infty \tag{38}$$

where γ is the adiabatic exponent, equal to the ratio of specific heats at constant pressure and constant volume. As the thermal portion of the total gas cloud energy, U, approaches zero asymptotically with time during the expansion, conservation of energy require that the kinetic energy approaches U. When the kinetic energy is nearly equal to U, the fluid expands by inertia. The average velocity of the gas cloud of mass M then approaches the constant limiting value $v_\infty = (2U/M)^{1/2}$. If the initial internal energy of the gas is determined predominantly by the latent heat of sublimation or evaporation of the protrusion material and some amount of superheating is possible, the ratio U/M is given by $\kappa\Sigma$ where κ is the superheat factor and Σ is the latent heat of sublimation/evaporation. Combining these factors, the expansion velocity of the flare plasma should be of the order

$$v = \left(\frac{4\gamma}{\gamma-1}\,\kappa\Sigma\right)^{1/2} \tag{39}$$

Assuming the flare plasma to act as a perfect gas at high temperatures, the ratio of specific heats is 5/3. According to Mesyats, exploding wire research has shown the superheat factor to be in the range 2 to 5. The

60

resultant flare expansion velocities would therefore be expected to vary from 1×10^6 to 2×10^6 cm/sec for the metals investigated. This is in agreement with experimental observations.

In a later paper (Ref. 41) Mesyats et al. reported a slight dependence of the flare expansion velocity on the rate of rise of the leading edge of the applied voltage pulse. By adjusting their experimental parameters so that the explosion would occur during the rise of the voltage pulse, Mesyats et al. could vary the specific energy evolved at the tip before it exploded. Figure 17 shows the dependence of the expansion velocity on the average rate of change in the field intensity F_c/t_r, where F_c is the peak value of the electric field at the tip of the protrusion and t_r is the rise time of the voltage pulse.

d. Electron Emission Following Emitter Explosion

Following the explosion of the emitting tip, Bazhenov et al. (Refs. 41, 51) observed that the diode perveance (electron flow from the cathode flare) exhibited a distinctive dependence on time that was invariant with the applied voltage and the electrode separation. Knowing the experimental perveance and the applied voltage, the average emission current density from the surface of the expanding flare can be estimated by assuming that the emission surface is a hemisphere of radius vt. Conservation of current then requires that the average emission density from the surface of the solid cathode be approximately twice the emission density from the expanding flare surface. With an applied voltage of 4×10^4 volts, the experimental perveance after 10 nanoseconds of current flow was 8×10^{-6} ampere/volt$^{3/2}$. If the expansion velocity was 2×10^6 cm/sec, the emission density

61
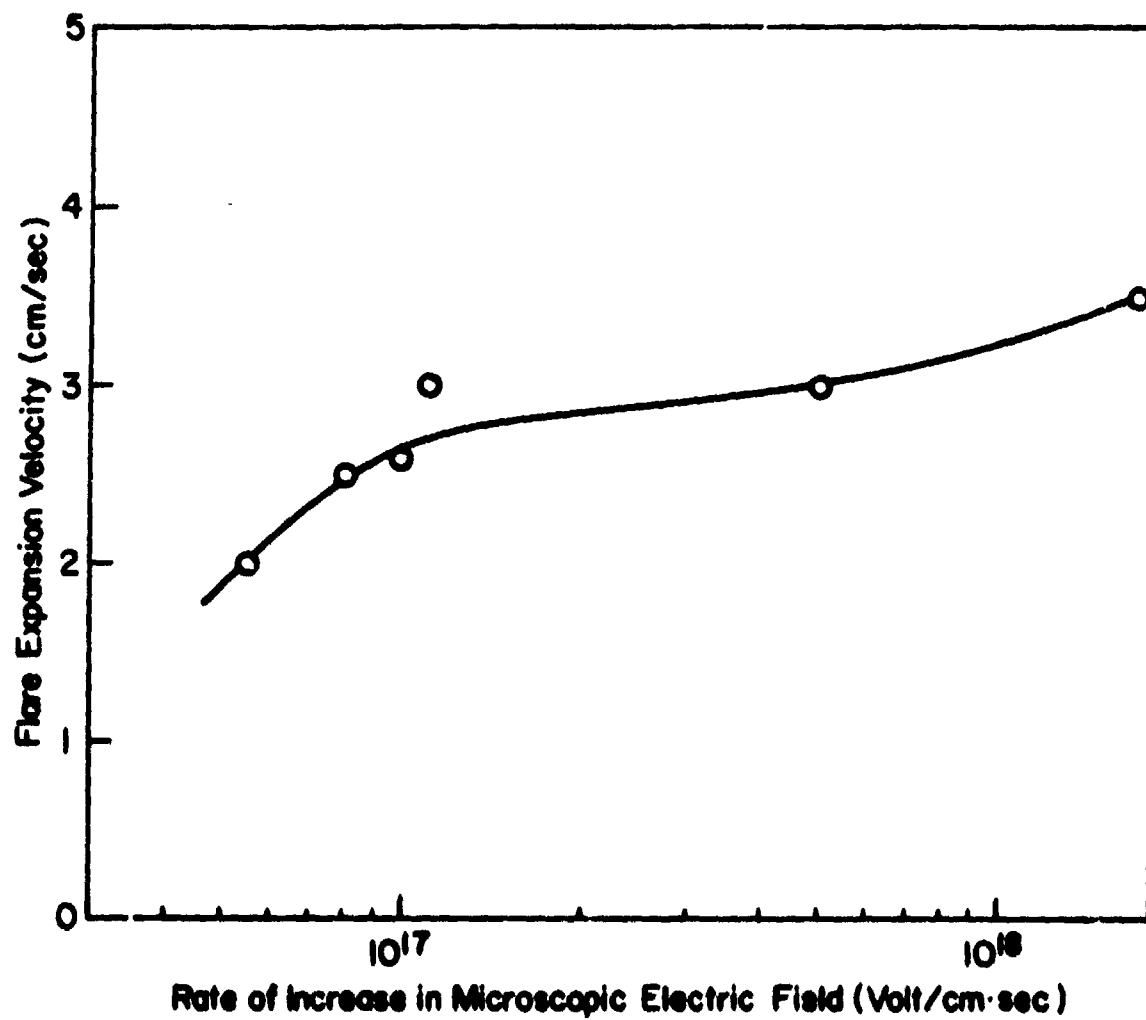
Figure 17. Dependence of the Flare Expansion Velocity on the Rate of
Increase in the Electric Field at the Emitter Tip

from the solid cathode was approximately 5.0×10^4 amperes/cm^2. To achieve this current density by T-F emission, the flare plasma must generate a Debye field of about 4.3×10^7 volt/cm. The Debye field at the surface of a conductor in contact with a plasma is given by

$$F_D = \frac{kT}{eL_D} = 1.25 \times 10^{-5} (nT)^{1/2} \qquad (40)$$

where L_D is the plasma Debye length, T is the temperature in °K, and n is the plasma density in particles/cm^3. To produce the required Debye field, the product nT must equal 1.1×10^{25}. Spectral measurements of line intensity indicated that the electron temperature was approximately equal to the Fermi temperature of the emitter. If $T = T_e = 8 \times 10^4$ °K, the plasma concentration must be on the order of 10^{20} cm^{-3}. Mass loss measurements indicated that the cathode protrusion provided a continuous supply of particles to the flare. While the initial density of these particles would be on the order of the density of the solid (10^{23} cm^{-3}), the average density in the cathode flare ranged from 10^{15} to 10^{17} cm^{-3}. These preliminary measurements, therefore, supported the hypothesis that the electric field required to emit the observed current densities through T-F emission is generated by charge separation within the plasma sheath formed at the boundary between the solid cathode and the cathode flare. The electron emission following emitter explosion can therefore be described as plasma-induced T-F emission.

6. SPACE-CHARGE LIMITED ELECTRON FLOW

Given an unlimited supply of zero-initial-velocity electrons, the current which can be drawn between the electrodes of a vacuum diode for a

63

fixed potential differential is limited by the electron space charge.
The electrons leaving the cathode constitute a space charge that exerts
a retarding field in the region of the cathode. The net field at the
cathode surface is then the difference between the retarding space-charge
field and the accelerating field produced by the positive voltage of the
anode. The electron density in the diode region and, hence, the retarding
component of the field at the cathode increase with increasing current.
When a given positive anode voltage is applied, the diode current builds
up rapidly to a value such that the average retarding field at the cathode
is equal to the accelerating field. The net field at the cathode is
therefore zero. An increase in the electron emission does not raise the
diode current because the increased space-charge potential forces the
additional electrons to return to the cathode.

To illustrate the dependence of the current on the diode geometry
and the applied voltage, the space-charge limited current density will be
derived for the case of a planar diode. The following assumptions are
made: (1) the cathode is capable of supplying more electrons than are
drawn to the anode; (2) the cathode and anode are parallel plates of infi-
nite extert, i.e., the electrostatic field is normal to the electrode
surface and uniform over the surface of any plane parallel to the elec-
trode; (3) the anode potential is sufficiently low that relativistic
effects can be neglected; (4) electrons supplied by the cathode have
negligible initial velocity after emission compared with the electron
velocity achieved during acceleration to the anode; and (5) the space
between the cathode and anode is sufficiently free of gas that electrons

do not lose energy by collision with gas molecules nor do a sufficient number of ions exist to reduce the electron space-charge depression of the potential.

The current-voltage relationship for the space-charge limited diode can be obtained from Poisson's equation, conservation of energy, conservation of current, and the boundary condition which requires that the net electric field at the cathode be zero. Poisson's equation reduces in one-dimension to

$$\frac{d^2 V(z)}{dz^2} = \frac{en(z)}{\epsilon_0} \tag{41}$$

where $V(z)$ is the potential (volts), e is the electronic charge (Coulomb), $n(z)$ is the electron density (cm^{-3}), and ϵ_0 is the permittivity of free space. Conservation of energy may be written

$$e\, V(z) = \frac{1}{2} m\, [v(z)]^2 \tag{42}$$

where m is the electron mass and $v(z)$ is the velocity (meter/sec). Conservation of current requires that the current density be independent of z. The current density at a point z may then be written in terms of the space-charge density $e\, n(z)$ and the velocity $v(z)$.

$$j = -e\, n(z)\, v(z) \tag{43}$$

The parameters $e\, n(z)$ and $v(z)$ can now be eliminated by writing

$$\frac{d^2 v(z)}{dz^2} = -\frac{j}{\epsilon_0} \left(\frac{m}{2e}\right)^{1/2} V(z)^{-1/2} \tag{44}$$

65

Integrating twice, with the two constants being zero because of zero electric field and potential at the cathode, the current density is given by

$$j(z) = \frac{4}{9} \, \varepsilon_0 \left(\frac{2e}{m} \right)^{1/2} V(z)^{3/2} \, z^{-2} \tag{45}$$

If the experimental values of e, m, and ε_0 are substituted in this equation, it is found that

$$j(z) = 2.33 \times 10^{-6} \, V(z)^{3/2} \, z^{-2} \tag{46}$$

If z is in centimeters, the current density is in amperes/cm^2. This relation was first derived by C. D. Child (Ref. 52) in a theoretical and experimental investigation of the magnitude of currents that could be carried by positive ions in low-pressure arcs. It was independently derived and applied to electron currents in high vacuum by I. Langmuir (Ref. 53). Multiplication of both sides of the equation by the cathode area yields the total current drawn across a finite planar diode. Use of the Child-Langmuir equation for the space-charge limited current density to predict the total current is justified only if r_0/d is large (r_0 is the radius of the finite cathode, and d is the diode separation). The requirement that r_0/d be large is necessary to minimize the edge effect.

The derivation of the Child-Langmuir law was illustrated above because of its simplicity. In many cases, however, the assumption which allowed this derivation are physically unrealistic. To more fully understand the ramifications of space-charge limited flow, the effects of each assumption should therefore be considered. If the first assumption is violated, a

66

a situation results in which all electrons that are emitted reach the anode. The electron flow would now be source limited.

If the diode geometry is modified, a change in the space-charge limited current result. Langmuir and Compton have derived expressions for space-charge limited electron flow in cylindrical and spherical geometries (Ref. 54). If Poisson's equation is used in cylindrical and spherical coordinates, the equation which corresponds to equation (44) may be written

$$\frac{d^2V}{dr} + \frac{\chi}{r} \frac{dv}{dr} = j \left(\frac{m}{2e}\right)^{1/2} / \left(\epsilon_0 \ V^{1/2}\right) \tag{47}$$

where χ is 1 for cylinders and 2 for spheres. To simplify the subsequent derivation, the variables V and r were replaced by two dimensionless variables, α and δ, which were defined by

$$\delta = \ln\left(r/r_e\right) \tag{48}$$

and

$$j = \frac{4}{9} \epsilon_0 \left(\frac{2e}{m}\right)^{1/2} V^{3/2} \ (r\alpha)^{-2} \tag{49}$$

where r_e is the radius of the emitter. By noting that the current density varies in proportion to $e^{-\chi\delta}$, the authors solved for α, a parameter which took the form of a power series in δ. For cylinders ($\chi = 1$), the appropriate series was as follows:

$$\alpha_1 = \delta - (2/5) \ \delta^2 + (11/120) \ \delta^3 - (47/3300) \ \delta^4 + 0.00168 \ \delta^5 \ . \ . \ . \tag{50}$$

which for $r/r_e > 10$ and an external collector can be approximated by

67

$$\alpha_1 \approx 1 + 0.9769 \left(r_e/r\right)^{2/3} \sin\left[1.0854 \log_{10}\left[\left(r/11.93\ r_e\right)\right]\right] \quad (51)$$

A similar expression has been derived for a sphere ($\chi = 2$).

$$\alpha_2 = \delta - 0.3\ \delta^2 + 0.075\ \delta^3 - 0.0143\ \delta^4 + 0.00216\ \delta^5 \ldots \quad (52)$$

For an external collector and very large values of r/r_e, the following equation gives a good approximation.

$$\alpha^2 = 2/3\ \delta + 0.5158\ \log_{10}\ (3.885\ \delta) \quad (53)$$

Values of α_1 and α_2 as a function of r/r_e are given in figure 18.

The current density j at any point between the cylinders is given by equation (49). With V in volts, the total electron flow I (amperes) between concentric cylinders (external collector) is limited to the following value.

$$I = \frac{8}{9}\ \pi\ \epsilon_0 \left(\frac{2e}{m}\right)^{1/3}\ L\ V^{3/2}\ \left(r\ \alpha_1^2\right)$$

$$= 14.7 \times 10^{-6}\ L\ V^{3/2}/\left(r\ \alpha_1^2\right) \quad (54)$$

where r is the collector radius and L, the length of the cylinders, is so great compared to the radius that end corrections are negligible.

Similarly, the space-charge limit for electron flow between concentric spherical electrodes is given by

$$I = \frac{16}{9}\ \pi\ \epsilon_0 \left(\frac{2e}{m}\right)^{1/2}\ V^{3/2}/\left(\alpha_2^2\right) \quad (55)$$

For electrons, when V is expressed in volts this becomes

$$I = 29.34 \times 10^{-6}\ V^{3/2}/\left(\alpha_2^2\right) \quad (56)$$

68
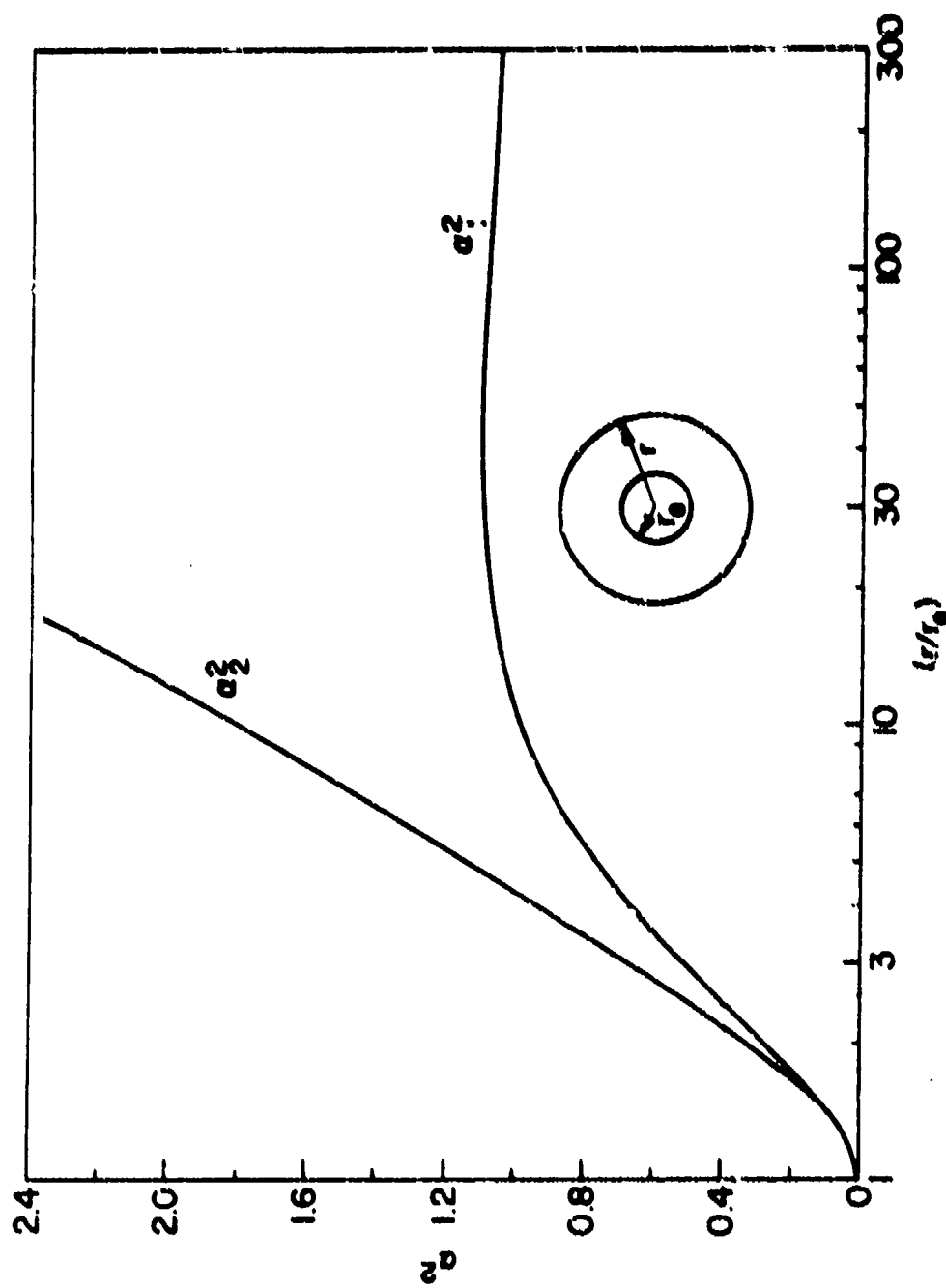
Fi. ire 18. Variation of α_1^2 and α_2^2 with the Ratio of Collector to Emitter Radii

69

The equations for space-charge limited electron flow have greater significance if written in terms of the diode perveance which is defined as $I/V^{3/2}$. The perveance of the planar, cylindrical, and spherical geometries are given by

$$P_{planar} \equiv I/V^{3/2} = 2.33 \times 10^{-6} \, A/d^2 \qquad (57)$$

$$P_{cylindrical} = 14.66 \times 10^{-6} \, L/\left(r \, \alpha_i^2\right) \qquad (58)$$

$$P_{spherical} = 29.34 \times 10^{-6}/\alpha_i^2 \qquad (59)$$

The utility of perveance in describing space-charge limited flow in a diode of given geometry is apparent when the invariance of this quantity with respect to voltage (neglecting relativistic effects) is noted. The perveance is a geometrical characteristic of diodes and electron guns which are operated under space-charge limited conditions and can therefore be determined by measuring the current at a single voltage. The current at any other voltage can then be calculated directly. Furthermore, the perveance is invariant to size if all dimensions are changed by a constant factor.

If the accelerating voltage is increased above a few kilovolts, the resultant electron velocity becomes a significant fraction of the speed of light, and relativistic effects can no longer be neglected a priori. The nonrelativistic, space-charge equation for the infinite-planar diode has been extended to the case of relativistic velocities by Ivey (Ref. 55). The results of his computation of the actual emission are compared with

the Child-Langmuir predictions in figure 19. As shown in the graph, the actual space-charge current density is less than that predicted by the nonrelativistic, Child-Langmuir approximation. This reduction results from the fact that the electron velocity for a given voltage is less than that calculated using nonrelativistic considerations. Consequently, the space-charge density is greater and the field in the vicinity of the cathode is further reduced.

The exact solution of the one-dimensional Poisson's equation for relativistic velocities is written in terms of elliptic integrals and is not amenable to rapid calculation. A more useful approximation has been derived by Friedlander et al. (Ref. 15). The Friedlander approximation, presented in table III, is also compared with the actual emission in figure 19. The graph indicates that this approximation differs from the exact emission by less than 10 percent for voltages greater than about 500 kV. At extremely high voltages, the actual emission curve approaches a linear relation on the logarithmic plot. This ultra-relativistic approximation is not valid until the accelerating voltage is on the order of 10^8 volts.

The presence of even modest concentrations of ions in the diode region represents an efficient source of space-charge neutralization. To minimize the possibility of space-charge neutralization, it is necessary not only to maintain adequate vacuum environmental conditions, but also to ensure that the anode is relatively free of surface contamination which could be released and ionized by electron bombardment. The high-vacuum Child-Langmuir derivation is easily modified to include the presence of a uniform

71
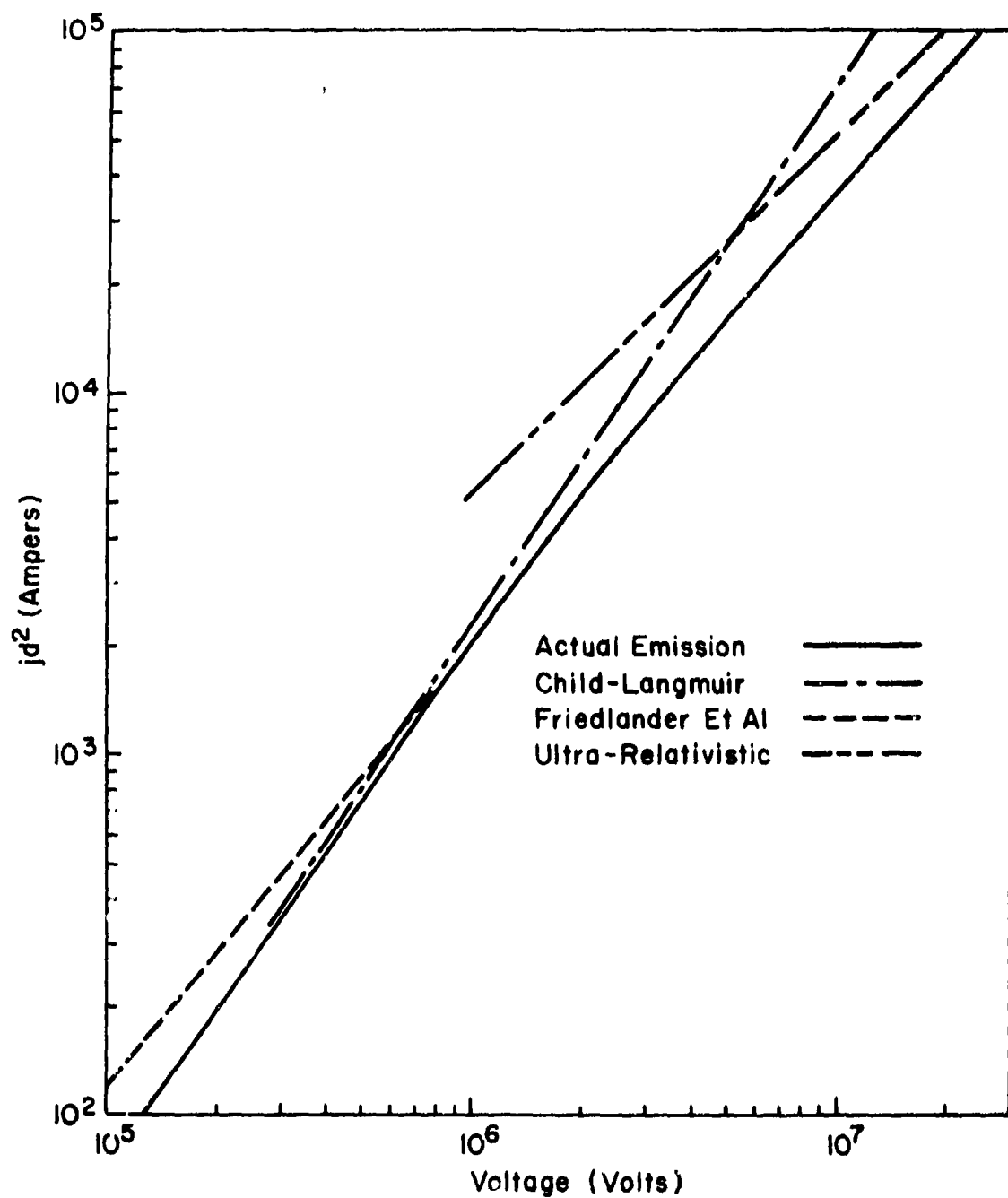
Figure 19. Comparison of Several Space-Charge Limited Flow Approximations with Actual Emission

Table III

APPROXIMATIONS TO THE RELATIVISTIC SPACE-CHARGE LIMITED CURRENT DENSITY

Approximation	Equation	Valid range (volts)
Child-Langmuir	$jd^2 = \dfrac{4}{9}\,\epsilon_0\left(\dfrac{2e}{m}\right)^{1/2} V^{3/2}$ $= 2.33 \times 10^{-6}\, V^{3/2}$	$0 < V < 5 \times 10^5$ (60)
Friedlander et al.	$jd^2 = \dfrac{2m_0\, c^3\, \epsilon_0}{e}\left[\left(\dfrac{eV}{m_0 c^2} + 1\right)^{1/2} - 0.8471\right]^2$ $= 2.72 \times 10^3 \left[\left(\dfrac{eV}{m_0 c^2} + 1\right)^{1/2} - 0.8471\right]^2$	$V > 5 \times 10^5$ (61)
Ultra-relativistic	$jd^2 = 2c\,\epsilon_0\, V$ $= 5.31 \times 10^{-3}\, V$	$V > 10^8$ (62)

73

concentration of singly charged ions in the anode-cathode region. The derivation is modified by rewriting Poisson's equation to include the ion density

$$\frac{d^2V}{dz^2} = -\frac{e}{\epsilon_0}\left(-n_e + n_i\right) \tag{63}$$

Since $v_e \gg v_i$ and n_i is at best on the order of n_e, the expression for the current density remains unchanged.

$$j = -n_e ev_e + n_i ev_i$$

$$\approx n_e ev_e \tag{64}$$

Completing the derivation yields the following expression for the electron current density, j_N, in a partially neutralized diode.

$$j_N = j_{C-L}\left(\frac{2}{2-f}\right) \tag{65}$$

where j_{C-L} is the Child-Langmuir current density and f is the ionization fraction n_i/n_e. Equation (65) indicates that ion concentrations less than $0.1\, n_e$ have little effect on the space-charge limited electron current drawn to the anode. As f approaches unity, however, the electron flow increases rapidly.

7. BEAM CONVERGENCE CRITERIA

The forces acting on an electron within the diode region have their origin in the following electromagnetic fields: (1) applied electric field; (2) electrostatic space-charge field; and (3) the azimuthal self-magnetic field resulting from the net current flow in the diode. The

74

applied and space-charged fields are strongly influenced by the diode geometry. In contrast, the azimuthal magnetic field is determined by the current enclosed by a line integral around the beam axis and is therefore essentially independent of geometry. As the ratio of cathode radius r_0 to diode separation d_0 (the aspect ratio) is increased, the radial component of the applied electric field becomes smaller and the applied field becomes predominantly axial.

In the limit of large r_0/d_0, the radial component of the space-charge field also approaches zero. The zero nature of this component can be demonstrated by the following post hoc ergo propter hoc, but nevertheless illustrative derivation. By applying Gauss' law in integral form to the surface surrounding the diode volume, the average radial space-charge field at the diode periphery is given by

$$\left\langle E_{rs}(r_0) \right\rangle = \frac{1}{2\pi \epsilon_0 r_0 d_0} \int_\tau en(z) \, d\tau + \frac{r_0}{2d_0} \left[\left\langle E_{zs}(0) \right\rangle + \left\langle E_{zs}(d_0) \right\rangle \right] \quad (66)$$

where E_{rs} and E_{zs} refer to the radial and axial components of the space-charge field. The space-charge density $en(z)$ within the diode volume and the net electric field at the anode and cathode surfaces can be approximated by their nonrelativistic Child-Langmuir values. The electron space-charge density, the net electric field within the diode $E(z)_{net}$, and the applied electric field E_a are then given by

$$en(z) = \frac{4}{9} \epsilon_0 V_0 d_0^{-2} \left(\frac{d_0}{z} \right)^{2/3} \quad (67)$$

75

$$|E_{net}(z)| = \frac{4}{3} \frac{V_0}{d_0} \left(\frac{z}{d_0}\right)^{1/3} \qquad (68)$$

and

$$|E_a(z)| = V_0/d_0 \qquad (69)$$

where V_0 is the magnitude of the applied voltage. The average radial space-charge field is therefore

$$\left\langle E_{rs}(r_0)\right\rangle \approx \frac{2}{3} \frac{r_0}{d_0} \frac{V_0}{d_0} + \frac{r_0}{2d_0}\left[\frac{V_0}{d_0} + \frac{1}{3}\frac{V_0}{d_0}\right] = 0 \qquad (70)$$

If the current flow in a high-aspect-ratio, planar diode is closely approximated by the infinite planar Child-Langmuir value, the radial component to the space-charge field must be negligible.

The lack of an outward space-charge force to balance the inward directed magnetic force in a planar diode will result in the convergence of the electron beam if the voltage and current exceed some level. Assuming the current I to be uniformly distributed over the cross section, the magnetic field at a radius r within the electron beam is given by

$$B_\theta(r) = \frac{\mu_0}{2} \frac{Ir}{\pi r_0^2} \qquad (71)$$

Since the radial self-magnetic force increases linearly with radius, the most extreme convergence will occur for the outermost electrons.

As shown in figure 20, an electron emitted from the edge of the cathode will be accelerated in crossed electric and magnetic fields. If the fields at the periphery of the beam can be approximated as being

76

static, uniform, and perpendicular, the resulting electron motion is cycloidal, i.e., a combination of circular motion and uniform translation. ince typical acceleration voltages are of the order of 10^6 volts, relativistic effects must be considered. A Lorentz transformation to a coordinate system moving with a velocity $\bar{u} = E \times \vec{B}/B^2$ with respect to the original reference frame simplifies the problem (Ref. 56). The Lorentz force equation for the electron in the moving frame is then

$$\frac{d\bar{p}'}{dt} = e(E' + \bar{v}' \times B')$$ (72)

where the primed variables are referred to the moving coordinate system. The fields E' and B' are given by

$$E'_{\shortparallel} = E_{\shortparallel} \qquad\qquad B'_{\shortparallel} = B_{\shortparallel}$$

$$E'_{\perp} = \gamma\left(E_{\perp} + \bar{u} \times B\right) \qquad B'_{\perp} = \gamma\left(B_{\perp} - \bar{u} \times E\right)$$ (73)

Inserting the choice for $\bar{u}$ in equation (73) yields

$$E'_{\shortparallel} = 0 \qquad\qquad B'_{\shortparallel} = 0$$

$$E'_{\perp} = \gamma\left(E_{\perp} + \bar{u} \times B\right) = 0 \qquad B'_{\perp} = \frac{1}{\gamma} B = \left(\frac{c^2B^2 - E^2}{c^2B^2}\right)^{1/2} B$$ (74)

In the moving frame the only field acting is a static magnetic field B, which points in the same direction as B, but is weaker than B by a factor of γ^{-1}. The motion in this frame is a spiraling around the lines of force. The gyration frequency is given by

$$\bar{\omega}_B = \frac{eB'}{m\gamma}$$ (75)

As viewed from the laboratory frame, this gyration is accompanied by a uniform translation perpendicular to E and B at a speed E/B. Since the circle of gyration turns with an angular velocity ω_B and "rolls" with a speed E/B, the radius of the circle of gyration is

$$r_B = \frac{E}{\omega_B B} = \left(\frac{m_0}{e}\right)\frac{E\gamma^2}{B^2} \tag{76}$$

where $\gamma^2 = c^2B^2/(c^2B^2-E^2)$. For the case of zero initial velocity, the resulting trajectory is shown in figure 21. The equations for this trajectory are

$$r = r_B\left(\omega_B t - \sin \omega_B t\right)$$

$$z = r_B\left(1 - \cos \omega_B t\right) \tag{77}$$

To estimate the limiting criterion for axial flow in the diode, consider the case for which $2r_B$ is equal to the diode separation d_0.

$$d_0 = 2r_B = \left(\frac{2m_0}{e}\right) E \left(\frac{\gamma}{B}\right)^2 \tag{78}$$

The self-magnetic field at the edge of the cathode is given by

$$B_\theta = \frac{\mu I_c}{2\pi r_0} \tag{79}$$

where I_c is the critical current required to produce a grazing trajectory. Substituting this value for B_θ into equation (78) yields

$$I_c = \frac{2\pi r_0}{\mu} \left[\left(\frac{2m}{e}\right)\frac{E}{d_0} + \left(\frac{E}{c}\right)^2\right]^{1/2} \tag{80}$$

78
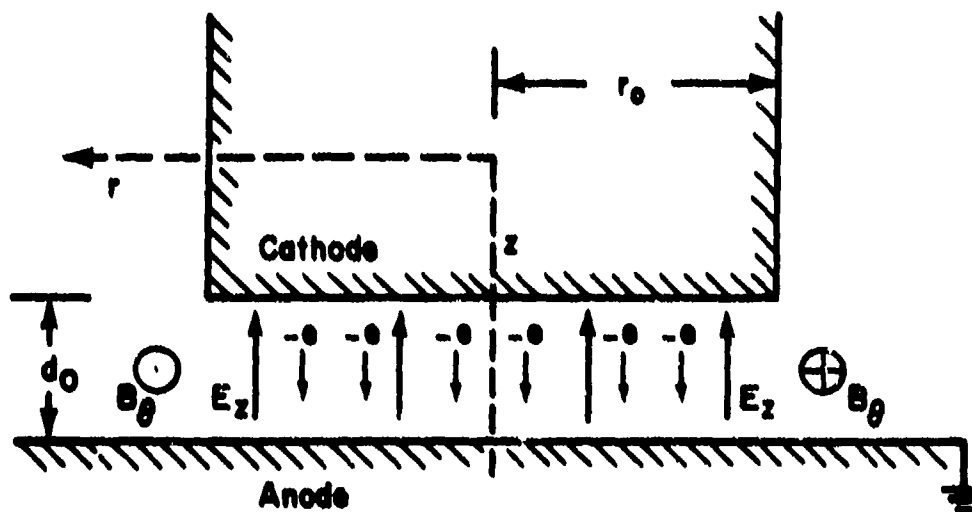
Figure 20. Field Configuration within Diode Prior to Pinch
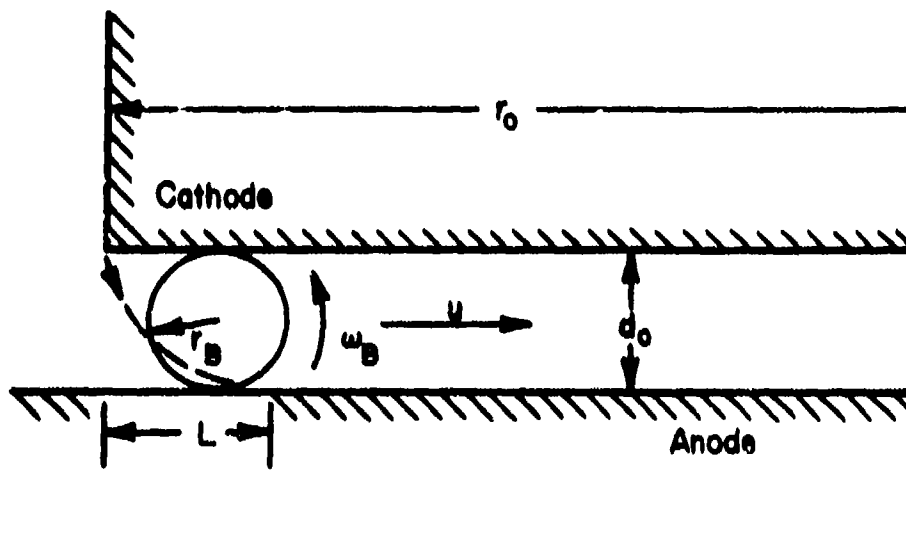
Figure 21. Pinch Trajectory of Peripheral Electron with Zero
Initial Velocity

Neglecting the fact that the applied electric field is modified by the space charge of the accelerated electrons, the electric field in the diode can be approximated by $E = V_0/d_0$. Equation (80) then becomes

$$I_c = \left(\frac{2m}{e}\right)^{1/2} 2\pi\varepsilon_0 \ c^2 \left(\frac{r_0}{d_0}\right) V_0^{1/2} \left[1 - \frac{eV_0}{2m_0 \ c^2}\right]^{1/2} \tag{81}$$

With further manipulation

$$I_c = 2\pi\varepsilon_0 \ \frac{m_0 \ c^3}{e} \ \beta\gamma \left(\frac{r_0}{d_0}\right)$$

$$= 8500 \ \beta\gamma \left(\frac{r_0}{d_0}\right) \tag{82}$$

When $t = \pi/\omega_B$, the equation for the radial component of the trajectory reduces to

$$r = L = \pi \left(\frac{m}{e}\right) \frac{c^2 E}{c^2 B^2 - E^2} \tag{83}$$

Inserting the value of the magnetic field at critical current yields

$$L = \frac{\pi}{2} \ d_0 \tag{84}$$

The magnetic field within the diode varies linearly with the radius. Since the above derivation of the critical current is based on an assumption of uniform magnetic field along the path from cathode to anode, the aspect ratio (r_0/d_0) of the diode must be large compared to $\pi/2$ for the derivation to remain valid.

The final limitation to this derivation is the assumption of a uniform electric field. The resulting error can be estimated by noting that the electron flow within the diode prior to attaining a critical value is space-charge limited. Under these conditions, the field within the diode can be more closely approximated by the nonrelativistic Child-Langmuir relation

$$E(z) = \frac{4}{3} \frac{V_0}{d_0} \left(\frac{z}{d_0}\right)^{1/3} \tag{85}$$

The error between the "actual" and the average fields exceeds 35 percent only for $Z < 0.125\ d_0$.

An enhanced appreciation of the diode "pinching" criterion results if the critical current relation is rewritten in terms of a useful dimensionless variable (Ref. 57). The constants preceeding the relativistic terms in equation (82) correspond to an "ideal" current which is defined as that current produced by unit charges aligned with a linear density of one per "classical" electron radius and moving at the speed of light. The resulting ideal current is given by

$$I_0 = \frac{4\pi\epsilon_0\ m_0\ c^3}{e} \tag{86}$$

The dimensionless variable ν is then defined as

$$\nu = I/\left(I_0\beta\right) \tag{87}$$

Using these relations, equation (82) then becomes

$$\left.\frac{\nu}{\gamma}\right|_{critical} = \frac{r_o}{2d_o} \tag{88}$$

If the ν/γ of the accelerated electron stream exceeds one half the diode aspect ratio, axial electron flow at the beam periphery is impossible and beam convergence will occur.

The limiting current criterion given by equation (82) was first derived heuristically by Friedlander et al. by setting the electron gyromagnetic radius in the self-magnetic field at the diode periphery equal to the diode separation. Although the derivation given above is physically more reasonable and provides more detail, the Friedlander approach has the distinct advantage of simplicity.

8. PARAPOTENTIAL FLOW

When the diode current is greater than its critical value, the electron flow is dominated by the self-magnetic field and is distinguished by a severe convergence of the electron beam within the diode. Although limited, the present theoretical understanding of crossed-field electron flow is based on the parapotential model advanced independently by D. C. dePackh (Ref. 58) and Friedlander et al. (Ref. 15). This description of electron flow is predicated on the assumed existence of a class of force-free electron trajectories in the diode.

The assumption of force-free electron motion has been justified by the following argument. Electron flow in excess of the critical current reduces the gyroradius of electrons emitted from the cathode perimeter to less than the diode separation. These electrons must therefore drift

82

toward the diode axis with an initial average velocity of $E/B \approx 5 \times 10^6$ $(V_0/I)(r_0/d_0)$ cm/sec. The resultant accumulation of space-charge reduces the axial electric field adjacent to the central portion of the cathode, and thus suppresses electron emission in this region. The instantaneous equipotential distribution is distorted by the excess space charge and can be approximated by that shown in figure 22. With the net electric field at interior radii reduced, the predominant electron emission must originate at the cathode periphery. Moreover, the distorted equipotential distribution represents an electrostatic field configured to oppose the inward-directed self-magnetic force. Space-charge accumulation must continue until the net force acting on the electrons is reduced to zero. Electrons emitted from the cathode edge will then exhibit force-free motion and drift along equipotential lines until they reach a region slightly in front of the anode. In this region parapotential flow will cease and the electrons must accelerate across the equipotentials to reach the anode.

By assuming azimuthally-symmetric parapotential flow, de Packh derived the following fundamental equation for steady-state electron flow:

$$\nabla^2 V = (2/r^2) \, dI^2/d^2 V \tag{89}$$

where r is the radial cylindrical coordinate, $V = V(r,z)$ is the potential, and $I = I(r,z)$ is the total current flowing within radius r through a plane of constant z. Using the nomenclature shown in figure 22, solution of this equation yields

$$I = \frac{8500 \, \gamma_m \, \ell n \left[\gamma_m^2 + \left(\gamma_m^2 - 1 \right)^{1/2} \right]}{\ell n \left(\tan \frac{\theta_m}{2} \right) - \ell n \left(\tan \frac{\delta}{2} \right)} \tag{90}$$

83
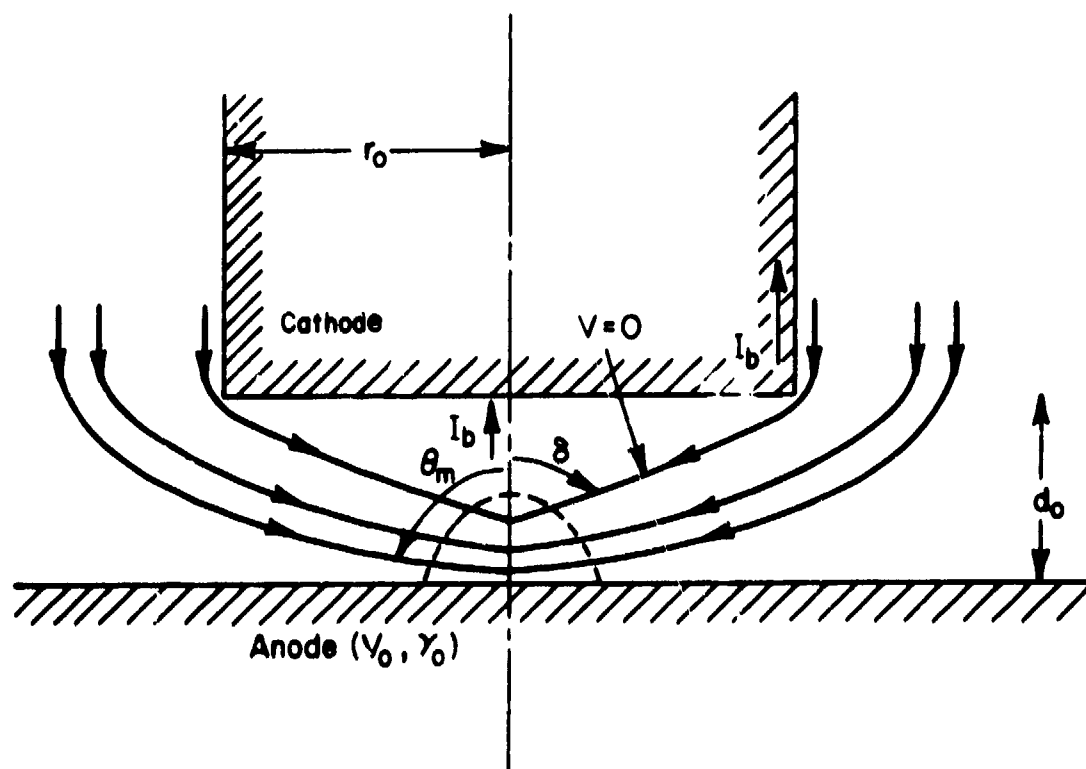
Figure 22. Model for Parapotential Flow

84

where γ_m is the relativistic factor associated with electron motion along the outer flow line θ_m. The interior flow line is $\theta = \delta$. To satisfy the conditions for this solution, an axial bias current I_b must flow within the minimum flow line $\theta = \delta$. The requirement for a bias current is derived from the fact that the current distribution is not specified at the electrode surfaces. As a result, one of the three parameters γ_m, θ_m, or I_b must remain undetermined. By specifying one of these, the other two can be determined. A choice of minimum bias current corresponds to electron flow along all equipotentials.

Creedon (Ref. 59) has simplified the problem by assuming an idealized equipotential distribution consisting of concentric cones converging to a point on axis at the anode. With this assumption, the variables δ, θ_m, and γ_m become

$$\tan \delta = \frac{r_o}{d_o}$$

$$\theta_m = \pi/2$$

$$\gamma_m = \gamma_o = 1 + eV_o/m_o c^2 \tag{91}$$

Equation (90) then reduces to

$$I = 8500 \left(\frac{r_o}{d_o}\right) \gamma_o \, \ell n \left[\gamma_o + \left(\gamma_o^2 - 1\right)^{1/2}\right] \tag{92}$$

This solution corresponds to a choice of minimum bias current. Since the interior flow line is aligned with the cathode perimeter, edge or shank emission is required to populate the exterior equipotentials.

Although this simplification is expected to be reasonable over most of the diode volume, the situation at the point of convergence is physically unrealistic. The electrons can not continue to drift force-free along the equipotentials until they reach the anode.

SECTION III

SURVEY OF PREVIOUS LOW-RESISTANCE DIODE STUDIES

1. INITIAL DIODE STUDIES

The initial investigations of low-resistance diode behavior were
accomplished by several groups, concurrent with their development of low-
impedance accelerators. Since the primary objective of these studies
was to quickly derive a functional diode design to match the charac-
teristics of a particular accelerator, the results were limited to an
empirical determination of the diode resistance as a function of such
parameters as the diode configuration, the anode-cathode separation, and
the cathode diameter. Because of the limited scope of these studies,
interpretations of the resultant data yielded very qualitative, and some-
times contradictory, descriptions of low-resistance diode phenomenology.

A more quantitative comparison of data was made difficult by the
diversity in the design of the various diode configurations, the varied
characteristics of the different accelerators, and the qualitative nature
of the initial measurements. Before discussing the results of these
initial studies, several of the distinctive features which differentiate
the individual experiments should be considered. First, the details of
the cathode designs varied widely, even though the basic diode configura-
tions were similar, i.e., right-cylindrical cathodes opposite a planar
anode. Where the group at Physics International used a dense cluster of
600 stainless steel needles, a 20-pin array was used at Ion Physics.
Following the suggestions of J. C. Martin of the AWRE, the Cornell group

87

used a metal-dielectric "plasma" cathode, formed by filling holes drilled in the face of a brass disk with either epoxy or plastic. To add to the variety, Ion Physics also used a graphite cathode, while the group at the Naval Research Laboratory settled on a spiral-grooved, aluminum-coated stainless steel design. The sintered tungsten cathode used at EG&G should also be mentioned.

Most of these cathode designs were expected to behave in basically the same manner. Nevertheless, each design had a particular feature which was intended to enhance some aspect of its performance. All cathode designs were observed to require some time delay before the resistance reached its characteristic value. The "plasma" cathode was designed to minimize this delay. Similarly, polished metal surfaces were observed to produce spotty emission patterns. To avoid this difficulty, the multi-needle cathodes were expected to localize the emission to the region of the needle points. In contrast, the graphite, sintered tungsten, and aluminum-coated stainless steel designs were intended to provide uniform emission from the entire cathode face.

The observed diode behavior was also affected by variations in the design of the cathode shank region. The need to minimize series inductance in a low-impedance accelerator places a premium on the interelectrode spacing which can be tolerated between that portion of the center electrode immediately behind the cathode face, and the metal which forms the ground contour. Minimal interelectrode spacing produces comparatively high electric fields along the cathode shank, which in turn can result in substantial electron emission from the shank region. The total electron flow therefore consists of contributions from the cathode face, edge, and

shank. Since the flow characteristics from these regions are quite different (see equations (57) and (58)), the observed diode behavior is partially determined by the fraction of the total flow which originates from each region.

The presence of a prepulse in some accelerations further complicates comparisons of diode behavior. In all pulse-charged accelerators, the voltage pulse used to charge the fast energy-storage network is capacitively coupled to the diode by the low-inductance switch. A prepulse voltage is thereby developed across the diode prior to the application of the main accelerating pulse. The relative magnitude of the prepulse has varied widely from one accelerator to another. While the Nereus accelerator developed at the Sandia Laboratories generates a prepulse, the magnitude of which is less than 1 percent of the pulse-charging voltage; the Gamble II accelerator at the NRL had a prepulse of approximately 15 percent. Although some groups worked to minimize the prepulse to avoid preconditioning or pre-ionizing the diode, others considered the presence of some prepulse to be useful in achieving rapid electron emission from the cathode. Unfortunately, the precise nature of the pre-conditioning was unknown, and the effects of the prepulse could not be anticipated with any precision.

Having begun the diode studies, one of the first observations was the decrease of the diode resistance with time. Some delay, on the order of 10 nanoseconds, was required before the diode reached its "steady" or characteristic value. Furthermore, if the pulse length was too long or the gap spacing too short, the diode would transition to a short circuit before the completion of the pulse. To circumvent the resistance

89

variation in time, the behavior of a specific diode configuration was characterized by its resistance at the instant of maximum current. Selection of that instant was advantageous since the instantaneous time derivative of the diode current is zero. Hence, the inductive component of the measured voltage signal vanishes, and the magnitude of the uncorrected signal corresponds to the resistive voltage developed across the diode. Using this approach, diode resistance data were compiled for several cathode types as a function of cathode radius, diode separation, and magnitude of the applied voltage pulse.

G. Yonas and P. Spence reported the results of one of the first of these studies (Ref. 16). The authors used a modified Model 730 Pulserad accelerator to investigate the response of a 6.35-cm diameter, multi-needle cathode located from 2 to 10 mm from a thin (1/2 mil) aluminized Mylar anode. To facilitate the generation of low-impedance beams, the 50-ohm Blumlein of the Model 730 Pulserad had been replaced by an 8.5-ohm coaxial transmission line. This combination of diode and pulse-forming line exhibited the following range of beam characteristics: accelerating voltage at peak current, 170 kV $\leq$ V $\leq$ 400 kV; peak current 140 kA $\leq I_{max} \leq$ 200 kA; and pulse width (FWHM), 50 nsec.

In spite of the fact that the peak current was slightly in excess of the critical current, and the existence of strong experimental evidence that the beam has pinched at the anode, Yonas and Spence reported that the variation of diode resistance with electrode separation was well approximated by the Child-Langmuir relation for space-charge-limited flow in an infinite planar diode. Their data were compared with the Child-Langmuir equation written in the following form

90

$$R = c \left(d_0/r_0\right)^2 V^{-1/2} \qquad (93)$$

where R is the diode resistance (ohms), and d_0 and r_0 are, respectively, the diode separation and the cathode radius. If the applied voltage V is given in megavolts, the theoretical value of the proportionality constant c is 136. Yonas and Spence, however, found that a best fit to their data could be obtained by setting the Child-Langmuir constant equal to 115.

Many other groups also found the resistance of high-aspect ratio $(r_0/d_0 \gg 1)$ diodes to scale quadratically with the reciprocal of the aspect ratio, and to be in qualitative agreement with the predictions of the Child-Langmuir relation. A summary of these results is shown in table IV which presents reported values for the Child-Langmuir constant. Note that a rather wide range of values for the constant have been observed.

Table IV

OBSERVED VALUES FOR THE CHILD-LANGMUIR CONSTANT

Laboratory	C-L Constant	Cathode Type
Physics International	115	Multi-Needle Array
EG&G	40	Sintered Tungsten
AWRE	70	Plasma
Cornell	80	Plasma
Sandia	43-170	Several Types

Two exceptions to this general consensus have been reported. Using the Gamble II accelerator at the Naval Research Laboratory, J. Block et al. (Ref. 19) found a very nonlinear variation of the resistance with diode separation. At relatively large separations, the diode resistance followed the Child-Langmuir predictions. As the separation was decreased, however, a point was reached beyond which the resistance fell quite rapidly. To illustrate this behavior, the authors stated that while using a 6.35-cm diameter, spiral-grooved cathode, a decrease in spacing from 0.85 cm to 0.80 cm lowered the diode resistance from approximately 2 ohms to a few tenths of an ohm. Since this same effect could also be achieved by slightly increasing the driving voltage, they concluded that the observed nonlinearity must be the result of some unspecified field effect.

The second contrasting observation was reported by S. E. Graybill et al. (Ref. 60). Using the Van de Graaff-charged FX-1 and FX-25 accelerators mismatached into low-resistance diodes, the authors observed a linear dependence of the diode resistance on the ratio (d_0/r_0). Graybill notes that this result is in agreement with the predictions of parapotential flow and disagrees with the Child-Langmuir law. Reported data indicate the use of two sizes of graphite cathode (1.7 cm and 5.1 cm diameter) and diode separations ranging from 0.6 cm to 1.5 cm. This disagreement can not be completely explained by arguing that the observed currents either approached or slightly exceeded the self-pinching criterion because the same condition held in the other experiments. Therefore, the significant difference may lie in the fact that the aspect ratios of the diodes used in the latter experiments were on the order of

92

or less than unity, while those used in the former were generally much greater than one.

These discrepancies and the wide range of observed values for the Child-Langmuir constant illustrate the complication which results from the existence of many partially understood phenomena which determine the diode behavior. This lack of information, when combined with the recognition that the propagation characteristics of the electron beam in a drift chamber are critically dependent on the phenomena occuring within the diode, served as the stimulus for more extensive examinations of low-resistance diode behavior.

A more detailed investigation of the operational characteristics of a low-resistance diode was initiated at Cornell University in conjunction with their development of a pulse-charged accelerator driven by either of two low-impedance (1.75 ohm and 2.0 ohm) Mylar Blumleins. This accelerator was capable of producing electron currents of from 30 to 100 kA at kinetic energies ranging from 200 to 500 keV, with a pulse duration of 50 nanoseconds. Using this device, J. Clark and S. Linke (Ref. 17) extended the results of these early studies by considering the current density distribution and the electron trajectories at the anode plane in conjunction with an analysis of the scaling of diode resistance with gap spacing. As shown in figure 23, their results support the original consensus of space-charge-limited flow. To match this data, the Child-Langmuir constant had to be set equal to 80.

In figure 23, two sets of data stand out as notable exceptions to the correlation with the Child-Langmuir law. Further consideration revealed that, unlike the other data points, the maximum current which characterized

93
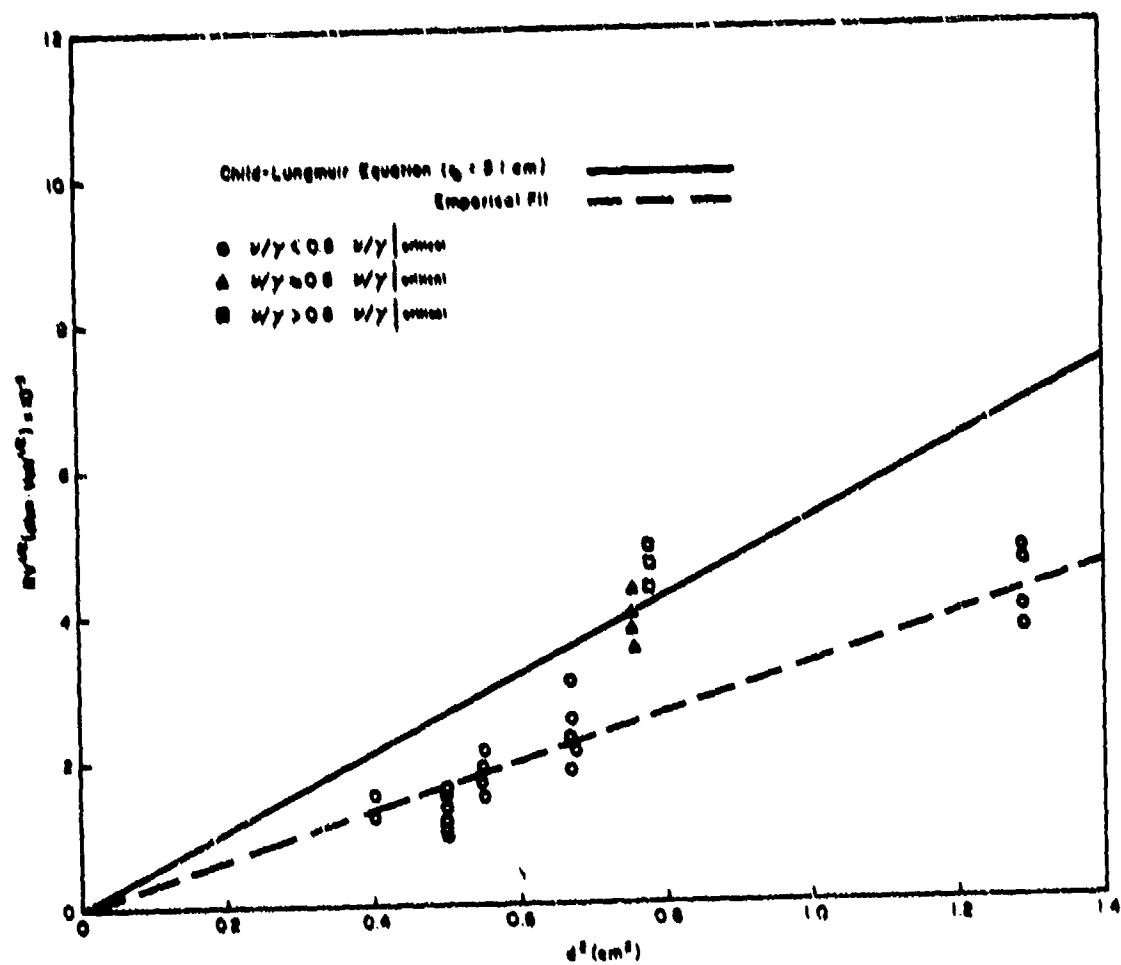
Figure 23. Comparison of Diode Data with Simple Child-Langmuir Data

94

these shots was approaching or in excess of the critical current given by the self-pinching criterion (see equation (82)). Since current flow in excess of the critical value results in beam convergence within the diode, the observed increase in diode resistance was attributed to beam pinching. Careful examination of the available data showed that the onset of pinching seemed to occur when the diode current exceeded 80 percent of the critical value. As shown in figure 23, current flow in excess of $0.8\ I_{critical}$ had essentially the same resistive characteristics.

To substantiate this interpretation, streak and framing camera photographs of the optical emission from specially designed anode structures which contained a plastic scintillator were taken to assess the current density distribution at the anode plane. Further information concerning the current density distribution was obtained from an analysis of radiographs of the X-ray emissions from the anode and distributed calorimeter measurements. Examination of this information revealed that diode pinching did indeed occur for measured values of ν/γ above 0.82 $(r_0/2d_0)$. Recall from the earlier derivation of the self-pinching criterion that beam convergence is expected within the diode when ν/γ exceeds one half the diode aspect ratio. For the case of current flow less than 0.82 $(r_0/2d_0)$, the radiographs of the current density distribution at the anode showed the honeycomb emission pattern expected from the "plasma" cathode design. Since this pattern has been maintained throughout the transit across the gap, the electron flow had to have been predominantly paraxial or laminar as required by the assumption of space charge limitation.

The self-pinching criterion was further substantiated by an experiment performed by G. Loda and P. Spence (Ref. 18) in which they quantitatively

95

measured the time-resolved current density distribution at the anode plane. For this experiment, Loda and Spence used the 100 kV Mylar stripline accelerator developed at Physics International. The accelerator, which consists of two parallel, 0.6-ohm Blumleins driving a variable resistance diode, produced a 300 kA pulse of 100 keV electrons with a pulse duration (FWHM) of 40 nanoseconds. To measure the current density, a series of shots were taken into an aperatured Faraday cup mounted on the anode plane. The final values for the current density shown in figure 24 were then obtained by normalizing each measurement to a fixed total current. The graph in figure 25 presents the critical current and the total diode current as a function of time. As required by the self-pinching criterion, the current density at the anode was shifted toward the diode axis when the diode current exceeded the critical current.

Evidence of the preconditioning which results from the presence of a prepulse can be seen by contrasting the time resolved resistance measurements of S. E. Graybill et al. (Ref. 60) with those of G. Yonas et al. (Ref. 16), and J. Block et al. (Ref. 19). The direct-current-charged, FX series accelerators used by Graybill did not have prepulse, while the pulse-charged Pulserad and Gamble II accelerators used respectively by Yonas et al. and Block et al. did. The modified Pulserad incorporated a prepulse switch in the diode design to minimize emission from the cathode before the transmission line was switched into the diode. The G-4 diode structure used on the Gamble II did not. The unspecified prepulse from from the Pulserad would therefore be expected to be less than the 15 percent prepulse generated by the Gamble II.

Figure 25. Time-Dependent Comparison of Diode
Current with Critical Current

Figure 24. Measurement of Time-Dependent
Current Density Distribution Showing
Self-Convergence

97

Comparing the time-resolved voltage and current pulses presented by the investigators, the diode resistance in the Pulserad and Gamble II accelerators was found to be finite at the beginning of the voltage pulse, i.e., measurable electron flow occurred simultaneously with the initial rise of the voltage pulse. The initial resistance of the unconditioned diode in the FX-25 accelerator however, was infinite. A 7- to 10-nanosecond formative time period was required before the diode reached its steady value. Having compared cathode types, Graybill et al. found that the graphite cathodes exhibited a shorter formative time period than did cathodes of aluminum, brass, or stainless steel. After the first several nanoseconds, all investigators observed a steady decrease in resistance with time.

2. PLASMA PHENOMENA IN THE DIODE

Contemporaneous with the initial experimental investigations of low-resistance diode behavior was an interesting series of studies which attempted to use numerical codes to extend the analysis of point-to-plane diodes to the planar geometry required for high-current flow. The present interest in these studies is not related to their attempted extension to planar geometries, but rather is centered on certain coincidental observations regarding plasma phenomena in high-resistance diodes. At the beginning of the study by Friedlander et al. (ref. 15) the analysis of a high-resistance, needle-to-plane diode was undertaken to establish the validity of possible models for the emitter surface. The needle-to-plane diode used in the FX series accelerators was chosen because a considerable amount of data was available for this configuration. The diode analyzed consisted of a 1/8-inch-diameter cylindrical cathode rod terminated by a 1/16-inch

radius hemispherical tip. The cathode was positioned 2.7 cm from a planar anode. Having been given the experimental values for the voltage and current (at the instant of maximum current) as well as the time-integrated current density distribution at the anode, the Varian developed computer program was then used to compute the electron beam transit across the diode. In an attempt to match the observed diode characteristics, the geometry of the cathode emission surface and the percentage of space-charge neutralization were varied. Comparison with the calculated trajectory plots lead to the following conclusions concerning the cathode emission characteristics: (1) the cathode exhibited substantial emission from the cylindrical portion of the rod (shank emission); (2) the effective cathode radius was appreciably larger than the physical radius; and (3) in all probability there was some degree of space-charge neutralization in the diode.

To explain the apparent cathode enlargement, the authors argued that the average field at the cathode tip (1.6×10^7 V/cm) was more than sufficient to cause the destruction of any cathode whiskers. With the current densities involved such breakdown should occur within a few nanoseconds. They then proposed that the source or electron emission throughout the remainder of the pulse be emission from a dense plasma cloud close to the surface of the emitter. In this case, the current density must be determined by the space-charge limitation within the diode, and not by the field emission process. The increased effective cathode size was therefore argued to result from an expansion of the plasma produced at the tip of the cathode. Such a plasma would not only increase the effective cathode radius, but also reduce the anode cathode separation.

In an addendum to a similar computer study, J. Uglam et al. (Refs. 61, 78) describes the results of two experiments which were performed to determine the spatial extent and time history of the cathode plasma predicted by Friedlander et al. For these measurements, the FX-25 accelerator was fitted with a 1/8-inch-diameter, sharpened, stainless-steel cathode positioned 1 cm from a carbon anode. A 0.25-meter Jarrel-Ash monochrometer, modified for spectrographic use, was aligned to spectrally resolve the spatial variation of visible and near ultraviolet from a narrow region extending from anode to cathode. At a residual pressure of 3×10^{-5} torr, the time-integrated spectrogram showed a strong continuum emission from the cathode. The anode was also seen to emit a continuum, but less strongly, while the gap emitted a large number of spectral lines. Similar results were obtained after replacing the stainless-steel cathode by first a carbon cathode, and then an aluminum cathode. In each case, the only recorded spectral lines corresponded to the neutral spectra of the cathode material.

To assess the time response of the cathode emission, a 0.5-meter Jarrel-Asn monochrometer equipped with an Amperex XP 1003 S-20 photomultiplier was focused approximately 1 mm off the cathode tip. The results indicated that a tenuous plasma formed quite quickly. Both cathode material and residual gas species were observed in the plasma, but the cathode material was the dominant contribution. These results are in complete agreement with the Friedlander assumption of whisker explosion, and subsequent electron emission from a plasma cloud adjacent to the cathode surface. The study did not, however, show the existence of any

residual gas ions in the diode gap which could have resulted in space-charge neutralization.

Further evidence of plasma motion in the diode was reported by Loda and Spence (Ref. 18). During the initial characterization of the electron beam from the Physics International 100-kV Mylar stripline accelerator, they found that the diode resistance decreased very rapidly with time. The diodes in this case were formed by broad-area (2.5 to 7.0 cm diameter), multi-needle cathodes positioned unusually close (1 to 2 mm) to the stretched aluminized-Mylar anode. The authors observed that the rapid decrease in diode resistance could be predicted with remarkable accuracy if they assumed space-charge-limited flow, and a constantly decreasing diode separation. To incorporate an electrode surface moving with constant velocity v (cm/sec), the Child-Langmuir law as rewritten as follows.

$$R = 136 \ V^{-1/2} \left(d/r_0\right)^2 \qquad (94)$$

where

$$d = d_0 - v\left(t-t_0\right) \qquad (95)$$

and d_0 is the original diode separation (cm), t_0 is the plasma formation time (sec), and the time t is given in seconds. To match their resistance data, Loda and Spence set v equal to 1.5×10^6 cm/sec, and t_0 equal to 10 nanoseconds.

Postulation of the formation and expansion of a highly conducting plasma was an obvious source of a moving electrode surface. To meet this requirement, Loda and Spence argued that the high-energy-density loading of the electron beam was sufficient to explode the anode within about

10 nanoseconds. To obtain a best fit between theory and experiment the anode plasma was assumed to expand about its midplane at a velocity of 1.5 cm/μsec. It should be noted however, that the expansion of the cathode plasma postulated by Friedlander et al. and observed by Uglam et al. would have had the same effect on the diode resistance.

3. PARAPOTENTIAL FLOW

When the diode current exceeds the critical current, the electron flow within the diode is dominated by its self-magnetic field. Under these circumstances, the approximation of paraxial, space-charge-limited flow is no longer valid. Although the precise nature of the subsequent, highly-convergent flow is not yet known, the only available theoretical model implies a parapotential flow.

Qualitative support for certain features of parapotential flow has been presented in a series of reports by B. Ecker (Refs. 62, 63, and 64). In these reports, Ecker described a series of experiments performed on the SNARK accelerator developed by Physics International. The SNARK, which is more completely described in Reference 65, is formed by eight, Mylar-dielectric Blumleins which drive a single, common diode. The SNARK was designed to accelerate a 1-MA pulse of 1-MeV electrons having a pulse duration (FWHM) of 60 nanoseconds. The diode used for these experiments consisted of an annular, hollow-disk cathode opposite a stretched-foil anode. At the cathode, the emission surface was formed by a dense cluster of steel roll pins inserted into the cathode base. The hole in the center of the cathode was found to retard the resistance collapse which resulted when the pinched beam exploded the anode foil near the axis. Throughout these experiments, the diode separation varied from 3.5 mm to 6.4 mm.

102

Variation in the cathode outer radius from 4.3 cm to 7.3 cm resulted in aspect ratios which ranged from 7.25 to 20.8.

Voltage and current data compiled during this study have been compared with the predictions for the grazing case. Since the derivation of the parapotential flow model assumed steady state, Ecker characterized the diode response by the data at that time when $\partial I/\partial t = 0$, i.e., $I_0 = I_{max}$. As shown in figure 26, the expression derived for the grazing case apparently predicted the diode resistance with reasonable accuracy over a wide range of voltages.

Having established this correlation, Ecker (Ref. 64) then examined several of the assumptions which form the basis for the parapotential model. To test the suppression of electron emission from the central portion of the cathode face, the total emission area of the cathode face was reduced by removing the inner roll pins. The inner radius of the annular cathode was thus increased from 3.9 cm to 5.5 cm, while the outer cathode radius and the radius to the outer diode wall (ground contour) remained fixed at 7.3 cm and 8.25 cm, respectively. Comparisons of the diode response for the two cathodes was based on time-resolved voltage and current data as well as current density measurements taken using a series of three annular Faraday cups. The geometry of the diode and the regions measured by the Faraday cup are shown in figure 27.

Although the area of the cathode face had been reduced by nearly a factor of two, little change was observed in either the time-resolved resistance or the total current wave forms. The current density measurement, however, disclosed a significant difference in the flow patterns for each case. These measurements verified the assumption that the

103

electron emission originates predominantly from the cathode periphery and/or shank. Furthermore, the diode resistance appeared to be fairly insensitive to the specific structure of the flow near the axis.

The grazing model for parapotential flow assumes that the current density distribution at the anode plane is very strongly peaked on axis. Ecker evaluated this assumption by considering the spatially resolved current measurements obtained from the annular Faraday cups. The current pulses shown in figure 28 correspond to the original cathode configuration (r_c = 7.3 cm and r_i = 3.9 cm). At best, the data showed only qualitative support for the assumed current distribution. In marked contrast to the assumed flow structure, significant current flow was observed at large radii throughout the entire pulse. Moreover, only 40 percent of the total current was observed within the innermost region. Certain features of the parapotential flow model however, were supported by those measurements. The Faraday cup data did show the existence of a strongly pinched flow. This was evident from the fact that 75 percent of the total current arrived at the anode at radii less than the inner radius of the hollow cathode. It would therefore appear that most of the electrons enter the diode near the cathode periphery, and then develop predominantly radial velocities.

The spatially-resolved current measurements also provided information concerning the time dependence of the pinching process. Figure 28 shows the collapse velocity of the pinched flow to be approximately 10^8 cm/sec, or 1 mm/nsec. At the voltages typical of these accelerators, characteristic electron velocities are on the order of 10^{10} cm/sec. Hence, the diode current flow does not change significantly during an electron transit time.

Radius Regions

#1 | #2 | #3 | #2 | #1

Anode

Hollow Cathode

|←3.9 cm→|

|← 7.3 cm →|

Radius Region #1: $r > 4.15$ cm

#2: 1.86 cm $\leq r \leq 4.15$ cm

#3: $r < 1.86$ cm
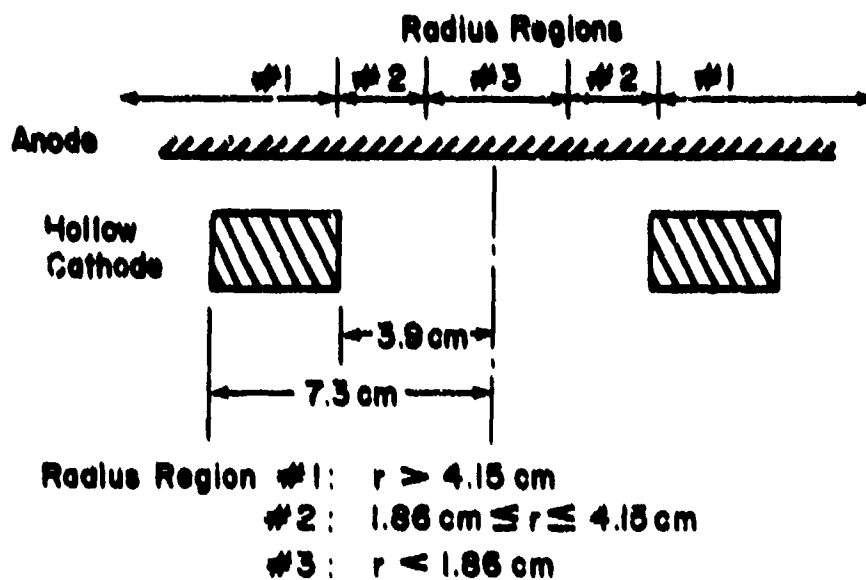
Figure 27. Radius Regions of Faraday Cup Measurements Relative to Cathode Inner and Outer Radii
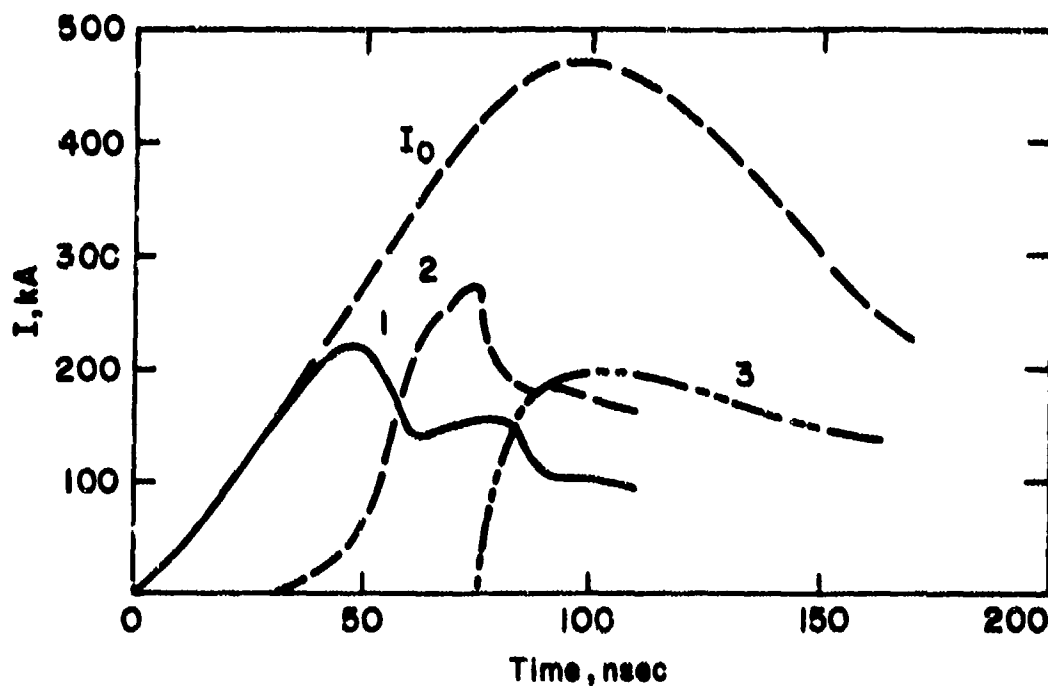
Figure 28. Currents in Radial Regions 1, 2, and 3 with $r_o = 7.3$ cm, $r_i = 3.9$ cm, $d = 4.0$ mm, Peak Voltage = 500 kV

106

Since the displacement current is negligible by several orders of magnitude, and the transit time is short compared to changes in the current flow, Eckər argued that the pinching process can be considered quasi-static, and that the assumption of steady-state is valid.

SECTION IV

ACCELERATOR DESCRIPTION

1. INTRODUCTION

The electron accelerator used during the present study was obtained by modifying the exploding bridge wire device which had been designed and constructed for the Air Force Weapons Laboratory by the Field Emission Corporation in 1963. The required modifications consisted of reversing the system polarity and installing an evacuated diode structure to replace the exploding wire transducer chamber. With these exceptions, the system remains as described in the literature (Refs. 66, 67, and 68).

Although this accelerator has electron beam characteristics similar to other moderate energy accelerators available throughout the country, it has several unique features which simplified the task of quantifying the phenomena underlying the behavior of low-resistance diodes. Among these features are a common time base for all diagnostic channels with a precision of $\pm$ 0.1 nanoseconds; clean, well-calibrated signals from all electrical diagnostics in the diode region; a pulse-to-pulse reproducibility of ± 2 percent; and the complete absence of a prepulse.

2. SUMMARY OF ACCELERATOR DESIGN

The design of the field emission system is sufficiently unique to justify a brief description. The basic design concept of the system is the paralleling of fifteen synchronized, 320-kV Marx generators into a common, matched-impedance transmission line. This approach was taken to minimize the system inductance, a low-system inductance being necessary

108

for a fast rise-time, low-impedance source. A cross-sectional view of the system in its original exploding wire configuration is shown in figure 29. The electrical energy is stored in the fifteen 70-ohm pulsers (E) which are connected in parallel to the 4.7-ohm coaxial transmission line (I and J). Each pulser consists of a stack of 26 energy storage modules which form a modified Marx circuit. The energy storage modules are LC lumped-constant storage lines, fabricated from high-dielectric-constant ceramic storage elements. At a maximum charging voltage of 32 kV, each pulser delivers a 4600-ampere, trapezoidally shaped current pulse at 320 kV into a matched 70-ohm resistive load. The pulse length is 50 nanoseconds (FWHM) and has a rise-time of approximately 4 nanoseconds between the 10 percent and 90 percent points. The output pulses are transmitted to the common transmission line through 70-ohm coaxial directive switches (F). When discharged into a matched 4.7-ohm resistive load, the system produces a 70,000-ampere current pulse at 320 kV. The output pulse has an 8-nanosecond rise-time and a 55-nanosecond (FWHM) duration. The maximum energy content of the output pulse is approximately 1 kilojoule.

If the rise-time of the combined output pulse is to be 8 nanoseconds, the firing time span of the total pulser array must be approximately 4 nanoseconds. To achieve this degree of synchronization, a combination of ultraviolet light, spark-gap illumination, and over-voltage of a trigger electrode was required (Ref. 68). When the UV pulser (B) is fired, the energy from the pulser is discharged through the spark gap in the UV trigger source (C), and then flows to ground through the multi-output, pulse-splitting transformer shown in figure 30. The individual voltage

A Charging Isolation Resistor
B UV Pulser
C System Trigger UV Source
D UV Pulser Trigger
E Pulser (one of 16)
F Discharge Directive Switch and Pulser
   Lead Chamber
G Tapered Transmission Line Shell
   (Outer Conductor, Ground)
H Tapered Transmission Line Cone
   (Inner Conductor, HV)
I Transmission Line, 18 inch Extension
   (Outer Conductor)
J Transmission Line, 18 inch Extension
   (Inner Conductor)
K Transducer Chamber, Outer Conductor
L Mounting Yoke Assembly
M Transducer Chamber, Inner Conductor
N Yoke Platform
O Transducer Chamber Base
P Vacuum Bell Jar
Q Transducer Lead (Experimental Area)

Figure 29.   Cross Section of the Field Emission
Corporation Pulsed-Power System

110

U.V. Pulser

U.V. Light Source

Load Chamber

Adapter

① Pulse Splitting Transformer

CVR

Trigger Signal Cable

Junction Box ②

Coupling Capacitor Feed Through

③

Charging Resistor

1 of 15 System Pulsers
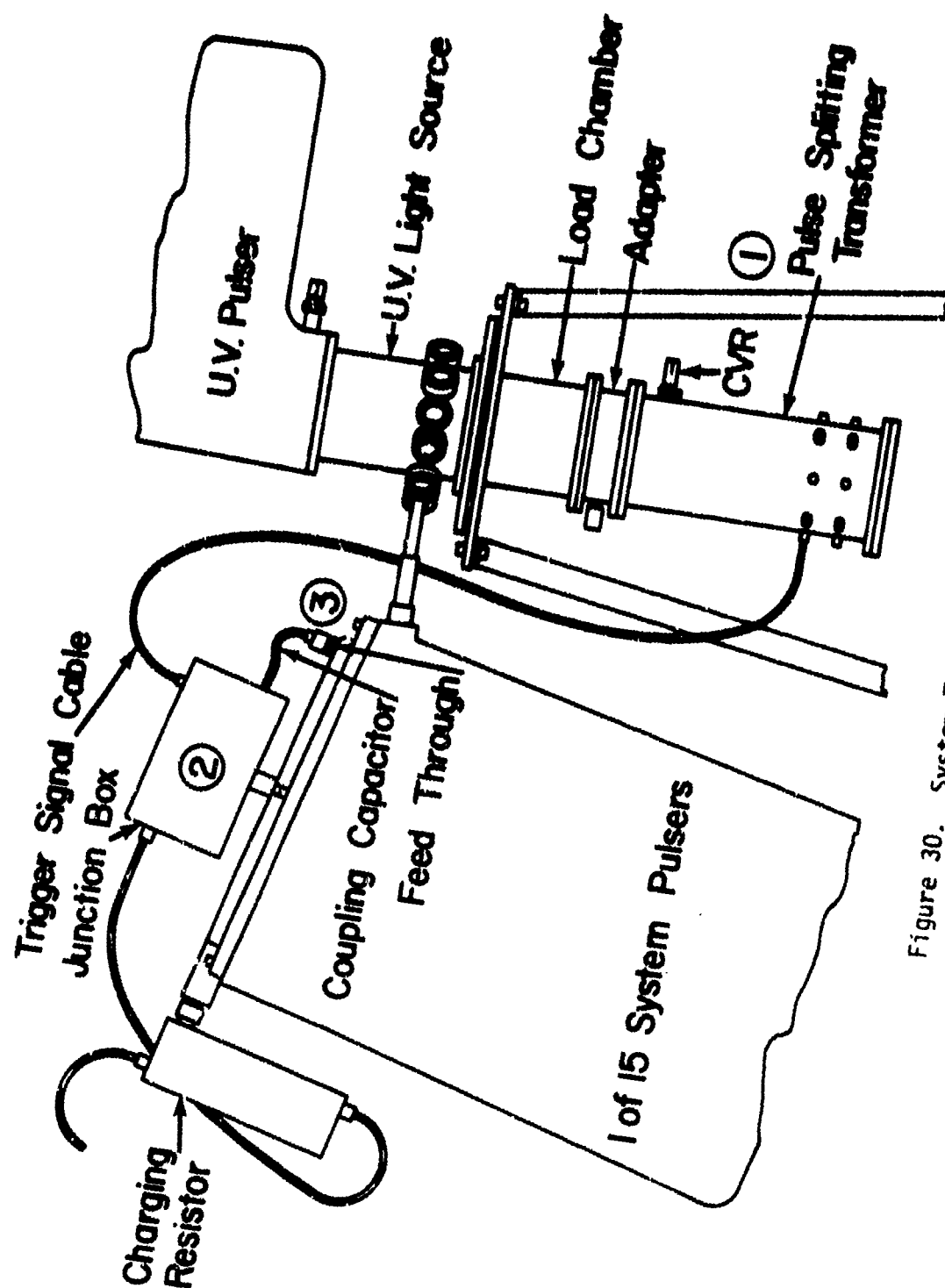
Figure 30. System Trigger Network

111

pulses from the transformer are applied to the trigger electrodes which
are positioned between the electrodes of the stop spark gap in each
pulser. The application of the trigger pulses is delayed 15 nanoseconds
relative to the UV illumination of the top gaps. For normal operation,
the pulsers are charged to within 10 percent of self-fire for a given
pressure.

The current output of the UV pulser is monitored to initiate the
timing of the diagnostic circuits. When triggered by the rise of the UV
current pulse, solid state circuits trigger the data oscilloscopes and
then, after a variable delay, generate a fiducial pulse which is injected
onto the trace of each oscilloscope. These fiducial markers provide a
common zero time for all diagnostic channels with a simultaneity of ± 0.1
nanosecond.

3. PULSER CIRCUIT

The design of the fast-energy-storage network used in the field emis-
sion pulsed-power system is predicated on the fact that the transient
behavior of an open-circuited transmission line can be approximated by an
equivalent lumped-parameter circuit. Where a square pulse is the output
of an ideal distributed-parameter line, an ideal lumped-parameter line
will generate a trapezoidally shaped pulse. In contrast to the more
common practice of using distributed-parameter pulse-forming lines, the
modified Marx generators used in this pulsed-power system combine the
voltage additive feature of the Marx circuit with the pulse-shaping
characteristics of a lumped-parameter network. Inside the pressurized
pulser case is an array of 25 energy-storage or pulse-forming modules
(see figure 31) stacked to form a modified version of the basic Marx
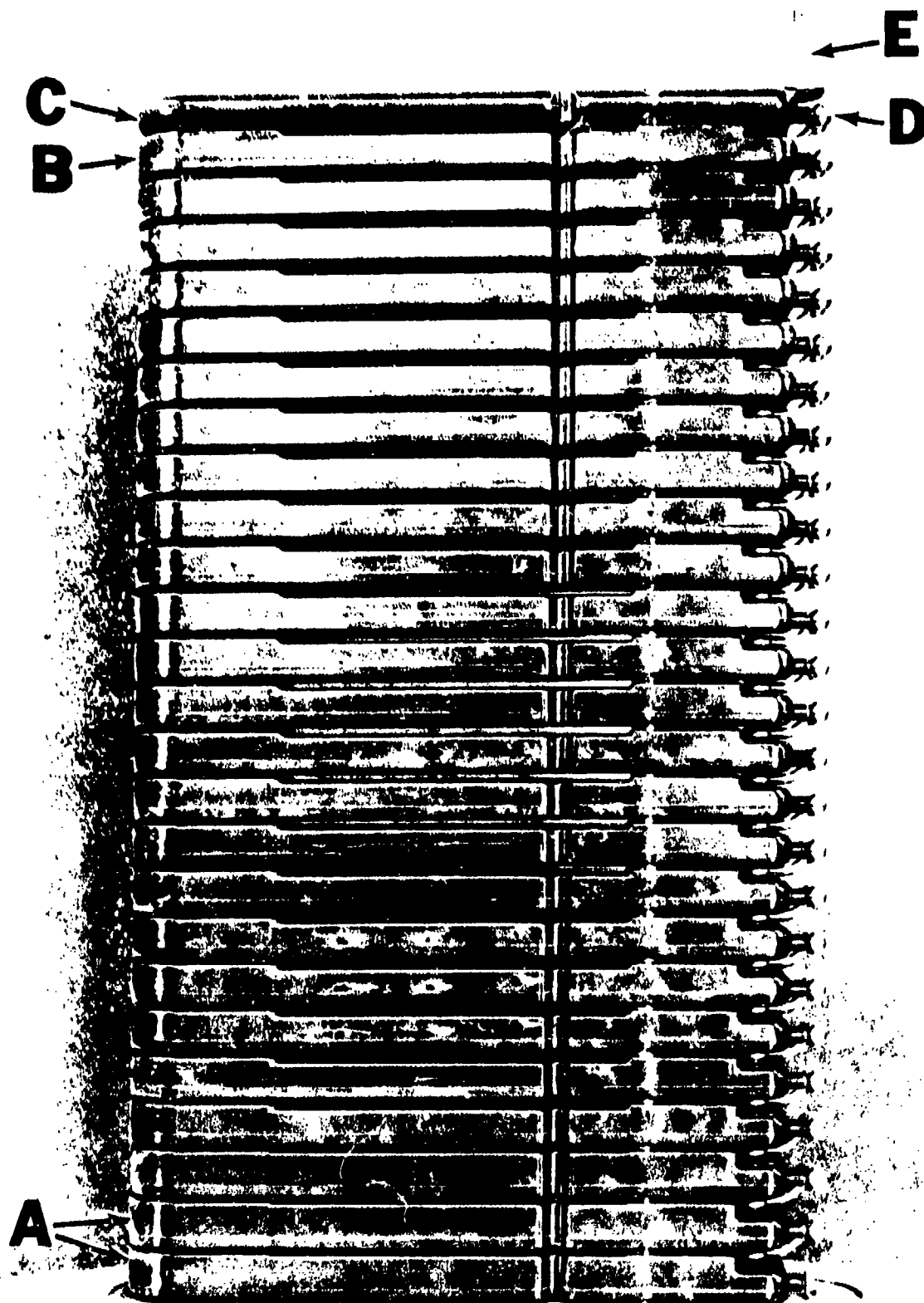
Figure 31. A Module Stack

113

circuit. Like the normal Marx circuit, the energy-storage modules are charged in parallel but discharged in series (see figure 32) to achieve the required high-voltage output. Unlike the original circuit, the capacitive elements which usually form the individual stages of the generator were replaced by lumped-parameter transmission lines, thus providing the pulse-shaping capability of the modified Marx circuit.

The energy-storage modules, the basic unit of the modified Marx generator, contain elements which determine the system performance in four important areas: (1) energy storage capacitors; (2) pulse-forming network; (3) high-inductance coils to provide hold-off isolation between the stages of the Marx during the discharge of the system; and (4) low-inductance switches to connect the Marx in series for discharge. The layout of the internal elements of a module can be seen in the photograph of a special module cast in transparent epoxy shown in figure 33. Energy storage is accomplished within the tightly packed, linear array of barium titanate disk capacitors. With the upper and lower surfaces of each ceramic disk coated with conducting material, the LC lumped-parameter line was formed by connecting the capacitors in parallel using a broad strap to ground the bottom surfaces, and a thin wire to connect the top. The section of wire between the capacitors provided the inductance for each section of the line.

Located at one end of the line are the high-inductance coils which provide connection for parallel charging of the module capacitors, and then protect the high-voltage power supply during the discharge period. Of the two electrodes mounted on the support arms which extend from the other end of the module, one is connected to the high-voltage side of
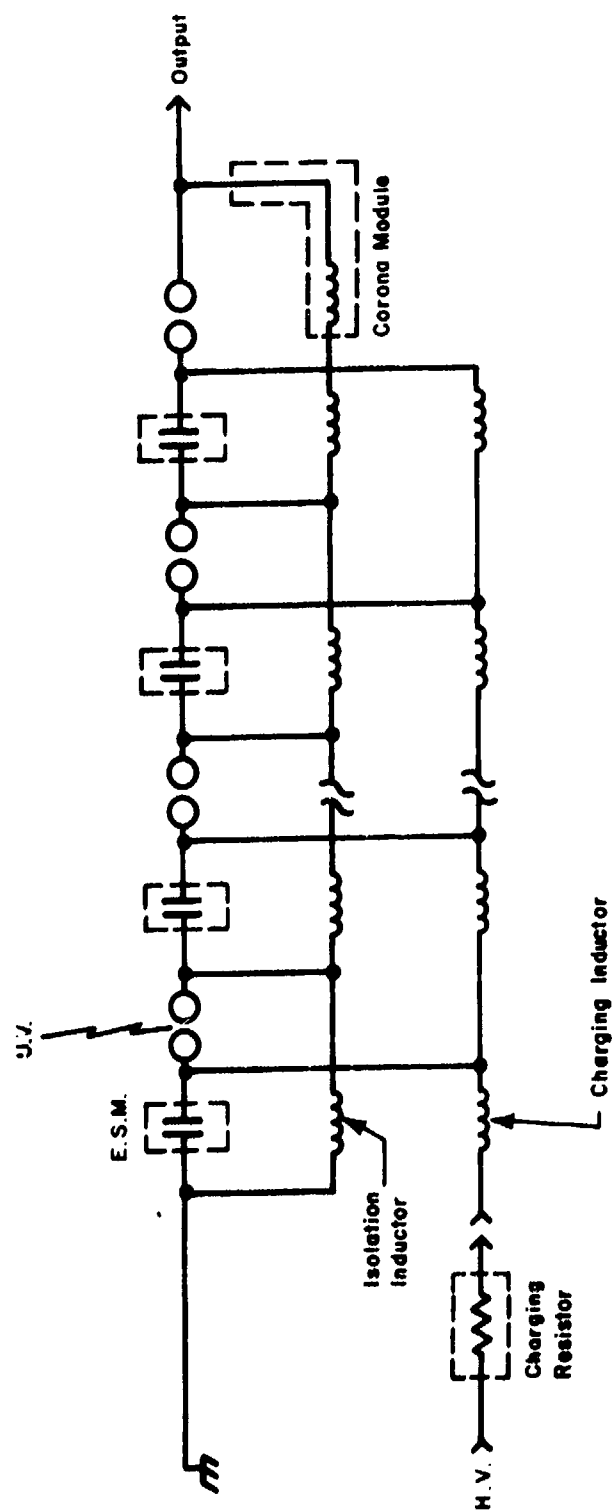
Figure 32. Schematic of the Module Stack

115
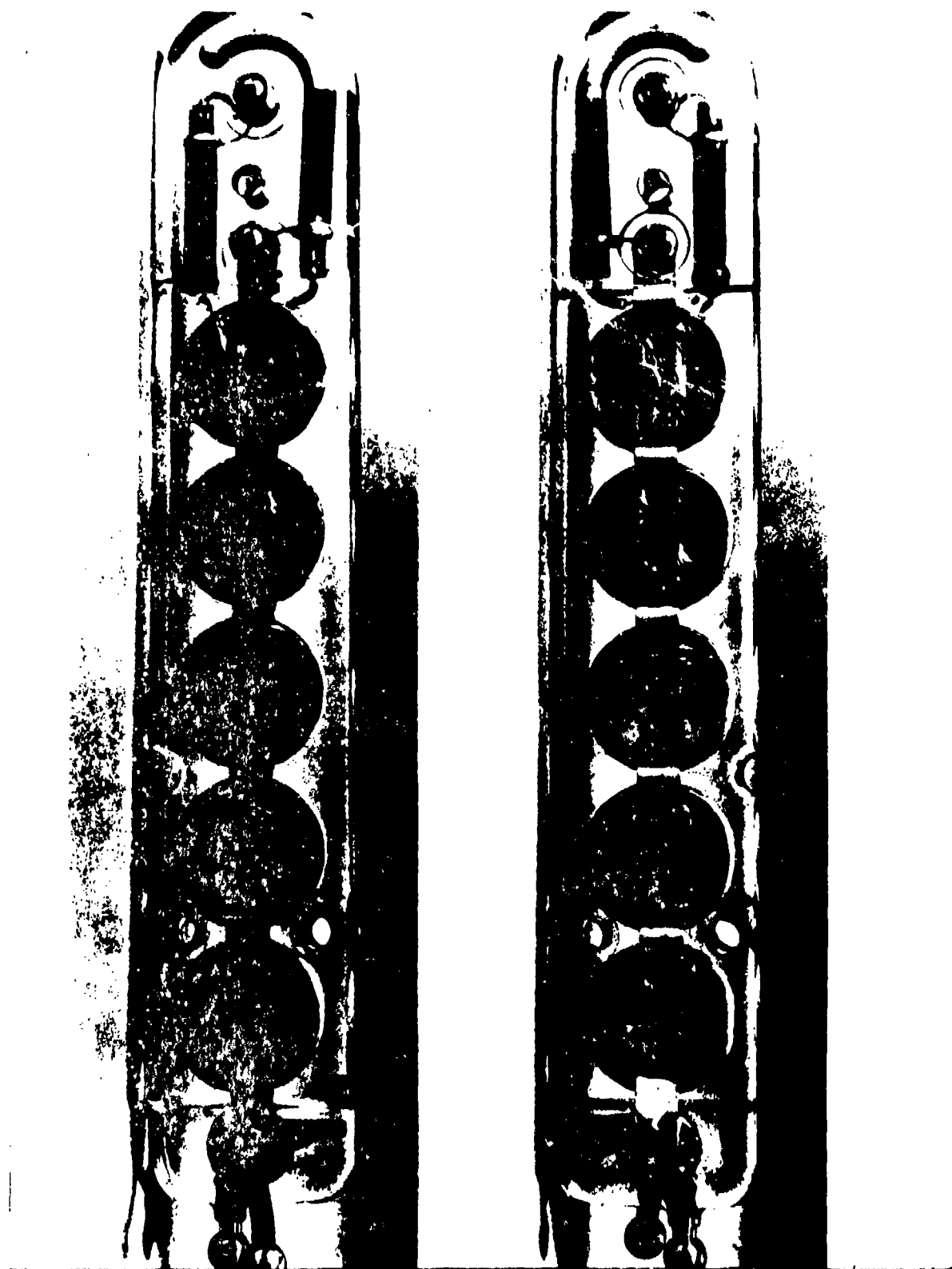
Figure 33.   Internal Components of a Module

the pulse-forming network, while the other is connected to ground through the isolation inductor. When the modules are stacked in the Marx array, these electrodes form the low-inductance, pressurized-gas switches which connect the Marx stages in series for discharge.

The lumped-parameter line of figure 33 is shown schematically in figure 34, as a set of high-dielectric-constant disk capacitors interconnected by inductors. Each LC combination is referred to as a section of the line. The characteristic impedance of the line is then given by the formula $Z_p = (L/C)^{1/2}$, where L and C are, respectively, the section inductance (henry) and capacitance (farad). The transmission line delay per section is given by $(LC)^{1/2}$, while the pulse length for the entire network is given by $\tau = 2N(LC)^{1/2}$, N being the number of line sections forming the network. The value of the output inductance L_t and output capacitance C_t were adjusted to trim the leading edge of the output pulse. By using five sections to form the module, the necessary energy storage capacity per module and desired pulse shape were obtained.

The output characteristics of each energy storage module can be easily estimated by approximating the pulse-forming network within the module by a parallel-plate transmission line or strip line with the same gross physical dimensions as the capacitor array. The strip line shown in figure 35 can, therefore, be used to describe the transient response of a charged energy storage module if its dimensions are set as follows: S = 1.04 cm; W = 4.32 cm; ℓ = 21.6 cm; and K_e = 1000, where K_e is the dielectric constant. The total capacitance of such a strip line is 7.9 nanofarads. When the strip line is charged to 30 kV, this results in a stored energy of 3.5 joules. The actual energy stored in a module charged to 30 kV is
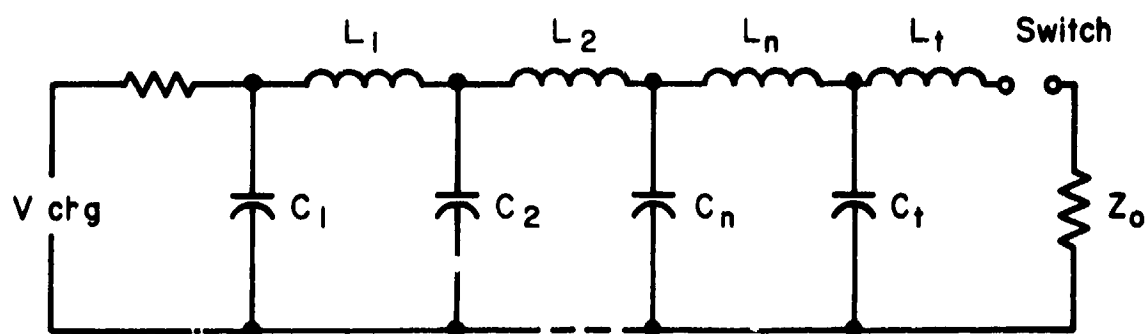
Figure 34. Schematic of Module Components
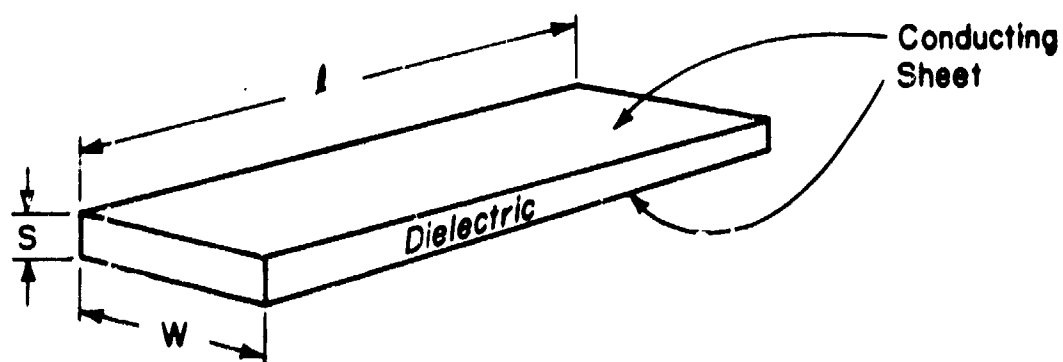
Figure 35. Strip-Line Equivalent of Module

118

3.2 joules. This agreement is quite reasonable as the area of the conducting surfaces in the strip line is somewhat larger than the corresponding surfaces in the energy-storage module. Since the characteristic impedance of the strip line, $Z_p = (L/C)^{1/2}$, is 2.9 ohms, the impedance of 25 such lines connected in series is approximately 72 ohms. As described earlier, the measured pulser impedance was 70 ohms. A similar agreement was found in the duration of the output pulse. The pulse length for the strip line approximation is given by $\tau_p = 2\ell \sqrt{K_e}/c$, where c is the speed of light. Inserting the appropriate values yields a pulse duration of 46 nanoseconds, while the actual pulse length (FWHM) was 50 nanoseconds.

4. INTERACTION BETWEEN THE PULSE-FORMING MODULES AND THE SYSTEM LOAD

Following the synchronous breakdown of the Marx spark gaps within each pulser, the voltage developed across the load resistance is determined by the interaction between the pulse-forming modules and the system load. As shown in figure 36, the modules are connected to the load by a network of matched-impedance coaxial lines. With the pulser impedance matched to the input impedance of the line network, the complex array of figure 36 can be simplified to the schematic shown in figure 37. In the simplified schematic, the parallel network of fifteen 70 ohm directive switches connected to the common 4.7 ohm coaxial line has been replaced by a single transmission line of equal total electromagnetic delay; i.e., the transit time of an electromagnetic impulse within the single line is equal to that of the parallel network. Similarly, the signal source in figure 37 represents the output characteristics of the 15 pulser array.

119
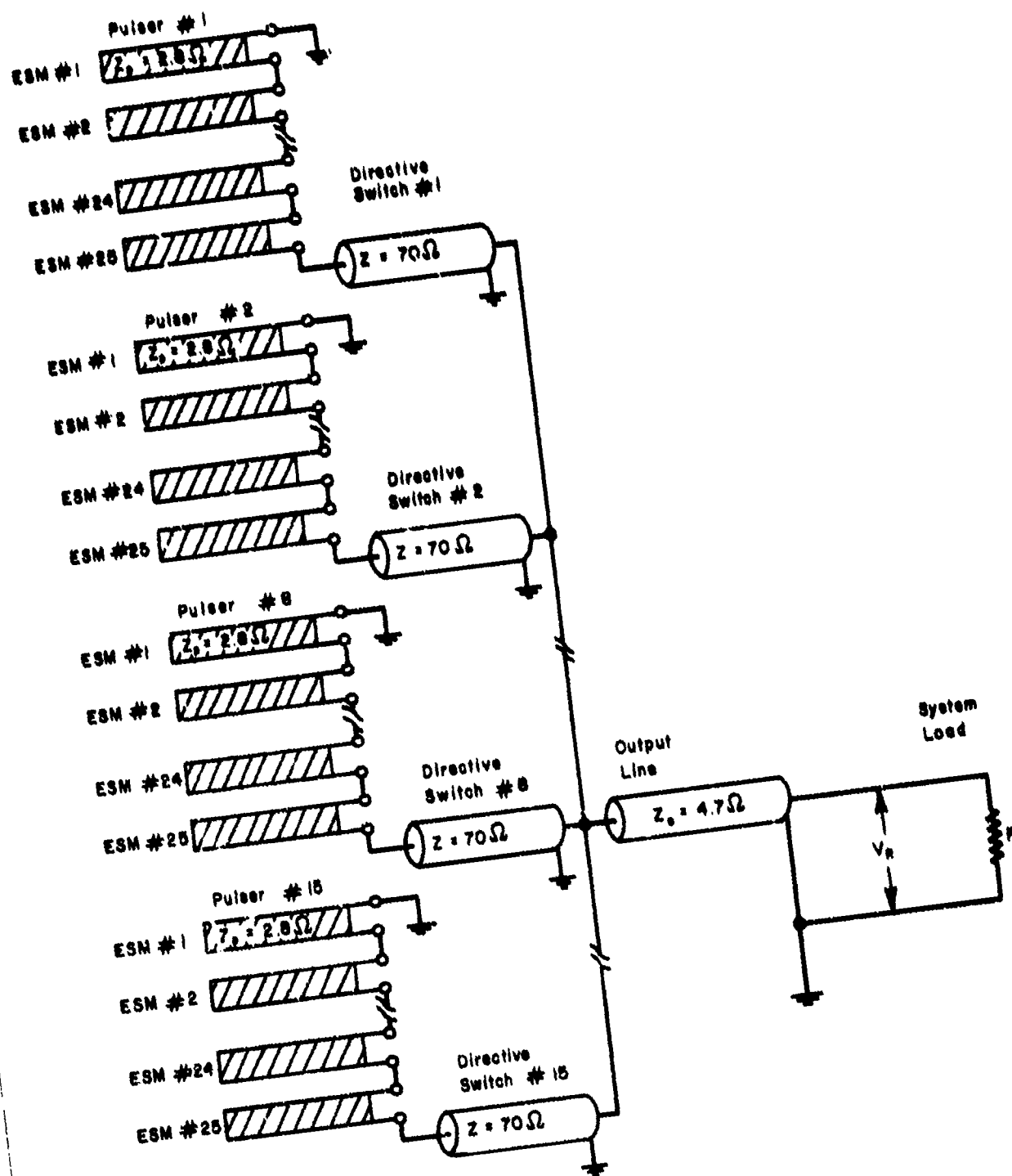
Figure 36. Electrical Schematic of Assembled System

120

To determine the output characteristics of the source, consider the schematic of a pulse-forming module shown in figure 38. The spatial and temporal variation of the potential between the parallel electrodes is governed by the transmission line equations

$$\frac{\partial V}{\partial x} = -L \frac{\partial i}{\partial t} \tag{96}$$

and

$$\frac{\partial i}{\partial x} = -C \frac{\partial V}{\partial t} \tag{97}$$

Combining these equations yields the following wave equation

$$\frac{\partial^2 V}{\partial x^2} = LC \frac{\partial^2 V}{\partial t^2} \tag{98}$$

where C and L are, respectively, the capacitance/meter and inductance/meter for the transmission line. For a uniform transmission line, the voltage is propagated along the line as a wave. Solutions to the wave equation take the form of two standing waves moving in opposite directions; i.e., $V(x) = F(x - vt)$ and $V(x) = g(x - vt)$, where the wave velocity $v = (LC)^{-1/2}$. The transmission line characteristics for parallel-plate and coaxial geometries are given in table V.

When the switch is closed, one end of the pulse-forming module remains as an open circuit and the other is connected to ground through the equivalent load R_p. Under Laplace transformation, and using the appropriate initial and boundary conditions, the wave equation can be solved to give the voltage developed across the load as a function of time.
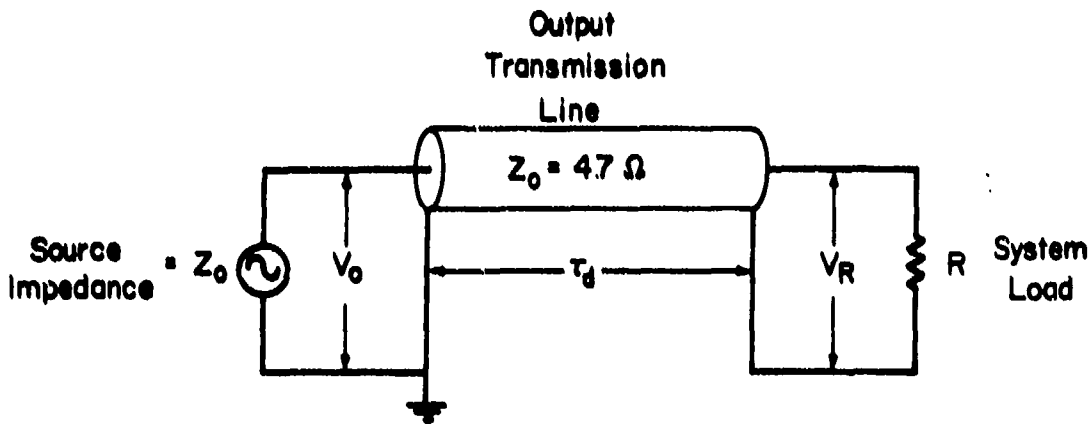
Figure 37.   Interaction Between Pulsed-Power System
and System Load

PULSE FORMING MODULE
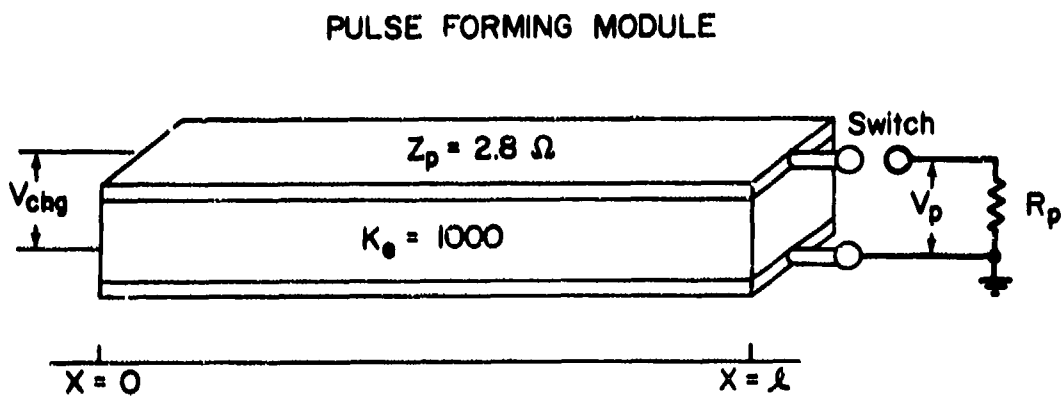
Figure 38.   Pulse-Forming Function of Energy Storage Module

Table V

TRANSMISSION LINE CHARACTERISTICS

Characteristics	Parallel-Plate	Coaxial	Units
C	$K_e \epsilon_0 \frac{b}{a}$	$2\pi K_e \epsilon_0 / \ln(r_0/r_i)$	farads/meter
L	$\mu \frac{a}{b}$	$\frac{\mu}{2\pi} \ln(r_0/r_i)$	henries/meter
Z_0	$\frac{120\pi}{\sqrt{K_e}}$	$\frac{60}{\sqrt{K_e}} \ln(r_0/r_i)$	ohm
v	$\frac{c}{\sqrt{K_e}}$	$\frac{c}{\sqrt{K_e}}$	meter/sec

$$V_{R_p}(t) = \frac{V_{chg} R_p}{Z_p} \, \mathcal{L}^{-1} \left\{ \frac{1}{s} \left(1 - e^{2s\ell/v} \right) \left[\left(1 + \frac{R_p}{Z_p} \right) + \left(1 - \frac{R_p}{Z_p} \right) e^{-2s\ell/v} \right]^{-1} \right\}$$

$$(99)$$

where Z_p is the characteristic impedance of the strip line, R_p is the equivalent load resistance, and V_{chg} is the final charging voltage. Since the impedance of the directive switch is matched to that of the 25 pulse-forming modules connected in series, the equivalent load resistance is equal to the characteristic impedance of the module. For the matched case, $Z_p = R_p$, equation (99) is reduced to

$$V_{R_p}(t) = \frac{V_{chg}}{2} \left[u_0(t) - u_{2\ell/v}(t) \right] \tag{100}$$

where $u_a(t)$ is the unit step function defined by

$$u_a(t) = \begin{cases} 0 & \text{when } t < a \\ \\ 1 & \text{when } t > a \end{cases} \tag{101}$$

With the 25 modules connected in series, the total voltage developed between the coaxial output terminals of each pulser is theoretically equal to

$$V(t) = \frac{25 V_{chg}}{2} \left[u_0(t) - \frac{u_{2\ell}(t)}{v} \right] \tag{102}$$

The duration of the output pulse is determined by the transit time of an electromagnetic wave within the dielectric material of the module. If all the pulsers are triggered simultaneously, the voltage pulses will be transmitted from each pulser to the system load without any significant

distortion. The parallel connection of the pulsers results in a current pulse equal to the summation of the fifteen pulses.

Returning to figure 37, the signal source has now been characterized as having a 4.7-ohm impedance, and producing the voltage pulse described by equation (102). After the last gap in the Marx stack has closed, the output pulse will be injected into the coaxial transmission line and transmitted without distortion to the system load. When the square wave reaches the load, some fraction of the wave may be reflected depending upon the value of the terminating resistance. The incident and reflected components, V_i and V_r respectively, of the injected wave are related through the reflection coefficient ξ.

$$V_r = \xi V_i \qquad (103)$$

where

$$\xi = \frac{R - Z_0}{R + Z_0} \qquad (104)$$

and R and Z_0 are, respectively, the load resistance and the characteristic impedance of the output transmission line. The voltage drop across the resistive load is then equal to the summation of the incident and reflected waves.

$$V_R = V_i + V_r = \left(\frac{2R}{Z + Z_0}\right) V_i \qquad (105)$$

Three particular values for the terminating resistance are of special interest: $R = 0$, $R = Z_0$, and $R \to \infty$. If R is equal to zero, corresponding to a short circuit, the reflection coefficient is -1, and the reflected voltage wave is of the same amplitude as the incident wave, but opposite in sign. For the matched case, $R = Z_0$, the reflection coefficient

125

is zero. There is no reflected wave and all of the power is absorbed in the pure resistance. Finally, if the load resistance approaches infinity, as the case when the line is open-circuited, $\xi = 1$, and reflection occurs without change in phase.

If the load is not matched to the line, $R \neq Z_0$, a wave ξV_1 will be reflected back toward the pulse-forming modules. Since the line and source impedances are matched, the reflected wave will be transmitted without distortion until the open-circuit termination of the pulse-forming module is reached. At this point, the wave is again reflected, but without change in phase. The subsequent reflection between the resistive and open-circuit terminations of the systems will continue until the energy of the wave has been totally dissipated in the resistive elements of the circuit, i.e., resistive load, skin resistance of the conducting surfaces, and plasma resistance in the spark channels within the gaps. The resultant pulse shapes for several values of R are shown in figure 39. For the matched load, the voltage across the resistance is described by

$$V_R = 25 \, V_{chg} \left(\frac{R}{R + Z_0} \right) \left[u_a(t) - u_b(t) \right] \tag{106}$$

where $a = \tau_d$ and $b = 2\ell/v + \tau_d$, giving a pulse duration of 50 nanoseconds. When the system was terminated by a constant-resistance load, the actual load voltage was found to be approximately 20 percent lower than the "ideal" value predicted by equation (106). The difference between these values was attributed to losses and slight impedance mismatches in the physical system.
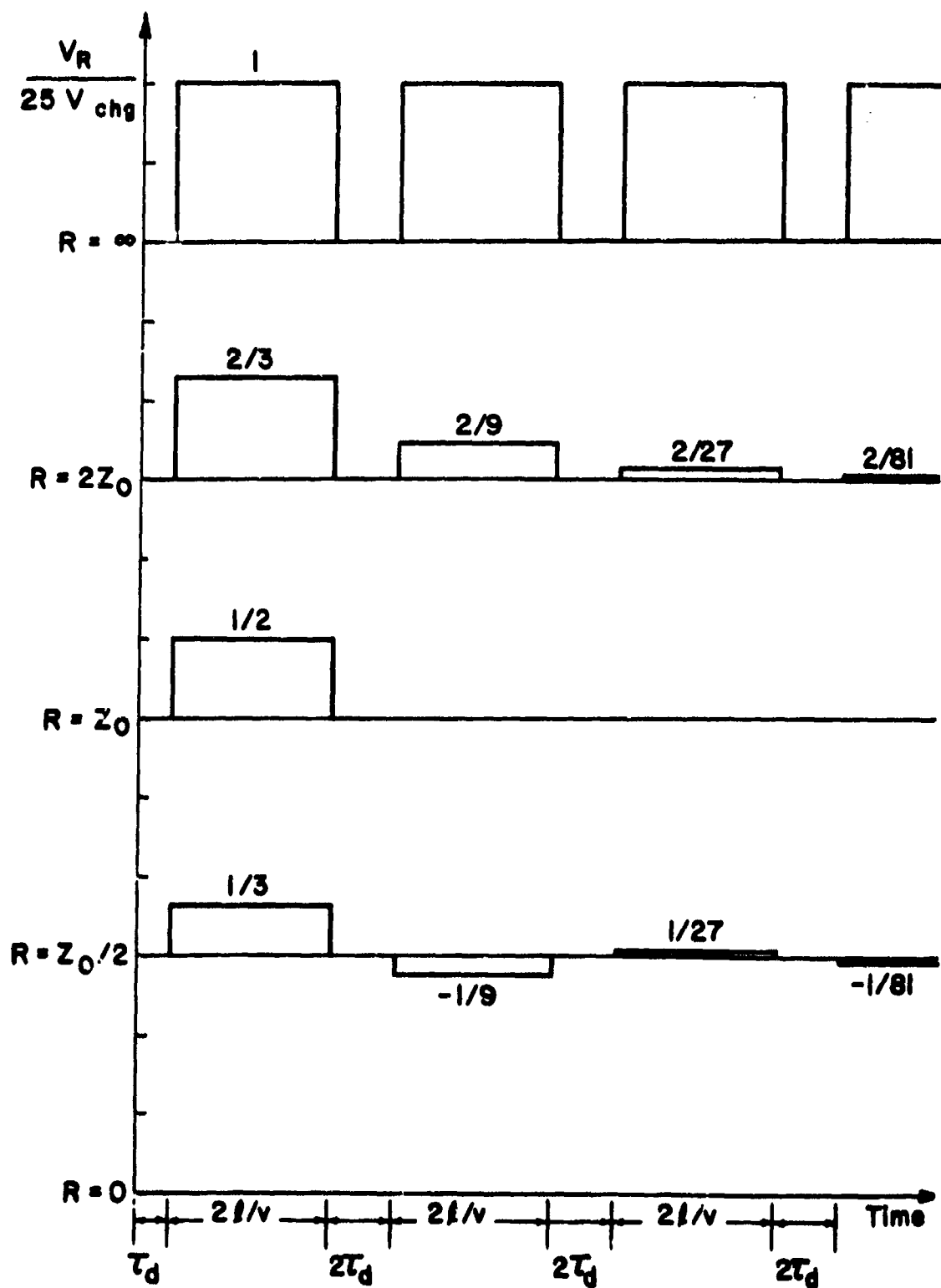
Figure 39. Variation in Output Waveform with Load Resistance

SECTION V

DIODE DESIGN

1. FUNCTIONAL REQUIREMENTS

To operate the pulsed-power system as a low-impedance, electron accelerator, the transducer chamber (P and Q in figure 29) of the exploding wire configuration had to be replaced by a structure incorporating the cold cathode and stretched-foil anode of a low-resistance, high-current diode. Like the transducer chamber, such a diode structure has the function of connecting the output of the pulsed-power system to the system load with a minimum of impedance mismatch. Furthermore, both assemblies must incorporate means of measuring the voltage across the load as well as the current and time rate of change in current flowing through the load. Lastly, these transmission line terminations must withstand the voltage across the load, and be capable of operation when the load region is evacuated to a high vacuum.

Unfortunately, certain of these functional requirements are mutually exclusive. On one hand, there is the requirement for a matched-impedance transition from the physical dimensions of the coaxial transmission line to those of the system load. Conflicting with this requirement, a satisfactory voltage holdoff capability must be maintained throughout the transition. Considering the catastrophic consequences of insufficient voltage holdoff, the breakdown characteristics of the terminal transition must take precedence. The subsequent failure to maintain the transmission line impedance up to the point of

128

connection to the system load results in an effective series inductance which can limit the current rise time in the load. The extent of this limitation is dependent upon the relative interelectrode spacing, which is determined by the environmental conditions in the region of the load.

Unlike the diode structure which must operate only at high vacuum, the transducer chamber had been designed to operate over a pressure range extending from high vacuum to several atmospheres. Consequently, several of the compromises necessary to achieve an optimum design for the chamber were biased toward the higher pressures within this range. Specifically, the hemispherical chamber geometry had been selected instead of an equivalent conical configuration, because volume break-down in air was determined to be the limiting factor in voltage holdoff at atmospheric pressures. Compared to an equivalent conical configura-tion, the voltage gradients within a hemispherical chamber are lower throughout most of the interelectrode volume. The field strength at the surface of the inner conductor is lower in the case of the conical geometry, however. Furthermore, the conical geometry offers a lower series inductance. In spite of these features, the demonstrated volume-breakdown problem dictated that the field configuration within a hemispherical chamber had to be favored.

To facilitate interchangeable transducer-chamber components, the oil-filled transmission line was connected to a short, matched-impedance line-section fabricated using a mica-filled epoxy dielectric. This section, designated as the transducer-chamber base, is shown at 0 in figure 29. The choice of a hemispherical transducer chamber resulted in radial electric field lines which are parallel to the plane of the

129

epoxy-air surface at the base of the transducer chamber. Since the dielectric constant of the epoxy is higher than that of the chamber gas, a slant or convoluted surface would have enhanced the field in the gas. Field lines parallel to the surface were, therefore, considered advantageous for operation at moderately high chamber pressures.

2. HIGH-VOLTAGE BREAKDOWN OF VACUUM-DIELECTRIC SURFACE

A more recent study of surface flashover by Ian Smith (Ref. 69) has shown that a slant dielectric surface is preferable for vacuum operation. To obtain optimum breakdown strength from a dielectric-vacuum surface, the angle between the surface and the field must be selected to inhibit secondary electron multiplication. The results of a similar study by A. S. Denholm et al. are shown in figure 40 (Ref. 1). As seen from these results, the probability of surface flashover is highest, and the voltage holdoff lowest, when the field lines intersect a dielectric surface at slightly negative angles. The parallel surface at the base of the hemispherical transducer chamber therefore represented a worst possible case for vacuum operation.

The anticipated use of transducer chamber components to form the support structure of the cold-cathode diode necessitated a careful evaluation of a potential surface-flashover problem during vacuum operation. In partial anticipation of such a problem, Field Emission had fabricated inner hemispheres (M in figure 29) of three different radii. These hemispheres offered a choice of 1-inch, 2-inch, or 3.3-inch inter-electrode spacings. From figure 40 the flashover point for an epoxy-vacuum surface parallel to the electric field lines should be approximately 140 kV/inch. The coaxial and spherical approximations for the

130
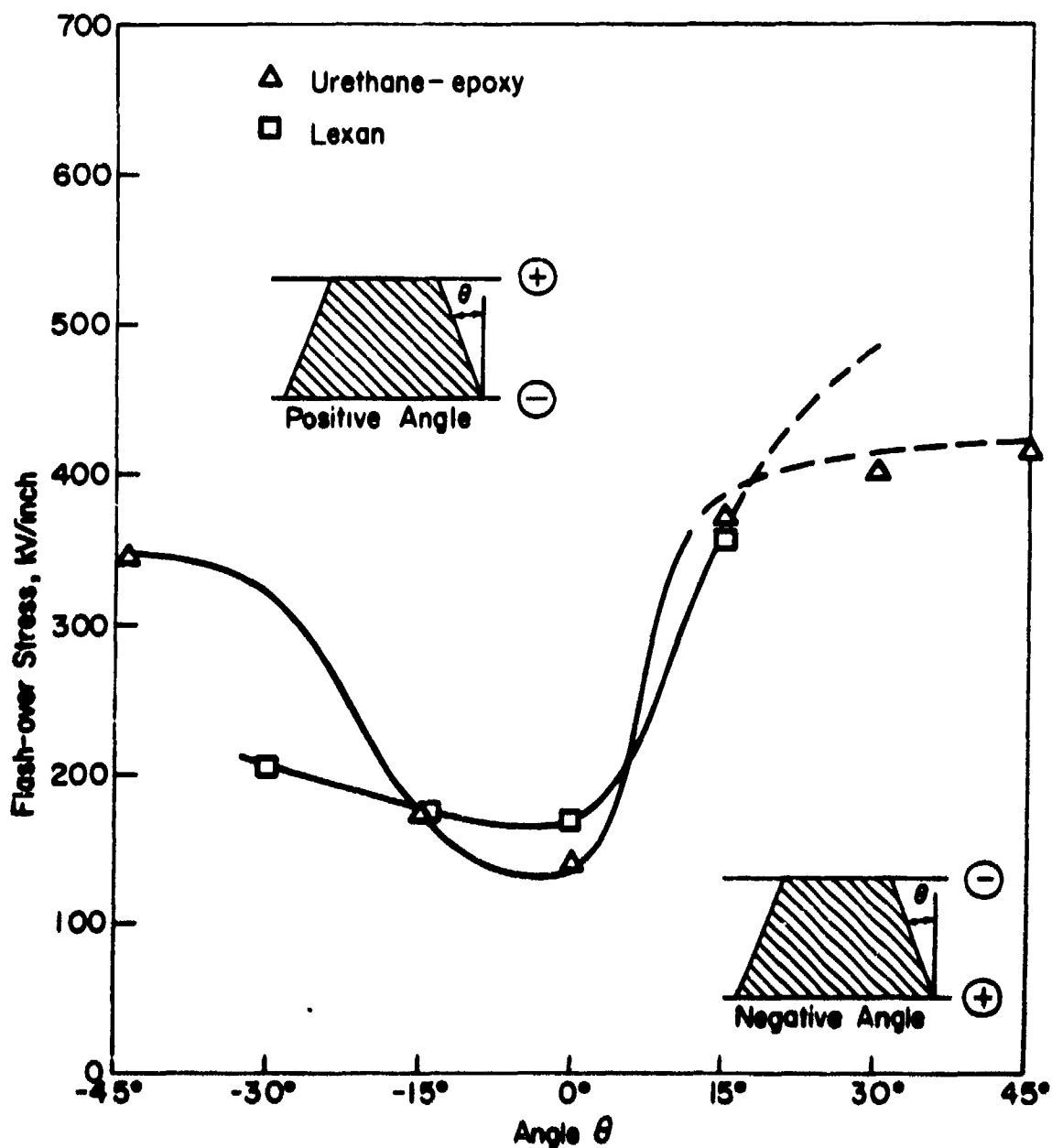
Figure 40. Comparison of Dielectric Flash-Over Performance

electric field at the surface of the smallest inner hemisphere yield 134 kV/inch and 190 kV/inch, respectively, if the applied potential is 300 kV. The actual field at the junction of the coaxial and spherical geometries must be between these extremes. Consequently, surface flashover of the epoxy surface and the subsequent short circuit of the output pulse can hardly be avoided when the fully-charged system is discharged into the evacuated transducer chamber. Open-shutter photographs of the epoxy surface graphically demonstrated the validity of these estimates.

To avoid the surface flashover problem but still retain the utility of the available hardware as well as certain of the advantages of the hemispherical geometry, the transducer chamber was modified to form the diode structure shown in figure 41. The outer hemisphere (B) remained at its original 6-3/8-inch radius. To minimize the chamber inductance but still retain adequate voltage holdoff, the intermediate inner hemisphere (A), 4-3/8-inch radius, was chosen. To insulate the epoxy surface and eliminate the flashover problem, a Lexan disk was inserted at (C). The region above the disk could then be pressurized with SF_6, an insulating electronegative gas, and the diode region below evacuated.

The basic electrical diagnostics for the diode region are a capacitive voltage-divider (D), a Faraday cup-calorimeter current monitor (E), and a set of four magnetic-pickup-loops (F) which respond to the time derivative of the current. In the configuration shown in figure 41, the diode is formed by the cylindrical cathode (D) and the graphite sensing disk (G) of the Faraday cup, which is located on the anode plane. For application other than the diode study, the Faraday cup is

132

METAL

EPOXY

LEXAN
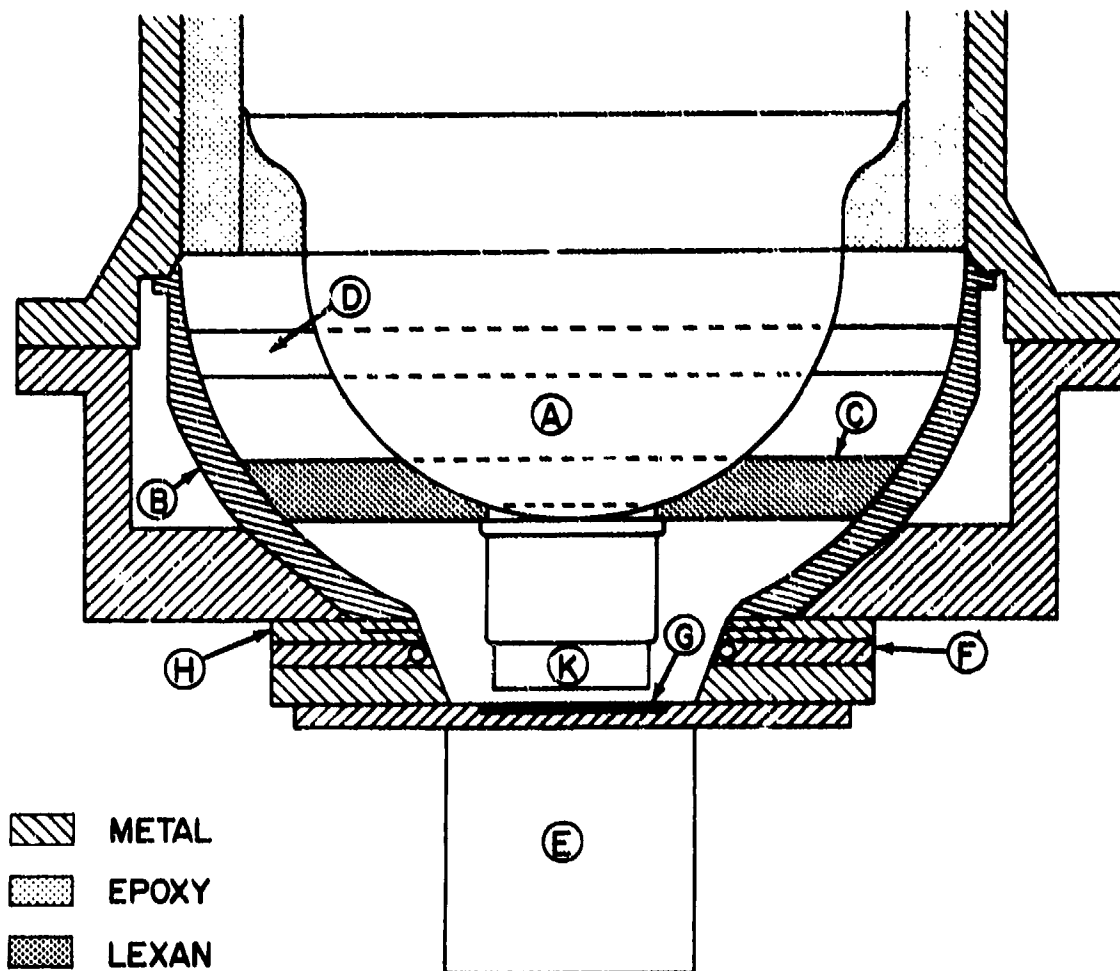
Figure 41. Schematic of the Diode Structure

133

replaced by an assembly which stretches a thin, aluminized-Mylar film across the anode plane. When the Faraday cup is removed, a second current monitor (H), a wall-current shunt, is used.

3. ELECTRIC FIELD ANALYSIS

The initial decision regarding the location of the dielectric disk was based primarily on mechanical considerations. Pressurization of the region above the disk in connection with evacuation of the region below necessitated mechanical support at the inner perimeter of the disk to facilitate a workable vacuum seal. To provide the necessary support, a smoothly radiused lip was incorporated into the base of the cathode shank. The lip also provided electrostatic shielding for the critical region of the dielectric-vacuum surface where the dielectric contacts the center conductor. Since surface flashover is initiated by secondary electron multiplication, it is extremely important to control the electric stress in this region (Ref. 70). The existence of any small gaps between the dielectric and the metal of the center conductor results in a stress enhancement at a most critical juncture. The pressure of the insulating gas pushing the disk against the lip on the cathode shank was thought to minimize this possibility.

Functional requirements dictated the choice of a dielectric material possessing excellent mechanical and electrical properties. Regarding surface breakdown under vacuum conditions, tests at the AFWL had shown Lexan to be one of the better dielectric materials available (Ref. 70). A 1-inch thick Lexan disk was, therefore, selected to

134

provide the required mechanical rigidity and to permit resurfacing if the dielectric surface were to be damaged by deposition of vaporized material and subsequent flashover.

Prior to fabrication, the proposed modification to the transducer chamber was carefully evaluated with respect to (1) the probability of surface flashover at the new dielectric-vacuum surface, (2) possible effects on the operation of the capacitive voltage-divider, (3) suppression of cathode-shank emission, and (4) inductive limitation to the current rise time in the diode. To determine the field strength at certain critical areas, the equipotential distribution within the proposed configuration was computed numerically (Ref. 72). The results of this calculation are shown in figure 42.

The probability of surface breakdown is determined by the angle with which the field lines intersect the dielectric-vacuum surface, and the stress at the surface. From figure 42, the field lines were found to intersect the Lexan-vacuum surface at a positive angle (see figure 40 for the definition of the sign of the angle) of approximately 60 degrees. The surface flashover data presented in figure 40 indicated that a Lexan-vacuum surface should withstand an applied field in excess of 190 kV/cm for such an angle. To determine the voltage holdoff capability of the Lexan disk, calculated values of the voltage gradients along the Lexan-vacuum surface were plotted in figure 43, assuming an applied potential of 300 kV. The maximum stress along the surface was found to be approximately 75 kV/cm. The combined effects of the lip at the base of the cathode shank and the transition from a hemispherical to a cylindrical center-conductor geometry suppressed the applied

135
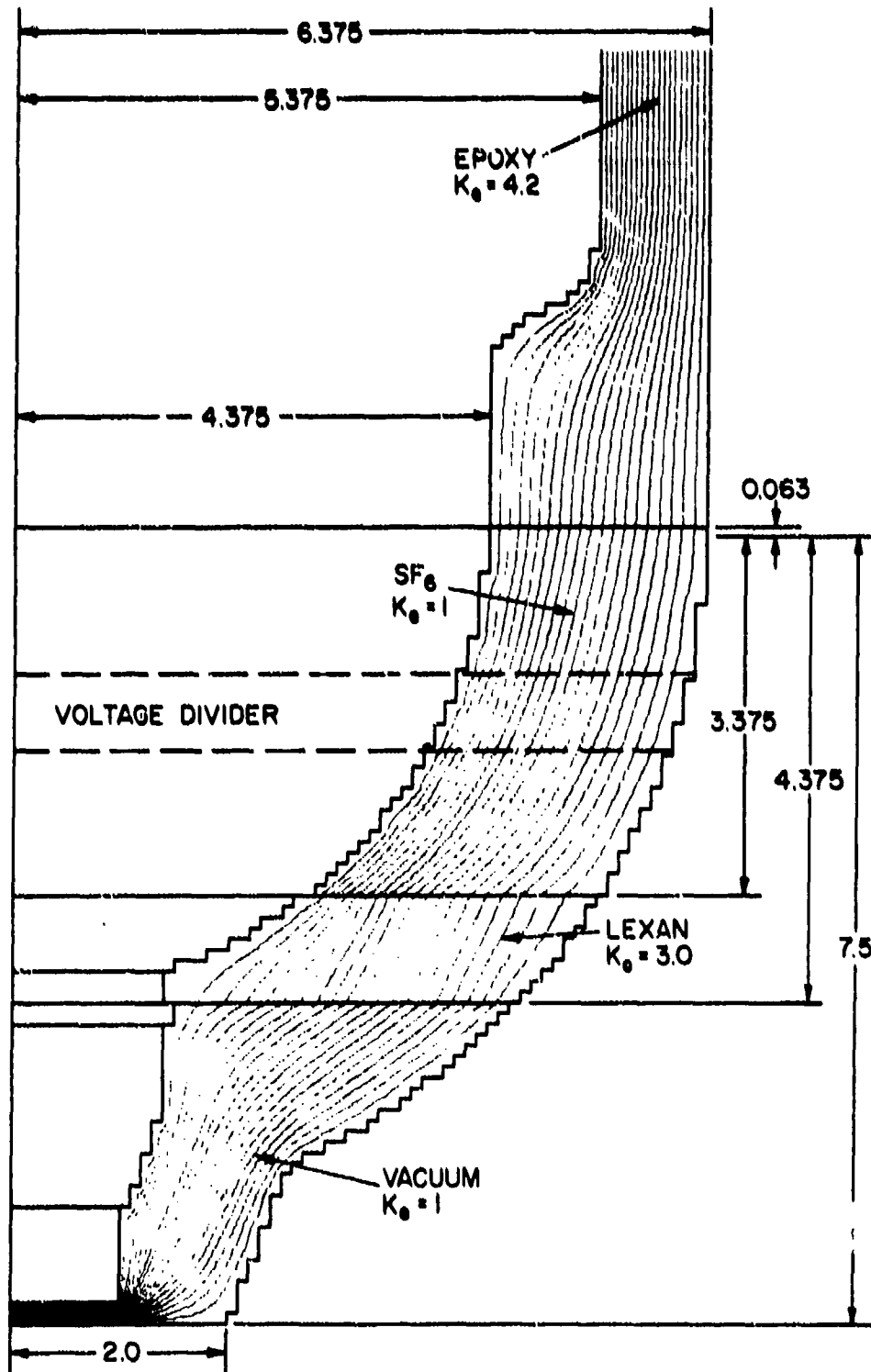
Figure 42. Equipotential Plot for the Diode Structure
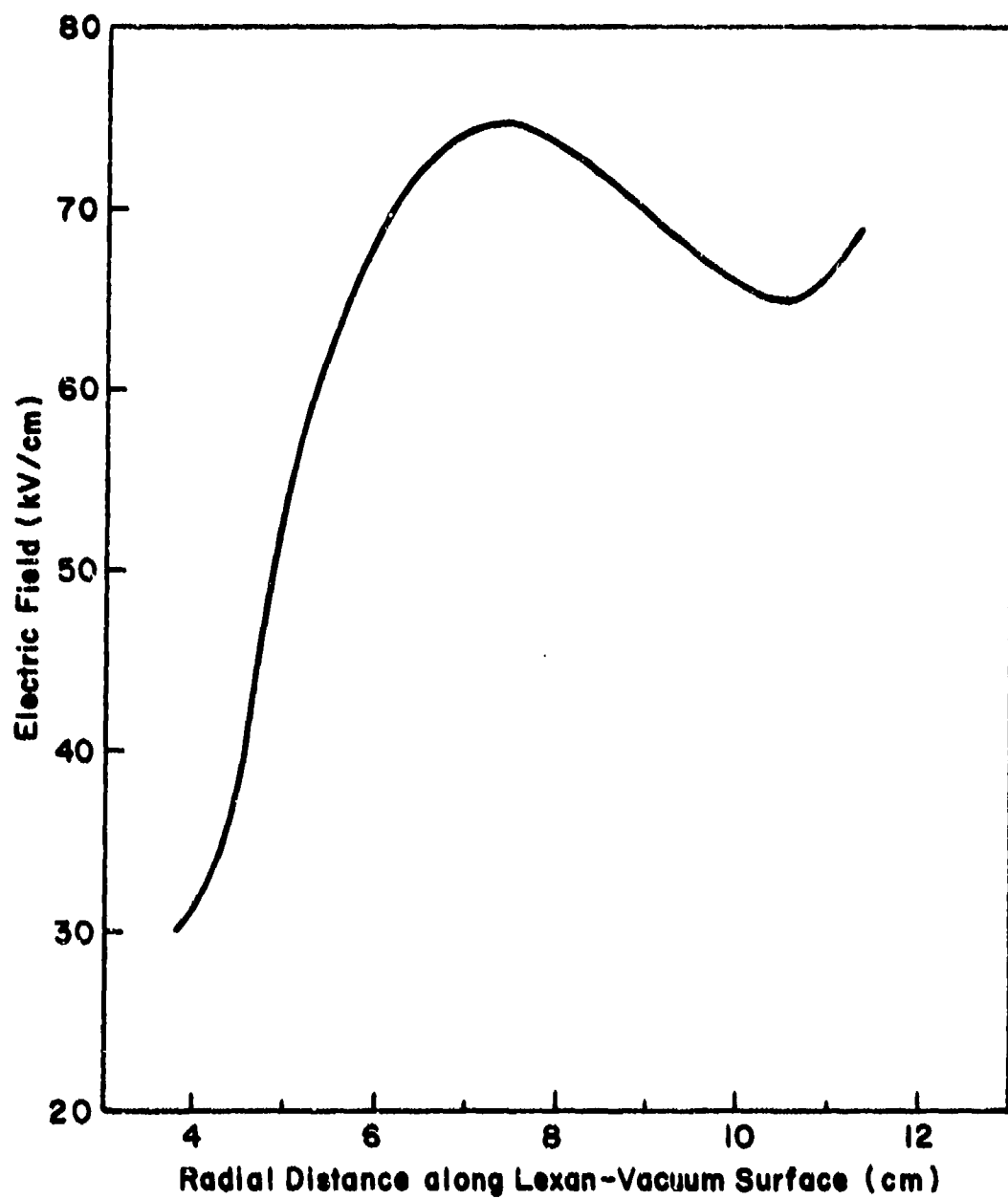
Figure 43.   Field Strength Along the Lexan-Vacuum Surface
Assuming a 300-kV Pulse

137

field at the critical inner periphery of the disk to approximately 30 kV/cm, however. The maximum voltage holdoff capability of the Lexan disk was therefore expected to be in excess of 760 kV, which is comparable to the safety factor designed into the original pulsed-power system.

The radial geometry of the electric field between the hemispheres of the transducer chamber was useful in determining the point at which the voltage was measured with the capacitive voltage-divider. Such a field configuration was readily amenable to calculation. Although the high dielectric constant of the Lexan distorted the field, the radial character in the region of the voltage divider was preserved by positioning the disk at a sufficient distance below the divider. The resultant location of the divider in the SF_6-filled region had the advantage of preventing spurious current flow between the divider strip and the center conductor, which would have degraded the measured voltage signal.

Analysis of the electron flow within the diode is simplified if electron emission from the cathode shank can be suppressed. To minimize the electric field at the surface of the cathode shank, the hemispherical geometry of the outer conductor was transformed into a conical configuration in the diode region. Again referring to figure 42, the maximum electric field along the brass cathode shank was determined to be approximately 190 kV/cm for an applied potential of 300 kV. Since a field on the order of 300 kV/cm is required to produce an emitted current density of roughly 1 ampere/cm^2 from a polished electrode

138

surface (Ref. 73), significant electron emission from this region was not anticipated.

The electron emission from the three regions of the graphite cathode was also evaluated. The field along the cathode surface is seen to be highest at the outer edge, lower and approximately uniform across the circular face, and lower yet along the cylindrical sides. A short distance behind the edge, the field along the cylindrical portion of a 5.08-cm diameter cathode was in the range of 200 kV/cm to 300 kV/cm for a 300 kV pulse. For the same cathode and pulse, the field across the face ranged from 500 kV/cm to 1.5 MV/cm, depending upon the diode separation. This indicated that electron emission from the cathode face and edge would have been predominant.

4. INDUCTANCE CALCULATIONS

Having biased the design compromises to obtain the necessary voltage holdoff capability, the diode structure did not represent a matched-impedance extension to the coaxial transmission line. Viewing the hemispherical chamber as a transmission line element, the input impedance at the plane of the epoxy-SF_6 surface was readily calculated to be 22.6 ohms. As the wavefront procceeded from this surface towards the Lexan disk, the impedance increased smoothly but rapidly to approximately 40 ohms. Below the disk, the wavefront encountered a series of impedance discontinuities resulting from variations in the contour of the electrode surfaces. Since the transit time of the wavefront from the base of the hemisphere to the diode region was short compared to the rise time of the wavefront, the distortion of the wavefront was

139

better treated by considering the reactances of the diode structure as lumped parameters.

The simplest method of predicting with reasonable accuracy the waveshape that might be expected to reach the diode would involve the calculation of reflection coefficients from a lumped-parameter equivalent circuit. These reflection coefficients would have frequency dependent amplitudes and phase shifts. Fourier analysis could then be used to resolve the frequency components of the output waveform from the pulser array. By applying the reflection coefficients to the frequency components of the incident wave, one could synthesize the waveform of both the transmitted and reflected waves at the input plane of the diode structure.

A detailed analysis such as this was considered unnecessary since the primary concern regarding the mismatched condition centered on the possible limitation to the current rise time within the diode. With this in mind, the capacitive reactance was ignored, and the diode structure in combination with the remainder of the system was treated as an inductor and series resistance, connected across the terminals of the common coaxial line. The resultant circuit, shown in figure 44, is similar to that used to illustrate the interaction between the pulser array and the system load. In the present case, an additional element, the inductance of the diode structure, has been added and the source impedance is shown explicitly. Assuming an idealized, square-wave output pulse, the waveform developed across the diode resistance is now given by

$$V_R(t) = 25 \, V_{chg}\left(\frac{R}{R+Z_0}\right)\left\{\left[1-\exp\left(-\frac{t-a}{\tau_L}\right)\right]u_a(t) - \left[1-\exp\left(-\frac{t-b}{\tau_L}\right)\right]u_b(t)\right\}$$

(107)

where τ_L is the time constant of the series LR network,

$$\tau_L = \frac{L}{R+Z_0}$$

(108)

$u_a(t)$ is the unit step function, and a and b are defined in equation (106). A sketch of the resultant waveform is shown in figure 45. The rise time of the idealized pulse between the 10 percent and 90 percent points, τ_r, is approximately equal to $2.2 \, \tau_L$. If the rise time of the actual waveform across a matched-resistance diode is to be on the order of 8 nanoseconds, the total uncompensated inductance of the diode structure must be less than approximately 34 nanohenries.

Inductance formulae may be readily derived for coaxial structures having axial symmetry from the relation

$$L = \int_V \frac{\mu \, dV}{(2\pi r)^2}$$

(109)

where L is the inductance of the structure, r is the radial distance from the axis of symmetry to the differential volume dV, μ is the permeability of the dielectric material, and V is the interelectrode volume within which the magnetic field is confined. Equation (109) is restricted to the determination of external inductance (that due to the magnetic field outside the conductors), but the current sheaths in the electrodes are quite thin because of the skin effect. As a result, internal inductances can be ignored without introducing significant error.

141
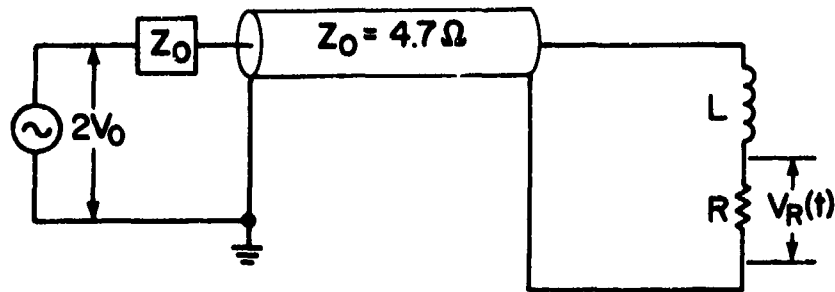
Figure 44.   Simplified System Schematic Including Diode
Structure Inductance
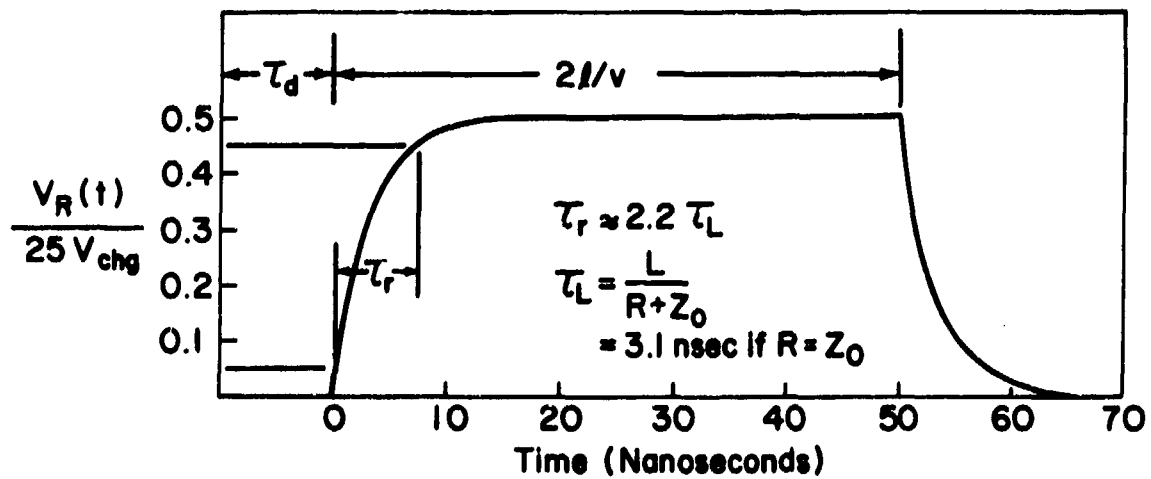
Figure 45.   Idealized Voltage Waveform Developed Across the Diode

142

To simplify the definition of the boundary conditions, the diode structure was divided into the six regions shown in figure 46. Application of the self-inductance relation given above to each region resulted in the expressions listed in table VI. The inductance of region VI was calculated assuming a uniform current distribution in the diode. Since the regional inductances are effectively connected in series, the individual values were summed to yield a total inductance of 28.7 nh. The waveform shown in figure 45 was calculated using this result. Since the 6.7-nsec rise time resulting from this inductance is less than the designed rise time of the system, the inductive properties of the diode structure were certainly acceptable.
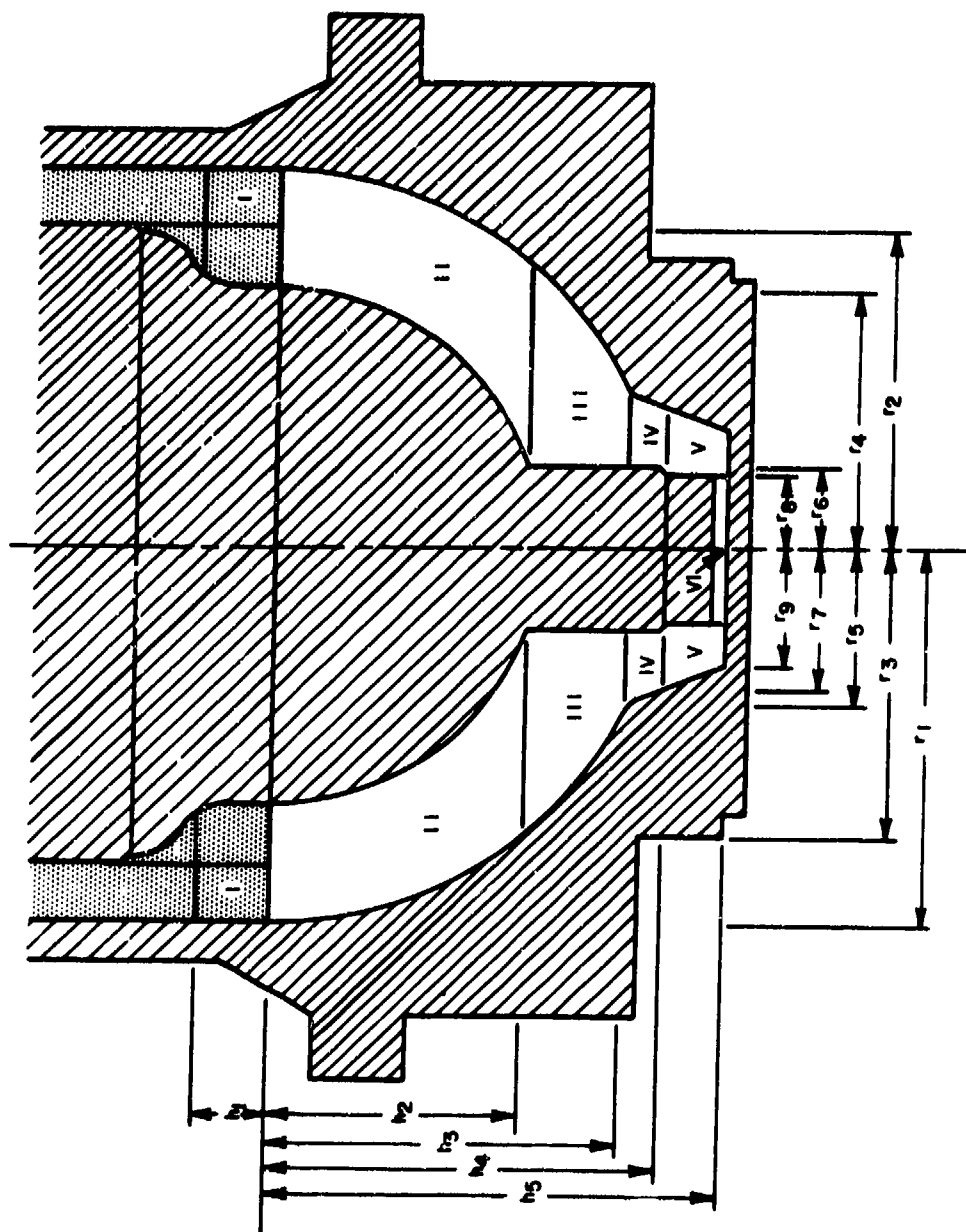
Figure 46.   Interelectrode Regions for Inductance Calculation

144

Table VI

INDUCTANCE RELATIONS

Region	Inductance

Region I

$$L_I = 2 \times 10^{-7}\, h_1\, \ell n\!\left(\frac{r_1}{r_4}\right)$$

$$= 2.4 \text{ nh}$$

Region II

$$L_{II} = 1 \times 10^{-7}\left[2\, h_2\, \ell n\!\left(\frac{r_3}{r_6}\right) + r_1\, \ell n\!\left(\frac{r_1 + h_2}{r_1 - h_2}\right) - r_4\, \ell n\!\left(\frac{r_4 + h_2}{r_4 - h_2}\right)\right]$$

$$= 8.3 \text{ nh}$$

Region III

$$L_{III} = 1 \times 10^{-7}\left\{2\, h_3\, \ell n\!\left(\frac{r_5}{r_6}\right) - 2(h_3 - h_2) - 2\, h_2\, \ell n\!\left(\frac{r_3}{r_6}\right)\right.$$

$$\left. + r_1\left[\ell n\!\left(\frac{r_1 + h_3}{r_1 - h_3}\right) - \ell n\!\left(\frac{r_1 + h_2}{r_1 - h_2}\right)\right]\right\}$$

$$= 9.8 \text{ nh}$$

Region IV

$$L_{IV} = 2 \times 10^{-7}\, (h_4 - h_3)\left[\ell n\!\left(\frac{r_7}{r_6}\right) + \left(\frac{r_5}{r_5 - r_7}\right) \ell n\!\left(\frac{r_5}{r_7}\right) - 1\right]$$

$$= 4.9 \text{ nh}$$

Region V

$$L_V = 2 \times 10^{-7}\, (h_5 - h_4)\left[\ell n\!\left(\frac{r_9}{r_8}\right) + \left(\frac{r_7}{r_7 - r_9}\right) \ell n\!\left(\frac{r_7}{r_9}\right) - 1\right]$$

$$= 3.1 \text{ nh}$$

Table VI (cont'd)

Region	Inductance

VI

$$L_{VI} = 0.5 \times 10^{-7} \, d$$

$$= 0.2 \text{ nh}$$

where d is the diode separation.

$$L_T = 28.7 \text{ nh}$$

EXPERIMENTAL TECHNIQUE

1. ANALYTICAL APPROACH

In view of the inherent complexity of high-current diode phenomena, a basic requirement for this study was the availability of a well-balanced array of accurate diode diagnostics. The primary component of this diagnostic array was a precisely calibrated combination of electrical sensors located in the diode region of the accelerator. These electrical diagnostics were supplemented by the calorimetric and photographic techniques necessary to substantiate the diagnostic calibration and to verify certain analytical assumptions concerning the current density distribution and plasma motion within the diode.

The first step in evaluating the diode response was to carefully resolve, on a common time base, the voltage, current, and di/dt signals generated by the electrical diagnostics in the diode region. The measured voltage signal was then corrected to remove the inductive component associated with the physical separation between the voltage monitor and the diode. The corrected voltage now corresponded to the resistive voltage developed across the diode. Finally, the corrected voltage and current waveforms were used to compute the time variation of such pertinent diode parameters as the diode perveance, resistance, v/γ, the electron dose deposited in the anode front surface, the power of the electron beam, and the total beam energy. The leading edge of these signals could, if justified, be used to develop a Fowler-Nordheim plot. If the stable field

147

emitted currents were of sufficient magnitude to be measurable using the available current diagnostics, these plots could be used to evaluate the characteristics of the initial electron emission sites.

Relying primarily on the time-dependent information provided by the electrical diagnostics, the response of a variety of diode configurations were investigated. The cathode types considered during this survey were selected to be representative of the wide variety used by the various accelerator developers. The basic configurations included in the survey were the graphite, the multi-needle, and the brass-epoxy "plasma" cathodes (see figure 47). In addition, several minor variations were tested to evaluate specific points of interest. Throughout the preliminary survey and the later more detailed study, cathode diameters ranged from 2.54 cm to 6.35 cm, and diode separations varied from 1 mm to 10 mm.

Although the results of the preliminary survey were qualitative and rather limited, the graphite cathodes exhibited a distinctively enhanced performance relative to the other designs in two critical areas. First, the formative or "turn-on" time of the graphite cathode was found to be 5 to 10 nanoseconds shorter than either the multi-needle or brass-epoxy cathodes. Given the complete absence of prepulse in the Field Emission system, this was an extremely important feature. Secondly, the shot-to-shot reproducibility of the diode response was noticeably improved. The improved performance was more than sufficient to warrant the detailed study being limited to diodes which incorporated a graphite cathode.

As the diode study progressed, several sets of data were selected for careful analysis and comparison with a proposed diode model. Supplemental measurements were then performed for these diode configurations using
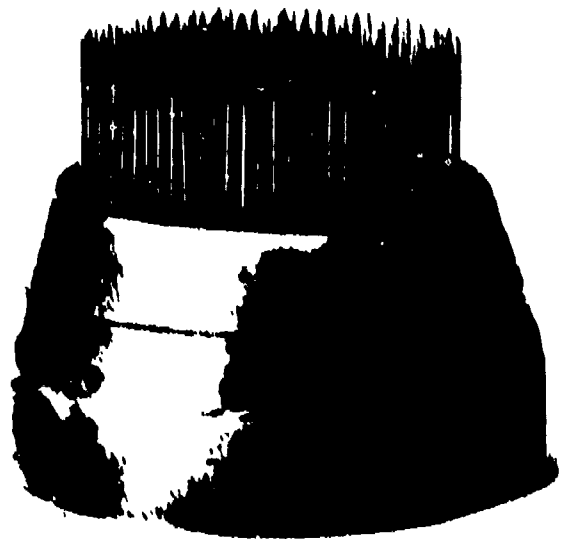
Figure 47. Cathode Designs Tested

149

photographic techniques to support certain of the fundamental assumptions underlying the model. With this objective in mind, streak photographs were taken perpendicular to the diode axis to provide qualitative evidence of plasma motion between the diode electrodes. In addition, the attenuator/scintillator anode assembly developed at Cornell University (Ref. 17) was used to obtain current density measurements at the anode plane. Streak and open shutter photographs of the optical emissions from the scintillating material provided time-dependent and time-integrated information concerning the current density distribution.

2. ELECTRICAL DIAGNOSTICS

As shown in figure 41, the electrical diagnostics in the diode region included a capacitive voltage-divider, two independent current monitors, and a combined set of four magnetic pickup loops. These sensors had been designed to provide accurate, time-resolved measurements associated with the electron flow in the diode. To substantiate the diagnostic precision and to provide the basis for a detailed error analysis, the response of each sensor was evaluated by considering equivalent, lumped-parameter circuits. Independent calibration of specific diagnostics then provided partial verification of the estimated response characteristics. The multiplicity of diode diagnostics permitted cross-calibration to complete the response analysis. Finally, the results of this analysis were presented in an appropriate form to provide detailed error estimates.

a. Capacitive Voltage Divider

The voltage developed across the diode was measured using a capacitive voltage divider. The active element of the divider consisted of a 5/8-inch wide strip of copper-clad Teflon (5-mil Teflon laminated between

2-mil copper foils) which had been recessed into the inner surface of the outer hemisphere. To take advantage of the radial electric field lines, the strip was mounted midway between the Lexan and epoxy surfaces. In this configuration, the exposed copper strip was electrically isolated from the inner strip which made good electrical contact with the grounded outer hemisphere. The exposed copper strip then acted as a third electrode having capacitance with respect to both the inner and outer hemispheres of the diode structure.

To obtain the necessary low-frequency response, a series combination of capacitive and resistive dividers was required. The resistive divider was formed by coupling the signal generated at the third electrode to a 50-ohm diagnostic cable through a Tektronix P6034 10X oscilloscope probe. The characteristic impedance of the output cable leading to the recording oscilloscope served as the small resistance leg of the resistive voltage divider. When properly terminated in the 50-ohm cable, the probe had a 500-ohm input resistance which extended the RC time constant of the divider network.

The equivalent circuit for the voltage divider is shown in figure 48. In this schematic, the symbols for the pertinent circuit parameters are as follows:

C_1 = capacitance between the inner hemisphere and the divider strip

= 2.06 pf

C_2 = divider strip capacitance

= 2,250 pf

R_p = probe resistance

= 450 Ω

151

Z_0 = characteristic impedance of diagnostic cable

R_s = terminal resistance at the oscilloscope

= Z_0 = 50 Ω

V_m = voltage waveform to be measured

V_1 = V_2 if signal distortion within the diagnostic cable can be neglected

V_2 = voltage waveform recorded at the oscilloscope

If the voltage waveform V_m can be approximated by a square wave such as that described by equation (106), the output waveform generated by the capacitive voltage divider would be

$$V_1(t) = \frac{Z_0\, C_1\, V_m}{\tau_{RC}} \exp\left[-\frac{(t-a)}{\tau_{RC}}\right]\left[u_a(t) - \exp\frac{b}{\tau_{RC}}\, u_b(t)\right] \quad (110)$$

where V_m is the magnitude of the voltage pulse between the electrodes of the diode structure, (b-a) is the pulse duration, and the RC time constant of the series divider combination is given by

$$\tau_{RC} = \left(R_p + Z_0\right)\left(C_1 + C_2\right)$$

$$= 1.126 \text{ μsec} \quad (111)$$

Figure 49 illustrates the distortion inherent in the divider network of figure 48. To minimize this distortion, the circuit parameters had to be adjusted to maximize the RC time constant under the constraint that the signal magnitude at the oscilloscope V_2 provide satisfactory vertical deflection. Using Tektronix Type 519 oscilloscopes, a signal of approximately 20 volts was required to achieve a full-scale vertical

152
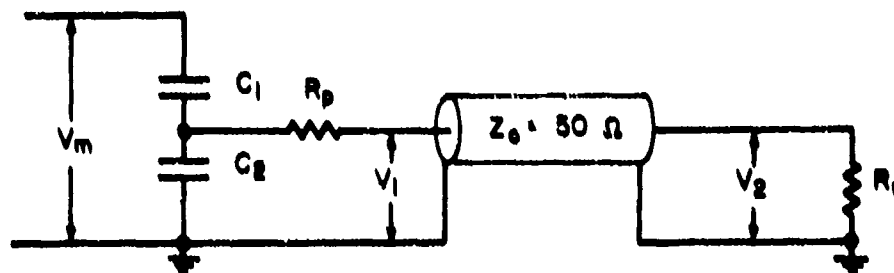
Figure 48. Capacitive Voltage Divider
Equivalent Circuit
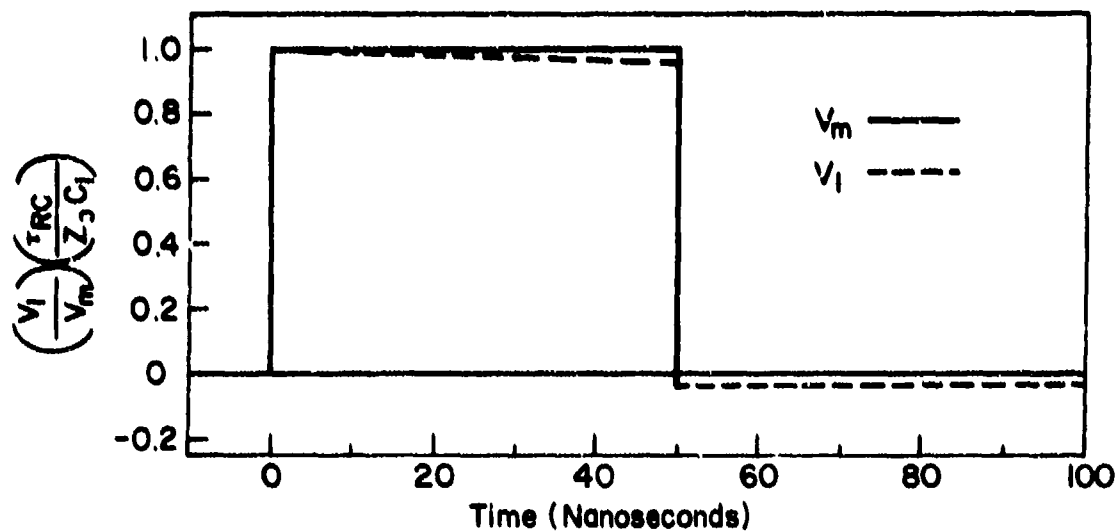
Figure 49. Response of the Capacitive Voltage Divider

deflection. Assuming a 300-kV pulse on the diode, the choice of divider parameters listed above would result in a 27-volt pulse at the oscilloscope. Since the RC decay associated with this choice of circuit parameters was only 4 percent after 50 nanoseconds, the output pulse from the divider was not corrected for this distortion. The relationship between V_m and V_1 was therefore assumed to be

$$V_1(t) = \frac{Z_0 C_1}{\left(R_p + Z_0\right)\left(C_1 + C_2\right)} V_m(t) \tag{112}$$

With this assumption, the resultant error in the voltage measurement would not become significant until late in the pulse, at which time the RC decay approaches 10 percent.

The initial calibration of the capacitive voltage divider in the exploding wire transducer chamber had been completed by the Field Emission Corporation (Ref. 67) during the final testing of the pulsed power system. Since the divider used in the diode structure was virtually identical, the same calibration procedure was followed. Specifically, a Ballantine Model 520 Direct Current Reading Capacitance Meter was used to measure the capacitances of the divider. The capacitive elements C_1 and C_2 were were found to be 2.06 pf and 2.250 pf, respectively. For comparison, the theoretical value of C_1 was calculated to be 1.97 pf. The output capacitance C_2 could not be calculated accurately because of slight variations in the thickness of the Teflon layer within the divider strip. Assuming the measured capacitance values to be correct, the overall divider ratio $(C_1 + C_2)(R_p + Z_0)/C_1 Z_0$ was 10,930.

The unavoidable physical separation between the divider strip and the diode resulted in the voltage waveform sensed at the divider being equal to the sum of two components: (1) a resistive component associated with electron acceleration in the diode, and (2) an inductive component proportional to the time dirivative of current flow in the diode. The measured voltage was, therefore, given by

$$V_m(t) = IR + L_1(di/dt) \qquad (113)$$

where R is the resistance of the diode, I is the diode current, di/dt is the time derivative of the current, and L_1 is the inductance associated with the interelectrode volume between the diode and the divider.

If the inductance L_1 can be determined and the time derivative of the diode current measured, the resistive potential drop across the diode V_R can be derived from the following expression.

$$V_R = V_m - L_1(di/dt) \qquad (114)$$

If L_2 is the diode structure inductance preceding the voltage divider, the total uncompensated inductance of the diode structure is the sum of L_1 and L_2. With this interpretation, figure 50 shows the relationship between the equivalent lumped-parameter components of the voltage divider and the appropriate components of the diode structure inductance. Using the techniques described in section V, L_2 was calculated to be 9.2 nh. Hence, the inductance L_1 associated with the recorded voltage waveform was theoretically equal to 19.5 nh.

155
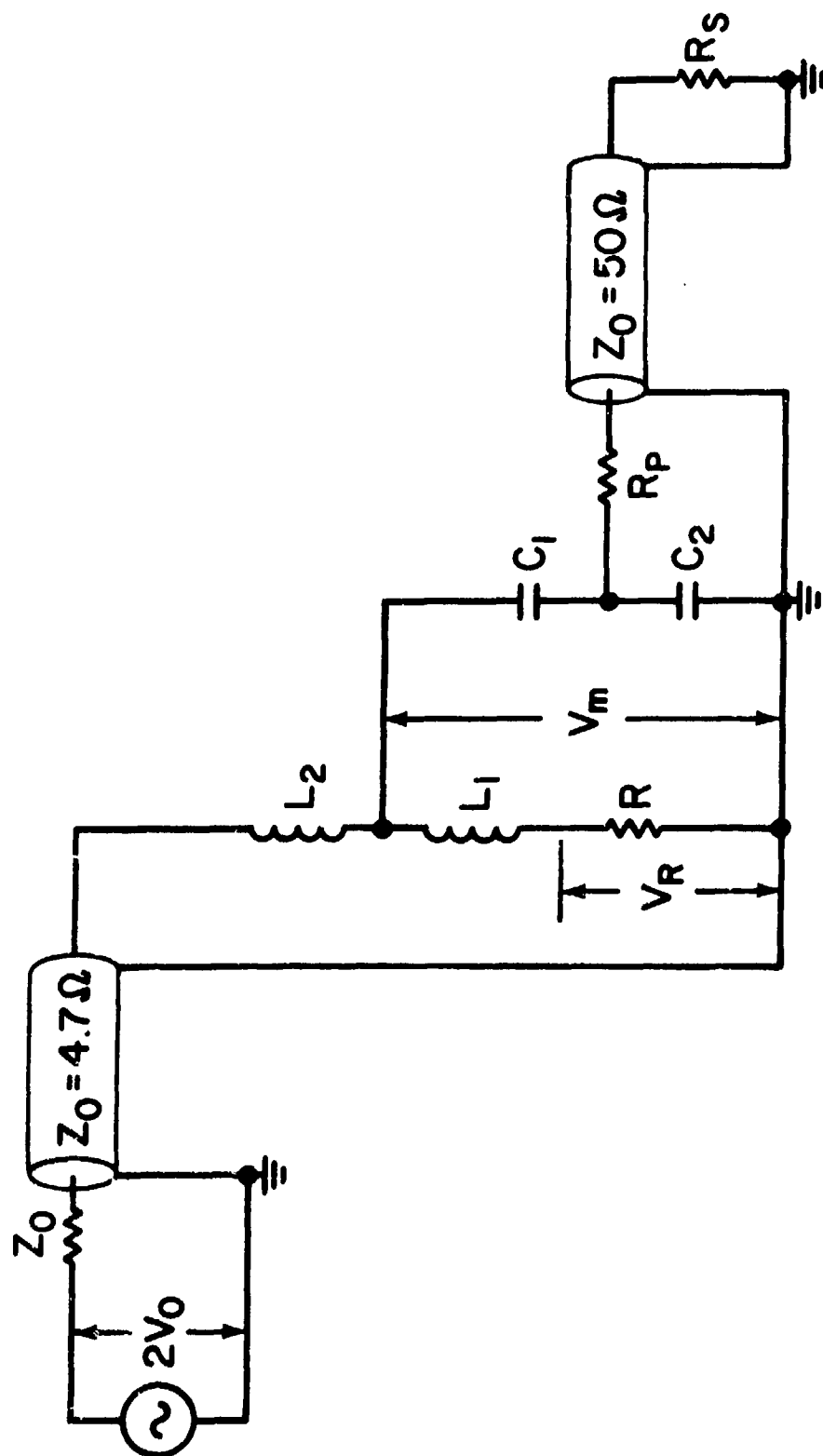
Figure 50. Relationship between the Lumped-Parameter Components of the Diode Structure and the Capacitive Voltage Divider

156

b. Magnetic Pickup Loops Array and Pulse-Additive Network

The time derivative of the current flow was monitored using an array of four single-loop, magnetic pickup coils mounted at 90-degree intervals around the diode axis. The voltage waveform induced in the single-loop probe can be related to the time rate of change in the current through the time-varying magnetic field which fills the volume between the electrodes of the diode structure. The magnetic induction B at some point r within the interelectrode volume can be determined from the primary current flow I by integrating the line integral in Ampere's circuital law. Within the cylindrically symmetric diode structure

$$B(r,t) = \frac{\mu_0 \, I(t)}{2\pi r} \tag{115}$$

where B is the magnetic induction in weber/meter^2, and r is the perpendicular distance from the axis of the center conductor to the point at which the magnetic induction is evaluated. The time variation of the diode current can then be related to the electromotance induced in a fixed loop through the following simplified from of the Faraday induction law

$$\oint \bar{E} \cdot d\bar{\ell} = -\int_{\mathcal{A}} \frac{\partial \bar{B}}{\partial t} \cdot d\bar{a} \tag{116}$$

where $\bar{E}$ is the induced electric field within the loop, $d\bar{\ell}$ is a differential length along the loop, $d\bar{a}$ is a differential area within the loop, and $\partial\bar{B}/\partial t$ is the partial derivative of $\bar{B}$ with respect to time evaluated at $d\bar{a}$. If the loop is positioned such that the normal to the plane of the loop is parallel to the magnetic induction, and the loop is sufficiently small that the instantaneous value of the magnetic induction is

approximately constant over the surface of the loop, the Faraday induction
law can be further simplified to

$$\oint \bar{E} \cdot d\bar{\ell} = \frac{\mu_0 A}{2\pi r} (di/dt) \qquad (117)$$

where r is the distance from the axis to the center of the loop, and A
is the area of the loop.

The active elements of a di/dt loop are shown in figure 51. The
di/dt loop array was formed by "sandwiching" the four loops and their
associated cables between two 3/16-inch-thick aluminum plates bonded
together using epoxy adhesive. The relative location of the di/dt loop
array and the diode was shown in figure 41. The four matched loops were
formed by wrapping lengths of No. 24 tinned-copper wire around a No. 26
drill bit. When removed from the improvised winding mandrel, the loops
expanded to their final 0.15-cm radius. To complete the loop assembly,
each coil was attached between the center and ground conductors of an
appropriate 50-ohm sub-miniature coaxial receptacle (Microdot No. 051-
0325). The output signal from the loop was then brought to an accessible
jack (Microdot No. 031-0034) located on the outer rim of the plate
through the appropriate 50-ohm coaxial cable and connector (Microdot
No. 032-0055). From this point, the signal was transmitted to the input
terminal of a Tektronix 519 oscilloscope through 50-ohm diagnostic cables.

The response of the di/dt monitor can be evaluated from an analy-
sis of the equivalent lumped-parameter circuit shown in figure 52. The
self-inductance of the loop can be easily estimated using inductance ex-
pressions derived by Grover (Ref. 74). For this estimate, the coil
attached to the receptacle was considered to be a 3/4 loop connected to

158
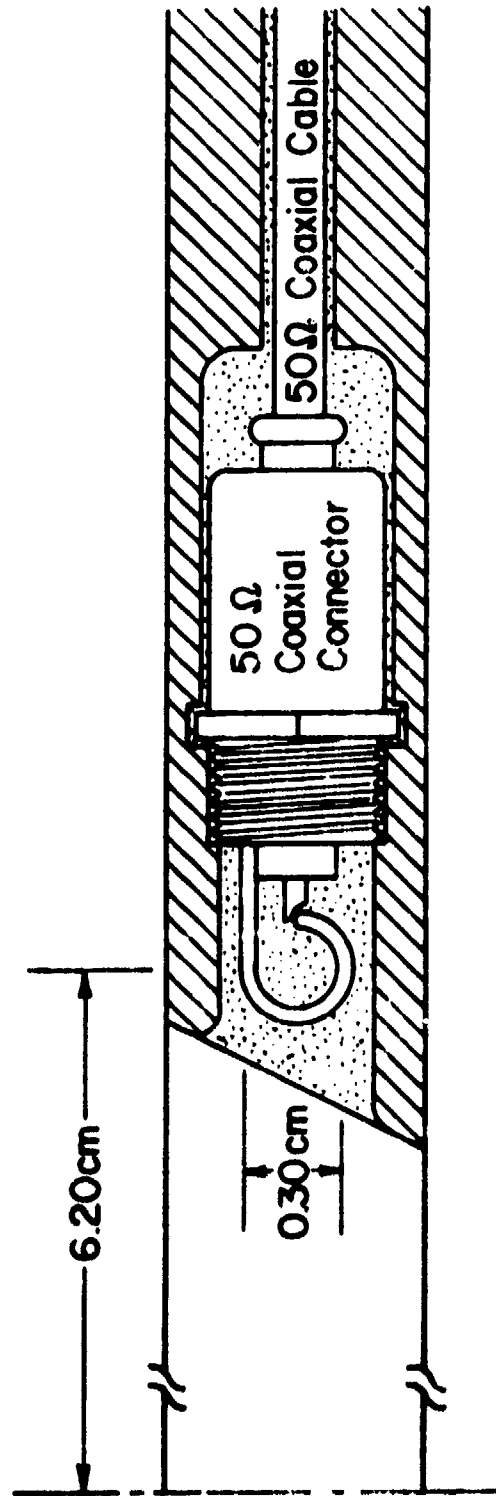
Figure 51. Magnetic Pickup Loop

50 Ω Coaxial Cable

50 Ω Coaxial Connector

6.20cm

0.30cm

two short segments of straight wire. The self-inductance of a single turn of a round wire with a cross-sectional radius ρ bent in a circle of mean radius r_ℓ is given by

$$L = 4\pi\ r_\ell \left(\ell n\ \frac{8\ r_\ell}{\rho} - 1.75\right) \qquad (118)$$

where L is in nanohenries, and the physical dimensions are in centimeters. Similarly, the self-inductance of a straight length ℓ of round wire can be computed from

$$L = 2\ell \left(\ell n\ \frac{2\ell}{\rho} - 0.75\right) \qquad (119)$$

Using these expressions L_ℓ was estimated to be 5.3 nh.

The loop resistance R_ℓ can be estimated using the following expression for the high-frequency resistivity of a round copper wire of cross-sectional radius ρ (cm).

$$\delta = \frac{4.15}{\rho}\ \sqrt{f} \times 10^{-8} \qquad (120)$$

where δ is the resistivity (ohm·cm), and f is the frequency of the signal (Hz). The radius of No. 24 wire is 2.55×10^{-2} cm. Assuming the dominant frequency to be determined by the pulse width of the current pulse, the frequency was taken to be 10^7 Hz. With these assumptions, the probe resistance was estimated to be approximately 6.6 milliohms.

If the driving voltage $V_1(t)$ were a square wave of duration (b-a), the voltage waveform $V_2(t)$ measured at the oscilloscope would be

$$V_a(t) = \frac{R_\ell V_i}{R_\ell + R_s} \left\{ \left[1 - \exp\left[-\frac{(t-a)}{\tau_\ell} \right] \right] u_a(t) - \left[1 - \exp\left[-\frac{(t-b)}{\tau_\ell} \right] \right] u_b(t) \right\} \tag{121}$$

where the time constant of the loop is

$$\tau_\ell = \frac{L_\ell}{R_\ell + R_s} \tag{122}$$

$$= 1.06 \times 10^{-10} \text{ sec}$$

For the response analysis, the loop resistance can be neglected because it is quite small compared to the 50-ohm series resistance of the input termination at the oscilloscope. The distortion of the circuit can be seen from a comparison of the relative waveforms of the driving and measured voltage pulses for a 2-nanosecond square wave (fig. 53).

With the probe assemblies recessed into the aluminum plate, the loops were partially shielded from the induced magnetic field. The correlation between the voltage waveform induced in the loop and the time rate of change in the total current must, therefore, incorporate a shielding factor f_s.

$$V(t) = \frac{\mu_0 A}{2\pi r} f_s (di/dt) \tag{123}$$

The overall probe sensitivity was determined by comparing the maximum value of the measured current signal with the maximum value of the time-integrated di/dt signal (measured in volts). The overall probe sensitivity was thus equal to the ratio of these maximum values. The
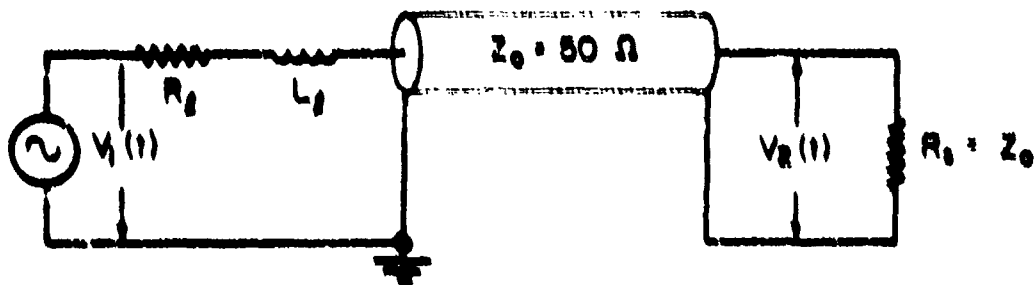
Figure 52. Magnetic Pickup Loop Equivalent Circuit
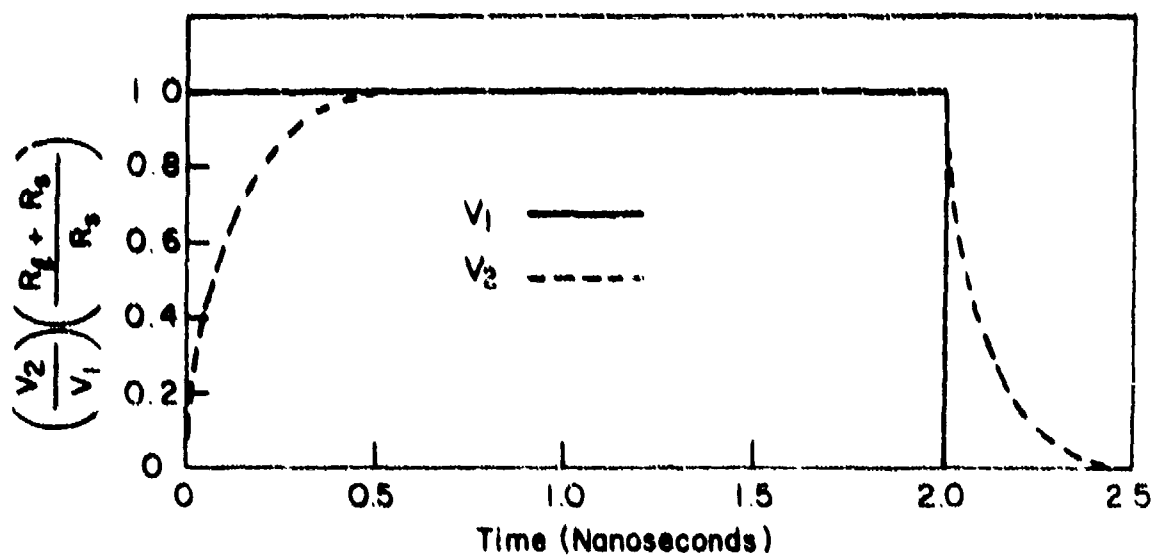
Figure 53. Response of Magnetic Pickup Loop

162

average sensitivity of the four loops was found to be 2.74×10^{-14} volt·sec/ampere. Variation among the loops was less than 6 percent. With peak values of di/dt expected to be on the order of 10^{11} ampere/sec, the maximum signal at the oscilloscope would be approximately 27 volts. Using the physical dimensions given in figure 51, $\mu_0 A/2\pi r$ was calculated to be $2.28 \times 1)^{-11}$ volt·sec/ ampere. The shielding factor resulting from the recessed position of the loop was therefore approximately 0.12.

If the distribution of current flow within the diode were to exhibit time varying asymmetries, the signal induced in a single di/dt loop would reflect these shifts. Since the measured di/dt signal must be proportional to the time derivative of the total current flow within the system load, a single magnetic pickup loop may not be satisfactory. To avoid this possible source of error, four loops were mounted at equal intervals around the axis. To then obtain a common signal, the individual outputs from the four loops were combined in a matched-impedance, pulse-additive network. Such a network generates an output pulse proportional to the sum of the input waveforms.

The pulse-additive circuit developed for this study used four Tektronix CT-1 nanosecond current transformers with P6040 probes to simultaneously induce the four output signals from the di/dt loops on a common 50-ohm coaxial cable. Although the CT-1 was designed to inductively monitor the current through a conductor, the signal path may be reversed and the CT-1/P6040 used to inject a signal onto a coaxial cable. When used as a current monitor, the sensitivity of the CT-1 was 5 mv/ma into a 50-ohm load. With the signal path reversed, the signal amplitude induced on a 50-ohm cable was 1/10 its original value. The LR time

163

constant of the CT-1 was approximately 5 μsec, and the transformer had a rise time of less than 0.35 nanoseconds. With the transformer core unsaturated, the pulsed response of the CT-1 was such that the output would exhibit a decay of approximately 2 percent after 100 nanoseconds. The peak pulsed current rating of the transformer was 100 amperes with and amp·sec product of 1 amp·μsec. Assuming the output of a di/dt loop to be approximately 27 volts with a 100-nsec duration, the anticipated amp·sec product would be 0.05 amp·μsec using 50-ohm diagnostic cables. Core saturation was therefore not expected to be a problem.

The transformer additive network was fabricated by mounting the four CT-1 transformers in the common center conductor of a Tektronix 50-ohm G.R. insertion unit. To minimize relative phase shifts along the induced signals, the transformers were placed immediately adjacent to each other. The signal delay associated with the physical separation between the first and fourth transformer was less than 0.2 nsec.

The pulsed response of a 50-ohm cable to the injection of a nanosecond signal from the CT-1 is such that two pulsed components of equal amplitude and opposite polarity are transmitted in opposite directions along the cable. The transformer additive network was operated with one end of the insertion unit connected to a 50-ohm diagnostic cable, and the other terminated with either a 50-ohm resistive termination or a short-circuit termination. If the resistive termination were used, the pulse transmitted toward the oscilloscope through the diagnostic cable would be recorded while the other would be dissipated without reflection in the matched-resistance of the thermination. If the resistive termination were replaced by the short-circuit termination, the pulse transmitted

164

toward the short circuit would be reflected with equal amplitude and
opposite polarity. The reflected pulse would then have the same polarity
and amplitude as the other pulsed component which had been originally
transmitted toward the oscilloscope. The pulse recorded at the oscillo-
scope would now be the additive sum of the two components. Having been
delayed by its transit and return from the short-circuit termination,
the reflected component would be approximately 0.3 nanoseconds out of
phase with the first. The disadvantage associated with the slight distor-
tion introduced by the shorted termination was more than compensated by
the fact that the amplitude of the output pulse would be doubled in this
configuration. Hence, the total attenuation of the additive network
would be reduced by one half.

The pulsed response of the additive network was evaluated by
simulating the output of the di/dt loops with the square-wave output from
a Tektronix Type 111 pretrigger pulse generator. To obtain four simul-
taneous square-wave pulses of identical amplitude and pulse duration, the
output of the pulse generator was divided through a network of three
coaxial power dividers (GR Type 8/4 TPD coaxial power divider). The four
identical pulses were then combined in the additive circuits. Having
recorded the orginal and recombined waveforms using a Tektronix Type RM45A
oscilloscope equipped with a Type 151 sampling plug-in unit, the response
of the pulse-additive network could be estimated by comparing the resulting
oscillographs.

The oscillograph in figure 54 shows the two superimposed pulse-
generator waveforms used for the response analysis. The leading pulse
had a duration of 20 nanoseconds, and was recorded at a sweep rate of

165

of 5 nsec/cm. The shorter pulse had a 2-nanosecond duration, and was recorded at 1 nsec/cm. The response of the transformer (resistive termination) adder can be estimated from the recombined waveforms shown in figure 55.

Using the resistively terminated transformer adder, the rise time of the pulse-generator output waveform was degraded from 0.8 nsec to 1.2 nsec. Additionally, a slight RC decay was observed toward the end of the longer pulse. Using the short-circuit termination, the output of the transformer adder was doubled and the rise time of the recombined waveform further degraded to 1.5 nsec. Rise-time limitations on this order were not expected to introduce significant error. The low-frequency response was identical to that of the resistively terminated mode. Assuming a di/dt of 10^{13} ampere/sec, the di/dt loops in combination with the resistively terminated pulse adder would generate a signal of approximately 10.8 volts at the oscilloscope. Under the same conditions, the short-circuit termination would yield a recorded signal of 21.6 volts.

c. Combined Faraday Cup-Calorimeter

The primary current monitor used throughout the diode study was designed and fabricated by the Arkon Scientific Laboratories specifically for this application. The dual current/energy measurement required of the combined Faraday cup-calorimeter was achieved by connecting a thermally insulated graphite disk to ground through a low-inductance, stainless-steel resistor. The physical dimensions of the graphite disk were chosen to be sufficiently large that, when the disk was mounted on the anode plane, all electrons emitted from the various anticipated

Original Waveforms

Leading Pulse:

Duration - 20 nsec
Sweep Rate - 5 nsec/cm

Trailing Pulse:

Duration - 2 nsec
Sweep Rate - 1 nsec/cm
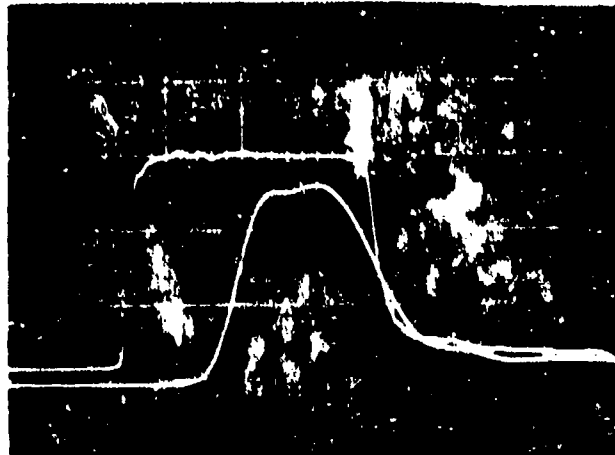
Figure 54.   .aveforms Used in the Response Analysis of the
Transformer Pulse Additive Network

Recombined Waveforms

Leading Pulse:

Duration - 20 nsec
Sweep Rate - 5 nsec/cm

Trailing Pulse:

Duration - 2 nsec
Sweep Rate - 1 nsec/cm
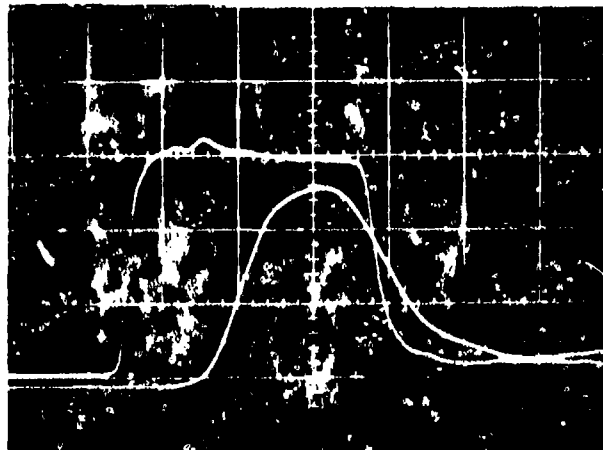
Figure 55.   Recombined Waveforms from the Transformer
Pulse Additive Network

cathode configurations (diameters ranging from 2.54 cm to 6.35 cm, and diode separations ranging from 0.1 cm to 1 cm) would be intercepted and stopped within the volume of the disk. The size of the disk was constrained however, by the additional requirement that the thermal equilibrium time of the disk be short compared to the time constant for heat loss.

As the accelerated electrons are collected within the disk, the accumulated charge must flow to ground through the 3.5 milliohm, thin-foil resistor. If the internal inductance of the resistor is sufficently low, the diode current can be directly related to the voltage developed across the resistor. To minimize the internal inductance, the coaxial resistive element was formed by two thin, stainless-steel foils separated by a 0.004-inch Mylar insulator. In addition to having a low inductance, this tubular configuration benefited from a high degree of magnetic field cancellation. According to the manufacturer's calibration, the Faraday cup exhibited a rise time of less than 3 nanoseconds. Since the current pulse generated by the pulsed-power system had a rise time of approximately 8 nanoseconds, the internal inductance of the Faraday cup was not expected to introduce a significant error in the current measurement.

With the collector (graphite disk mounted on a thin copper structure) of the Faraday cup thermally isolated, the total energy deposited in the collector could be related to its increase in temperature. To monitor the temperature rise, three ion-constantan thermocouples were recessed into the thin copper plate to which the graphite disk was attached. Knowing the mass and specific heats of copper and graphite

168

components, and the sensitivity of the thermocouples, the total thermal energy could then be determined from a time dependent record of the voltage ceneratred at the thermocouples.

Throughout most of the diode study, the combined Faraday cup-calorimeter was mounted directly on the anode plane, and the beam stopped within the graphite disk. In this configuration, the total electrical energy expended in accelerating the electron beam (determined from the electrical diagnostics) could be directly compared with the thermal energy deposited in the graphite (measured calorimetrically). If the entire accelerated-electron pulse were collected within the graphite disk, and if the coincident energy deposition did not result in a significant mass loss at the front surface of the calorimetric disk, the two energy measurements should be identical. A comparison of these two values would, therefore, provide a cross-correlation of the diagnostic calibration.

The choice of the material for the calorimetric disk was predicated on the need to minimize front-surface damage. In early electron beam studies using high-impedance accelerators with average electron kinetic energy exceeding several million electron volts, graphite was found to be the best general purpose calorimetric material because of its high spall threshold. Where aluminum and copper spalled at pulsed electron fluences of from 80 to 100 cal/cm^2, graphite had been used up to approximately 500 cal/cm^2 with no evidence of surface failure (Ref. 75). At the lower electron kinetic energies (100 keV to 300 keV) characteristic of the electron beam generated by the modified field emission system, the upper limit for graphite must be reduced to approximately 100 cal/cm^2 to avoid front surface damage. As expected, the relative merit of available

169

calorimetric materials remained unchanged. The calorimetric disks for the Faraday cup were therefore fabricated from graphite.

d. Wall-Current Shunt

For those applications in which the electron beam must be extracted from the accelerator, the total-stopping calorimeter had to be removed from the anode plane. In preparation for this mode of operation, the diode structure had been designed to incorporate a second current monitor, a wall-current shunt, which could measure the current flow indirectly. A wall-current shunt does not measure the primary current carried by the center conductor of a transmission, but rather requires the equal but oppositely directed image or "wall" current induced in the external conductor to flow through a low-inductance, resistive element which interrupts the continuity of the current return path.

The active elements of the wall-current shunt are illustrated in figure 56. The resistive element of the shunt was laminated between the Lexan and brass plates which formed the 3/8-inch-thick shunt assembly. The annular resistive element was fabricated from 0.5-mil manganese alloy (Texas Instruments P alloy; 73 percent-Mn, 17 percent-Cu, and 10 percent-Ni) foil chosen for its high resistivity (170 μ ohm·cm). The upper plate of the assembly consisted of a brass ring to connect the inner parimeter of the resistor to ground, and an annular Lexan plate to insulate the signal side of the circuit. The outer perimeter of the resistor was soldered to the brass plate which formed the lower half of the shunt assembly. To insulate the lower surface of the resistive foil, a 5-mil Teflon film was inserted between the foil and the brass plate.
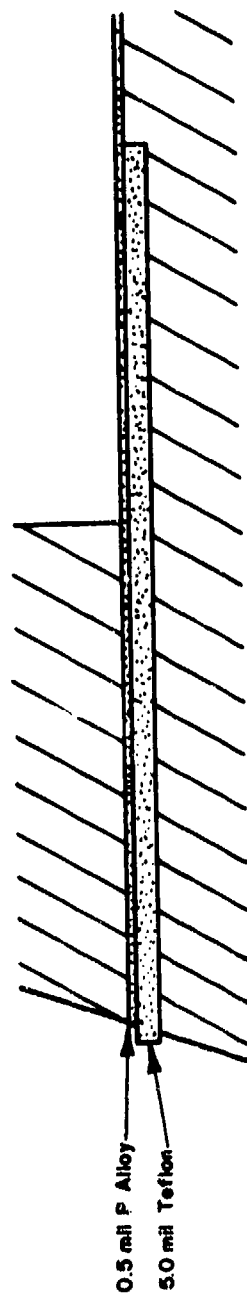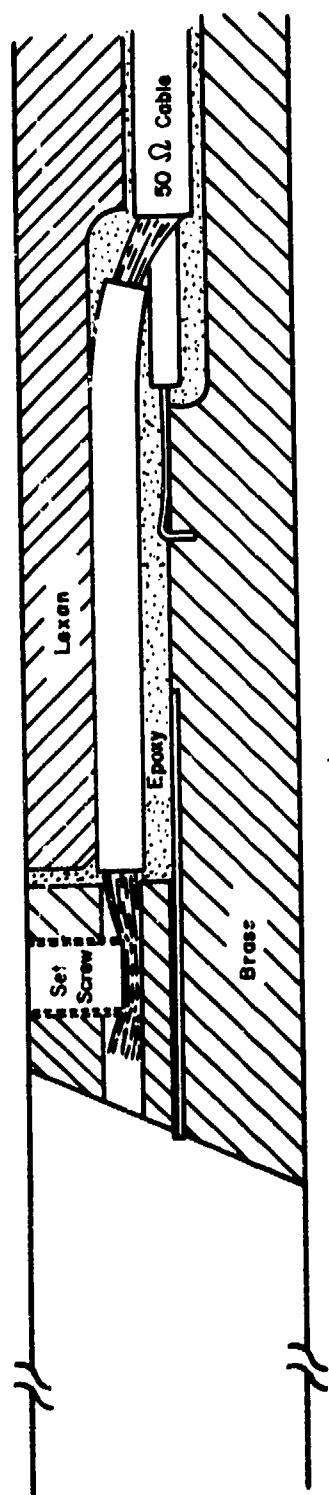
Figure 56. Schematic of the Wall Current Shunt

171

The voltage pulse developed across the 1.31-milliohm resistor was transmitted to the external diagnostic cable through four lengths of 50-ohm subminiature coaxial cables embedded at equal intervals around the shunt assembly. These internal cables were then terminated by subminiature jacks (Microdot No. 031-0034) mounted at the outer periphery of the laminated plate.

The equivalent circuit of the shunt can be considered as a series resistance and inductance shunted by a parallel capacitance. As in the case of the coaxial resistor used in the Faraday cup, the radial design of the resistive element in the wall-current shunt should benefit from a high degree of magnetic field cancellation. At the high frequencies of interest, the shunt capacitance represents a comparatively high-impedance path compared to the 1.31-milliohm of the resistor, and can also be neglected. Although the dc resistance of the shunt was calibrated using a Kelvin bridge, there was unfortunately no opportunity to determine the pulsed response of the shunt.

3. PHOTOGRAPHIC DIAGNOSTICS

The current density at the anode plane was measured by replacing the Faraday cup-calorimeter by the anode assembly shown in figure 57. This assembly had been designed to hold a thin 20-mil sheet of plastic scintillator (Pilot B) behind an electron attenuator positioned on the anode plane. For these measurements, the attenuator was a thin graphite or aluminum foil. The foil thickness was chosen to be approximately 90 percent of the electron range in the attenuator material. With this selection, the effect of the attenuator was to reduce the electron dose reaching the scintillator to a level which minimized the physical damage. The

172
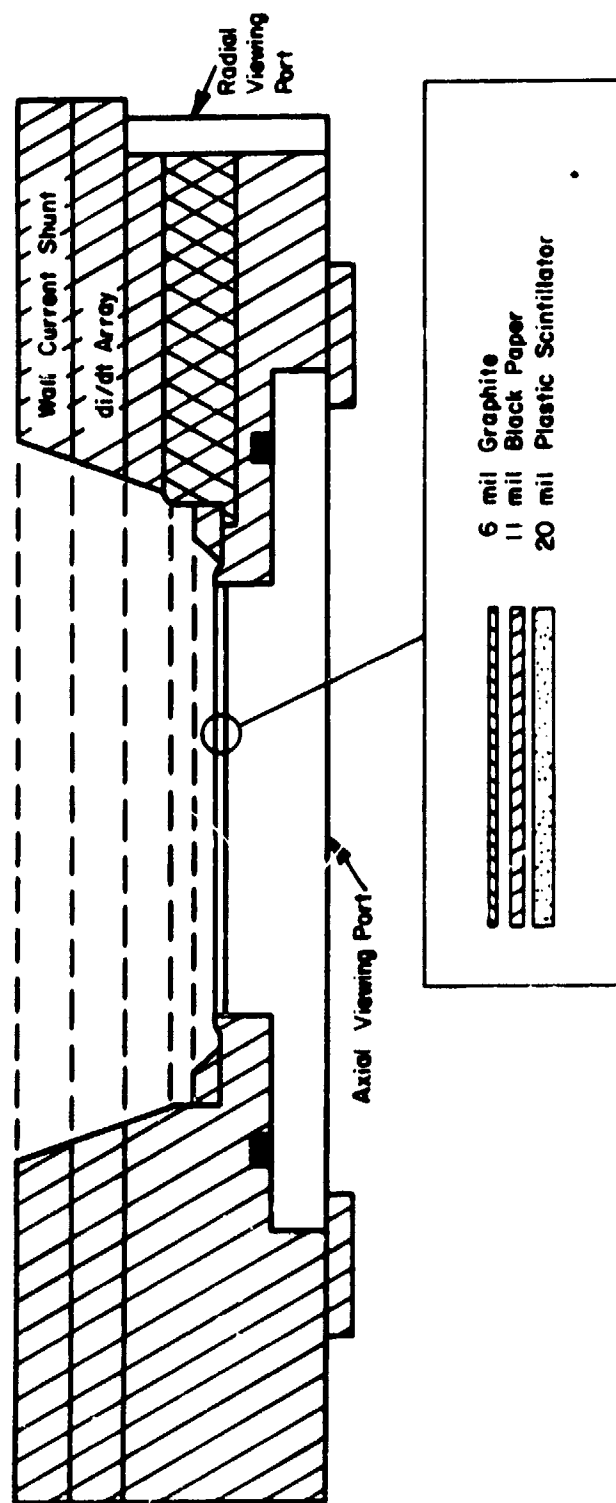
Figure 57. Schematic of the Anode Scintillator Assembly

Radial Viewing Port

Wall Current Shunt

di/dt Array

Axial Viewing Port

6 mil Graphite
11 mil Black Paper
20 mil Plastic Scintillator

173

sheet of black paper between the attenuator and the scintillator provided a nonreflecting background for the optical photons emitted from the pilot B, and also served to buffer the scintillator from thermal or shock damage.

Using the axial viewing port, open-shutter photographs of the optical emissions generated within the scintillator by electron energy loss provided time-integrated evidence of the relative current density. Optical densitometer scans of the photographic negative then yielded a more quantitative measure of the desired current density information. The most significant advantage of the open-shutter photographs was the excellent spatial resolution obtained from the negative.

Similar current density information, but time resolved, was obtained by using a TRW image converter camera operated in either the streak or framing mode. To facilitate the streak photography, the axial viewing port was masked with the exception of a 2-mm wide slit which intersected the diode axis. The camera gate pulse was monitored to synchronize the photographic information with the signals from the electrical diagnostics. Unlike the open-shutter photographs, the electronic imaging of the image converter camera was the factor limiting the spatial resolution.

The inherent spatial resolution of the attenuator/scintillator technique was limited by the electron scatter within the attenuator. Since the electron range at the kinetic energies of interest (100 keV to 300 keV) was less than one millimeter in the attenuator materials, the spatial resolution was estimated to be on the order of several tenths of a millimeter.

Discrimination against target bremsstrahlung produced in the attenuator was achieved by using a sheet of scintillator sufficiently thin to pass the X rays with negligible optical excitation. Whereas, the X-ray mean-free-path in the scintillating material was on the order of centimeters, the corresponding electron mean-free-path was less than a millimeter. The discrimination between the two types of ionizing radiation was further enhanced by the fact that the sensitivity of pilot B to electron energy deposition was more than 10^3 that of X rays.

The anode assembly of figure 57 also incorporated a radial viewing port which permitted optical measurement of axial plasma motion within the diode. Using this port, streak photographs were taken perpendicular to the diode axis to provide qualitative evidence of plasma motion between the diode electrodes.

4. DATA ACQUISITION AND ANALYSIS

The value of quality diagnostic instrumentation to subsequent interpretation of results can hardly be overstated. The availability of high fidelity signals from the sensing probes in the diode region was not sufficient in itself to ensure an accurate analysis of pertinent diode parameters. For such an analysis, the information for the three basic electrical sensing probes (voltage, current, and di/dt) had to be converted to digital amplitude and time values which could then be numerically manipulated within a computer using an appropriate data reduction and analysis program. The various components employed in the processes of data acquisition and reduction are indicated in the block diagram of figure 58. To minimize the total error of the data handling sequence, the probable

175
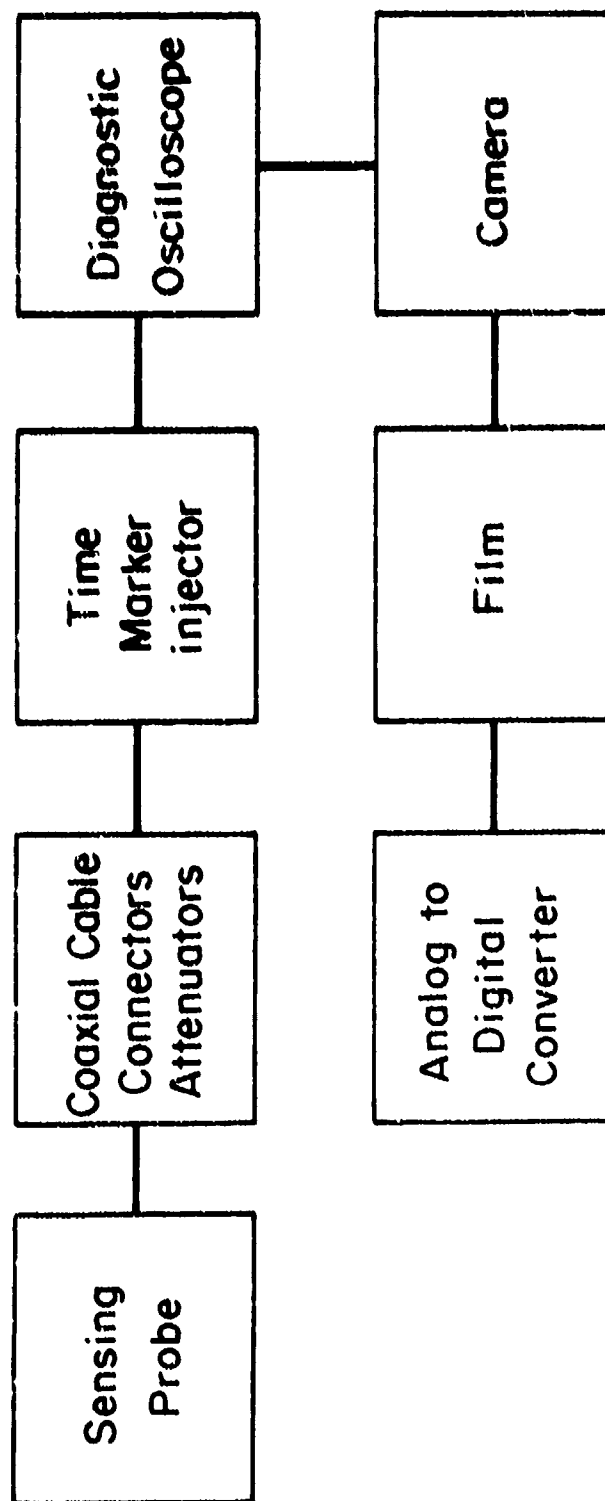
Figure 58. Interrelationship of Diagnostic Recording Components

176

sources of error associated with each component had to be identified and evaluated.

Being the principal component in the data handling sequence, the electrical diagnostics for the diode region were selected with particular care. The response of each of these sensors has been discussed in the preceding paragraphs. With the possible exception of the late-time response of the capacitive voltage divider, the inherent distortion in the output signals was negligible.

To accomodate the diagnostic requirements, the input termination of four diagnostic cables were located immediately adjacent to the transducer region of the accelerator. Signals input at this point were transmitted to a remotely located screen room through 50-ohm, 1/2-inch Stryoflex cables approximately 58 feet long (70-nsec delay). Inside the screen room, an additional 75 nsec of RG-8 cable was required to compensate for the erection time of the pulsers. Throughout this network, the cables were properly shielded and terminated. It was therefore assumed that the cables and connectors did not attenuate or otherwise alter the pulse waveshape.

Uncertainties in the timing of diagnostic information was considered to be a major source of error. To compute the diode parameters of interest, the signals generated by the sensing probes had to be corrrelated on a common time base. Because of the rapid time rate of change in the amplitude of these signals during the rise and fall of the high-voltage pulse delivered by the pulsed-power system, substantial errors would result from slight shifts in the relative timing of the diagnostic signals. Timing errors were considered insignificant if the degree of

177

simultaneity among all data channels could be maintained at approximately ±0.1 nanoseconds.

Fortunately, considerable effort has been expended during the development of the system at field emission to provide the ancillary equipment necessary to satisfy this timing requirement. The block diagram shown in figure 59 illustrates the data acquisition system designed for this purpose. The principal components of the timing network are identified as the delay unit, the scope trigger generator, and the zero time marker generator.

The operational sequences of the timing network proceeded as follows. Subsequent to the discharge of the UV pulser, a signal was taken from the current viewing resistor (see figure 30 for the location of the CVR) on the pulse-splitting transformer, and transmitted to the delay unit. When triggered by the UV pulser signal, a silicon avalanche transistor stage at the input of the delay unit generated a sharply peaked nanosecond pulse. This pulse was then fed through an adjustable delay unit which consisted of switchable lengths of miniature coaxial cable. The delayed pulse triggered a pulse level discriminator formed by a germanium tunnel diode deriving an avalanche transistor output stage. Since the pulse level discriminator triggered at a fixed voltage level on the leading edge of the delayed pulse, accurate time delay calibration was achieved regardless of pulse distortion caused by the longer lengths of delay cable.

The output pulse from the delay unit was then transmitted to the scope trigger generator and the zero time marker generator. These units were composed of avalanche transistor stages, each capable of driving seven

178
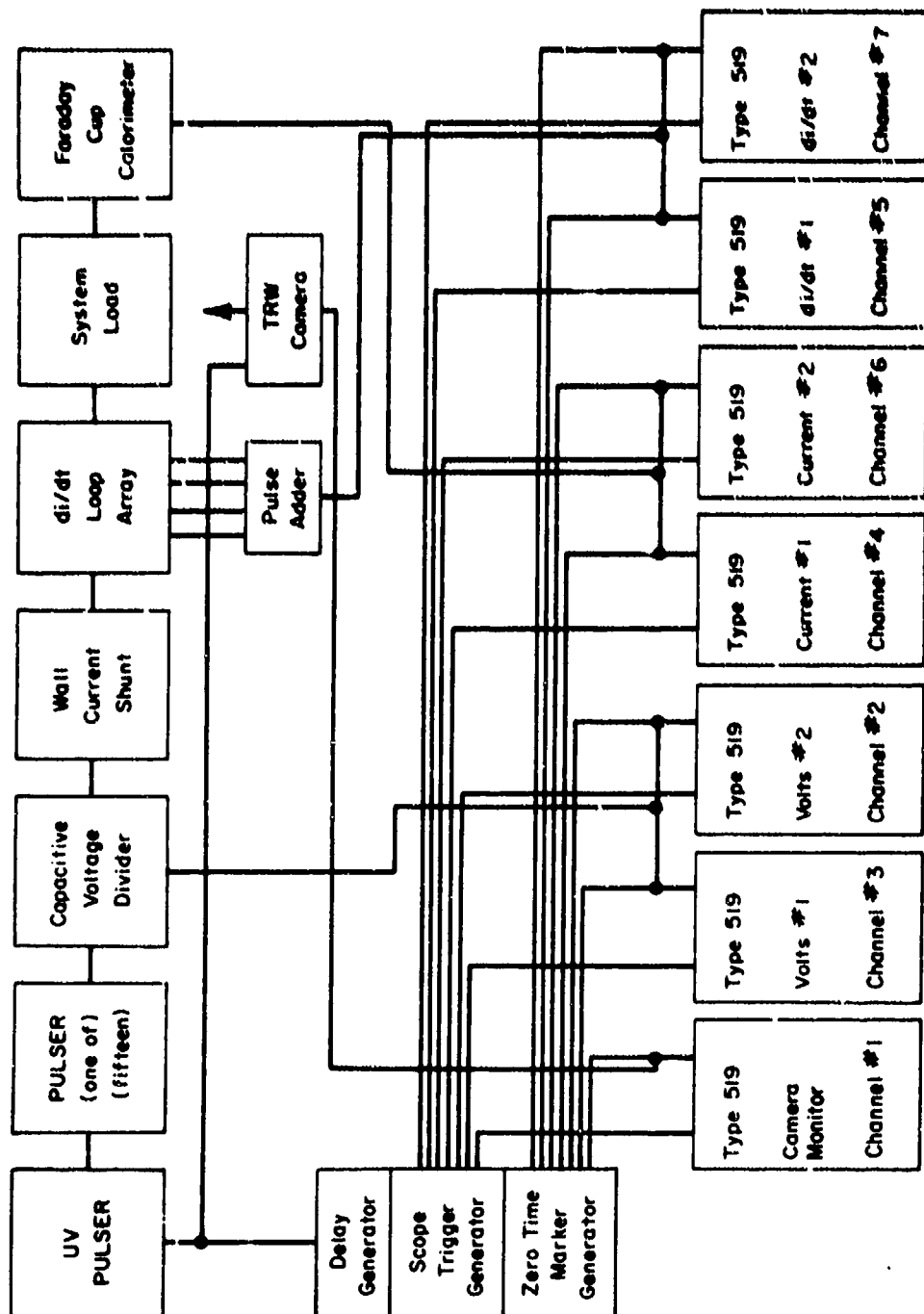
Figure 59.   Block Diagram of the System Timing Network

179

50-ohms loads. The seven outputs of the trigger generator were applied to the external trigger inputs of an equal number of diagnostic oscilloscopes. The zero time marker generator produced a sharply peaked 10-volt pulse with a 1-nanosecond duration, which was applied to the common juncture of seven 50-ohm cables. The fiducial pulses injected in the cables were then applied to the verical inputs of the recording oscilloscopes through zero signal injectors. The fiducial markers were delayed by approximately 20 nanoseconds relative to the scope triggering pulses so that the zero point would appear after the initial nonlinear portion of the oscilloscope trace. With careful measurement of the relative differences in the length of the cables connecting the zero time marker generator outputs to the zero signal injectors at th scilloscopes, the degree of simultaneity of the fiducial markers on the seven data channels was better than +0.1 nanosecond.

The zero signal injector was a device developed by Field Emission to inject the zero time marker into the vertical signal channels of the oscilloscopes without appreciably disturbing the vertical signal information. The injector consisted of a Tektronix CT-1 current transformer which had been mechanically modified to fit into a Tektronix 125-ohm insertion unit. Unlike the transformer pulse-additive network which employed a 50-ohm insertion unit, the zero signal injector attenuated the 10-volt fiducial pulse by a factor of 6.25. The 0.4 percent impedance discontinuity resulting from the insertion impedance of the CT-1 was regarded as insignificant.

The simultaneous injection of the zero time markers insured a common zero point on the time base of all data channels, but had no effect on

the quality of information at later times. The correlation of information at times other than zero was dependent on both the frequency response of the data oscilloscope and the precision of the oscilloscope sweep rate. The frequency response requirement was met by employing Tektronix Type 519 oscilloscope which had a rise time of less than 0.3 nanosecord. The remaining requirement for time base precision was satisfied by determining the average sweep rate and the linearity of the horizontal deflection for each oscilloscope.

To perform the necessary time base calibration, a high-frequency, sinusoidal signal was applied to the oscilloscope input. The frequency of the applied signal was chosen such that five complete cycles would occur per centimeter of deflection. The appropriate signal was then obtained from an RF oscillator, and the frequency determined using an accurate frequency counter. A photograph of the oscilloscope display was then analyzed to provide both an accurate horizontal sweep speed and the necessary linearity information.

The sweep rates were determined as a function of horizontal displacement by measuring the distance between consecutive signal maxima using an optical comparitor. Knowing the frequency of the applied signal, the distance between maximum points could then be interpreted in terms of the sweep rate. The calibration results for two Type 519 oscilloscopes are shown in figure 60. Although the time base was found to be slightly non-linear (less than 3 percent neglecting the first centimeter), linearity was assumed for simplicity, and the average sweep rate was used throughout the data analysis.

181
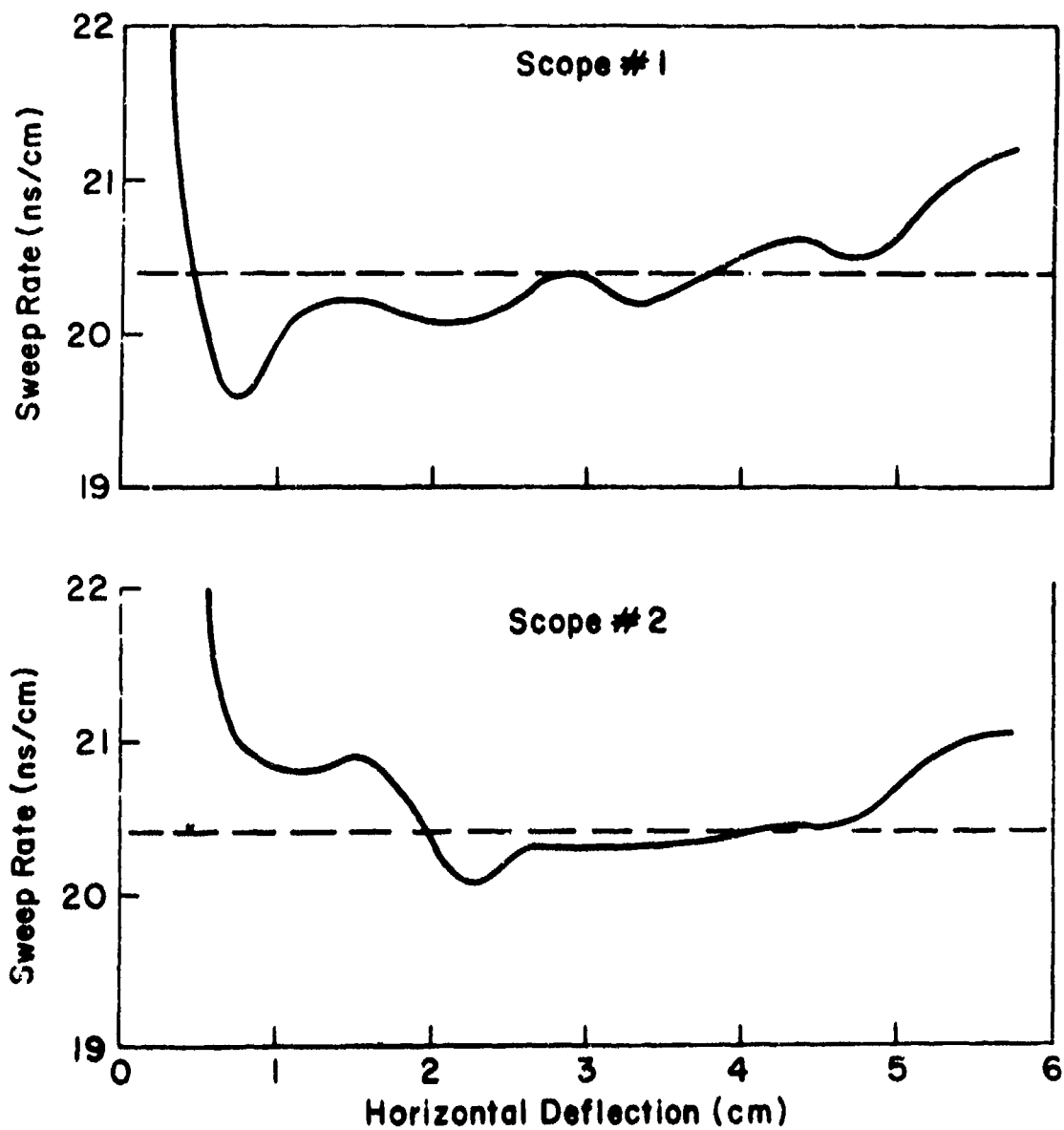
Figure 60. Sweep Rate as a Function of Horizontal Deflection

The consequences of this assumption were evaluated in an experiment devised to test the precision of the system timing network as well as the data acquisition and reduction processes. For this experiment, the 20-nanosecond duration square-wave pulse generated by a Tektronix Type 111 Pretrigger Pulse Generator was split into two identical pulses using a power tee. These pulses were then applied simultaneously to two of the calibrated oscilloscopes. The pretrigger pulse from the Type 111 was used to initiate the system timing network which in turn triggered the oscilloscopes and injected the zero time markers. Photographs of the resulting oscilloscope displays were then converted to digital data using the optical comparitor and the data processed through the data reduction program. The program made all necessary corrections for such factors as the vertical sensitivity of the oscilloscope, the average sweep rate, and the magnitude of the camera lens.

The superposition of the two recomposed waveforms, shown in figure 61, illustrates the anticipated difficulty in the time correlation of pulses characterized by rapid time variation. As seen from the illustration, substantial error resulted only at the leading and trailing edges of the pulse. Error estimates were obtained by examining the time shifts between the half-maximum points at the leading and trailing edges. For this example, the timing error at the leading edge was 1.4 nanoseconds. The error in the two pulse duration (FWHM) measurements was 2.4 percent. A careful analysis of the possible errors in the data handling sequence indicated that the dominant source of error was the nonlinearity of the oscilloscope sweep rates. Errors associated with the width of the

183
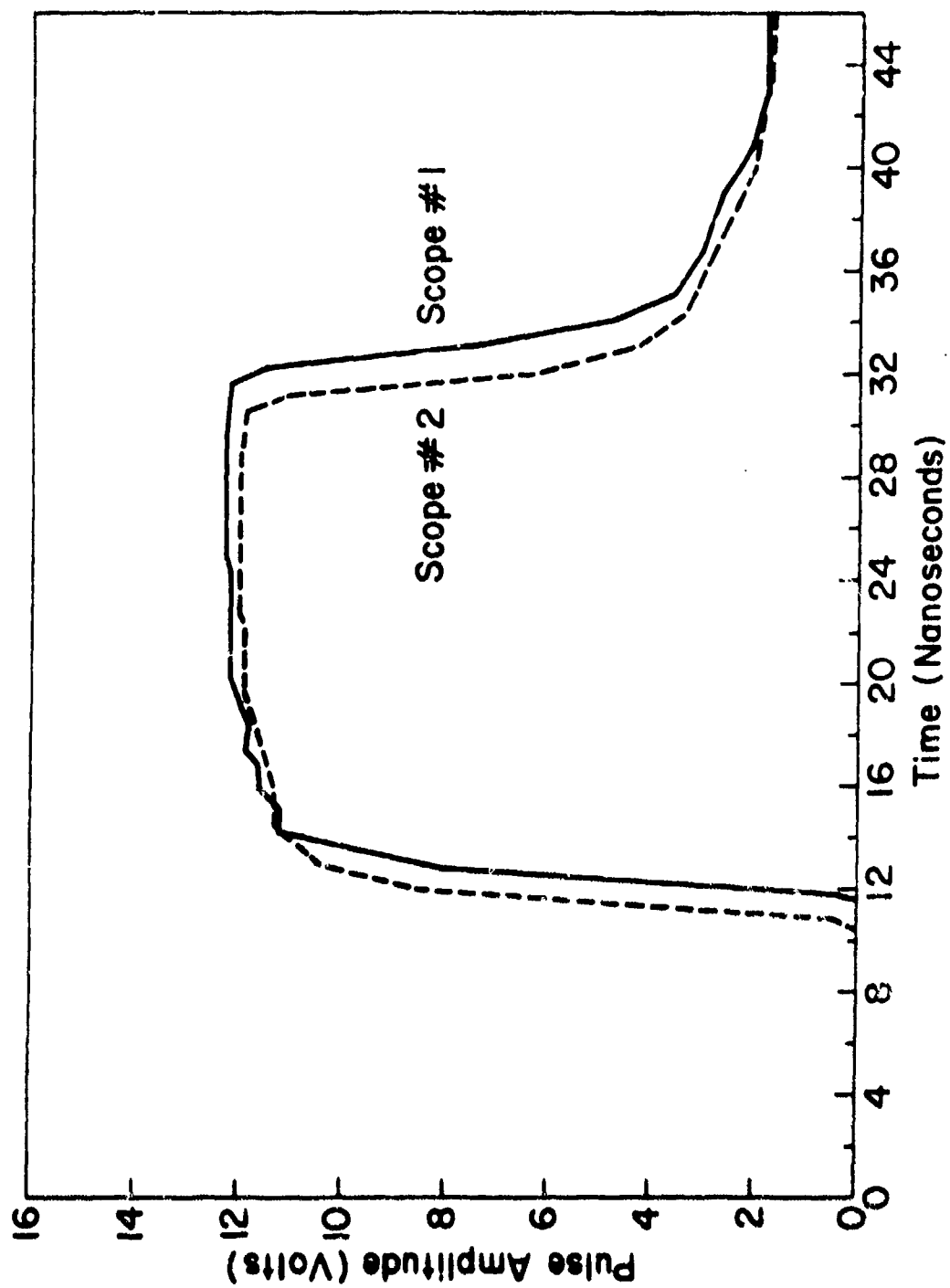
Figure 61. Results of Time Base Test

184

oscilloscope trace, the precision of the optical comparitor, camera distortion, etc., would total only several tenths of a nanosecond.

To record the entire duration of the delivered energy pulse, the sweep rate of the data oscilloscopes was normally set at 20 nsec/cm. Under these conditions, the estimated error associated with a particular point in time could become as large as ± 1.0 nanosecond. When attempting to quantify certain aspects of diode phenomenology such as whisker explosion, an imprcved precision was required. In this case, the information of interest was associated with the leading edge of the voltage pulse.

The approach devised to circumvent the timing limitations is illustrated in figure 59. For those instances when the leading edge of the pulse was thought to be significant, two oscilloscopes were used to monitor the signal generated by each of the three diagnostic probes. The sweep rate of the first set was selected to record the entire pulse (20 nsec/cm), while that of the second set was adjusted to monitor only the leading edge (10 nsec/cm). Using this arrangement, the primary oscilloscopes were biased to minimize the total timing error, and the secondary set was biased for the leading edge. The basis for the selection of time shifts will be described in the following paragraphs.

5. SYSTEM LOAD ANALYSIS

As the final step in the diagnostic analysis, three distinctly different types of system load were used to terminate the common transmission line of the accelerator. In the first phase of this exercise, the system was terminated with a short-circuit load fabricated from a short length of 2-inch-diameter copper pipe. Since this termination had effectively a zero resistance, the voltage waveform at the capacitive voltage divider

185

was proportional to di/dt (see equation (113)). Furthermore, the constant of proportionality was the interelectrode inductance which resulted from the physical separation between the load and capacitive voltage divider. The ratio of the two signal amplitudes therefore provided an experimental measurement of the inductance L_i (see figure 50).

For the second set of experiments, the line was terminated with an aqueous-salt resistive load. Within certain constraints, such a load can be used to terminate the system in a constant resistance. In spite of the physical constancy of the load resistance, resistance values calculated from the diagnostic signals exhibited a monotonic decrease in time. An analysis of the apparent time variation in the load resistance provided an excellent estimate of the time dependent error in the corrected voltage waveform.

Finally, the accelerator was terminated by the diode formed by placing a 6.35-cm-diameter graphite cathode at a distance of 4.52 mm from the graphite disk of the Faraday cup-calorimeter. This configuration allowed a comparison between the electrical energy expanded in accelerating the electron beam, and the thermal energy deposited by the electron beam in the calorimetrically monitored graphite disk. Since the expended electrical energy is given by the time integral of the V_R I dt product, this comparison provided a cross-calibration of the combined Faraday cup-calorimeter and the capacitive voltage divider sensitivities.

a. Short Circuit Load

If the interelectrode inductance associated with the capacitive voltage divider were to be determined by dividing the measured voltage by the corresponding value of the di/dt, the question arose as to which

186

instant of time the error in the comparison would be minimal. One approach was to let the computer determine the experimental inductance at nanosecond intervals throughout the pulse, and then average the resultant values. The results from such a determination are shown in figure 62. In this presentation, the relative error between the specific value determined by the ratio of the signal amplitudes and the average value are plotted as a function of time. This format allowed an interesting comparison with the anticipated effects of the RC decay in the voltage divider signal.

To evaluate the effects of the RC decay for a short-circuit load, the di/dt signal was approximated by a sequence of ramp and square waveforms. Since the hypothetical voltage pulse would be proportional to this idealized di/dt waveform, the appropriate Laplace transform analysis could be easily performed to estimate the distorted output waveform from the voltage divider equivalent circuit. The results of this analysis, presented in terms of the time dependent relative error in the measured voltage waveform, are shown by the dashed line in figure 62.

The correlation between the relative error in the inductance measurements and the calculated error in the short-circuit voltage waveform indicated that the RC decay was a significant source of error not only late in the pulse but also during the time interval near maximum current when the di/dt signal approached zero. Considering the extremely rapid time variations in the di/dt waveform, the dominant source of error throughout the remainder of the pulse was the nonlinear character of the oscilloscope time base.
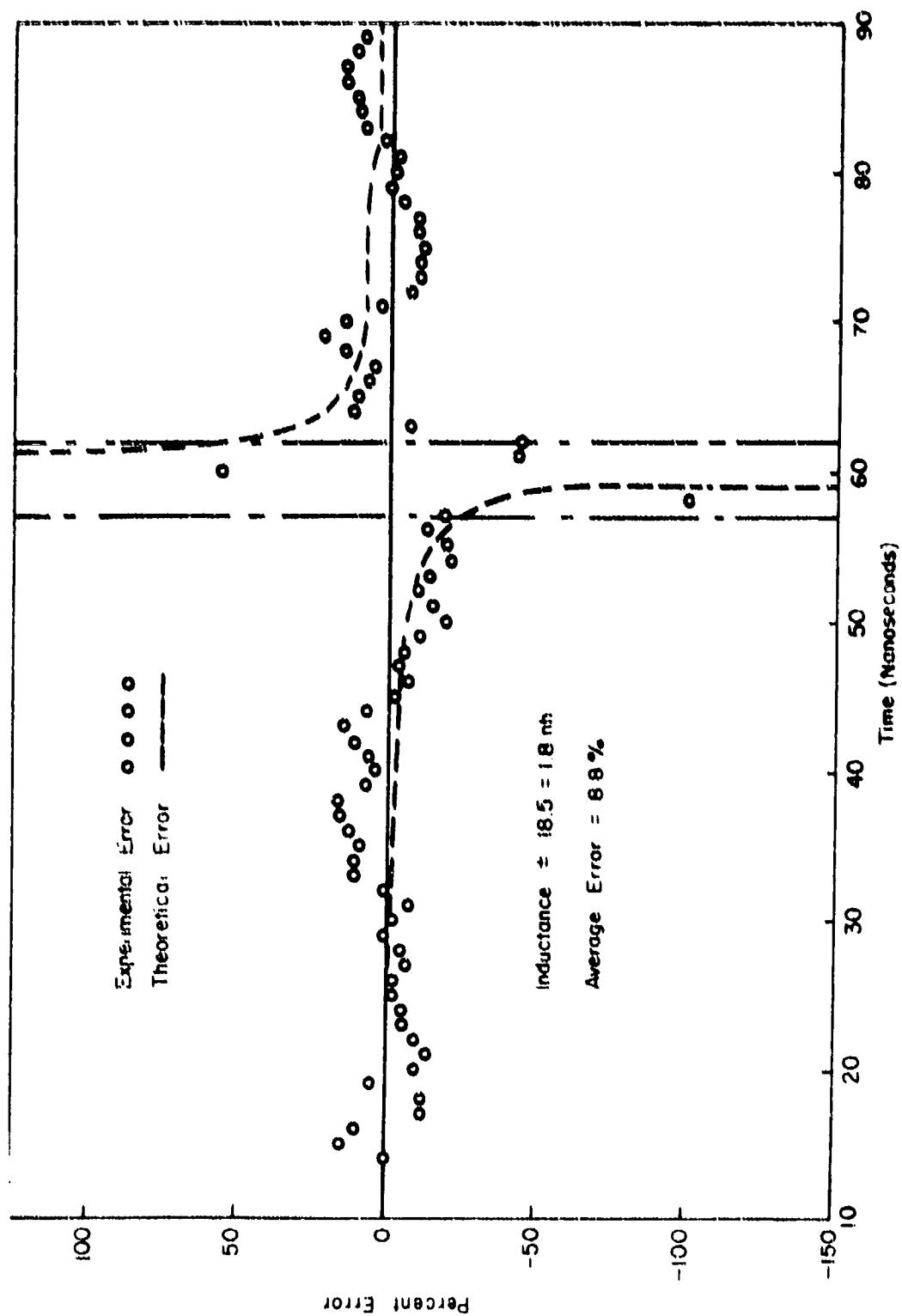
187

Figure 62. Error in Inductance Measurement

188

The average inductance determined from the short-circuit analysis was 18.5 ± 1.8 nh. For comparison, the corresponding theoretical value was calculated to be 19.5 nh. To avoid this undue error in the average value, data points in the time interval near the instant of zero di/dt were excluded from the calculation. The excluded region is indicated in figure 62.

Since current and di/dt signals were both monitored, it was possible to evaluate the accuracy of the Faraday cup-calorimeter current signal by comparing the magnetic pickup loop waveform with the di/dt waveform obtained by numerically differentiating the recorded current signal. Such a comparison is presented in figure 63 which also shows the short-circuit current pulse. The excellent agreement between the calculated and measured di/dt waveforms substantiated the manufacturer's calibration for the current monitor. The small deviations observed were attributed to time base nonlinearity and the inherent error associated with the process of numerical differentiation.

b. Resistive Load

Termination of the pulsed-power system in an aqueous-salt, resistive load provided an opportunity to compare the known resistive properties of a system load with the time dependent resistance values measured using the entire diagnostic array under operational conditions. A previous study of the electrical and thermal properties of several aqueous-salt solutions had shown that a resistor of this type best satisfied the requirements of a system termination (Ref. 6). The primary requirement for a resistive termination was that the load maintain a constant resistance while absorbing the total energy delivered by the pulsed-power system.
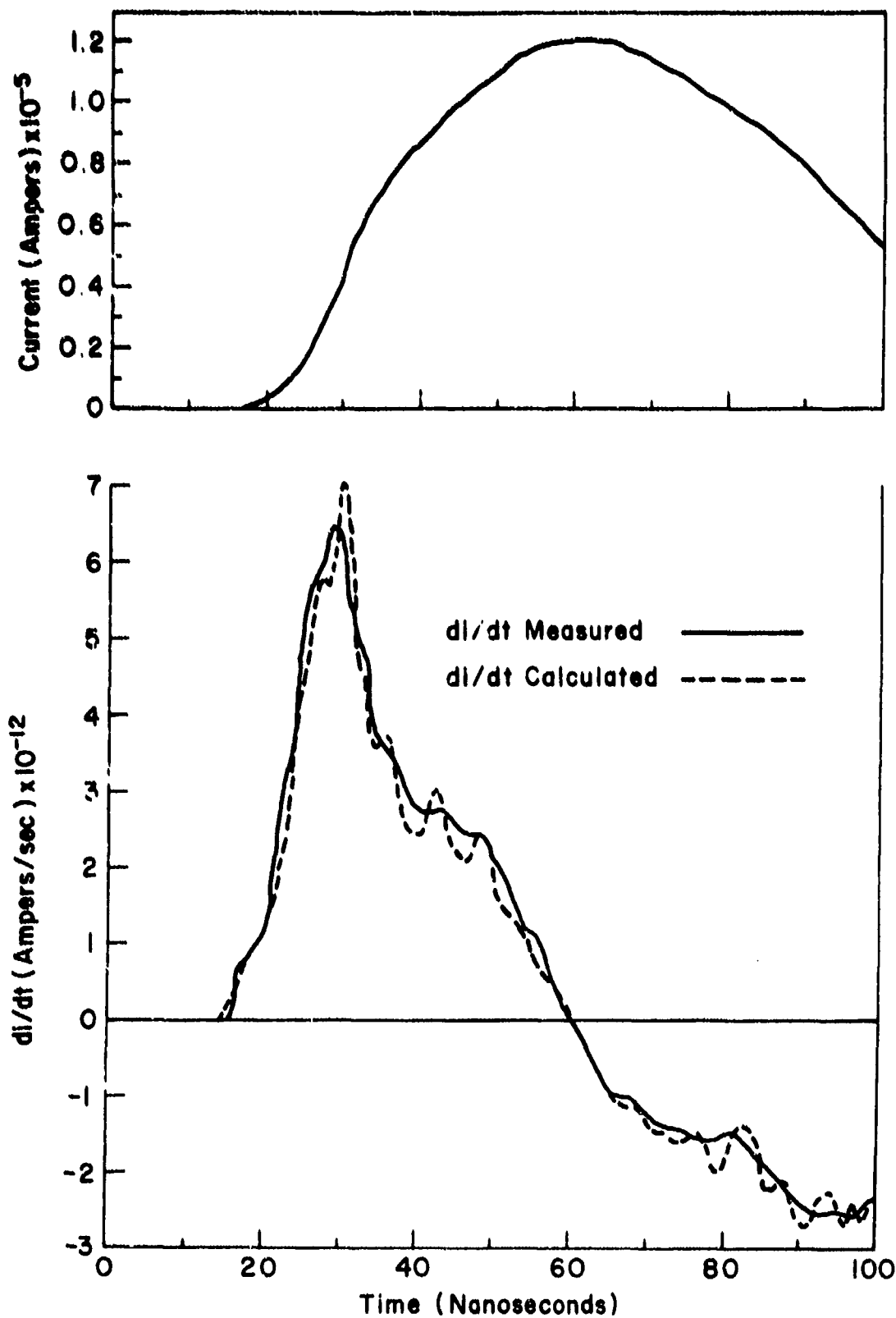
189

Figure 63. Comparison of Measured and Calculated di/dt Waveforms

The only factor found to significantly degrade the performance of an aqueous-salt load was a relatively high temperature coefficient of resistivity (in general negative). This was not considered to be a serious limitation in view of the moderate energy content (approximately one kilojoule) of the accelerator output pulse. Due to the high heat capacity of the aqueous solutions and the quantity of liquid required to fill the 2-inch-diameter load configuration temperature increases during the pulse were limited to a few degrees centigrade. Using a copper sulfate solution, the resultant decrease in resistance was approximately 10 percent.

An example of the voltage, current, and di/dt waveforms obtained by discharging the system (charged to 26.0 kV) into a 4.5-ohm resistive load are shown in figure 64. The time-dependent load resistance and the dissipated energy as calculated from these signals are shown in figure 65. The observed decrease in resistance can be attributed not only to the negative temperature coefficient of resistivity, but also to an apparent decrease caused by the RC decay in the signal generated by the capacitive voltage divider.

The magnitude of the error associated with the corrected voltage waveform was estimated by first calculating the time-dependent relative error for a particular set of resistance measurements. The averaged error computed for five successive sets of diagnostic waveforms is shown in figure 66. The time base in this presentation corresponds to that of the diagnostic waveforms shown in figure 64. The error limits on each data point represent the root-mean-square error of the five measurements for a specific instant in time.
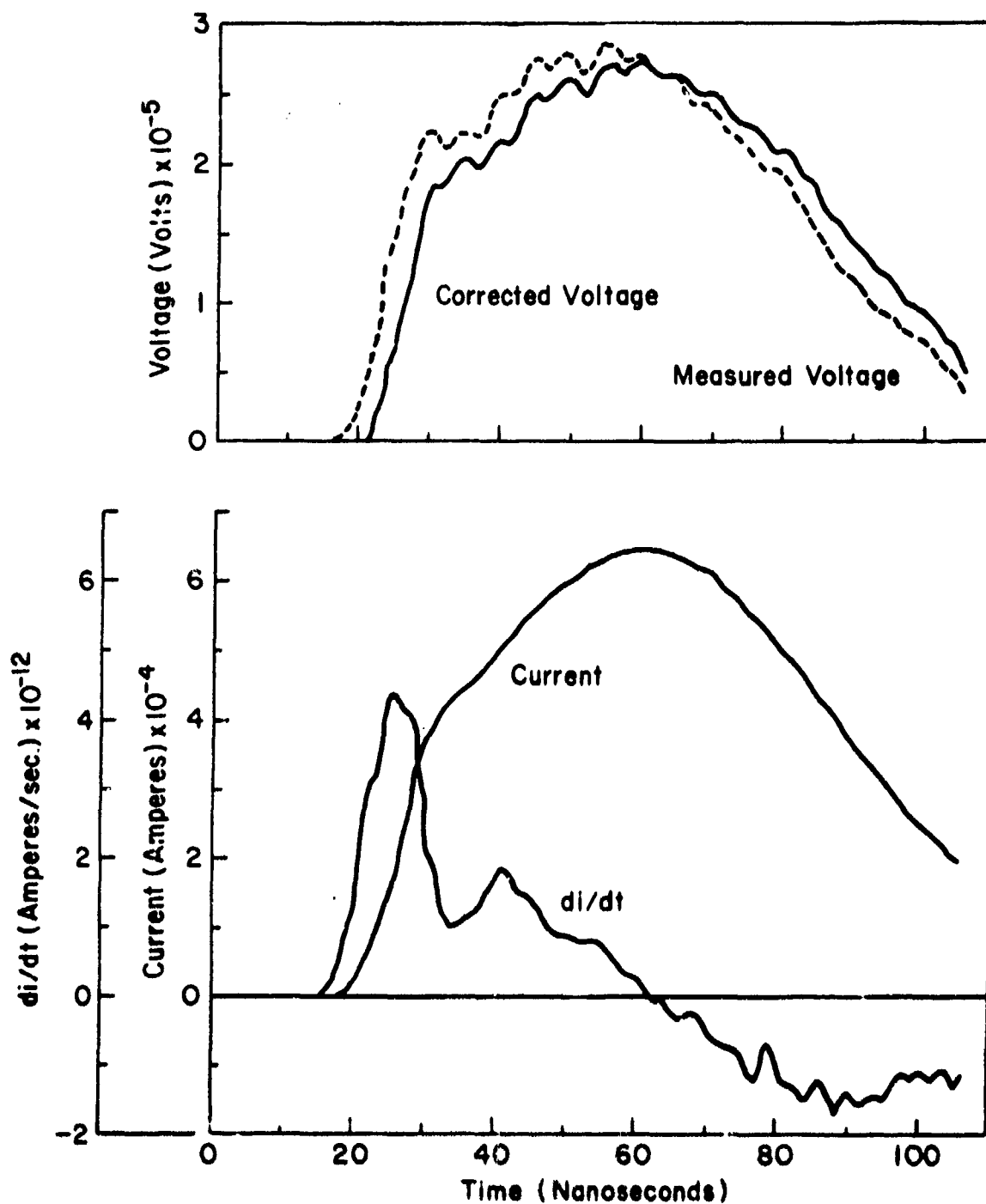
191

Figure 64. Voltage, Current, and di/dt Waveforms Obtained Using a Resistive Load
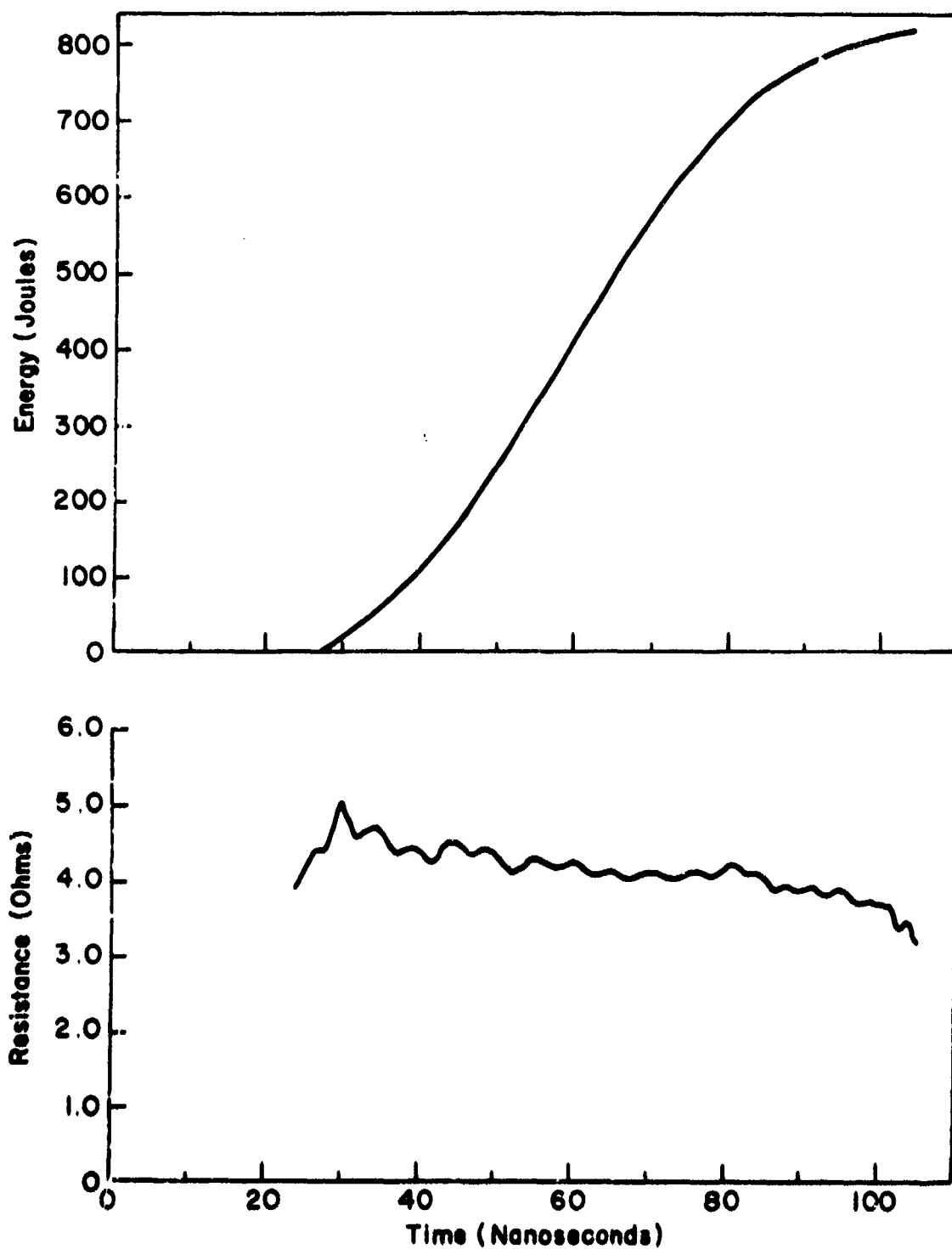
Figure 65.   Measured Resistance and Dissipated Energy
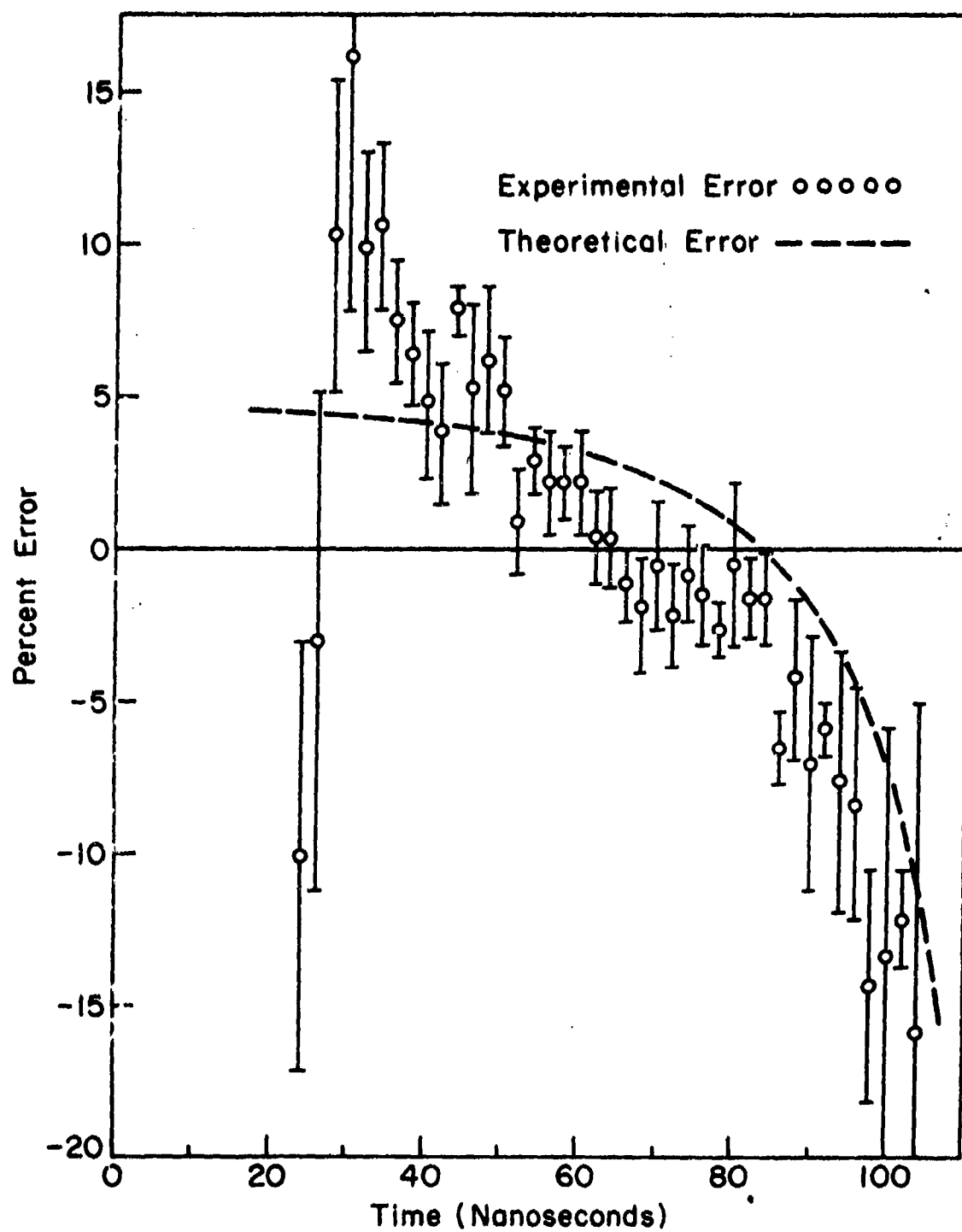
Figure 66. Error in Resistance Measurement -
Data Recorded at 20 nsec/cm

194

To calculate the expected error in these measurements resulting from the RC decay of the voltage divider, the measured current was approximated by a sequence of ramp and square waveforms. The corresponding di/dt would then be composed of a series of square waveforms. Since both the inductance L_1 and the resistive properties of the load were known, the idealized voltage waveform could be calculated from equation (113). Using the transform function for the voltage divider equivalent circuit, the hypothetical voltage waveform generated by the voltage divider was calculated. After removing the L_1 di/dt component, the voltage signal was divided by the "idealized" current waveform to yield a theoretical estimate of the time dependence in the resistance measurements. The results of this calculation are shown by the dashed line in figure 66.

The correlation between the theoretical and experimental error estimates during the last 70 nanoseconds of the pulse confirmed the dominance of the voltage divider error throughout this time interval. The rather substantial error observed during the first 20 nanoseconds was related to the correction of the voltage signal to remove the L_1 di/dt component. The magnitude of this error was determined by the need to make large percentage corrections to small signal amplitudes, as well as the rapid time variation of the signal amplitudes. Small errors in the relative timing between voltage and di/dt information in this time interval would therefore result in the observed error.

As described earlier, the procedure employed to further minimize time base error duing the leading edge of the pulse was to simultaneously record all diagnostic signals on a second set of oscilloscopes which had

195

been set for a sweep rate of 10 nsec/cm. The results of a similar error analysis for these data channels is shown in figure 67. Although the error at the leading edge was improved, the need to correct comparatively small voltage amplitudes to remove substantial inductive components still resulted in large errors during the first 10 nanoseconds of the pulse.

The error limits shown throughout the remainder of this report were estimated by attributing the time dependent relative error shown in figures 66 and 67 to the corrected voltage signal. On the assumption that the Faraday cup-calorimeter produced a distortion-free signal proportional to the diode current, the error associated with the current measurement was set at ± 3 percent to acknowledge oscilloscope and data reduction errors. These error limits were considered to be conservative.

c. Low-Resistance Diode

For the final step in the diagnostic calibration, the accelerator was terminated in the low-resistance diode formed by placing a 6.35-cm diameter graphite cathode 4.52 mm from the graphite disk of the Faraday cup-calorimeter. The corrected voltage and current waveforms obtained as a result of discharging the accelerator (charged to 26.0 kV) into this diode are shown in figure 68. Using the data from these waveforms, the time dependence of the diode resistance and the energy expended in accelerating the electron beam were calculated. The electrical energy expended prior to the time t is given by $\int^t V(\tau) I(\tau) d\tau$. The resultant plots of these parameters are shown in figure 69. For comparison, the voltage measured across the thermocouples within the calorimetric disk is shown in figure 70. As expected, the thermal energy deposited in the

196
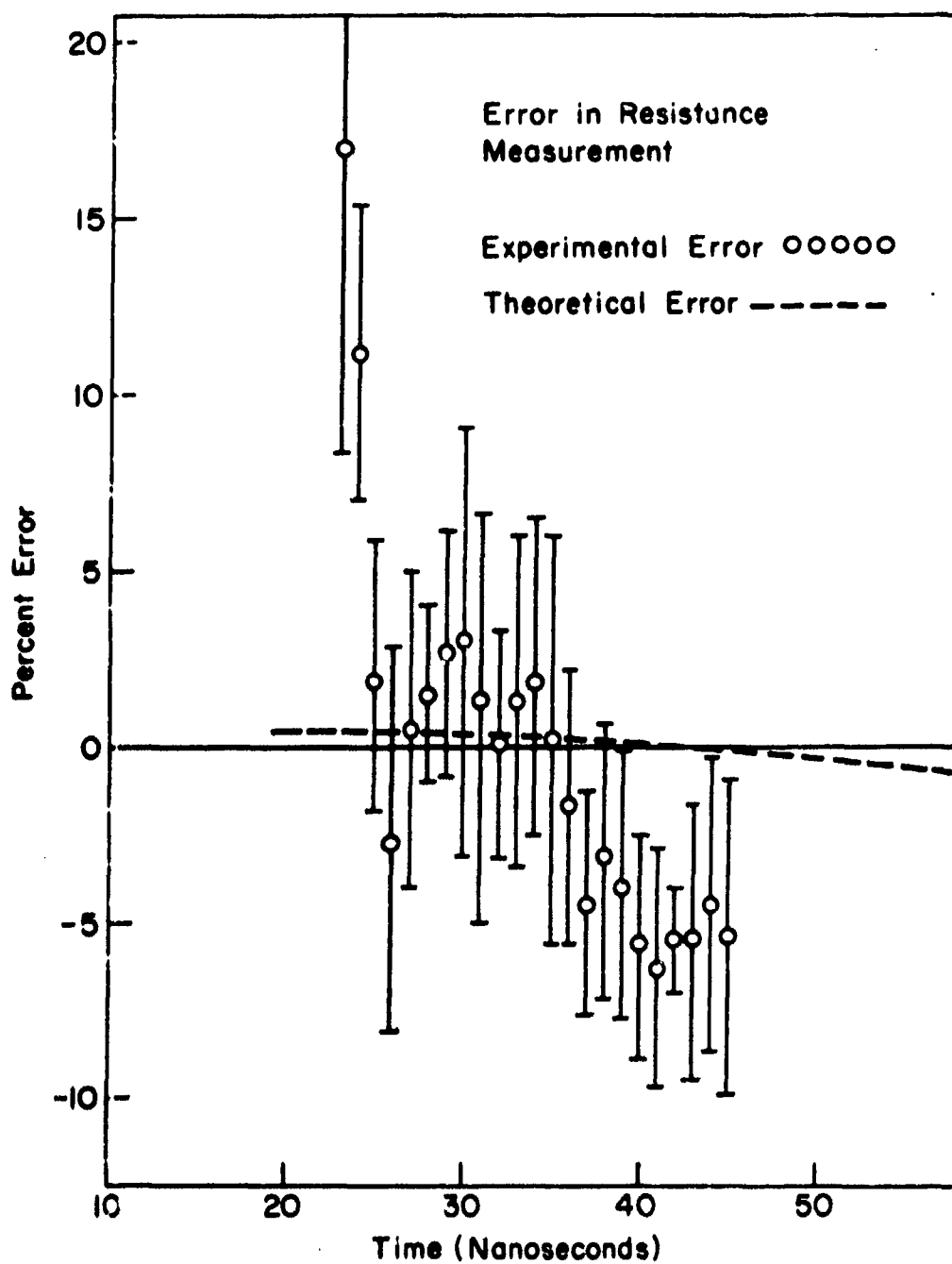
Figure 67. Error in Resistance Measurement -
Data Recorded at 10 nsec/cm

197
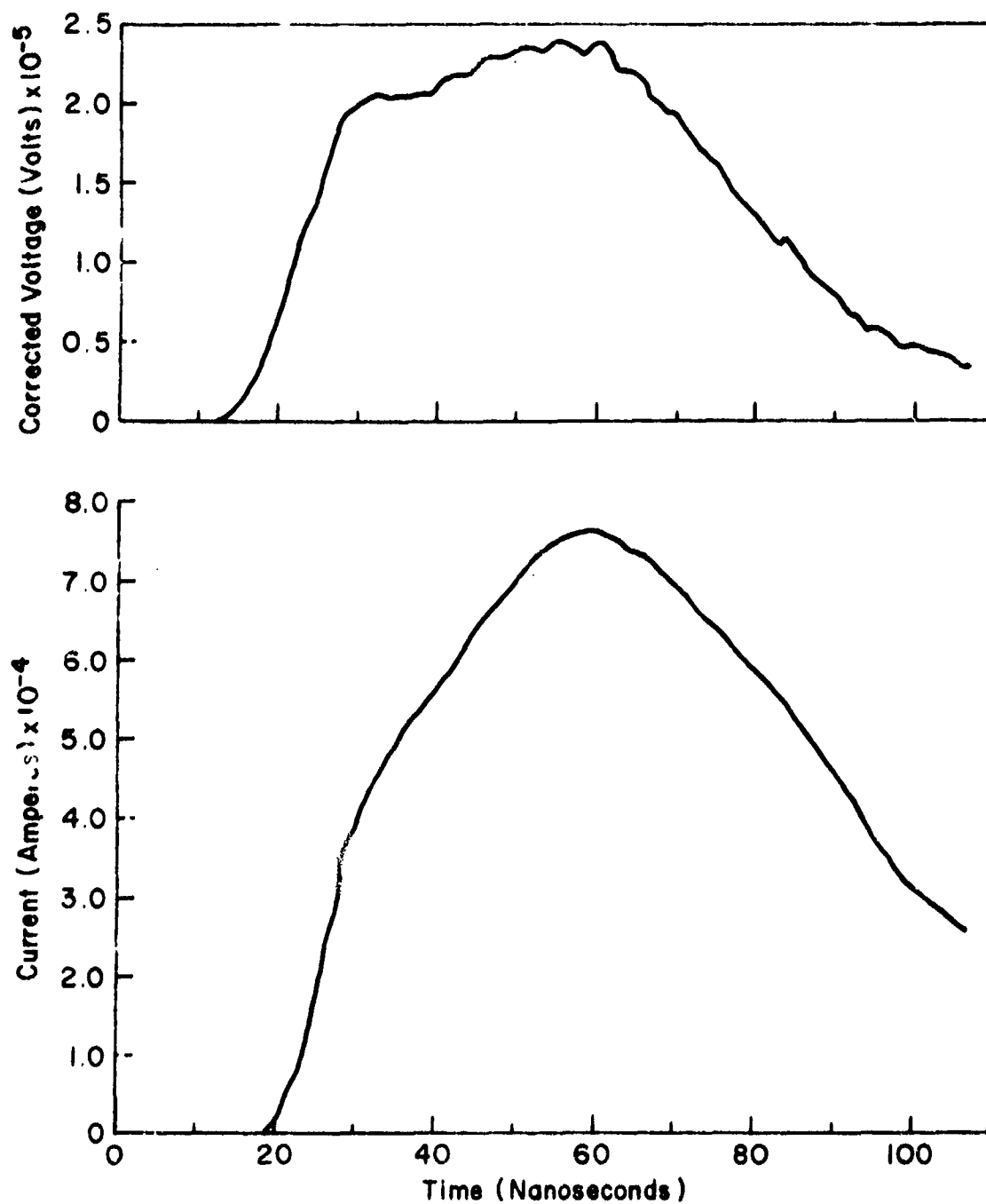
Figure 68. Corrected Voltage and Current Waveforms Obtained Using
a Low-Resistance Diode (Graphite Cathode - 6.35 cm Diameter;
Diode Separation - 4.52 mm)

198
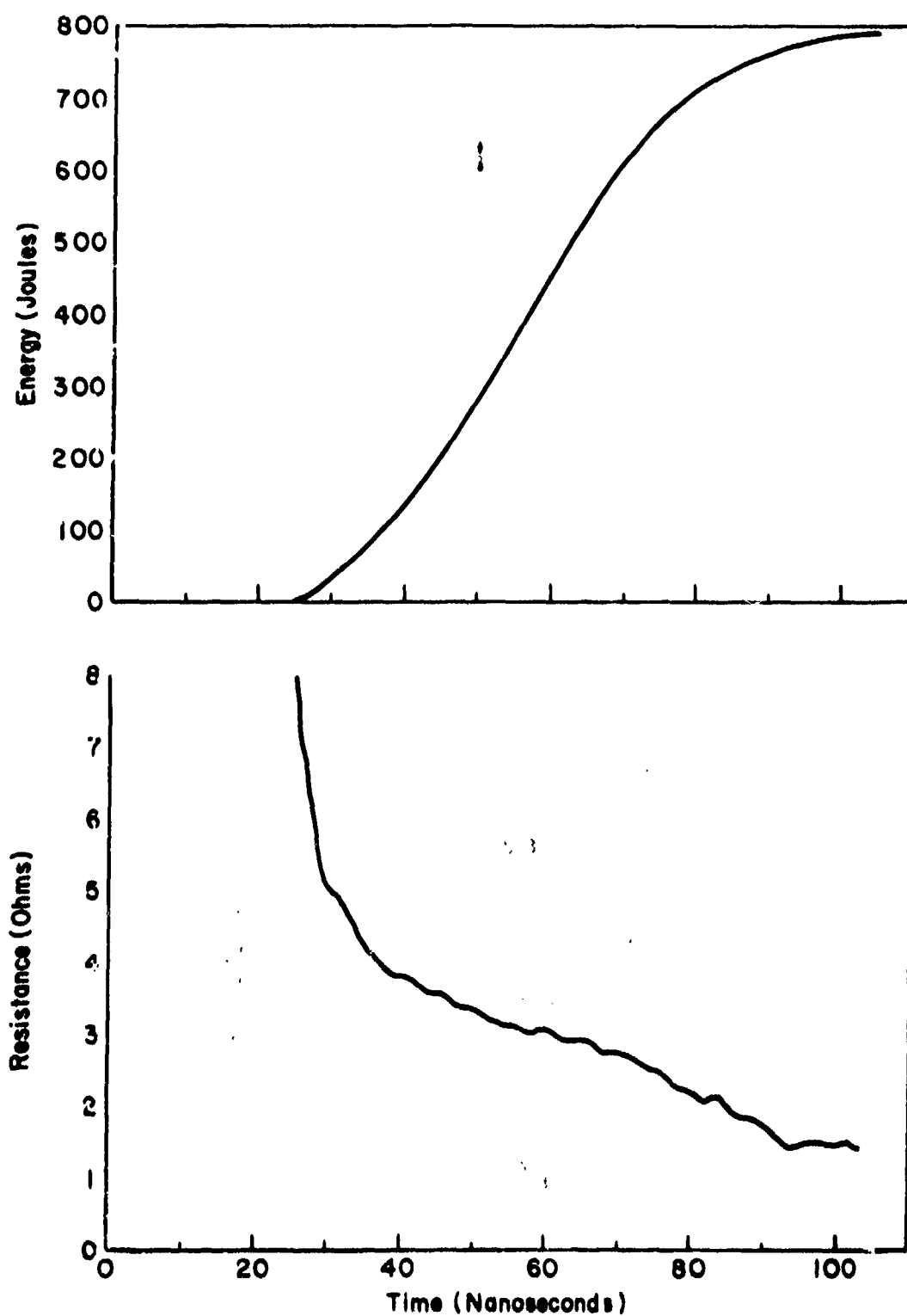
Figure 69. Diode Resistance and Electron Beam Energy
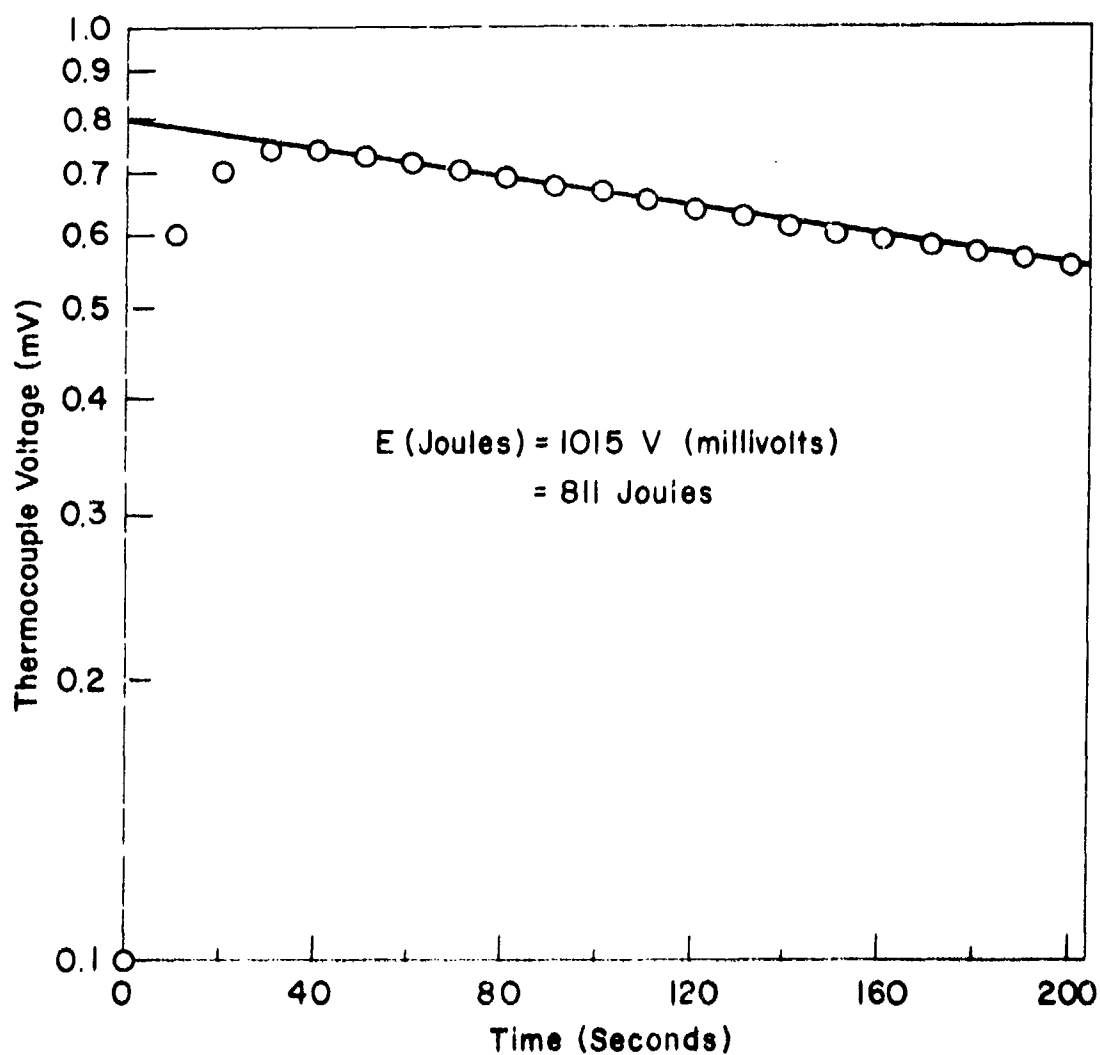
Figure 70. Thermocouple Voltage as a Function of Time

200

graphite disk (811 joules) was in excellent agreement with the electrical measurement of the expended energy (798 joules). The less than 2-percent error between the measurements was interpreted as a satisfactory verification of previous diagnostic calibration.

The remainder of this report will now be directed toward a detailed description of diode phenomenology as exemplified by the time-dependent resistance shown in figure 69.

SECTION VII

DIODE MODEL

1. INTRODUCTION

By synthesizing and extending several of the concepts and observations discussed in sections II and III of this report, the sequential processes expected to determine the electron flow characteristics within a broad-area, cold-cathode diode can be postulated. Throughout this development, selection of the operative electron emission and vacuum breakdown phenomena has been based on the range of parameters encountered within the high-aspect-ratio diodes employed in low-impedance, electron accelerators. In these electron beam generators, the accelerating potential between the diode electrodes is produced by a fast rise-time voltage pulse of short duration. Typically, the applied electric field is greater than 10^5 volts/cm, and the pulse duration is much less than 1 microsecond. In general, the diode configuration consists of a right-cylindrical cathode positioned at a distance greater than 1 millimeter from a planar, thin-foil anode.

In addition to these general constraints, no attempt has been made to define a model for the range of electron flow substantially in excess of the self-pinching criterion. With the moderate characteristic impedance ($Z_0 = 4.7 \Omega$) and the limited high-voltage capability (a maximum of 320 kV into a matched load) of the modified Field Emission pulsed-power system, this range could not be attained experimentally. The proposed model is therefore concerned primarily with the explosive

202

nature of intense field emission, the dominant plasma effects within the diode, and the mode of high-current electron flow at levels less than and equal to the critical self-pinching value.

2. PROPOSED MODEL

Any proposed diode model must be capable of predicting the time dependent phenomena which determine the observed features of the accelerated electron beam. Since many of these features are manifested in the time evolution of the pulsed accelerating potential and the diode current, the following discussion will be directed toward a detailed analysis of the corrected voltage and current waveforms. As an initial example, consider the corrected voltage and current waveforms shown in figure 71. These were obtained by discharging the modified Field Emission system into the high-aspect-ratio diode formed by placing a 5.08-cm diameter graphite cathode a distance of 6.05 mm from a planar graphite anode.

To simplify the initial analysis, the possibility of space-charge neutralization resulting from the ionization of residual background gas was removed by evacuating the diode region to 2×10^{-5} torr. Subsequent analysis was further simplified by minimizing the probability of plasma formation at the anode front surface. This latter simplification was achieved by limiting the energy content of the electromagnetic pulse incident on the diode to approximately 60 percent of its normal value, and by maximizing the kinetic energy of the incident electrons. The reduction in energy content was accomplished by limiting the system charging voltage to 20 kV, while the increased electron kinetic energy

203
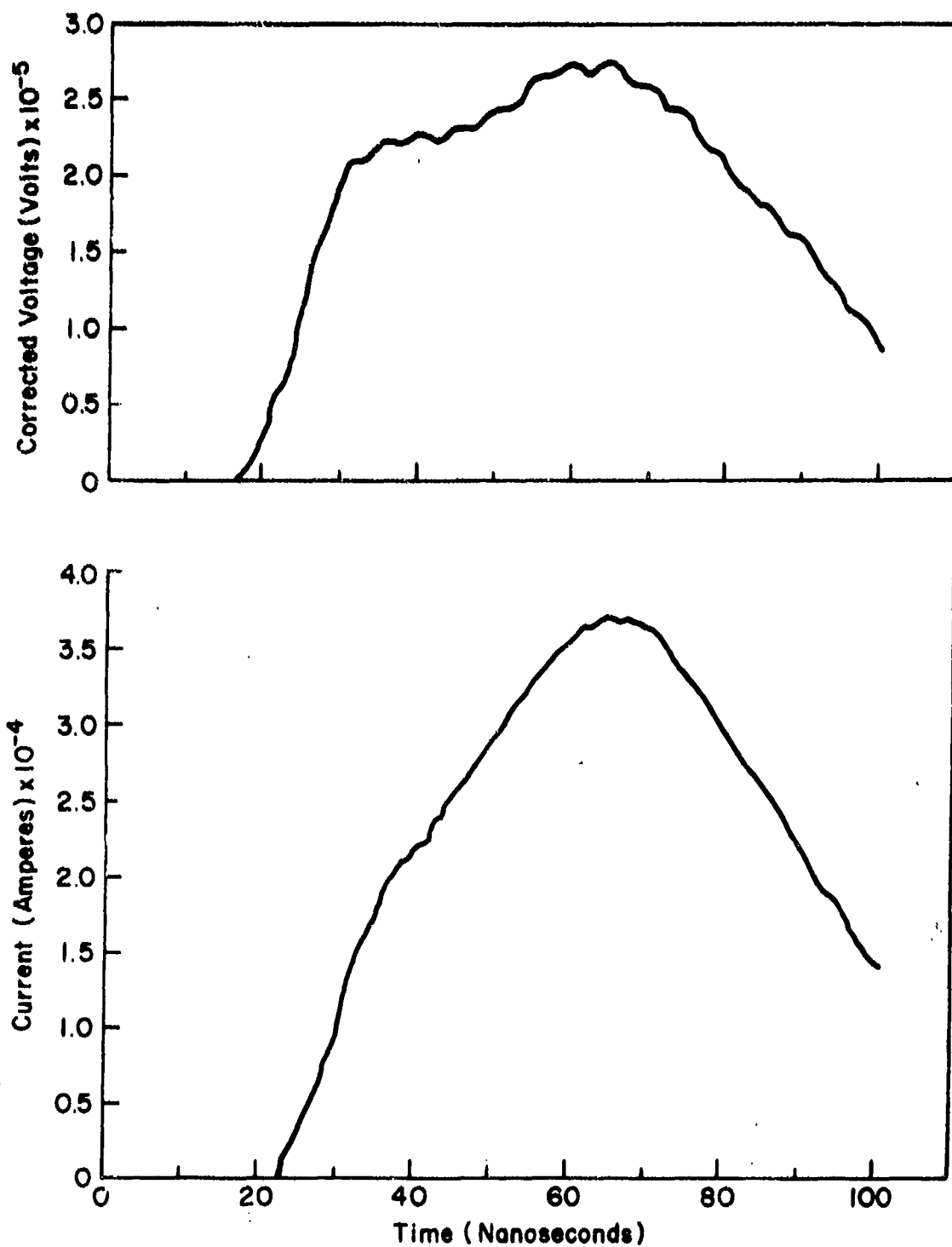
Figure 71. Corrected Voltage and Current Waveforms; Graphite Cathode: 5.08-cm Diameter; Diode Separation: 6.05 mm; System Charging Voltage Reduced to 20.0 kV

204

was obtained by selecting a comparatively high-resistance diode configuration.

As seen from figure 71, the appearance of a measurable electron emission from the cold cathode was delayed by approximately 6 nanoseconds relative to the leading edge of the applied voltage pulse. Within another 10 nanoseconds, the diode resistance had dropped from "infinite" to 14.5 Ω. The dominant processes which determine this diode transition from an essentially nonconducting to a highly conducting state can be postulated by invoking several of the concepts derived from the study of high-voltage vacuum breakdown.

The sequential breakdown processes at the cathode surface can be summarized as follows. The initial emission from the cold cathode surface must be attributed to field emission from the tips of cathode whiskers (Ref. 27). As the accelerating potential continues to rise, the field emitted current density will increase exponentially. When the current density exceeds approximately 10^6 amperes/cm^2, the applied field acting on the emitting surface will be substantially reduced by the electron space charge accumulating in the vicinity of the whisker top (Ref. 31). The intense emitted current density distinctive of field emission must also generate significant resistive and Nottingham heating within the cathode protrusions. The combined effects of space charge limited emission and excessive heating of the emitting whiskers create a regenerative thermal instability which can result in the rapid destruction of the emission site (Ref. 49). The onset condition for the instability has been correlated with the whisker tip temperature reaching a value corresponding to a vapor pressure of approximately

205

10^{-4} torr (Ref. 21). At the critical temperature, there is sufficient evaporation and subsequent ionization of the tip material to partially neutralize the electron space charge. As the space charge suppression of the applied field is removed, the emitted current density and hence the resistive heating will rapidly increase with a catastrophic effect.

Under steady-state or long pulse conditions, the emitted current density required to heat the tip of a typical whisker to the critical temperature may range from 10^6 to 10^8 amperes/cm^2, depending upon the cathode material and the whisker size and shape. Since the field emitted current density is exponentially dependent on the surface electric field, the corresponding breakdown field is limited to the rather narrow range extending from 5×10^7 to 8×10^7 volts/cm. If the duration of the applied pulse is short compared to a microsecond, the critical breakdown field will be somewhat higher.

Once the critical tip temperature has been exceeded, the emitting projections will rapidly explode to form cathode flares (Ref. 43). Following the destruction of the initial emission sites, the flare plasmas will continue to expand at a constant velocity. The electron flow subsequent to flare formation is then determined by space-charge-limited emission from the expanding surface of the cathode flares.

If the applied field is of sufficient magnitude, the concentration of flares on the cathode surface will be sufficiently dense that the flare plasmas can rapidly merge to form a uniform plasma sheath covering the entire cathode surface. Once the plasma sheath has formed, the electron flow within the diode can be described as space-charge-limited emission from a constantly expanding plasma cathode. Given the range

206

of applied fields generally encountered in the diodes of cold-cathode, relativistic electron accelerators, the sequence described above can be completed within several nanoseconds. The remainder of this section will, therefore, be concentrated on a correlation of observed diode response with the model proposed above.

a. Microscopic Effects

Since the present study was constrained to the use of broad-area cathodes under the operational conditions encountered within the diode of a pulsed, high-current, electron accelerator, the microscopic processes which initiate the transition to breakdown could not be directly observed. However, the macroscopic ramifications of these processes can be enumerated and their correlation with several of the observed features of the initial diode response determined. As shown in figure 71, the initial diode response was distinguished by a several nanosecond delay between the initial rise in the applied field, and the emission of a significant electron current. Within the next several nanoseconds, the diode resistance rapidly dropped to a finite value on the order of that predicted by the infinite-planar, Child-Langmuir theory. The existence of this transition, its timing relative to the corrected voltage waveform, and the resistance to which the diode evolved must therefore be evaluated for their correlation with the consequences of cathode-initiated vacuum breakdown.

In considering the initial electron flow in the diode, the presence of the cathode whiskers has the effect of not only enhancing the applied field by factors perhaps as large as several hundred, but also constraining the resultant emission to the whisker tips where the

207

surface field is most enhanced. The total field enhancement encoun-
tered across the face of the right-cylindrical cathode used to obtain
the waveforms presented in figure 71 can be estimated by combining the
microscopic and macroscopic enhancement curves shown in figures 5 and
7, respectively. Near the diode axis, the field at the whisker tips is
given by $m_1 E$. For the diode separations of interest, the microscopic
enhancement factor m_1 should vary from perhaps 200 to 300.

The field encountered at the cathode periphery would be further
enhanced by the presence of the edge. To estimate the magnitude of
this enhancement, the average radius of curvature at the edge was
measured to be 9×10^{-3} cm. From figure 7, the macroscopic enhancement
m_2 at the edge would therefore be approximately 5.4. The total field
enhancement experienced by microprojections along the cathode perimeter
would then be equal to the product of the microscopic and macroscopic
enhancements. The microscopic field at the perimeter is therefore
given by $m_1 m_2 E$. With total field enhancements on this order, the
apparent contradiction of significant field emission with applied
fields ranging from 10^5 volts/cm to 10^6 volts/cm is removed.

With the electron emission constrained to the whisker tips dur-
ing the initial phase of the diode response, the magnitude of the stable
field emission can be estimated by specifying reasonable limits to the
number and physical size of the emission sites. Reported estimates for
the concentration of emission sites have ranged from approximately 1
whisker/cm^2 to perhaps 10^4 whisker/cm^2. Observed microprojections have
typically been on the order of 1 micron in height with a base radius of
approximately 0.1 micron. The shapes of these whiskers were such that

the mean radius of the emission area at the tip would be smaller than the base radius. To complete the estimate, the emitted current density cannot exceed the range 10^6 to 10^8 amperes/cm^2 if the whiskers are to remain thermally stable. By combining these estimates, the average current density observed at the anode during the stable field emission phase of the diode response can be expected to range from microamperes/cm^2 to perhaps amperes/cm^2. Since the current densities generally associated with the operation of low-impedance, pulsed-electron accelerators are on the order of tens of kiloamperes/cm^2, the measured diode resistance must be effectively "infinite", while the emission is limited to the microscopic area of the whisker tips.

For the cathode emission to evolve beyond the stable field emission phase, the microscopic field at the whisker tips must at least exceed the critical steady-state breakdown value. The time delay required for the most intensely emitting whiskers to reach the lower limit of the range in steady-state breakdown field can be estimated by applying the enhancement factors derived above to the corrected voltage waveform. When these estimates are combined with the measured electrode separation, the microscopic field at the tips of whiskers located along the cathode perimeter will equal 5×10^7 volts/cm when the corrected voltage has risen to the range 2×10^4 to 3×10^4 volts. As seen from figure 71, the corrected voltage passed through these points from 3 to 4 nanoseconds before the onset of first measurable current. The absence of measurable electron emission during the first several nanoseconds of the voltage pulse would therefore be consistent with the assumption of field emission from the tips of cathode microprojections.

209

Once the applied field has exceeded the critical steady-state breakdown value, the destruction of the emission sites must follow. The timing of this explosive destruction relative to the applied voltage waveform is determined by the transient heating processes within the whisker. A quantitative measure of the breakdown delay is available from the Soviet study (Ref. 44) which reported the time delay observed between the application of a square-wave voltage pulse and the initial formation of cathode flares. As seen in figure 14, this delay was a sensitive function of the applied field, but only moderately dependent on cathode material.

Before this breakdown delay data can be used to estimate the onset of measurable current flow within the diode, two complicating factors must be considered. First, the microscopic field acting at the whisker tips was not known in either experiment because of the use of broad-area cathodes. Secondly, the shape of the voltage waveforms were different during the transition to breakdown. Where the voltage pulse in the Soviet experiment had a 1-nanosecond rise time, the diode voltage continued to increase lineraly with time during the interval of interest.

To overcome the initial complication, the Alpert field enhancement data were used in both cases to estimate the corresponding microscopic electric field. From figure 5, gap spacings of a few tenths of a millimeter should have resulted in microscopic enhancement factors of about 100. Since the electrodes in the Soviet experiment were configured to suppress any macroscopic enhancement, no additional enhancement need be considered. Using the factor of 100, a microscopic field in excess of 8×10^7 volts/cm would be required to produce a breakdown delay of

210

less than 3 nanoseconds. From the measured values of the corrected voltage and the enhancement factors derived earlier, the microscopic field at the tips of the cathode whiskers located along the cathode edge was estimated to be in the range of 5×10^7 to 7.5×10^7 volts/cm at 3 nanoseconds prior to the onset of measurable current. At the instant of first measurable current, the microscopic field would have been in the range of 1×10^8 to 1.8×10^8 volts/cm. Regardless of the difference in voltage waveform, these estimates were certainly consistent with the assumption of the initial flare formation at the cathode periphery being coincident with the onset of measurable current.

If the onset of first measurable current was coincident with the initial flare formation, the rapid increase in the diode current during the next 15 to 20 nanoseconds must be related to subsequent flare formation across the remainder of the cathode face. For this to be true, the microscopic field at the tips of whiskers located near the diode axis must increase to values in excess of approximately 6×10^7 volts/cm (corresponding to breakdown delays of less than 5 nanoseconds) during the same time interval. Fourteen nanoseconds into the pulse, the diode voltage was measured to be 2.08×10^5 volts. This would correspond to an estimated microscopic field on the order of 1.1×10^8 volts/cm.

b. Macroscopic Effects

Several elements from the preceding description of the macroscopic events on the cathode surface can now be combined to provide a model for the diode response throughout the remainder of the pulse. Subsequent to flare formation, Mesyats has shown the effective emission

211

surface to be that of the expanding cathode flare. If the concentration of thermally unstable emission sites is sufficiently high, the rapid merger of the resultant flares would form a plasma sheath covering the entire cold-cathode surface. Assuming the expansion velocity, v, to be constant, the effective plasma cathode would then move toward the anode at a constant rate.

Applying the concept of a plasma cathode, the effective emitting surface within the diode at time t following the initial flare formation could be expected to appear as shown in figure 72. By this time, the flares located on the cathode face would have expanded to form a planar plasma surface located a distance vt from the original cathode surface. Similarly, flares on the circumferential edge would have expanded radially to form a half torus of minor radius vt. The voltage gradient along the surface of the torus, and hence the emitted current density, will decrease as the angle θ increases. No attempt has been made to specify this dependence. Rather, an effective emitting surface described by that segment of the torus surface where θ is less than 45 degrees was assumed. As a final assumption, the emitted current densities from the planar and circumferential regions were assumed to be uniform and equal.

According to Mesyats, the electron emission from the expanding plasma surface was space-charge-limited. Assuming this to be true, the diode perveance would be a viable concept. An appropriate perveance expression for the cathode surface shown in figure 72 must include terms to describe the effects of electron flow from the circular face, as well
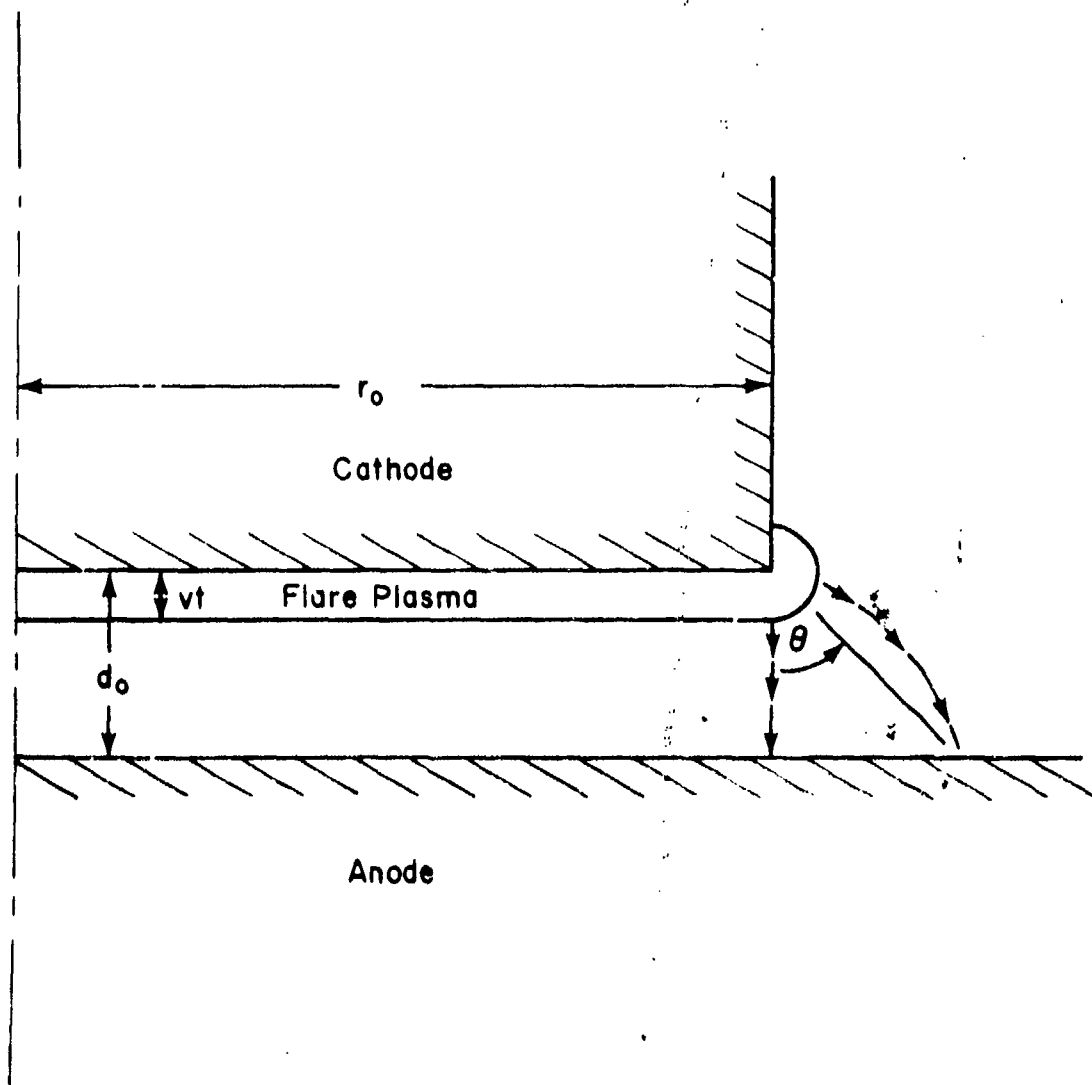
Figure 72. Schematic of the Plasma Cathode

213

as the circumferential edge. Moreover, the time dependence resulting from the plasma expansion must also be included.

The effects of edge emission can easily be incorporated by noting the geometrical similarity between the envelope of peripheral electron trajectories shown in figure 72, and a segment of electron flow between concentric cylindrical electrodes enclosed by an angle θ. The perveance of electron flow in a coaxial diode was previously given in equation (58). Since only the segment enclosed by θ is of interest, the appropriate perveance expression for the edge emission would be as follows.

$$P_{edge} \approx (\theta/2 \ \pi) \ P_{cylinder} \tag{124}$$

Using the notation from figure 72, equation (124) can be combined with equation (59) to yield

$$P_{edge} = \frac{14.66 \times 10^{-6}}{8} \left[\frac{2\pi r_0}{\left(d_0 \alpha_1^2\right)} \right] \tag{125}$$

where α_1^2 (shown in figure 20) is now a function of d_0/vt.

Following a similar argument, an appropriate perveance expression for the electron flow in the planar region of the diode can be derived from the infinite planar Child-Langmuir equation. Substituting the dimensions given in figure 72 resulted in the following relation.

$$P_{planar} = 2.33 \times 10^{-6} \ \pi r_0^2/d^2 \tag{126}$$

where d is the effective diode separation, and is set equal to $d_0 - vt$. To complete the derivation, the perveance of the total electron flow

from the cathode edge and face is equal to the sum of the component
perveances.

$$P_{diode} = P_{planar} + P_{edge} \tag{127}$$

The experimental perveance for the 5.08-cm diameter graphite
opposite the planar anode was derived from the corrected voltage and
current waveforms presented in figure 71. A comparison between the
experimental perveance and that predicted by equation (127) is shown
in figure 73. A best fit for the theoretical model was obtained by
assuming the flare expansion velocity to be $2.5 \pm 0.1 \times 10^6$ cm/sec.
In the figure, the edge perveance is given separately. One notes a
discontinuity in the experimental perveance when the formation of the
plasma sheath at the cathode periphery is completed and the emission
from that region becomes space-charge-limited. During the next 10 to
12 nanoseconds, the perveance continues to increase as the flare for-
mation extends over the remainder of the cathode face. The excellent
agreement between theory and experiment throughout the remainder of
the pulse is indicative of space-charge-limited electron emission from
an effective plasma cathode which expanded toward the anode at a con-
stant rate of 2.5×10^6 cm/sec. For the sake of a later comparison,
the Child-Langmuir perveance for the planar portion of the cold cathode
surface has been included in figure 73.

In developing the perveance model which resulted in equation
(127), the emitted current densities from the planar and circumferen-
tial regions were assumed to be uniform and equal. Additionally, the
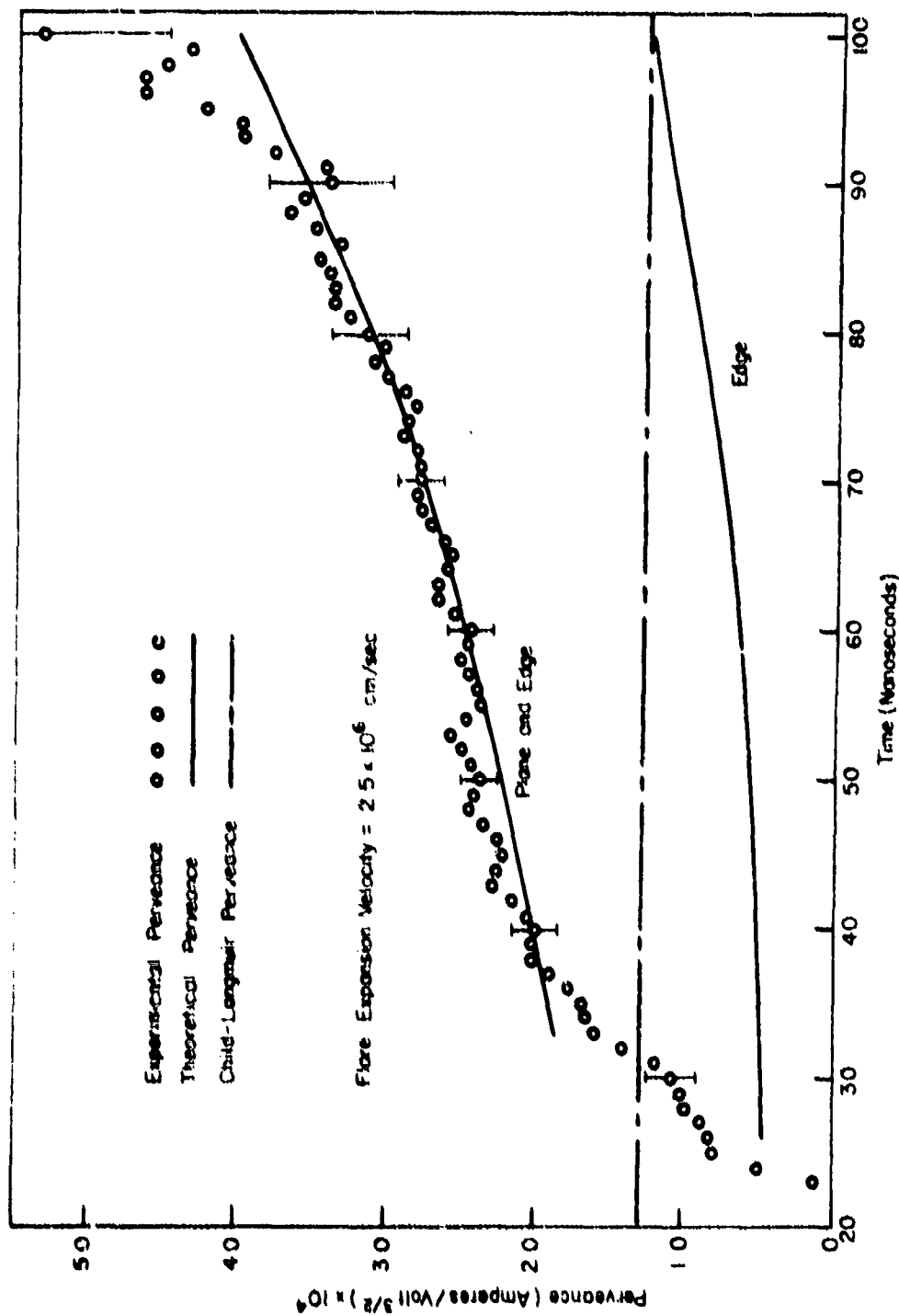emitting segment of the half torus was assumed to be approximately 45

215

Figure 73. Perveance Comparison for the Diode Formed by Positioning a 5.08-cm Diameter Graphite Cathode a Distance of 6.05 cm from a Planar Anode

degrees. To verify these assumptions, the Faraday cup-calorimeter was replaced on the anode plane by the graphite attenuator/plastic scintillator assembly shown schematically in figure 57. The time-integrated current density distribution was then recorded by photographing the optical emissions from the Pilot B using an open-shutter camera. The resultant photograph is shown in figure 74. To provide a more quantitative measure of the current density distribution, an optical densitometer scan along an image diameter is presented in figure 75. The sharp peaks at either extreme of the scan corresponded to the edge of the 7.62-cm diameter scintillating disk, and served as a useful dimensional reference.

As seen from the densitometer scan, the current density distribution exhibited a certain amount of structure. Nevertheless, the averaged distribution varied by only $\pm$ 15 percent from center to edge. The full width at half maximum of the distribution was measured to be 6.28 cm. The distribution, therefore, extended approximately 6.0 mm beyond the cathode radius. An extension of this magnitude would correspond to $\bar{\theta}$ being equal to 44.8 degrees.

An assumption implicit to the derivation of the perveance expressions combined in equation (127) was that the electron trajectories within the diode are parallel to the electrostatic lines of force. For this assumption to be valid when dealing with high-current electron flow, the self-magnetic forces acting on the electrons must be negligible. A criterion for evaluating the effects of the self-magnetic force has been derived by using the dimensionless electron beam parameter ν/γ to relate the critical self-pinching current to the

217

Figure 74.   Open-Shutter Photograph of Current Density Distribution
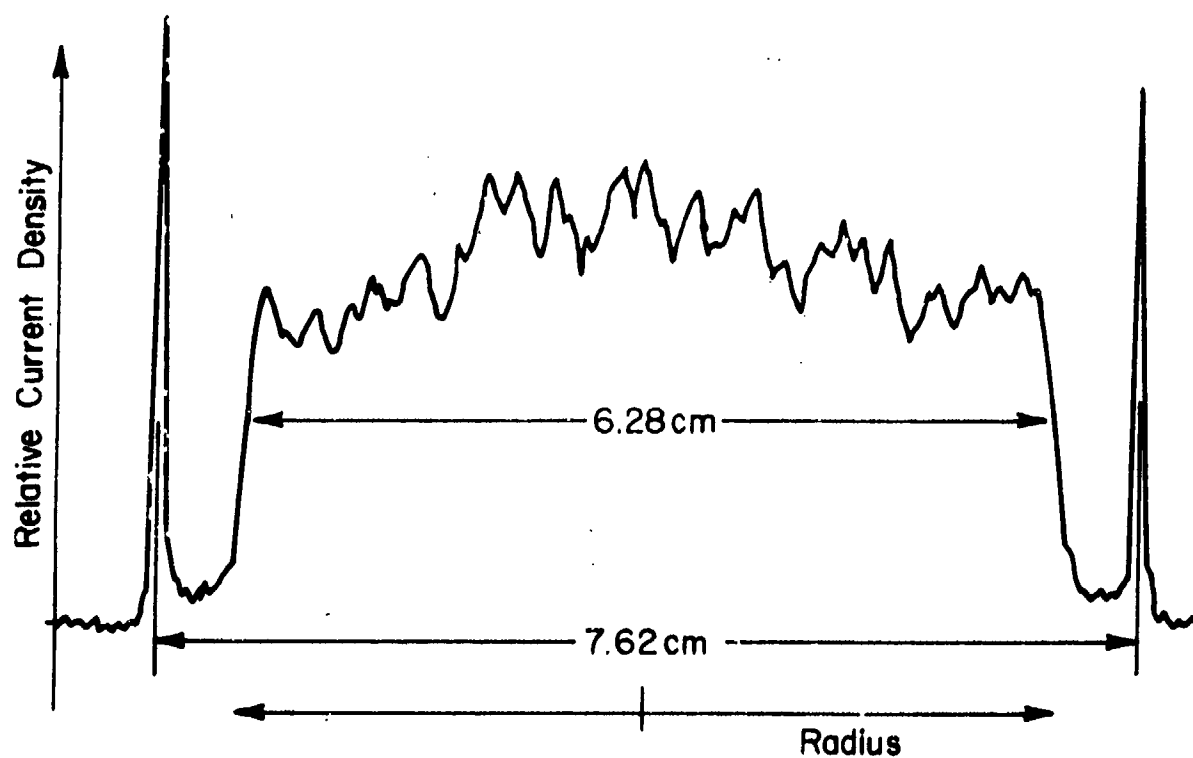

Figure 75.   Optical Densitometer Scan of the Photographic Negative

diode geometry. Using this relation, the self-magnetic forces acting within the diode will become dominant when the v/γ of the electron beam exceeds one-half the diode aspect ratio, i.e., $v/\gamma > r_0/2d$. For the diode considered above, the experimental v/γ at the instant of maximum current was 1.9. If the effective emission surface is indeed defined by an expanding plasma sheath, the diode aspect ratio must be time dependent. Assuming the expansion velocity as determined by the perveance analysis to be 2.5×10^6 cm/sec, the $r_0/2d$ for the diode at the instant of maximum current would be 2.54. Since $r_0/2d > v/\gamma$, the electron beam was not expected to exhibit significant pinching within the diode, and the effects of the self-magnetic forces on the diode perveance would therefore be negligible.

In closing the discussion of this particular diode, a final observation is worthy of note. As seen in figure 74, the emitted electron density distribution from the region of the sharp cathode edge exhibited a distinctive pattern of radial striations. As stated by Bradley et al. (Ref. 76), such striations are associated with electron emission from all sharp edge cathodes. The striations were orthogonal to the cathode edge and always had the same spatial frequency for a given edge geometry. According to Toepfer and Bradley (Ref. 77), the observed striations are dependent on the existence of a plasma emission surface, and are consistent with a tearing instability of the plasma near the cathode surface.

c. Anode Effects

In the initial diode experiment, the accelerated electron beam characteristics were carefully chosen to avoid the complicating effects

219

of plasma formation at the anode, and diode self-pinching. Since these effects are normally significant, a second diode experiment will now be considered in which the diode parameters were selected to enhance the anode front-surface dose, and to decrease the diode resistance. To achieve the desired effects, the same 5.08-cm diameter graphite cathode was moved to within 2.79 mm of the graphite anode. The system charging voltage was then increased to 26.0 kV. As before, the diode region was evacuated to a pressure of 2×10^{-5} torr. The corrected voltage and current waveforms which resulted are shown in figure 76.

Tne relative timing observed between the onset of first measurable current and the initial rise in the voltage pulse was again consistent with the thermal instability proposed by Dyke et al., and the breakdown delay measurements by Mesyats et al. By assuming the enhancement factor at the edge to be three and the microscopic enhancement to vary from 200 to 300, the emission from whiskers located at the cathode periphery would be expected to become space-charge-limited 1 to 2 nanoseconds before the onset of first measurable current. At the instant of initial flare formation, the voltage on the diode was approximately $\theta \times 10^{4}$ volts. Using the higher value for the microscopic enhancement factor, this would correspond to a microscopic field strength of approximately 1.3×10^{8} volts/cm. From the Mesyats breakdown data, a field of that magnitude would result in a delay of less than a nanosecond. As in the discussion of the first example, the conversion from macroscopic to microscopic fields in interpreting the breakdown curve was accomplished by assuming an enhancement factor of 100. Following the initial breakdown, flare formation would spread rapidly across the
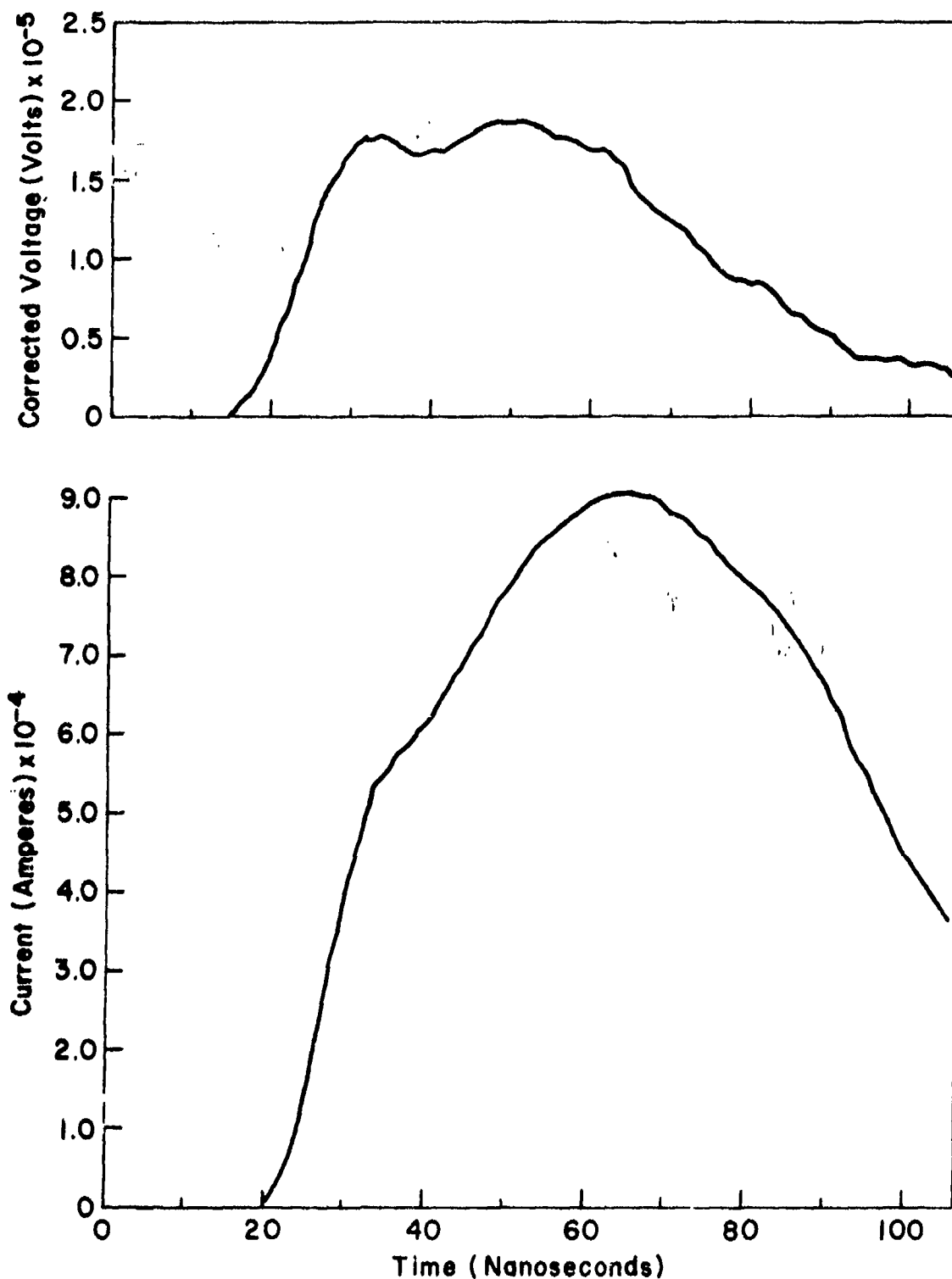
220

Figure 76. Corrected Voltage and Current Waveforms;
Graphite Cathode: 5.08-cm Diameter; Diode Separation: 2.79 mm;
System Charging Voltage: 26.0 kV

cathode face as the voltage continued to rise. When the formation of the cathode plasma sheath was completed, the electron flow in the diode would be space-charge-limited.

In the first diode experiment, the space-charge limitation was characterized by a time varying perveance determined by the constant expansion rate of the effective plasma cathode. As seen in figure 77, this simple description was valid in the second experiment for only the time interval extending from 30 to 65 nanoseconds. Beyond 65 nanoseconds, the experimental perveance increased more rapidly than predicted.

One possible explanation for this discrepancy would be the formation of an anode plasma, the expansion of which would increase the effective rate of diode closure. Working from this assumption, the predicted cathode plasma expansion velocity was derived by obtaining a best fit for the theoretical perveance model to the experimental data between 30 and 65 nanoseconds. The displacement of the postulated anode plasma was then numerically unfolded from the experimental data throughout the remainder of the pulse, and plotted with the predicted cathode motion in figure 79.

To test the validity of these assumptions, streak photographs were taken with the slit parallel to the diode axis. The appropriate photograph is shown in figure 78. The comparison shown in figure 79 was then completed by superimposing the displacement of the electrode plasma luminosity on the displacements unfolded from the perveance data. Although the relation of the luminous front to the plasma front is not clear, the qualitative correlation shown in figure 79 supports the
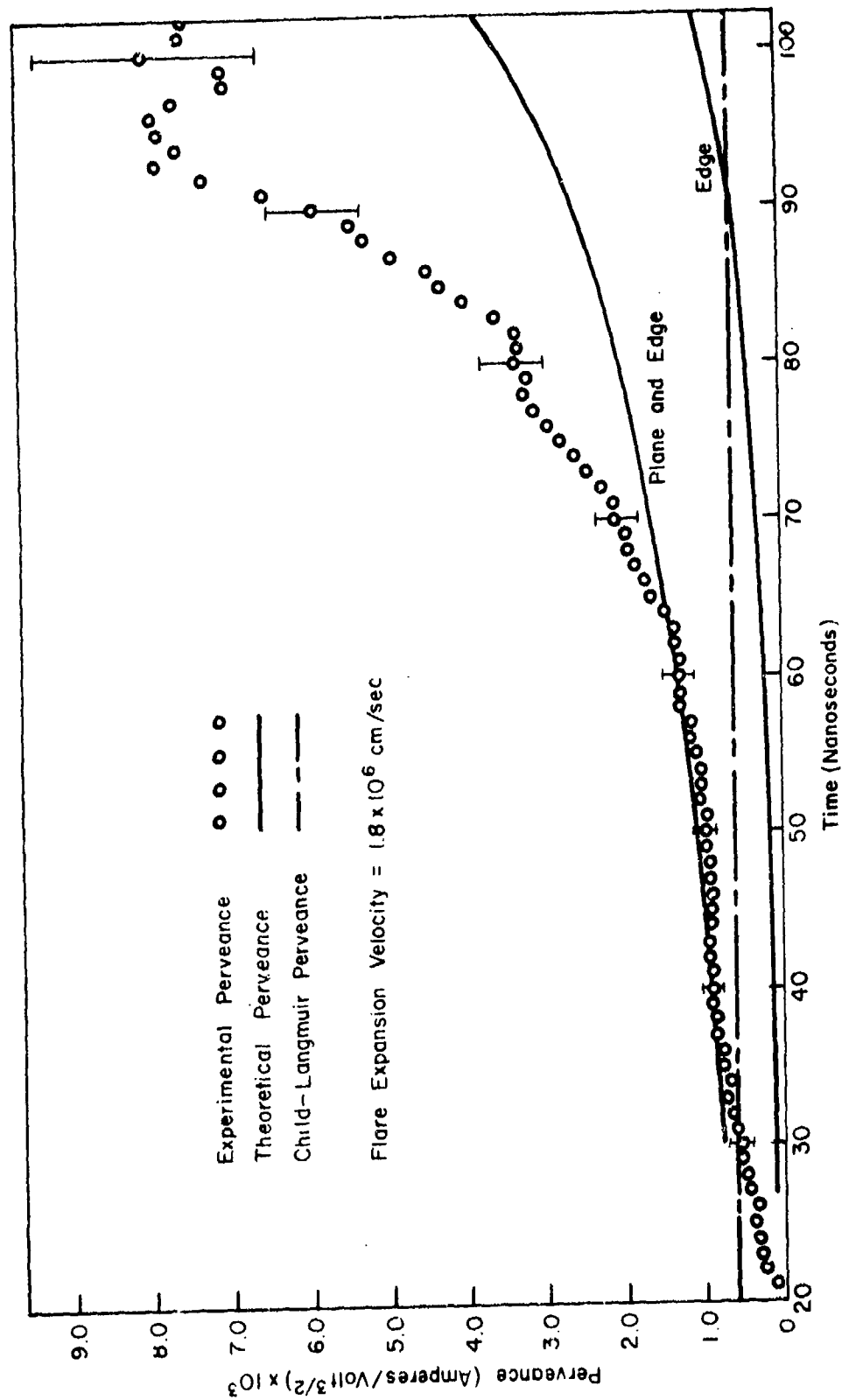
222

Figure 77. Perveance Comparison for the Diode Formed by Positioning a 5.08-cm Diameter Graphite Cathode a Distance of 2.79 mm from a Planar Anode
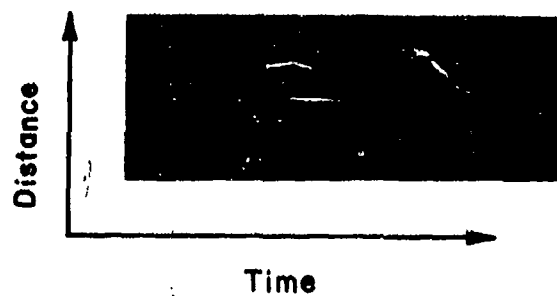
223

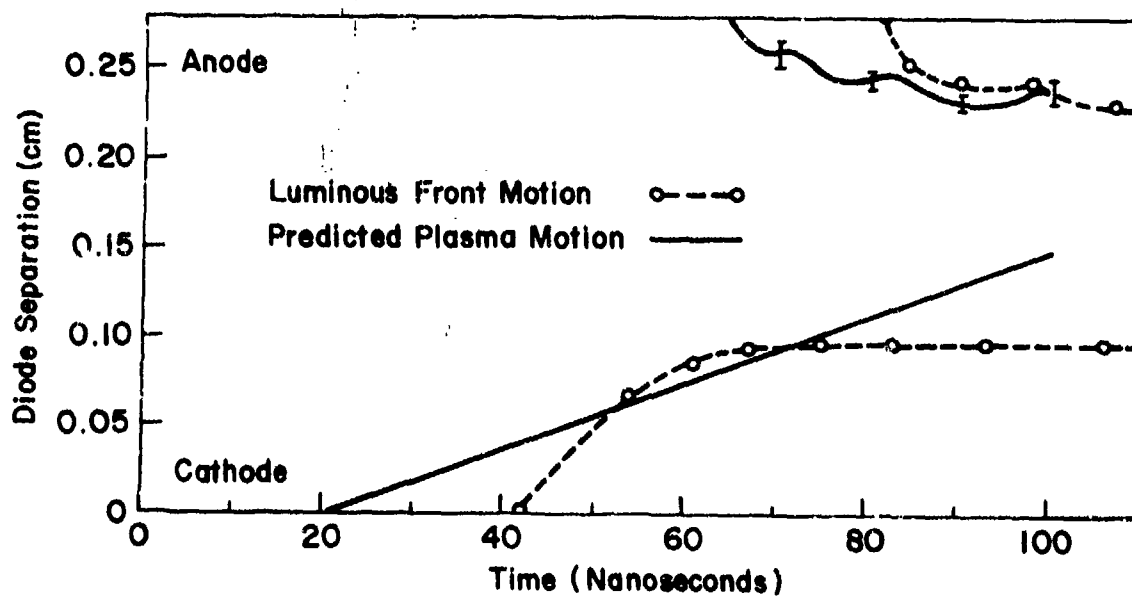Figure 78.   Streak Photograph of Plasma Motion within Diode

Figure 79.   Comparison of Diode Plasma Motion

224

assumption of initial cathode motion followed at some later time by anode plasma formation and expansion.

Since the incident electron flux and the electron kinetic energy were known as a function of time, the time dependence of the front surface dose deposited in the anode could be computed using the procedure described by Spencer (Ref. 78). If the deviation between the experimental and theoretical perveance values can be attributed to the formation of an anode plasma, the absorbed front-surface dose required to produce the plasma could then be noted. Having surveyed the results of the various diode configurations which incorporated a graphite anode, the front-surface dose which corresponded to a divergence in the perveance comparison was found to vary from 80 to 120 cal/cm. Since this range in absorbed dose is more than an order of magnitude less than that required to vaporize graphite, the source of the observed anode plasma was assumed to be adsorbed gases.

Severe self-pinching of the electron beam within the diode would rapidly increase the diode resistance and decrease the perveance. Although the maximum value of the experimental ν/γ was approximately twice the $r_0/2d_0$ of the diode configuration, no such decrease was observed in the perveance data presented in figure 77. To resolve this discrepancy, the experimental ν/γ of the electron beam was compared with the time dependent $r_0/2d(t)$ derived from the effective gap separation which had in turn been unfolded from the perveance analysis. As seen in figure 80, the experimental ν/γ never exceeded the $r_0/2d(t)$. Severe self-pinching should, therefore, not have occurred and the electron trajectories should have been predominantly para-axial.
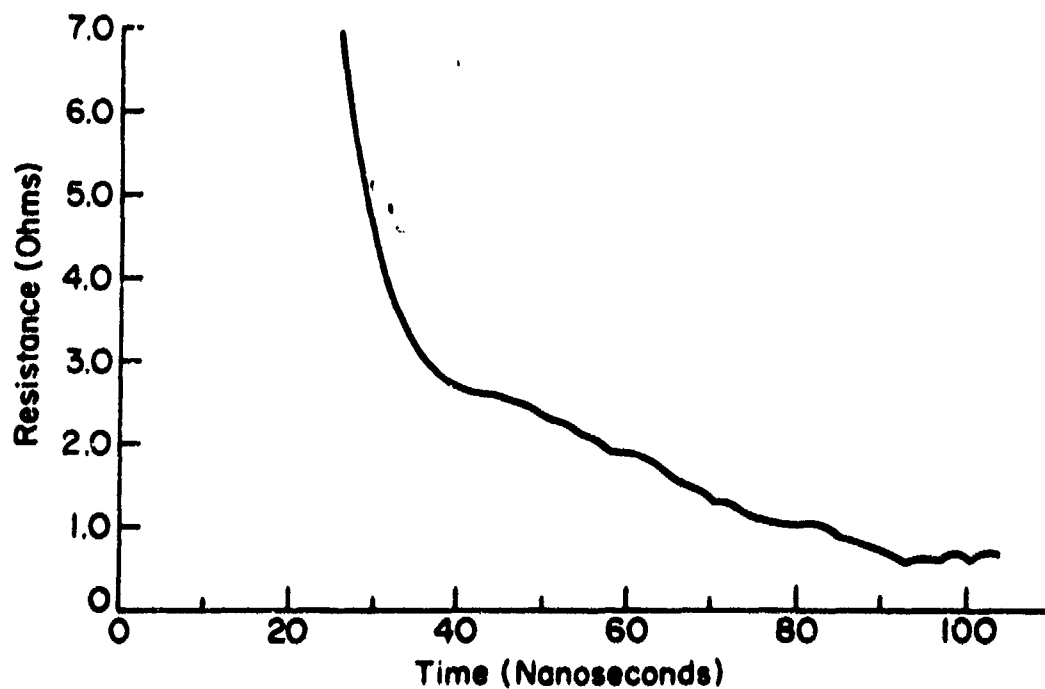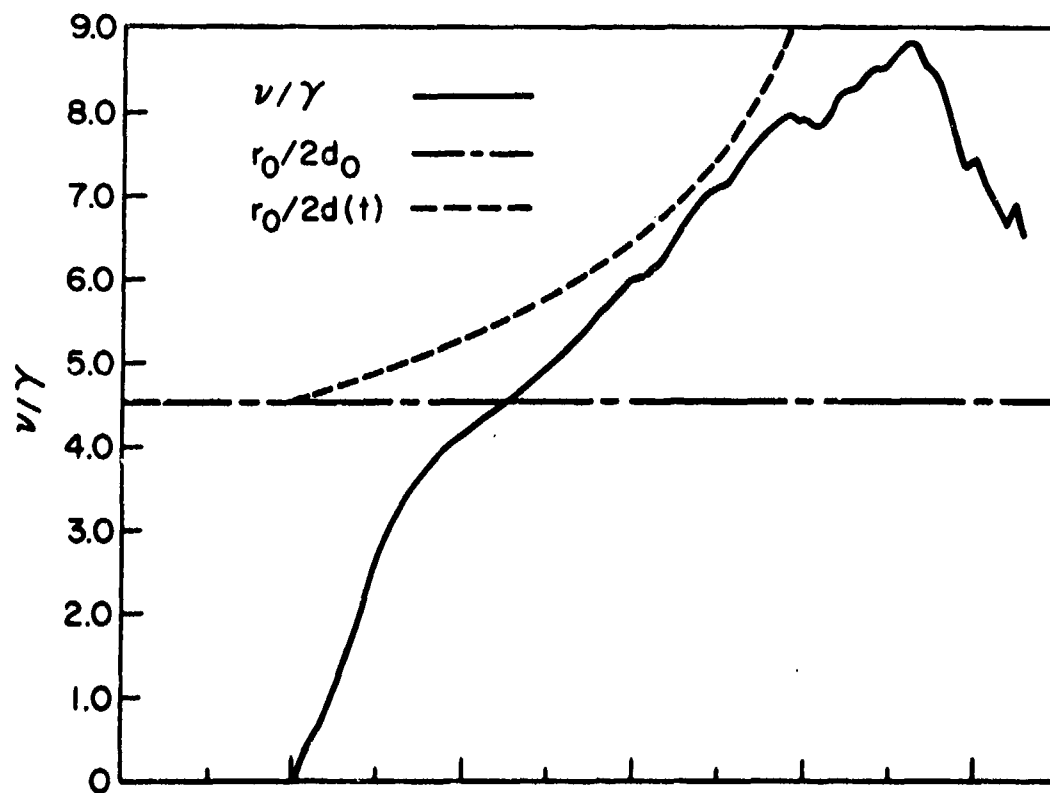
225

Figure 90. ν/γ and Diode Resistance Derived from Corrected Voltage and Current Waveforms; Graphite Cathode: 5.08-cm Diameter; Diode Separation: 2.79 mm

To further substantiate the absence of severe self-pinching, the time dependent current density distribution at the anode plane was monitored by taking a streak photograph of the optical emissions from the attenuator/scintillator assembly. The limited spatial resolution inherent in the image-converter photograph was partially overcome by taking a simultaneous open-shutter photograph of the same image. The resultant photographs are shown in figure 81. A more quantitative measure of the time-integrated current density distribution was provided by the optical densitometer scan shown in figure 82.

A careful time correlation of the streak photograph with the corrected voltage waveform confirmed that the exposure in both photographs corresponded to the 33-nanosecond interval extending from 29 to 62 nanoseconds during which the accelerating potential was at its maximum value. Examination of the streak photograph revealed a 6 percent reduction in the beam radius during this interval. A decrease of that magnitude was judged to have a minimal, if not undetectable, effect on the measured diode perveance, since it would affect primarily the edge emission. As in the first example, the beam radius at the anode was in reasonable agreement with the assumed emission angle of 45 degrees at the cathode periphery. Specifically, the value of 0 corresponding to the distribution shown in figure 82 was 49.8 degrees.

3. OPERATIONAL DIODES

The desired operation characteristics of the accelerator required the definition of a diode configuration which would produce an electron beam with maximum current density and electron kinetic energies in excess of 200 keV. Moreover, the beam was to be capable of uniformly
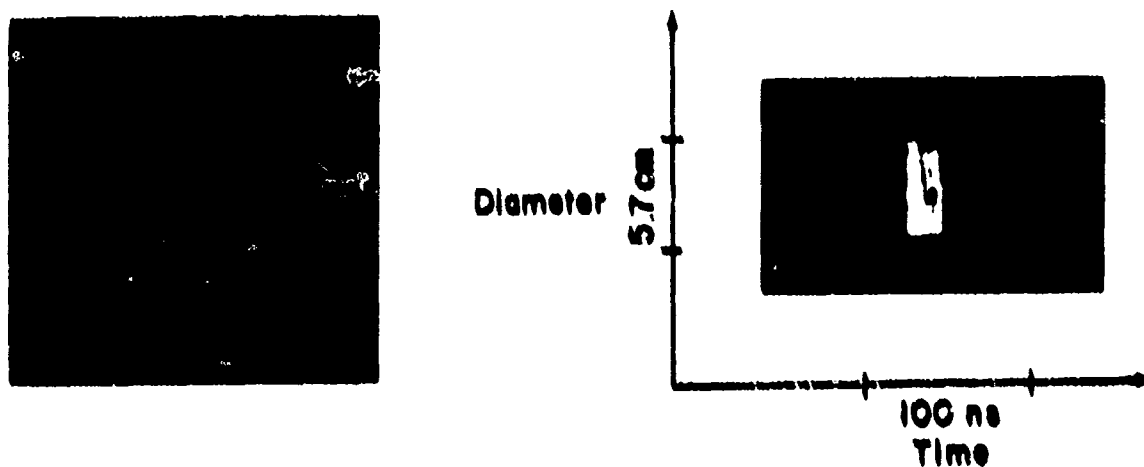
227

Figure 81. Open-Shutter and Streak Photographs of the Current
Density Distribution; Graphite Cathode: 5.08-cm Diameter;
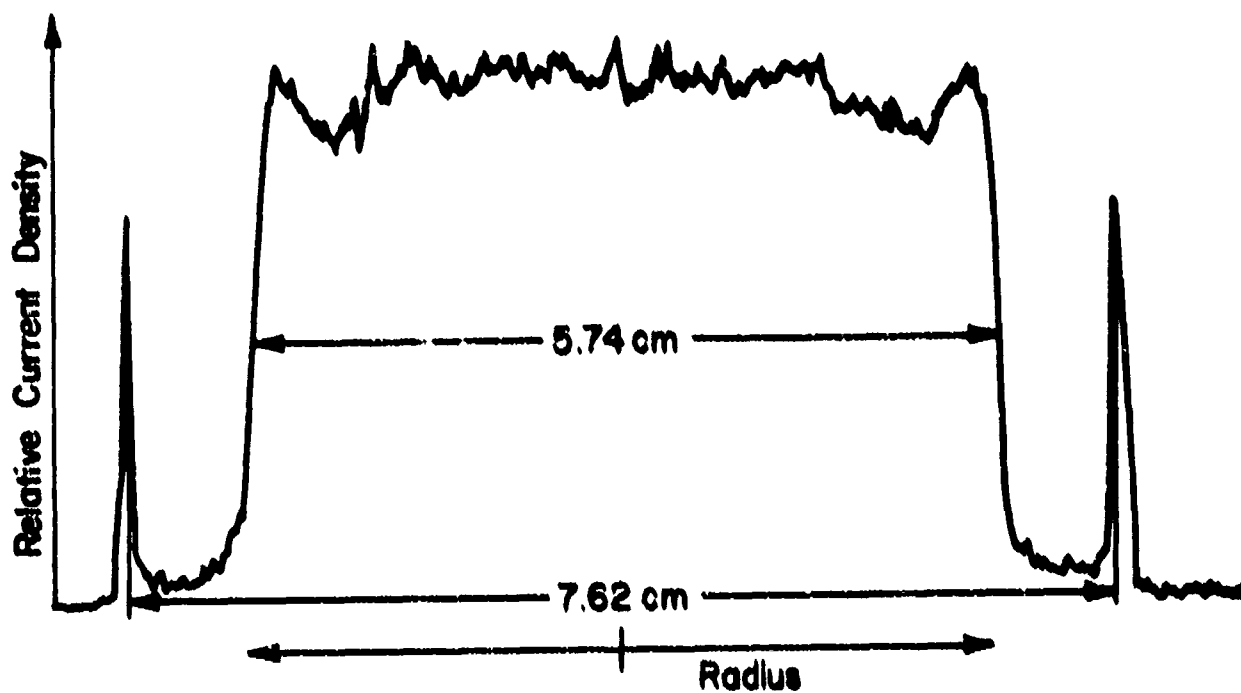Diode Separation: 2.79 mm

Figure 82. Optical Densitometer Scan of the Photographic Negative;
Graphite Cathode: 5.08-cm Diameter; Diode Separation: 2.79 mm

irradiating a cross sectional area in excess of several square centimeters. To satisfy these requirements, two diode configurations based on a fixed cathode-anode gap to cathode were ... tested. The higher resistance diode (~ Ω), formed by positioning the cathode 1.76 mm from the anode, produced a 800 keV electron beam. A lower resistance diode (~ 1 Ω), with the cathode only 0.56 mm from the anode, generated a 700-keV beam.

In the operational configuration, the ... stopping graphite disk had to be replaced by a thin, steel and foil anode. To minimize the electron scatter within the anode foil, aluminized Mylar was used. These two diode configurations merit consideration since both were indicative of the anode effects associated with the use of thin conductive films to define the anode plane. More significantly, the higher resistance diode typified the response of the proposed space charge-limited model, while the lower resistance configuration exhibited a moderate degree of self-pinching.

The corrected voltage and current waveforms obtained by discharging the pulsed power system into the e⁻ diode are shown in figure 83. As seen in figure 84, the proposed perveance model was an excellent match for the experimental values, if the cathode expansion velocity were assumed to be 2.8 × 10⁶ cm/sec. With the exception of the leading edge, the correlation persisted throughout the entire pulse. Since the increased rate of diode closure characteristic of anode plasma expansion was not observed, the anode was assumed to have remained stationary at least until the main accelerating pulse had been completed. The total dose absorbed by the anode during this interval (the first 80

Figure 83. Corrected Voltage and Current Waveforms; Graphite Cathode:
2.54-cm Diameter; Anode: 1/4-mil Aluminized Mylar; Diode Separation:
3.68 mm; System Charging Voltage: 26.0 kV

Figure 84. Perveance Comparison for the Diode Formed by Positioning a 2.54-cm Diameter Graphite Cathode a Distance of 3.68 mm from a Planar, Aluminized-Mylar Anode

nanoseconds of the current pulse) would have been approximately 560 cal/gm. To support the assumption of space-charge-limited flow, unrestricted by the effects of self-magnetic field, the experimental ν/γ is shown in figure 85. Since the ν/γ of the beam remained less than the time dependent $r_0/2d$, self-pinching could not have occurred.

By reducing the electrode separation from 3.68 mm to 2.56 mm, the initial diode aspect ratio was increased from 3.45 to 4.96, and the resistance was reduced by a factor of two. The corrected voltage and current waveforms which characterized the response of the lower resistance diode are shown in figure 86. The experimental values for the diode perveance, derived from these waveforms, are plotted in figure 87.

In contrast to the previous examples of diode perveance which increased monotonically in time, the present diode exhibited a distinctive decrease below the theoretically predicted values at about the time the current reached its maximum value. For the perveance to decrease below a value determined by the diode geometry, the electron flow had to be restricted by an effect not included in the space charge derivation. Should the ν/γ of the electron beam exceed one-half the time dependent diode aspect ratio, beam self-pinching within the diode would disrupt the paraxial flow, and result in an increased resistance. As seen from figure 88, the experimental ν/γ did in fact exceed $r_0/2d(t)$ a few nanoseconds before the decrease in perveance was observed.

Meaningful streak photographs of the current density distribution could not be taken because of the inability of the thin attenuator foils to protect the scintilator from the intense electron beam

232

Figure 85. ν/γ and Resistance Derived from Corrected Voltage and Current Waveforms; Graphite Cathode: 2.54-cm Diameter; Anode: 1/4-mil Aluminized Mylar; Diode Separation: 3.68 mm
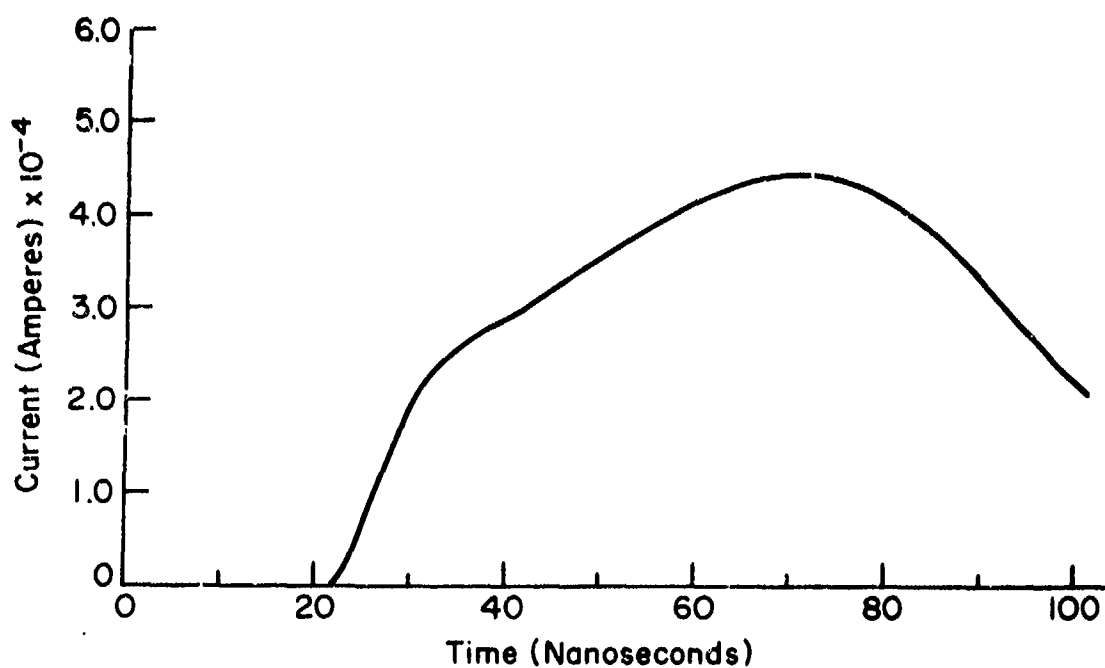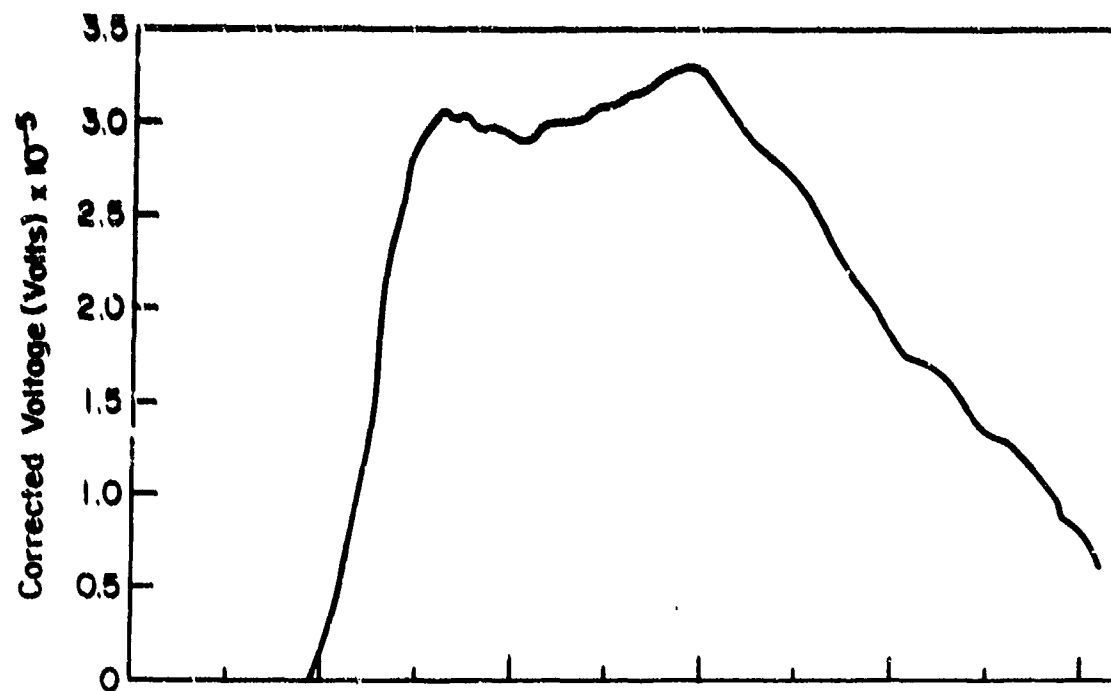
233
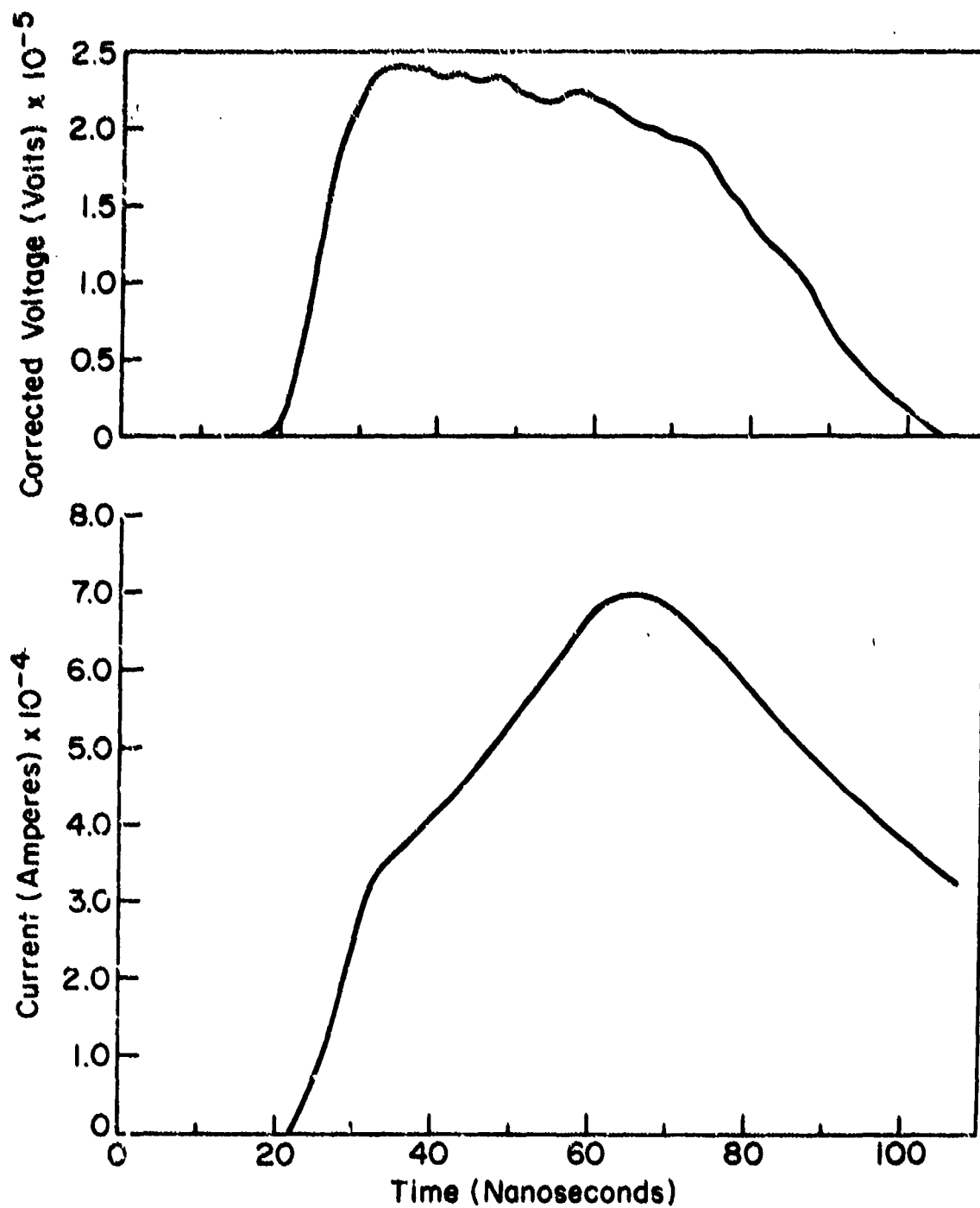
Figure 8b. Corrected Voltage and Current Waveforms; Graphite Cathode:
2.54-cm Diameter; Anode: 1/4-mil Aluminized Mylar;
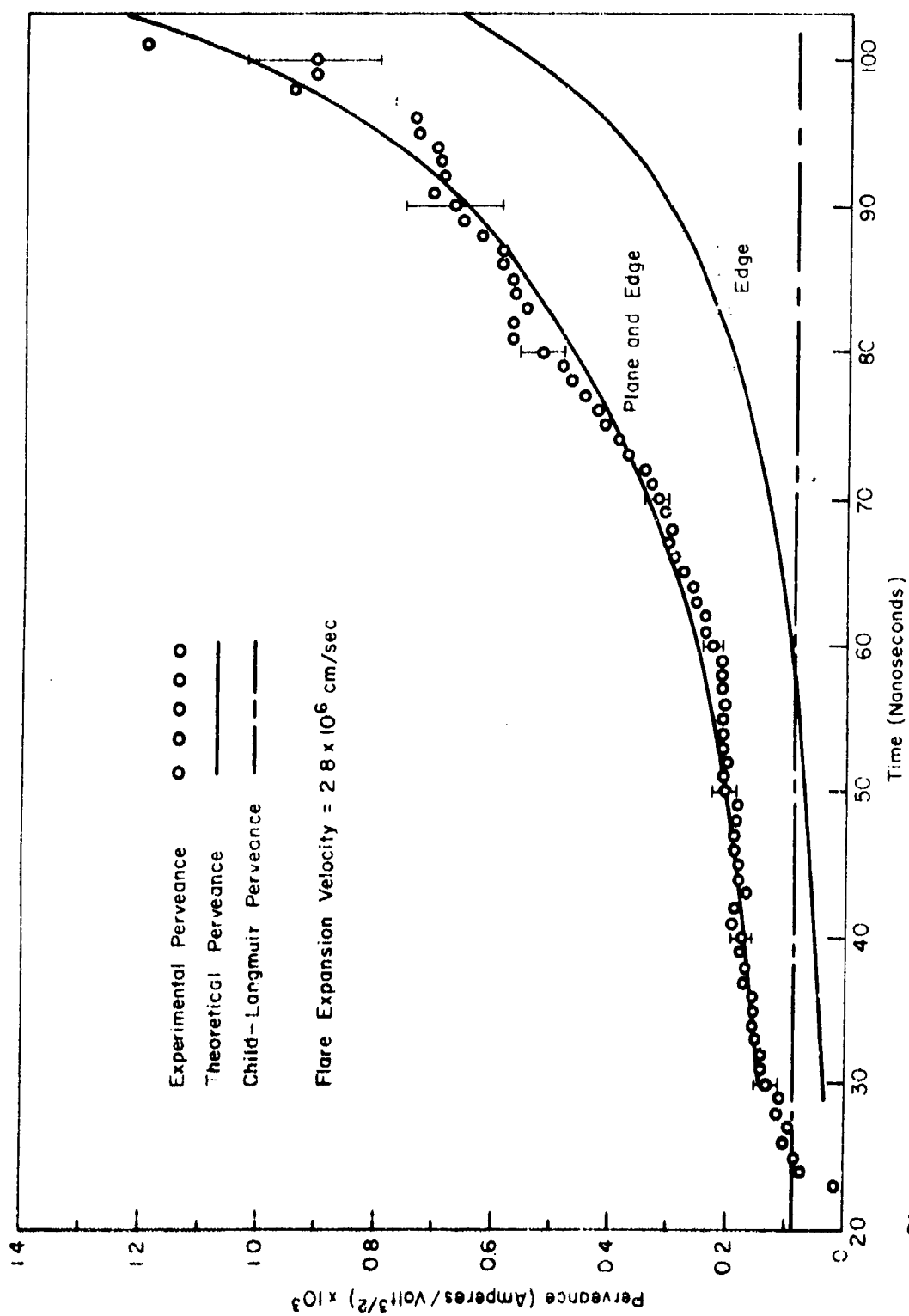Diode Separation: 2.56 mm; System Charging Voltage: 26.0 kV

234
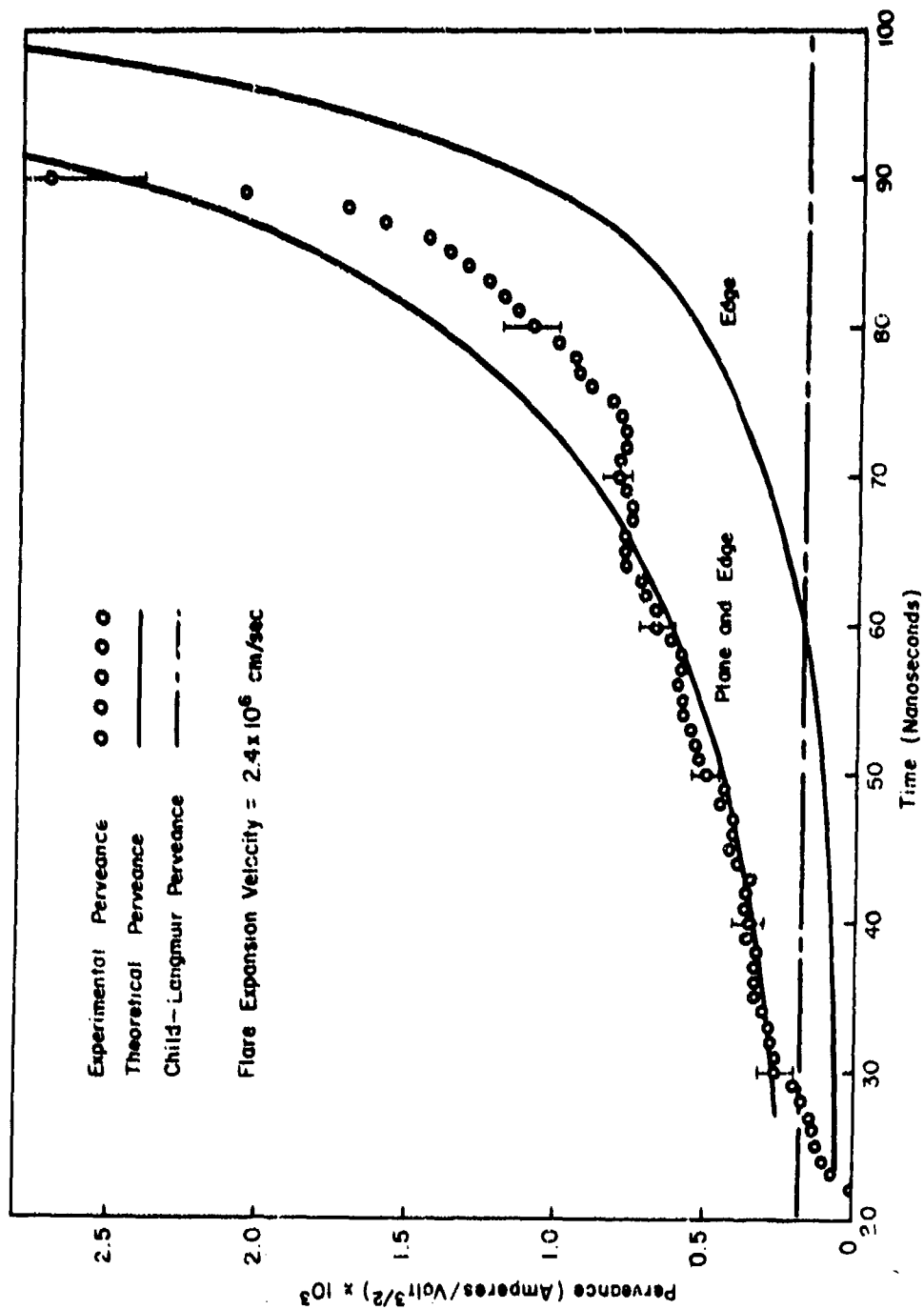
Figure 87. Perveance Comparison for the Diode Formed by Positioning a 2.54-cm Diameter Graphite Cathode a Distance of 2.56 mm from a Planar Aluminized Mylar Anode
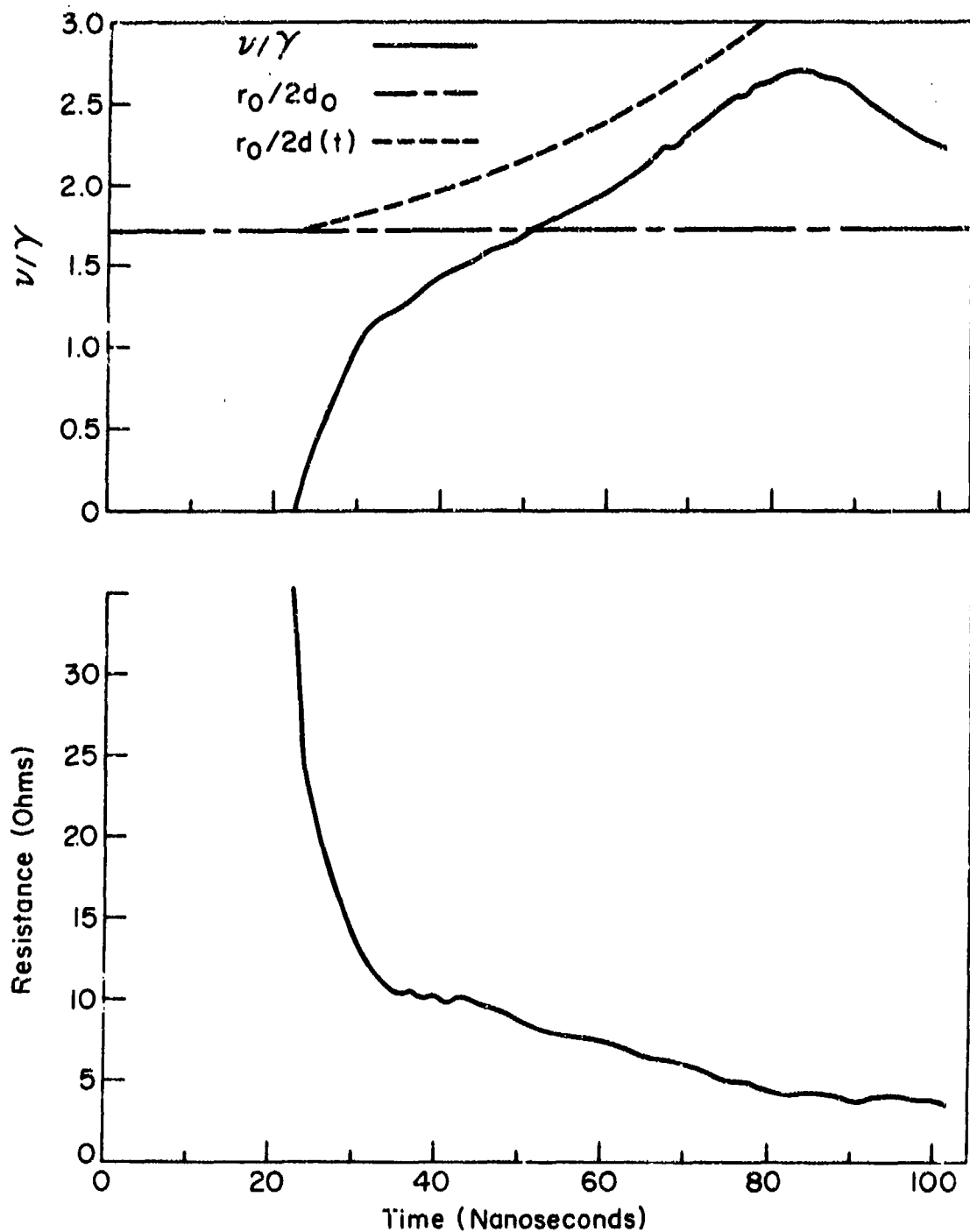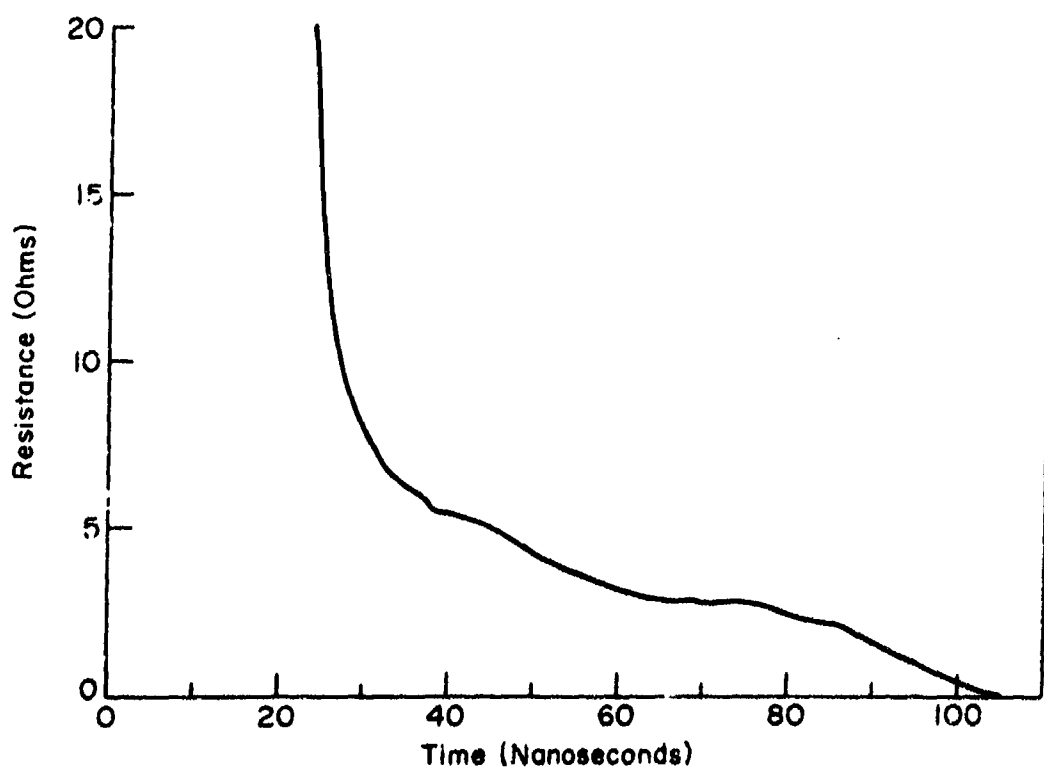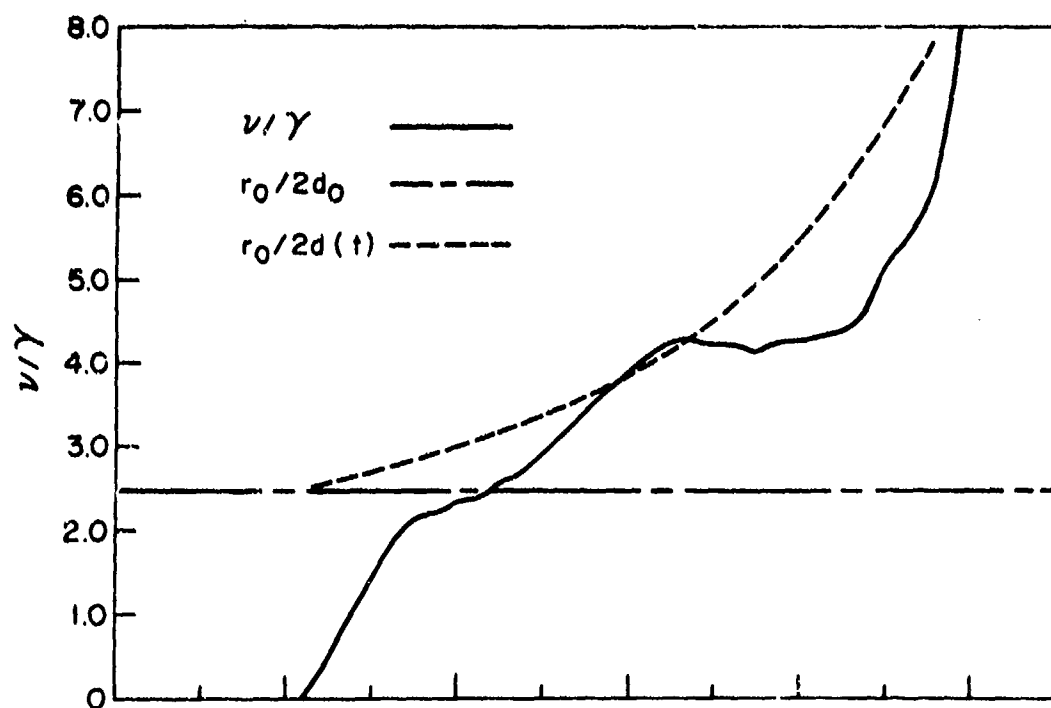
Figure 88. ν/γ and Resistance Derived from Corrected Voltage
and Current Waveforms; Graphite Cathode: 2.54-cm Diameter;
Anode: 1/4-mil Aluminized Mylar; Diode Separation: 2.56 mm

236

generated in this configuration. Nevertheless, qualitative evidence of the pinch was obtained by placing an aluminum witness plate on the anode plane in a separate experiment. Examination of the damage pattern indicated an enhanced energy deposition at radii less than approximately 7 mm. The transition from classical space-charge-limited flow was therefore interpreted as being indicative of the onset of self-pinching. Since this transition occurred within a few nanoseconds after the diode current exceeded the critical value, the self-pinching criterion proposed by Friedlander et al. (Ref. 15) can be considered definitive.

Careful examination of the diode resistance shown in figure 88 indicated the probable existence of anode plasma expansion. Approximately 20 nanoseconds after the onset of self-pinching, the diode resistance began to fall at an increased rate. Extrapolating from the rate of closure determined by the cathode motion, the diode would have become a short circuit at approximately 129 nanoseconds on the common time base. In actuality, the resistance had decreased to zero by 104 nanoseconds. To account for the increased rate of closure, the existence of an expanding anode plasma must be assumed, even though its effect on the observed perveance was masked by the self-pinching. If the initial expansion of the anode plasma were assumed to correspond to the rapid decrease in resistance at approximately 85 nanoseconds, the critical absorbed dose would be on the order of 600 cal/gm.

SECTION VIII

GENERAL OBSERVATIONS AND COMPARISONS
WITH PREVIOUS RESULTS

1. INVARIANCE OF PERVEANCE TO APPLIED VOLTAGE

Early observations of space-charge-limited flow within low-resistance planar diodes were based on qualitative agreement between the diode resistance measured at the instant of maximum current, and the resistance predicted by a simple modification to the infinite-planar Child-Langmuir equation. Using the Child-Langmuir formulation, the diode resistance R in ohms was predicted to be

$$R = 136 \times 10^3 \left(\frac{d_0}{r_0}\right)^2 V^{-1/2} \tag{128}$$

where V is the voltage corresponding to the maximum current in volts, and d_0 and r_0 are, respectively, the physical dimensions of the electrode separation and cathode radius. If the electron flow were space-charge-limited, $R\sqrt{V}$, the reciprocal of the diode perveance, would vary linearly with d_0^2 for a given cathode geometry, and be independent of the amplitude of the accelerating potential.

To relate the present analysis to the results of the previous studies (see for example figure 23), the data obtained by varying the relative position of a 6.35-cm diameter graphite cathode to a planar graphite anode from 1.28 mm to 9.22 mm are presented in figure 89. With the exception of the data point at d_0^2 equal to 0.88 cm^2, the data were in reasonable agreement with the predicted linear dependence on d_0^2. As

238
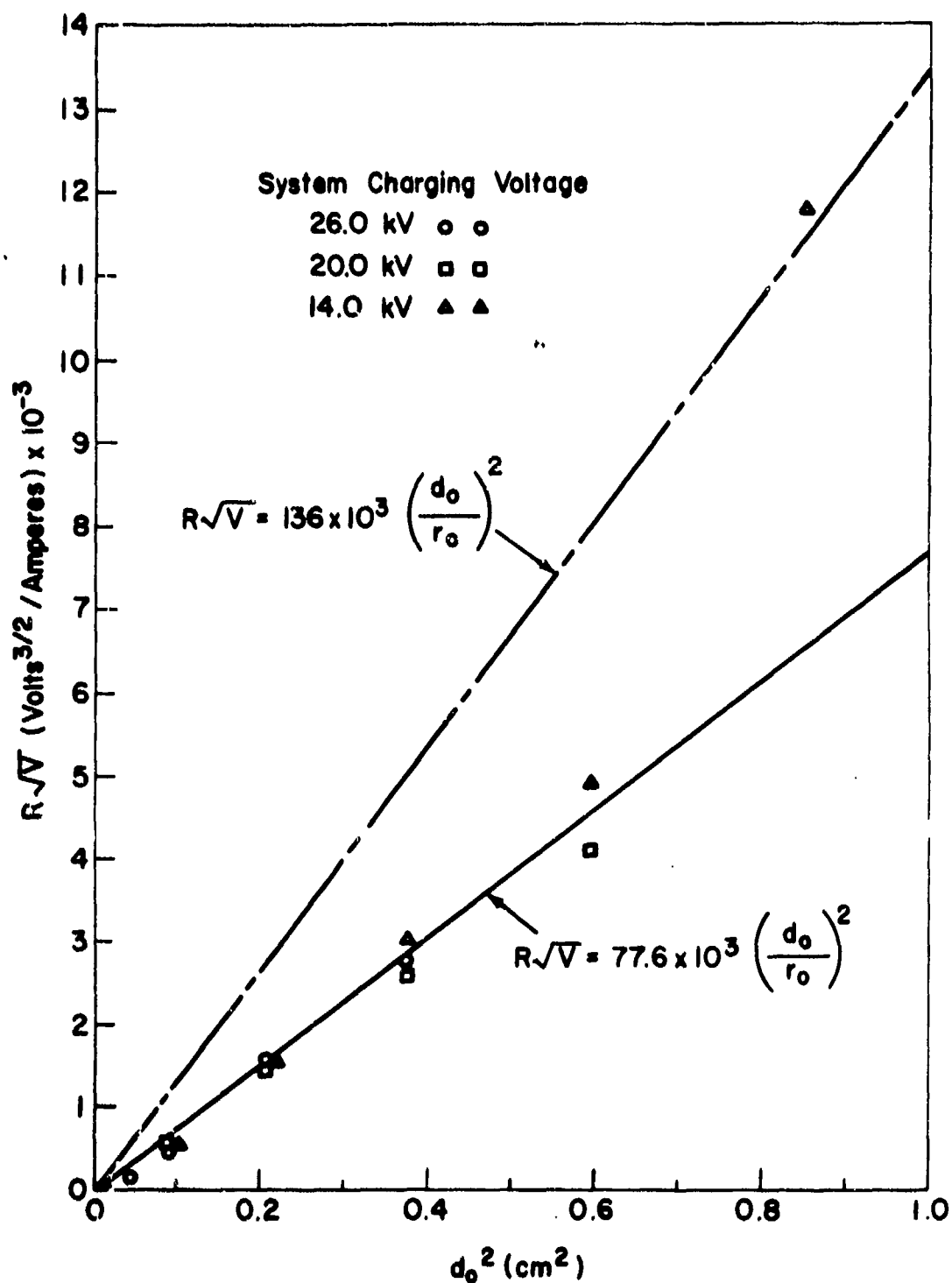
Figure 89. Comparison of $R\sqrt{V}$ with the Infinite-Planar, Child-Langmuir Model

239

noted in the early studies, the slope of the line which provided the best fit with the experimental data was approximately one half that predicted by the simple Child-Langmuir theory. Typically, the decreased resistance was explained by appealing to either plasma effects within the diode or space-charge neutralization resulting from the ionization of residual background gas.

In the preceding section, these qualitative observations were clarified by demonstrating that an excellent correlation between the theoretical and experimental perveance could be achieved by postulating the constant expansion of a highly conductive plasma sheath which acted as the effective cathode surface. Since electron flow from the cathode edge could not be neglected, a perveance term was also included to describe the peripheral flow. To facilitate rapid comparison with the format of figure 89, the Child-Langmuir, infinite-planar perveance has been included in all perveance plots.

a. Space-Charge Neutralization

The contention that the cathode plasma expansion was the dominant mechanism for lowering the diode resistance would be further clarified if the possibility of significant space-charge neutralization could be eliminated. To determine the lower limit for effective ionization of the background gas, the variation in the response of the diode formed by positioning the 6.35-cm diameter graphite cathode 3 mm from the graphite anode was evaluated, as the background pressure was increased from 10^{-5} to 10^{-1} torr. For the initial example, consider the response when the diode region was evacuated to approximately 10^{-5} torr. The corrected voltage and current waveforms obtained by discharging the pulsed-power

240

system charged to 26.0 kV into this diode are shown in figure 90. The experimental perveance derived from these waveforms (figure 91) was in excellent agreement with the assumption of an expanding cathode surface for the first 50 nanoseconds of the pulse, if the plasma expansion velocity were assumed to be 2.3 cm/μsec. The onset of anode plasma expansion, which occurred at approximately 66 nanoseconds on the common time base, corresponded to an estimated anode front-surface dose of about 96 cal/gm. As unfolded from the experimental perveance data, the anode plasma expansion velocity was estimated to be 1.1 cm/μsec.

From the base pressure of 10^{-5} torr, the background pressure was increased in decade increments until an immediate transition to a short circuit was observed. In the range 10^{-5} to 10^{-3} torr, no variation in the diode perveance was observed. When the pressure was increased to 1.5×10^{-2} torr, a small degree of space-charge neutralization was observed after approximately 20 nanoseconds of current flow. At 1.8×10^{-1} torr, the transition to an arc was immediate. In the examples of diode response analyzed in the preceding section, the residual pressure within the diode region was held below 10^{-4} torr. The data shown in figure 91 would, therefore, ensure that space-charge neutralization resulting from the ionization of background gas could not have had a significant effect on the electron flow.

b. Plasma Cathode Formative Time

An uncritical application of the infinite-planar Child-Langmuir theory to the total current flow within a planar diode would require $R\sqrt{V}$ as measured at the instant of maximum current to be invariant to the amplitude of the applied voltage pulse. Although the data in

241
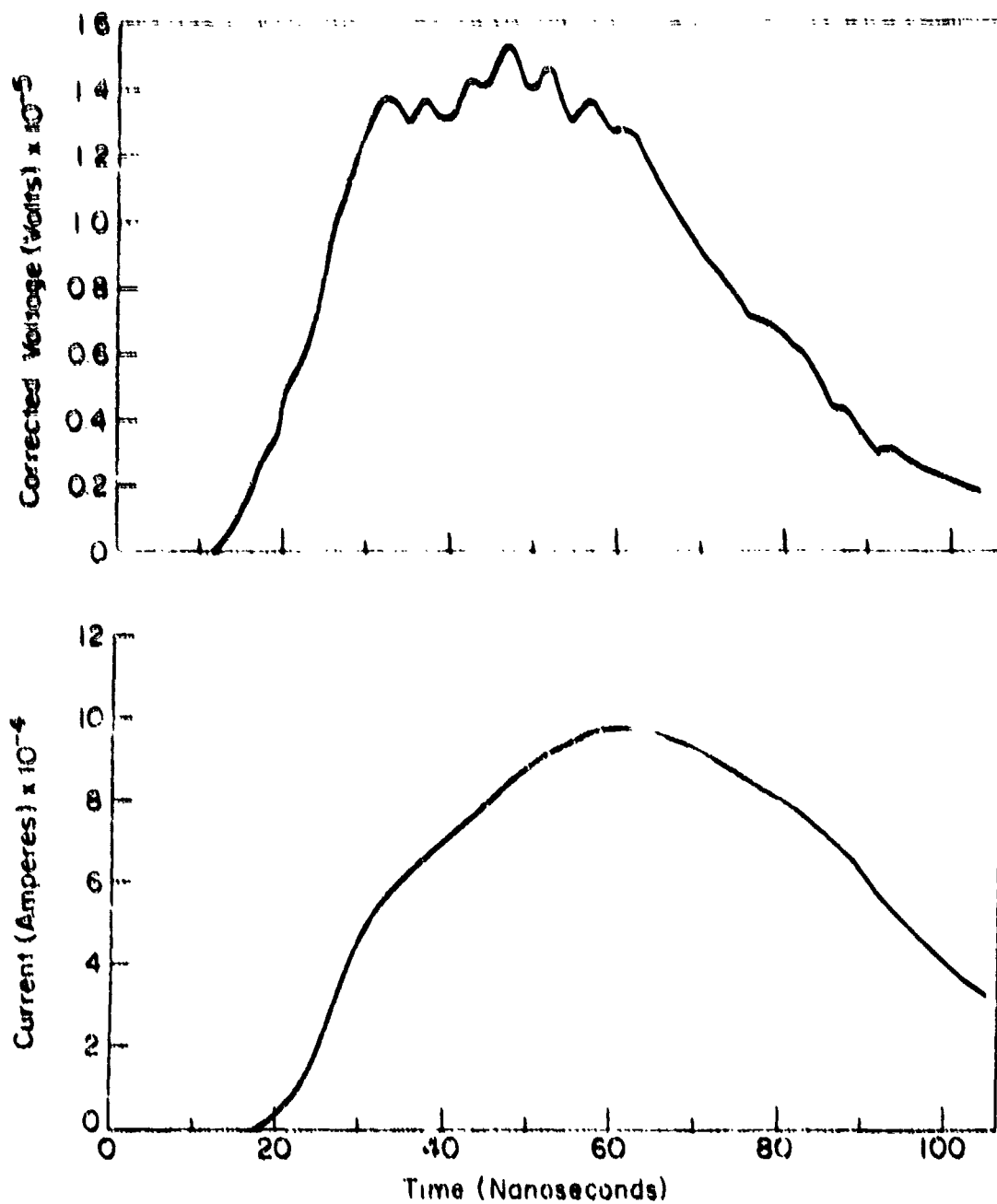
Figure 90. Corrected Voltage and Current Waveforms;
Graphite Cathode: 6.35-cm Diameter; Diode Separation: 3 mm;
System Charging Voltage: 26.0 kV

242
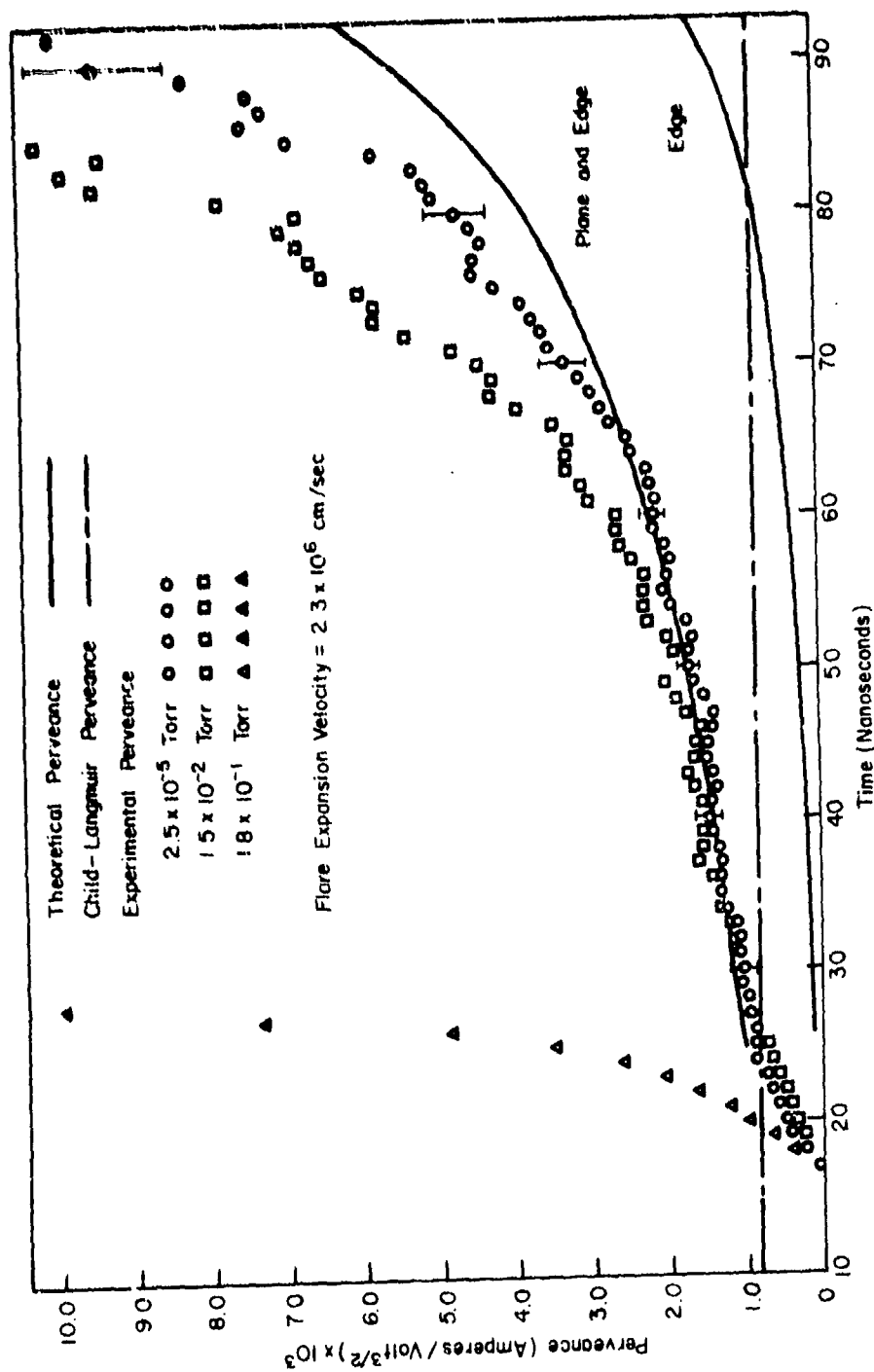
Figure 91. Variation in the Diode Perveance with Increasing Background Pressure

figure 89 supported this corollary of space-charge-limited flow at small electrode separations, an increasing dependence on the voltage amplitude was observed at the larger spacings. The explanation for this apparent deviation from the consequences of space-charge-limited flow has its origin in the derivation of the perveance relation and the plasma nature of the effective electrode surfaces.

In the basic space-charge equations the current density is the dependent variable. To apply these expressions to the total electron flow from a broad-area cathode, a uniform emission density is normally assumed for the entire cathode surface. Since the effective emission surface is not the cold surface of the cathode, but rather the plasma sheath formed by the expanding cathode flares, the plasma sheath must rapidly cover the entire cathode for this assumption to be valid.

After the plasma sheath formation is completed, the perveance is dependent only on the diode geometry. If at some time during the pulse an anode plasma were to result from either the vaporization of anode material or ionization of adsorbed molecules, the effective electrode surfaces would both be plasma in nature. The observed time dependence in the diode perveance must, therefore, be related to the formation and motion of these electrode plasmas.

To demonstrate the invariance of the diode perveance to the voltage amplitude in a manner which incorporates the plasma formative times, consider the effects of a reduced voltage waveform incident on the diode configuration used in the preceding paragraphs to illustrate the pressure dependence of space-charge neutralization. The reduction in the amplitude of the voltage pulse was accomplished by limiting the

244

system charging voltage to first 14.0 kV and then 20.0 kV. The corrected voltage and current waveforms which resulted are shown in figures 92 and 94, respectively. The derived perveance plots are presented in figures 93 and 95. The waveforms which resulted when the charging voltage was increased to 26.0 kV were shown in figure 90. To assist a more detailed comparison, the resultant perveances corresponding to the three incident voltage waveforms are superimposed in figure 96. For this comparison, the time base was adjusted so that the onset of first measurable current in each case would be coincident.

Although the perveances were quite similar, subtle differences could be noted. From the arguments presented above, these differences must be interpreted as the consequence of causal relationships between the applied voltage waveform and the formation and subsequent energetics of the electrode plasmas. To illustrate these relationships, the time evolution of the diode perveance must be considered in detail.

The onset of first measurable current has been attributed to the explosion of the most intensely emitting whiskers. By maintaining the same diode configuration throughout the three experiments, all macroscopic field enhancements were held constant. Furthermore, the extremely large number of whiskers present on the cathode surface would ensure that the enhancement at the tips of the dominant whiskers would not vary significantly from set to set. If the relationship between the applied voltage and the microscopic field remained constant, the applied voltage at the instant of first measurable current would have been identical in each case. In actuality, the appropriate breakdown voltage averaged 3.1×10^4 volts with a variance of $\pm 0.2 \times 10^4$ volts.

245
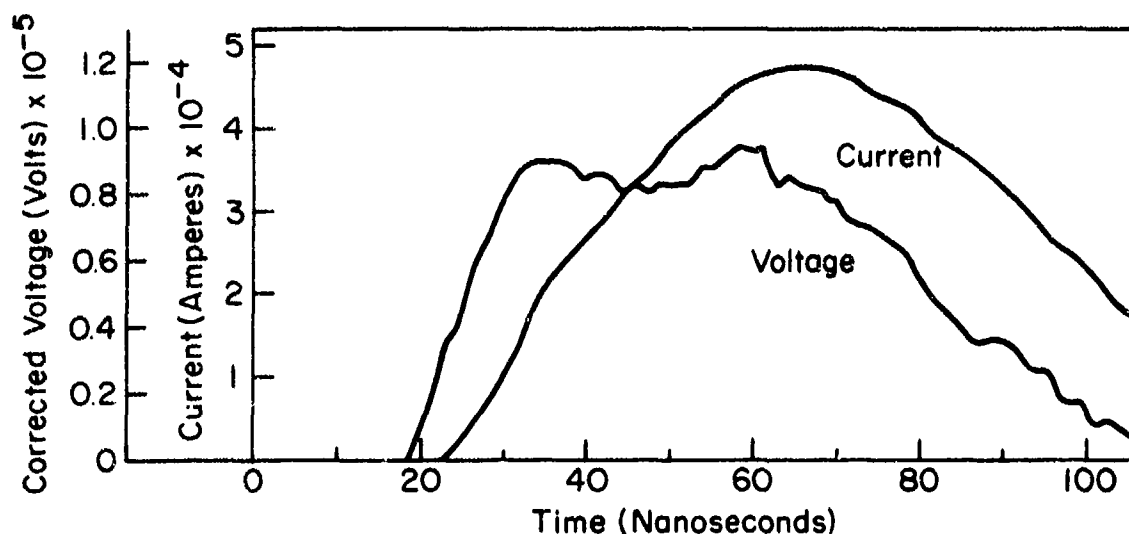
Figure 92. Corrected Voltage and Current Waveforms;
System Charging Voltage: 14.0 kV
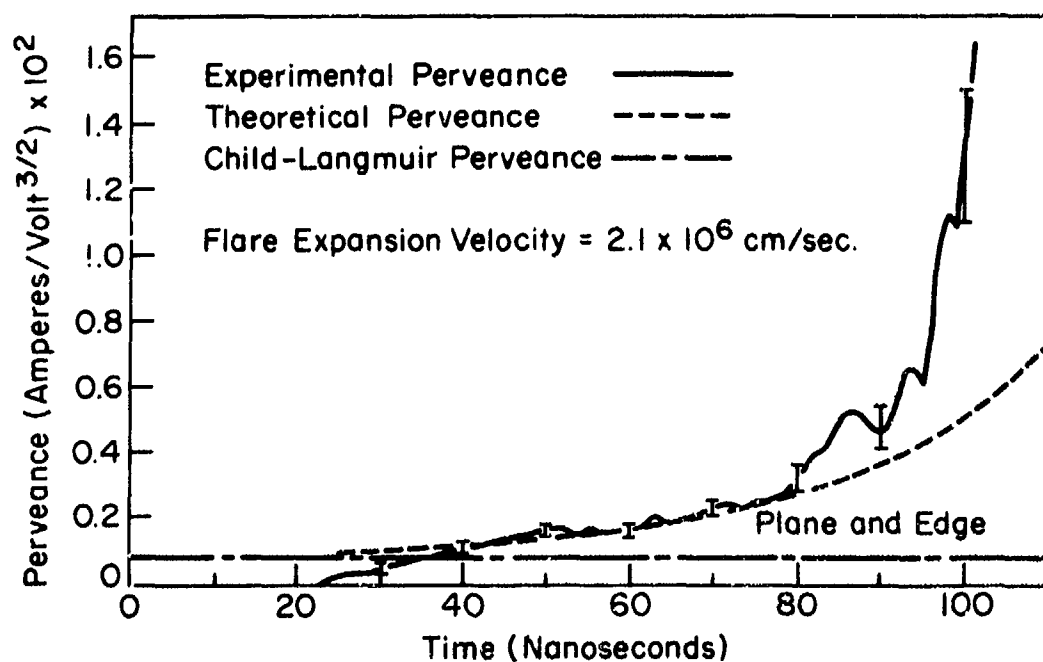
Figure 93. Perveance Comparison; Graphite Cathode:
6.35-cm Diameter; Diode Separation: 3 mm

246
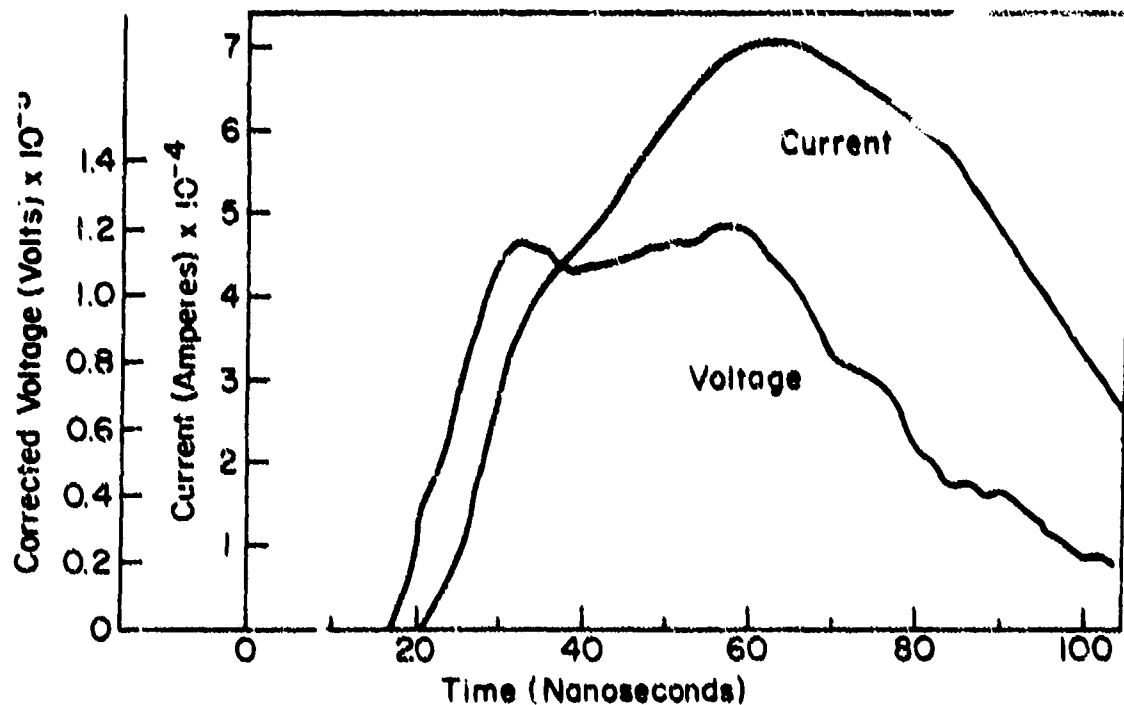
Figure 94. Corrected Voltage and Current Waveforms;
System Charging Voltage: 20.0 kV
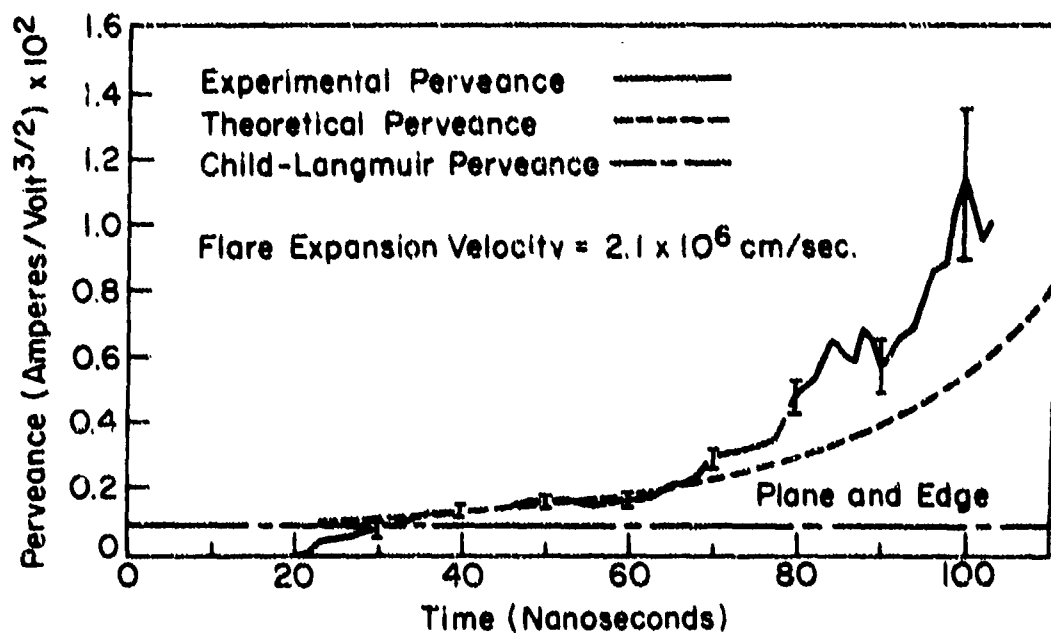
Figure 95. Perveance Comparison; Graphite Cathode:
6.35-cm Diameter; Diode Separation: 3 mm

247

Figure 96. Invariance of Perveance to Applied Voltage

In the Soviet studies, the delay between the application of a pulsed, fast-rise-time electric field in excess of the critical breakdown value, and the formation of the initial cathode flare was found to be an extremely sensitive function of the microscopic field. The time interval between the initial flare formation and flare plasma merger to form a uniform emission surface covering the entire cathode should exhibit a similar dependence. For convenience, this interval was defined as the plasma sheath formative time. To measure this interval, the plasma sheath was assumed to be complete when the experimental perveance first reached a value corresponding to uniform emission from the entire cathode face and edge. From figure 96, the plasma sheath formative time for the diode under consideration was found to vary from approximately 8 to 19 nanoseconds.

Since the voltage rise time was on the same order as the sheath formative time, a correlation between the formative time and a unique value for the applied field could not be derived. The desired relationship could be estimated, however, by using the peak voltage at the leading edge of the pulse to calculate an average field at the cathode surface. With this approach, a representative set of data was compiled for graphite cathodes ranging from 2.54 cm to 6.35 cm in diameter. The results of this compilation are shown in figure 97. The primary conclusion to be drawn from this presentation is that fast cathode "turn-on" times are achieved for graphite if the average applied field is in excess of 4×10^5 volts/cm.

The gradual divergence in $R\sqrt{V}$ observed in figure 89 as the diode separation increased can now be interpreted as the result of

249
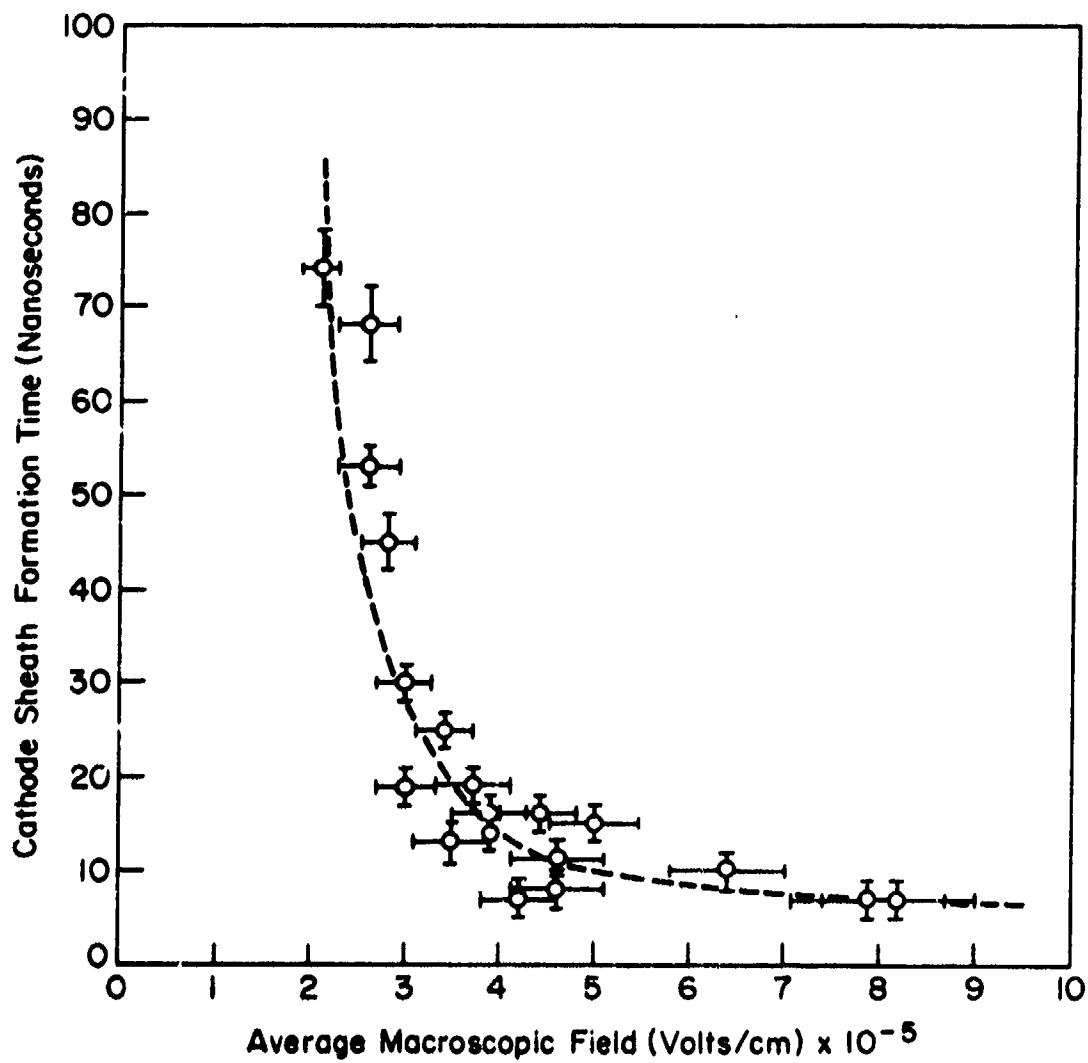
Figure 97. Dependence of Sheath Formative Time on
Average Macroscopic Electric Field

increasingly limited sheath formation as the applied field was decreased. This hypothesis was substantiated by a more detailed analysis of the corrected voltage and current waveforms (see figure 98) which represented the most divergent data point in the $R\sqrt{V}$ plot shown in figure 89. To obtain these waveforms, the pulsed-power system, charged to 14.0 kV, was discharged into a diode in which the electrode separation had been increased to 9.2 mm. As seen from the perveance plot included in figure 98, the cathode edge was the dominant source of electron emission throughout a large fraction of the pulse.

In figure 96, there is an interval of time after the plasma sheath has formed in which the electron flow in the three experiments can be described as space-charge-limited emission from a constantly expanding plasma cathode. To obtain a best fit with the experimental data throughout this interval, the plasma velocity was used as an independent variable. Within this set of experiments, the "best fit" velocities were found to vary from 2.1×10^6 cm/sec to 2.3×10^6 cm/sec. A compilation of data from many diode configurations using graphite cathodes indicated a range in velocities from 1.8 cm/μsec to 2.8 cm/μsec.

c. Dependence of the Flare Expansion Velocity on (F/t)

The justification for fitting the predicted perveance to the experimental data by adjusting the plasma expansion velocity would be further strengthened if a functional relationship between the derived velocities and some property of the applied voltage waveform could be established. Such a relationship was reported in the Soviet studies. Using etched, single-crystal, tungsten emitters, Mesyats et al. were
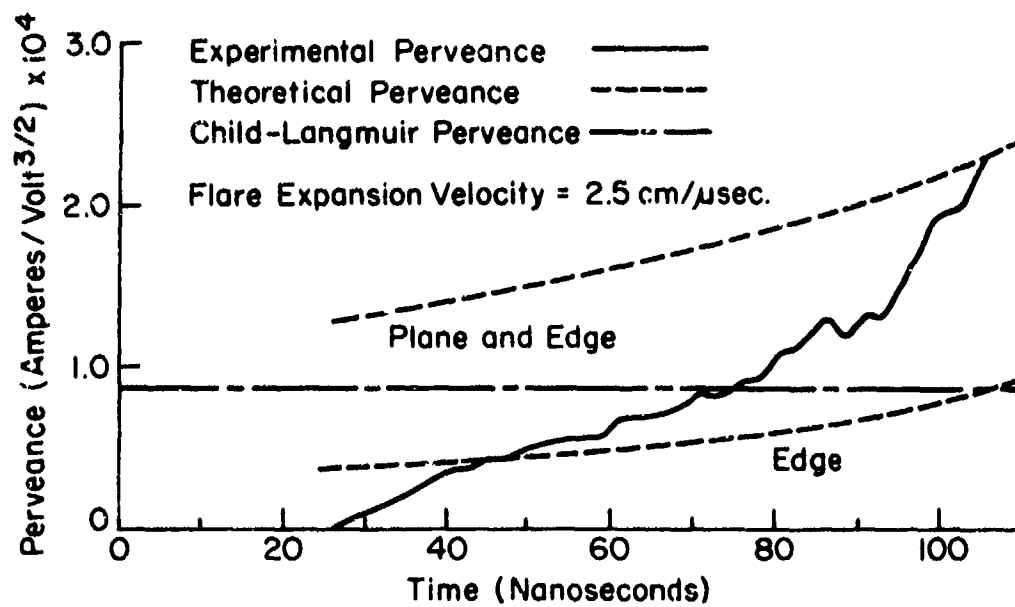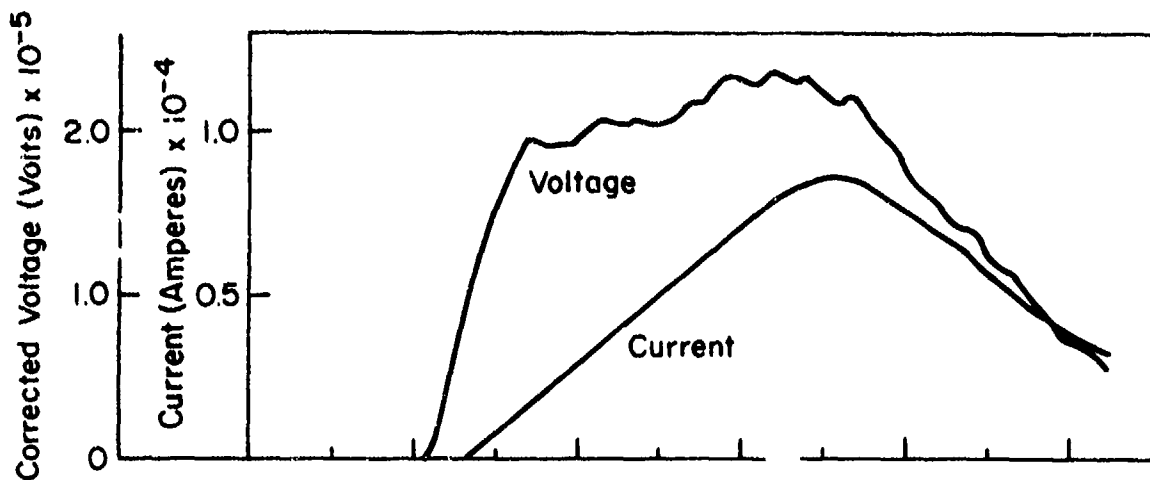
Figure 98. Corrected Voltage Current and Perveance;
Graphite Cathode: 6.35-cm Diameter; Diode Separation:
9.2 mm; System Charging Voltage: 14.0 kV

able to demonstrate a slight dependence of the flare expansion velocity on the rate of increase in the applied microscopic field (see figure 19). To establish a unique relationship, their experimental parameters were adjuster to that the emitter would explode during the 1-nanosecond rise in the pulsed field.

A similar analysis of the expanding plasma sheath covering a broad-area cathode would be weakened by several significant uncertainties. First, if the whisker explodes during the leading edge of the voltage pulse, the specific energy evolved at the tip before it explodes is determined by the rate of increase in the microscopic field. In the experiment using single-point emitters, the relationship between the applied voltage pulse and the microscopic field at the tip of the emitting point was known. With a broad-area cathode, the initial field emission will occur at the tips of a very large number of whiskers having varying degrees of field enhancement. To estimate the total effective enhancement and, hence, the microscopic field operative on each of a large number of emission sites, one must assume that the sites which initiate breakdown are those with the largest enhancement, and that within this subset the variation in specific enhancement is small. These assumptions were not unreasonable in view of the small degree of scatter in the Alpert total enhancement data used in the preceding section to relate the amplitude of the applied voltage pulse to the effective microscopic field.

By using a single-point emitter, the expansion of a single cathode flare, created under known conditions, was observed in the Soviet studies. For a broad-area cathode, the plasma sheath represents

the average expansion of an extremely large number of cathode flares. The average expansion velocity derived from the perveance analysis can, therefore, be related only to an effective rate of increase in the microscopic field acting on many single-point emitters.

In spite of these uncertainties, there was some evidence that a definitive relationship could be established between the applied macroscopic field and the expansion velocity of the plasma sheath. Throughout the diode study, the reproducibility of the derived plasma sheath expansion velocity was typically ± 0.1 cm/μsec for a specified set of diode parameters (cathode diameter, electrode separation, and system charging voltage). Furthermore, Mesyats observed a unique dependence of the time delay before initial flare formation on the magnitude of the applied macroscopic field. This dependence was effectively used in the preceding section to predict the onset time of first measurable current.

The effects of the applied voltage pulse-shape on the subsequent energetics of the expanding plasma sheath were evaluated by comparing the derived expansion velocity with the maximum rate of increase in the microscopic field during the leading edge of the corrected voltage waveform. The conversion from macroscopic to microscopic field was accomplished by using the Alpert enhancement curve. The data included in this compilation were limited to those diode configurations in which the plasma sheath formation was completed during the rise time of the corrected voltage. The results of this compilation are shown in figure 99. For comparison, the broad-area graphite cathode data has been plotted with the single-crystal tungsten data reported by Mesyats. The

254
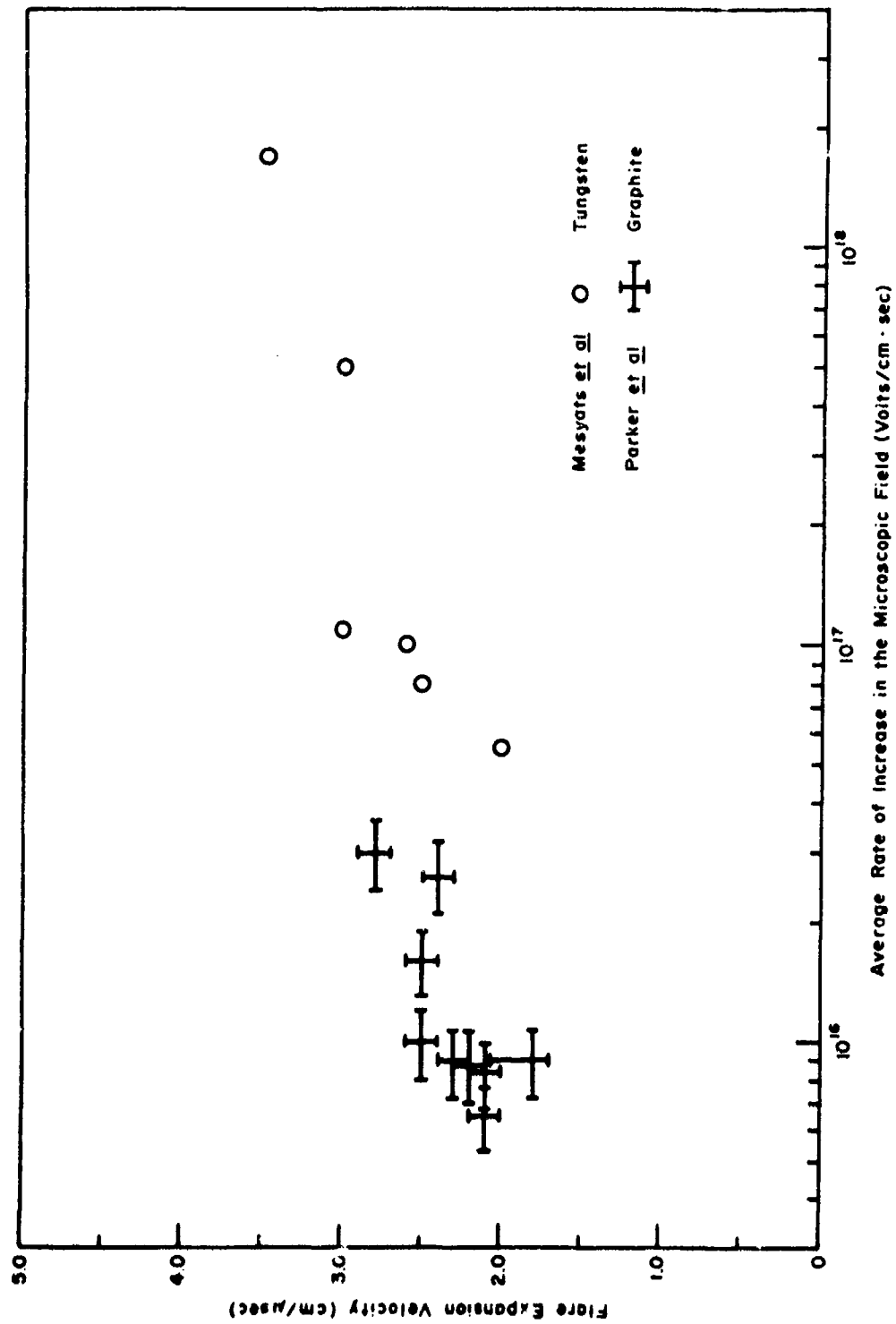
Figure 99. Dependence of the Flare Expansion Velocity on the Average Rate of Rise in the Microscopic Electric Field

255

relative position of the two data sets was as expected since the graphite emitters would explode much more quickly for a given applied field. One should not attempt to describe the two data sets by a single continuous curve. In both cases, however, the plasma expansion velocity exhibited a slight increase with higher rates of rise in the microscopic field.

d. Critical Dose for Anode Plasma Formation

One final topic remains to be considered relative to the perveance comparison in figure 96. Regardless of the amplitude of the applied voltage pulse, the experimental perveance late in the pulse was observed to diverge from that predicted by assuming only cathode plasma motion. In previous discussion, this divergence has been attributed to the initial expansion of an anode plasma. From figures 93, 95, and 91, the initial divergence resulting from anode motion was observed to occur at varying intervals following the onset of measurable current. For the assumption of anode plasma formation to be valid, the total dose deposited at the front surface of the graphite anode prior to the formation of the anode plasma should have been independent of the accelerating voltage and the total beam current. Using the procedure described by Spencer, the time dependent front surface dose was calculated for each case. In order of increasing accelerating voltage, the values of critical dose at the instant of the initial divergence in the experimental from the theoretical perveance were found to be 82, 76, and 96 cal/gm, respectively. From the experimental perveance data, the anode expansion velocities were estimated to range from approximately 1.1 cm/μsec to 2.2 cm/μsec.

2. ANALYSIS OF ELECTRON FLOW

The interrelationship between the space-charge-limited and self-pinch-limited modes of electron flow within the diode are shown in figure 100. Since the expressions for parapotential flow (equation (129)), and the self-pinching criteria (equation (13)) are both linearly dependent on the diode aspect ratio, the presentation of the diode voltage-current characteristics was simplified by expressing the total electron current as the ratio of current to aspect ratio. To further simplify the comparison, the infinite-planar, Child-Langmuir equation was assumed to represent space-charge-limited flow. Negligible error will be introduced by this assumption if the diode aspect ratio is much greater than one. The Child-Langmuir equation has a quadratic dependence on the aspect ratio and therefore appears as a family of straight lines if a semilogarithmic format is used.

A diagram of this type could readily be used to predict the resistance and mode of electron flow within a high-aspect-ration diode if the time dependence of the diode geometry were included. As emphasized throughout the preceding discussions, the existence of an expanding plasma sheath covering the cathode surface is a prerequisite to the emission of the intense electron currents associated with the operation of cold-cathode, relativistic electron accelerators. Even if the formation and subsequent expansion of an anode plasma could be suppressed, an increase in the diode aspect ration would result from the constant expansion of the cathode plasma. An analysis of the electron flow must therefore include the effects of diode closure if possible errors in interpretation are to be avoided.

257
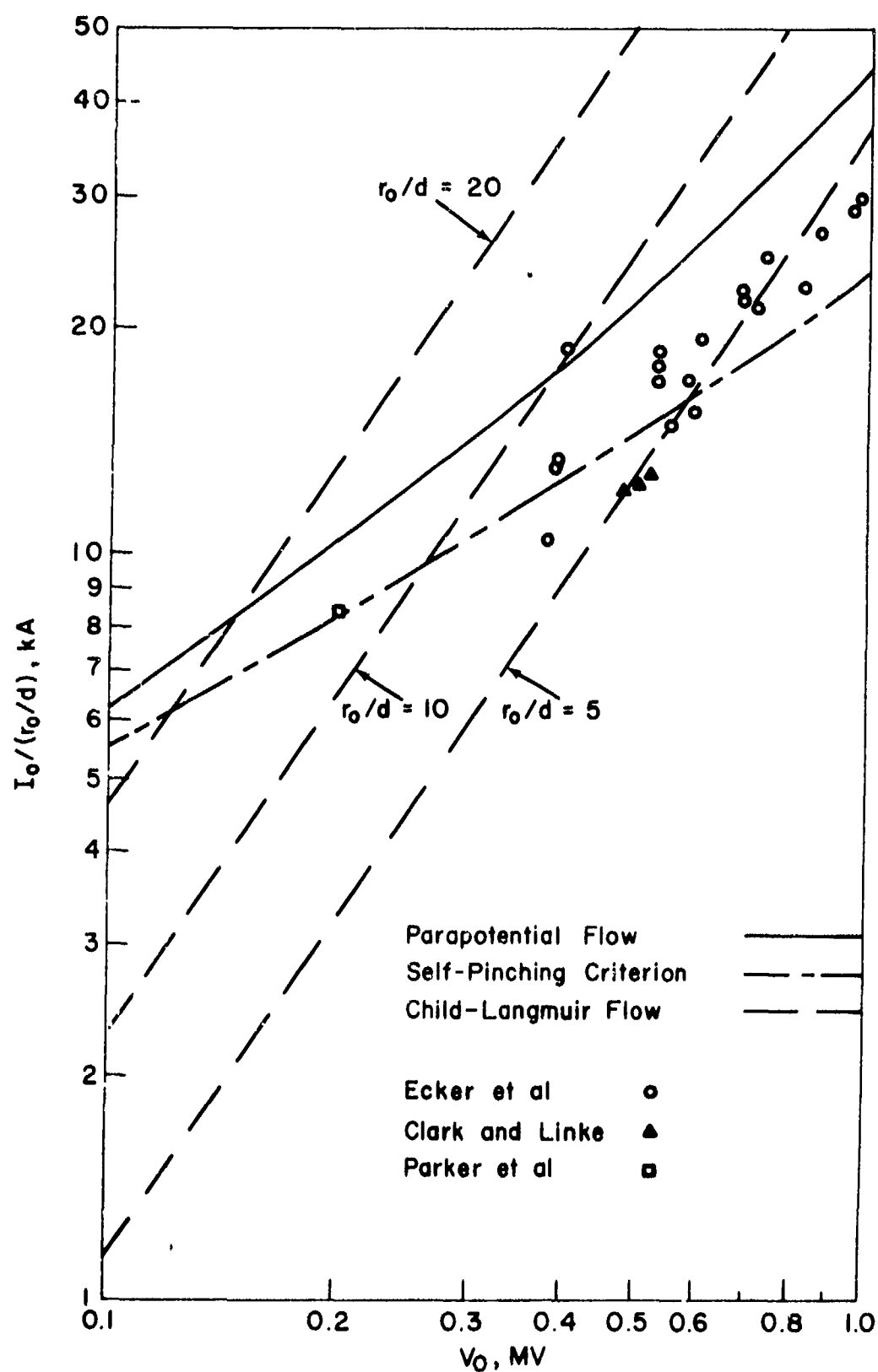
Figure 100. Relationship between Space-Charge-Limited and
Self-Pinching-Limited Modes of Electron Flow

While the total current remains below the critical self-pinching value, the electron flow within the diode can be accurately predicted by the appropriate space-charge expressions if the time dependent diode geometry is properly defined. If the applied voltage is increased until the space-charge-limited current exceeds the self-pinching criterion, the electron flow will become dominated by the self-magnetic field. It should be noted, however, that the increase in current with voltage need not be restricted to a fixed value of r_0/d. If the time required for this transition is on the order of d_0/v, the trace corresponding to the diode response will shift to higher values of r_0/d as time progresses.

To date the only analytical model for electron flow in excess of the self-pinching criterion has been based on the concept of parapotential flow. By idealizing the distorted equipotentials within the diode into concentric conical surfaces with apexes collocated at the intersection of the diode axis and the anode plane, Creedon (Ref. 59) was able to derive the following expression

$$I_{max}/(r_0/d) = 8500\, \gamma_{max}\, \ln\left[\gamma_{max} + \left(\gamma^2_{max} - 1\right)^{1/2}\right] \qquad (129)$$

where I_{max} is the maximum value of the diode current, $\gamma_{max} = 1 + eV_{max}/m_0c^2$, and V_{max} is the accelerating voltage which corresponds to I_{max}. According to Ecker et al. (Ref. 62), this expression was in agreement with a series of diode measurements spanning the range $7.26 \leq r_0/d \leq 20.8$, and $370\ kV \leq V_{max} \leq 970\ kV$ (see figure 26). In each case the diode response was characterized by the voltage and current at the instant of I_{max}.

Since the authors make no mention of any corrections for diode closure, one must assume that the aspect ratios used in their analysis were based on the initial diode dimensions. To evaluate the consequences of this simplification, their data were replotted in figure 100 after including conservative estimates for the cathode plasma motion. In estimating the effects of diode closure, the time delay between the onset of first measurable current and the current maximum was taken to be 90 nanoseconds. To compensate for the slow rise time of the SNARK accelerator, the cathode flare expansion velocity was assumed to be 1 cm/μsec. Since the initial diode separations ranged from approximately 2.5 mm to 4.5 mm, the effect of the diode closure was to lower the data points from their previous agreement with the parapotential equation to a distribution approaching the self-pinching criterion. If the expansion of an anode plasma were also included, the correlation with the self-pinching criterion could be improved still further.

For comparison, the data points representing pinched electron flow within the diodes of two additional accelerators are also included in figure 100. The three data points clustered at 500 kV were reported by Clark and Linke (Ref. 17) using the Cornell accelerator. The diode configuration employed at Cornell had a 9.2-cm diameter brass-epoxy cathode located a distance of 8.75 mm from a planar anode. Since the time delay between the formation of the cathode plasma and the current maximum was only 50 nanoseconds, the effects of diode closure were minimal. The final data point corresponds to the operational diode configuration described in the preceding section to illustrate the effects of self-pinching on the diode perveance.

260

The arguments presented in the preceding paragraphs should not be interpreted as a contradiction of the parapotential flow model, but rather as an attempt to emphasize the need to carefully consider the time dependent diode geometry. If in the analysis of cold-cathode diodes the effects of electrode plasma expansion are ignored, serious errors in interpretation can result.

SECTION IX

SUMMARY AND CONCLUSIONS

1. INTRODUCTION

That class of high-current cold-cathode diode distinguished by non-self-convervent electron flow has been studied to (1) define the operative electron emission mechanisms, (2) to determine the dominant plasma effects within the interelectrode volume, (3) to classify the modes of electron flow, and (4) to verify the Friedlander beam convergence criterion. A basis for unfolding these elements of observed diode behavior was developed from a detailed analysis of the time-dependent voltage-current characteristics of the diode. Since the electron flow throughout the predominant portion of the accelerating pulse was space-charge limited, separation of the interrelated diode phenomena was facilitated by representing the voltage-current data in terms of the diode perveance. To confirm certain of the assumptions fundamental to the interpretation of the perveance data, streak photography of plasma luminosity motion within the diode was combined with measurements of the time-integrated as well as time-dependent current density distribution at the anode plane. When correlated with the theory of high-voltage breakdown previously formulated by Dyke, Charbonnier, Mesyats, and others, the results of this diode study provide a comprehensive, self-consistent description of the dominant processes acting within a high-current cold-cathode diode.

2. SUMMARY

Within this model, six distinct phases of diode response can be identified. If a high-current, relativistic electron accelerator is to generate the high-power electron beam for which it was designed, the diode must evolve through at least the first four of the six phases. These phases, in sequential order, are as follows:

    a. Stable field emission from microscopic, whisker-like cathode projections

    b. Transition to cathode-initiated vacuum breakdown

    c. Whisker explosion and the formation of a cathode plasma sheath

    d. Space-charge limited emission from the expanding plasma sheath

    e. Transition to self-convergent flow

    f. Development of a highly convergent electron flow

Before proceeding, it should be noted that the microscopic processes which determine the diode evolution through the first two phases and the initial steps within the third could not be observed directly because of the operational constraints of the present experiment. Nevertheless, sufficient information was available from previous vacuum breakdown studies to define the operative mechanisms. There were, however, several instances where the observed features of the initial diode response could be compared with the ramifications of these postulated microscopic processes. In every case, the agreement was complete.

From a macroscopic vantage point, the initial diode response was distinguished by a several nanosecond delay between the initial rise in the applied field and the emission of a significant electron current. Within the next several nanoseconds, the diode resistance rapidly dropped

263

to a finite value on the order of that predicted by the infinite-planar Child-Langmuir theory. The existence of this transition, its timing relative to the applied voltage waveform, and the resistance to which the diode evolved were consistent with the consequences of cathode-initiated vacuum breakdown.

a. Stable Field Emission

The cathode processes which determine the initial phase of the diode response can be described as follows. As the applied voltage begins to rise, the initial electron flow is field emitted from the tips of microscopic, whisker-like projections which appear on the cathode surface. The presence of these whiskers has the effect of not only enhancing the applied field by factors perhaps as large as several hundred but also constraining the resultant emission to the whisker tips where the surface field is most enhanced (Ref. 30). While the first consequence removes the apparent contradiction of drawing signi-ficant field emission with mean applied fields of only 10^5 to 10^6 volts/cm, the second limits the electron flow during the stable field emission phase to total currents that are insignificant compared to the magnitude of current observed during the reaminder of the pulse. With the electron emission limited to the microscopic area of the whisker tips, the diode resistance is effectively "infinite" for the first several nanoseconds of the voltage pulse.

b. Transition to Breakdown

For the cathode emission to evolve beyond the stable field emission phase, the microscopic electric field at the whisker tips must exceed some critical value. Previous studies of cathode-initiated

vacuum breakdown using either steady or pulsed voltages with durations longer than a microsecond have shown that the transition from stable field emission can be attributed to the onset of a regenerative thermal instability within the whisker (Ref. 31). For the instability to be initiated, the whisker tips must be heated to a critical temperature which corresponds to a vapor pressure of the protrusion material on the order of 10^{-4} torr (Ref. 21).

The conditions which trigger the instability have their origin in the combined effects of the electron space charge and the elevated tip temperatures produced by intense emission. The calculated current densities required to raise the steady-state temperature of a typical whisker to the critical value is on the order of 10^7 amperes/cm^2. Emitted current densities of this magnitude are more than sufficient for the space charge to suppress the surface field acting at the tips of the microscopic emitters (Ref. 31). With the applied field reduced by the negative space charge, the emitted current density is substantially less than that which would result if the space charge were to be removed.

As the tip temperature increases, cathode material is evaporated into the region immediately beyond the whisker tip. Evaporation into this region maximizes not only the probability of the cathode vapor being ionized by electron collision but also the effect of the resultant ions in neutralizing the electron space charge. With the space-charge limitation thereby reduced, extremely rapid increases in the emitted current density and the subsequent resistive heating follow immediately. The

regenerative nature of this cycle will, therefore, result in the rapid destruction of the emission site once the critical tip temperature has been attained.

This sequence implies that, for a given set of cathode conditions, steady-state vacuum breakdown should occur at a well-defined current density. When using a broad-area cathode, however, the effects of such parameters as surface impurities and whisker geometry can not be predicted. The critical current density for any individual whisker may consequently vary over a wide range, typically from 10^6 to 10^8 amperes/cm^2. Fortunately, the emitted current density is a strong function of the applied field and the corresponding breakdown fields are, therefore, constrained to the rather narrow range extending from approximately 5 to 8 x 10^7 volts/cm (Refs. 27, 29).

Following the application of a pulsed field in excess of the critical value, a delay on the order of 1 to 100 nanoseconds is required before the thermal processes associated with intense field emission from microscopic cathode protrusions can raise the tip temperature to the critical value. The functional dependence of this delay on the physical properties of the cathode material and the magnitude of the applied field can be estimated by integrating the adiabatic heat flow equation and combining the resultant expression with the Child-Langmuir relation for space-charge limited flow (Ref. 62). With this derivation, the breakdown time delay, t_b, is given qualitatively by

$$t_b \sim \frac{\rho c}{\Omega} T_{critical} \cdot F^{-3} \tag{130}$$

where ρ, c, and $\varkappa$ are, respectively, the density, specific heat, and resistivity of the protrusion material evaluated at the critical temperature; F is the microscopic field, and $T_{critical}$ is the tip temperature which corresponds to a vapor pressure of 10^{-4} torr. In spite of the simplistic derivation, the functional relationships predicted by this expression have been experimentally verified by recent studies of nanosecond breakdown (Ref. 53).

c. Whisker Explosion

The mode of whisker destruction and the cathode processes which follow were first revealed in a series of Soviet reports concerning nanosecond breakdown. Mesyats et al. observed that the application of fields in excess of the critical value caused the emission sites to explode within nanoseconds to form cathode flares (Ref. 48). Coincident with the first flare formation, the total current drawn from the cathode increased to a measurable value which corresponded to a mean current density (total current divided by macroscopic cathode area) of approximately 10 amperes/cm^2. Following the explosion, the radial expansion of the flare plasma proceeded at a constant inertial velocity in the range 1 to 3 cm/μsec. Electron emission subsequent to flare formation was found to be a complicated process whereby the Debye field developed within the plasma acted on the cold cathode surface to field emit electrons (Ref. 41). The electron flow to the anode, however, was determined by space-charge limited emission from the expanding vacuum-plasma surface of the flare.

Several elements from the preceding description can now be combined to explain the observable aspects of the initial diode response

267

and to provide a model for the electron emission throughout the remainder of the pulse. These arguments would imply that the onset of the diode transition from an effectively nonconducting state to the highly conducting state normally associated with its operation must be coincident with the initial flare formation. In support of this assumption, the experimental time delay between the initial rise in the applied field and the onset of first measurable current was found to be in agreement with the sum of the time required for the field to reach a value corresponding to the critical field at the tips of the dominant whiskers and t_b, the time required for these whiskers to explode.

Since the emission from the surface of the expanding cathode flare is space charge limited, the remainder of this transition to a conductive state is more easily interpreted in terms of the diode perveance. The diode analysis is facilitated by this approach because the perveance is independent of the applied voltage but directly related to the effective diode geometry. If the electron flow is unneutralized, the cathode emission area, the effective diode separation, and the beam envelope are the only parameters that can affect the perveance.

Following the onset of first measurable current, the experimental perveance rose rapidly to a value approximated by the infinite-planar Child-Langmuir theory. Having reached this value, the diode perveance continued to increase but at a much slower rate. In the paragraphs above, it was argued that the cathode surface cannot be an efficient emission source until the whiskers have exploded. The initial rapid rise in the diode perveance must therefore correspond to an

equally rapid increase in the total emission area. Such an increase would be caused by a rapid succession of whisker explosions occurring across the cathode face and the subsequent expansion of the cathode flares. If the concentration of thermally unstable whiskers is sufficiently high, the flares formed by their explosion quickly merge to form a "uniform" plasma sheath covering the entire cathode surface. For the sheath formative time to be short and the cathode to "turn on" quickly, the applied field must be of sufficient magnitude to explode a large percentage of the available whiskers.

    d. Space-Charge Limited Emission

    Once the plasma sheath has formed, the diode response is distinguished by space-charge limited emission from a constantly expanding plasma cathode. The perveance can now be predicted by specifying the time-dependent emission surface and the appropriate beam envelope. For the case of the high-aspect ratio diode formed by a right-cylindrical cathode positioned opposite a planar anode, the diode perveance during the fourth phase is given by

$$P_{diode} = \frac{I}{V^{3/2}} = 2.33 \times 10^{-6} \frac{\pi r_0^2}{d^2} + 1.83 \times 10^{-6} \frac{2\pi r_0}{d_0 \alpha^2} \tag{131}$$

where $d = d_0 - vt$ and

$$\alpha = \ln(d_0/vt) - 0.4 \left[\ln(d_0/vt)\right]^2 + 0.0917 \left[\ln(d_0/vt)\right]^3$$

$$- 0.0142 \left[\ln(d_0/vt)\right]^4 + \ldots$$

269

REFERENCES (cont'd)

75. Link, W. T.: private communication.

76. Bradley, L. P.; Parker, R. K.; Martin, T. H.: "Characteristics of
     Relativistic Field-Emission High-Current Diodes," paper presented
     at the Fifth International Symposium on Discharges and Electrical
     Insulation in Vacuum, unpublished, 1972.

77. Toepfer, A. J.; Bradley, L. P.: Bulletin of the American Physical
     Society, 16, 1221B, 1971.

78. Spencer, L. V.: Energy Dissipation by Fast Electrons, NBS Monograph 1,
     National Bureau of Standards, US Department of Commerce, Washington,
     DC, September 1959.

and where I and V are, respectively, the diode current (amperes) and the accelerating voltage (volts), r_0 and d_0 are, respectively, the cathode radius and the initial diode separation (centimeters), v is the plasma sheath expansion velocity (centimeters/second), and t is time (seconds). Since vt is the distance the sheath has expanded, t is initialized at the onset of first measurable current. The first term in the expression corresponds to electron emission from the planar cathode face, while the second approximates the emission from the circumferential half torus formed by the whiskers which exploded at the cathode periphery.

If the circumstances are such that the diode remains in this mode for perhaps 20 to 30 nanosecond, the average sheath expansion velocity can be determined by adjusting the velocity term in the perveance equation until a best fit between theory and experiment is obtained. Expansion velocities derived in this manner were found to be in qualitative agreement with that determined by streak photography of plasma luminosity motion within the diode.

Since the effects of the expanding cathode plasma are already incorporated into the theoretical perveance equation, any subsequent deviation of the experimental perveance from this model must be the consequence of either further variation in the diode geometry or violation of the assumed beam envelope. Given the intense electron bombardment at the anode, an obvious geometry change would result after sufficient energy had been deposited to vaporize the thin anode foil. The expansion of the resultant anode plasma would then act with the already expanding cathode plasma to decrease the diode separation.

270

By invoking the microscopic processes leading to vacuum break-
down, Charbonnier has shown that the whisker explosion must preceed the
anode vaporization if the voltage pulse is less than a microsecond in
duration (Ref. 21). In the present experiment, the time delay between
plasma sheath formation and anode vaporization was sufficient to allow
a determination of the cathode expansion velocity. With the cathode
velocity known, the increasing deviation between the theoretical and
experimental perveance could be unfolded to yield an estimate of the
anode expansion velocity. These estimates were in qualitative agreement
with those derived from the streak photographs. The photographs also
showed that the cathode plasma expansion did indeed preceed the anode
vaporization.

e. Transition to Self-Convergent Flow

By defining the electron flow in the manner of equation (131),
one has implicitly assumed that the effects of the self-magnetic field
on the beam envelope can be neglected. For the case of a planar diode
of high-aspect ratio, this assumption remains valid over a wide range
in current. Since the diode current increases with the 3/2 power of the
accelerating voltage, the self-magnetic forces must become dominant at
some point. Once the self-magnetic field becomes dominant, the electron
flow would be characterized by a severe convergence within the diode.

Friedlander has postulated that the critical current which
defines this limit must generate a self-magnetic field of sufficient
strength that the gyroradius of an electron emitted from the cathode
periphery be equal to the diode separation (Ref. 15). From this crite-
rion the critical current $I_{critical}$ (amperes) can be shown to be

271

$$I_{critical} = 8500 \; \beta\gamma \; (r_0/d) \tag{132}$$

where β and γ are the relativistic parameters of the electron and r_0 and d are as above. If rewritten in terms of the dimensionless parameters ν/γ, the self-convergence criterion becomes

$$\nu/\gamma \; critical = \frac{r_0}{2(d_0 - vt)} \tag{133}$$

If the diode current were to exceed the critical value or,,alternatively, the beam ν/γ were to exceed one half the time-dependent aspect ratio, the resultant constriction of the electron flow would reduce the experimental diode perveance. Since the perveance analysis provided not only an accurate measure of the time-dependent diode geometry but also a distinctive indication of any transition in the mode of electron flow, it was possible to definitively verify the self-convergence criterion.

f. Highly Convergent Electron Flow

Considerable interest in the details of this electron flow mode has been stimulated within the past 2 years. Unfortunately, the characteristics of the Field Emission pulsed-power system were such that this mode could not be achieved experimentally.

3. CONCLUSIONS

A principal feature of the events described above is that the existence of an expanding plasma sheath which acts as the effective cathode surface is a prerequisite to the emission of the intense current densities associated with the operation of a high-current cold-cathode diode. When

designing a diode for a specific accelerator, several ramifications of this basic concept must be considered.

a. If the cathode is to remain unaffected by the prepulse, the prepulse voltage must develop microscopic fields less than 5 to 8 x 10^7 volts/cm. Since the microscopic enhancement of the whiskers is on the order of 200 to 300, the average prepulse field must be less than 1 to 2 x 10^5 volts/cm. If the cathode shape produces a macroscopic enhancement, the prepulse voltage must be reduced proportionally.

b. In those regions of the cathode where emission is required, the surface should be roughened or irregular to provide a maximum local enhancement. The physical dimensions of these surface irregularities should be small compared to vt, however, if the uniformity of the plasma sheath is to be maintained. Moreover, the cathode material used in these areas should be chosen to minimize the breakdown time. In both respects, graphite is an excellent material. Of the readily available cathode materials, it has the smallest value of $(\rho c/\Omega)T_{critical}$.

c. To achieve a rapid sheath formation using a graphite cathode, an applied field in excess of 400 kV/cm is required. The higher the applied field, the denser the concentration of thermally unstable emission sites and the more uniform the resultant plasma sheath. With a uniform plasma sheath the nonparaxial component of the surface field and hence the resultant contribution to the initial transverse kinetic energy of the beam are both minimized.

d. Using a graphite cathode, the expansion velocity was found to vary from 1.8 to 2.8 cm/μsec. With a faster rate of rise in the applied field, the flare expansion is more rapid.

273

e. If the objective is to design a constant resistance diode which can be matched to the output impedance of the pulsed-power system, the initial diode separation must be large compared to vt_p, where t_p is the duration of the applied voltage pulse.

f. In those regions of the cathode where electron emission is detrimental, a highly polished surface of a material with a high $(\rho c/\Omega)^T_{critical}$ is advantageous.

REFERENCES

1. Denholm, A. S.; Nablo, S. V.; et. al.; The Feasibility of Designing High-Voltage X-Ray Tubes as Intense Gamma and Neutron Sources, AFWL-TR-65-62, Air Force Weapons Laboratory, Kirtland AFB, NM, December 1965.

2. Brewster, J. L.; Anderson, R. E.; Barbour, J. L.; et al.; Feasibility of High-Voltage X-Ray Tubes as Intense Gamma and Neutron Sources, AFWL-TR-65-63, Air Force Weapons Laboratory, Kirtland AFB, NM, November 1965.

3. Creedon, J.; Ford, F. C.; Martin, D.; et al.; Advanced X-Ray Tube Development, AFWL-TR-65-64, Air Force Weapons Laboratory, Kirtland AFB, NM, January 1966.

4. Levine, L. S.; Vitkovitsky, I. M.; IEEE Transactions on Nuclear Science, NS-18, 255, 1971.

5. Winterberg, F.; Physical Review, 174, 212, 1968.

6. Eden, M. J.; Saunders, P. A. H.; Nuclear Fusion, 11, 37, 1971.

7. Babykin, M. V.; Zavoisky, Ye. K.; et al.; Nuclear Fusion, 12, 75, 1972.

8. Keefe, D.; Scientific American, 226, 23, 1972.

9. Bzura, J. J.; Fessenden, T. J.; et al.; Physical Review Letters, 29, 256, 1972.

10. Stallings, C.; Benford, J.; Schneider, R.; Bulletin of the American Physical Society, 17, 1031, 1972.

11. Goldenbaum, G. C.; Burton, J.; et al.; Bulletin of the American Physical Society, 17, 1031, 1972.

12. Kapatanakos, C. A.; Hammer, D. A.; et al.; Bulletin of the American Physical Society, 17, 1032, 1972.

13. Rosinskii, S. E.; Rukhadze, A. A.; Soviet Physics--Technical Physics, 16, 1989, 1972.

14. Kainer, S.; Dawson, J. D.; et al.; Physics of Fluids, 15, 493, 1972.

15. Friedlander, F.; Hechtel, R.; Jory, H.; et al.; Megavolt-Megampere Electron Gun Study, DASA 2173, Varian Associates, Palo Alto, CA, September 1968.

REFERENCES (cont'd)

16. Yonas, G.; Spence, P.; et al.; <u>Dynamic Effects of High v/γ Beam Plasma Interaction</u>, DASA 2296, Physics International Company, San Leandro, CA, November 1970.

17. Clark, J. J.; Linke, S.; <u>Operational Characteristics and Entrance Conditions of a High-Current, Relativistic Electron Beam Accelerator</u>, LPS 23, Laboratory of Plasma Studies, Cornell University, Ithaca, New York, August 1967.

18. Loda, G.; Spence, P.; <u>High v/γ Electron Beam Generation Using a 100-kV Mylar Stripline</u>, PIIR-4-71, Physics International Company, San Leandro, CA, November 1970.

19. Block, J.; et al.; "NRL Relativistic Electron Beam Program," in <u>Record of the 11th Symposium on Electron, Ion, and Laser Beam Technology</u> (R. F. M. Thornley, ed.), San Francisco Press, CA, 1971.

20. Fowler, R. H.; Nordheim, L. W.; <u>Proceedings of the Royal Society</u>, <u>A119</u>, 173, 1928.

21. Charbonnier, F. M.; Bennette, C. J.; Swanson, L. W.; <u>Journal of Applied Physics</u>, <u>38</u>, 627, 1967.

22. Boyle, W. S.; Kisliuk, P.; Germer, L. H.; <u>Journal of Applied Physics</u>, <u>26</u>, 720, 1955.

23. Bennette, C. J.; Swanson, L. W.; Charbonnier, F. M.; <u>Journal of Applied Physics</u>, <u>38</u>, 634, 1967.

24. Little, R. P.; Smith, S. T.; <u>Journal of Applied Physics</u>, <u>36</u>, 1502, 1965.

25. Tomaschke, H. E.; Alpert, D.; <u>Journal of Vacuum Science and Technology</u>, <u>4</u>, 192, 1967.

26. Tomaschke, H. E.; Alpert, D.; <u>Journal of Applied Physics</u>, <u>38</u>, 881, 1967.

27. Alpert, D.; et al.; <u>Journal of Vacuum Science and Technology</u>, <u>1</u>, 35, 1964.

28. Utsumi, T.; <u>Journal of Applied Physics</u>, <u>38</u>, 2989, 1967.

29. Charbonnier, F. M.; "High-Current Density Field Emission and the Transition to Vacuum Breakdown," paper presented at the First International Symposium on the Insulation of High Voltage in Vacuum, unpublished, October 1964.

REFERENCES (cont'd)

30. Vibrans, F. E.; <u>Field Emission in Vacuum Voltage Breakdown</u>, Technical Report No. 353 (AD602844), Lincoln Laboratory, Massachusetts Institute of Technology, Cambridge, MA, May 1964.

31. Dyke, W. P.; Dolan, W. W.; "Field Emission," in <u>Advances in Electronics and Electron Physics VIII</u> (L. Marton, ed.), Academic Press, New York, 1956.

32. Nottingham, W. B.; <u>Physical Review</u>, <u>59</u>, 907, 1941.

33. Ahearn, A. J.; <u>Physical Review</u>, <u>50</u>, 238, 1936.

34. Dyke, W. P.; et al.; <u>Physical Review</u>, <u>91</u>, 1043, 1953.

35. Cranberg, L.; <u>Journal of Applied Physics</u>, <u>23</u>, 518, 1952.

36. Van Atta, L. C.; et al.; <u>Physical Review</u>, <u>43</u>, 158, 1933.

37. Fursei, G. N.; et al.; <u>Soviet Physics--Technical Physics</u>, <u>12</u>, 1370, 1968.

38. Gofman, I. I.; et al.; <u>Soviet Physics--Solid State</u>, <u>2</u>, 1203, 1961.

39. Charbonnier, F. M.; "A Brief Review of Vacuum Breakdown Initiation Processes," paper presented at the Third International Symposium on Discharges and Electrical Insulation in Vacuum, unpublished, September 1968.

40. Levine, P. H.; <u>Journal of Applied Physics</u>, <u>33</u>, 582, 1962.

41. Mesyats, G. A.; Proskurovskii, D. I.; <u>JETP Letters</u>, <u>13</u>, 4, 1971.

42. Mesyats, G. A.; Rotshtein, V. P.; Fursei, G. N.; Kartsev, G. K.; <u>Soviet Physics--Technical Physics</u>, <u>15</u>, 1202, 1971.

43. Bugayev, S. P.; Iskol'dskii, A. M.; Mesyats, G. A.; Proskurovskii, D. I.; <u>Soviet Physics--Technical Physics</u>, <u>12</u>, 1625, 1968.

44. Bugayev, S. P.; Mesyats, G. A.; Proskurovskii, D. I.; <u>Soviet Physics--Doklady</u>, <u>14</u>, 605, 1969.

45. Kartsev, G. K.; Mesyats, G. A.; Proskurovskii, D. I.; Rotshtein, V. P.; Fursei, G. N.; <u>Soviet Physics--Doklady</u>, <u>15</u>, 475, 1970.

46. Fursei, G. N.; Vorontsov-Vel'yaminov, P. N.; <u>Soviet Physics--Technical Physics</u>, 12, 1377, 1968.

47. Fursei, G. N.; Kartsev, G. K.; <u>Soviet Physics--Technical Physics</u>, <u>14</u>, 1442, 1970.

48. Mesyats, G. A.; Litvinov, E. A.; Proskurovskii, D. I.; "High-Speed Processes During Pulse Breakdown of Vacuum Gap," paper presented at the Fourth International Symposium on Discharges and Electrical Insulation in Vacuum, 82, unpublished, 1970.

49. Mesyats, G. A.; Bugayev, S. P.; et al.; "Study of Initiation and Development of Short Vacuum Gaps Pulse Breakdown in Nanosecond Range, Part I," paper presented at the Third International Symposium on Discharges and Electrical Insulation in Vacuum, 212, unpublished, September 1968.

50. Zel'dovich, Ya. B.; Raizer, Yu. P.; Physics of Shock Waves and High-Temperature Hydrodynamic Phenomena, Vol I (W. D. Hayes and R. F. Probstein, eds.), Academic Press, New York, 1966.

51. Bazhenov, G. P.; Baksht, R. B.; et al.; "Cathode Flares During Pulse Breakdown in Vacuum," paper presented at the Fourth International Symposium on Discharges and Electrical Insulation in Vacuum, 116, unpublished, 1970.

52. Child, C. D.; Physical Review, 32, 492, 1911.

53. Langmuir, I.; Physical Review, 2, 450, 1913.

54. Langmuir, I.; Compton, K. T.; Review of Modern Physics, 3, 191, 1931.

55. Ivey, H. F.; Journal of Applied Physics, 23, 208, 1952.

56. Jackson, J. D.; Classical Electrodynamics, J. Wiley and Sons, New York, 1962.

57. Lawson, J. D.; Journal of Nuclear Energy, Part C: Plasma Physics, 1, 31, 1959.

58. De Packh, D.; Radiation Project Internal Report Number 7, Naval Research Laboratory, Washington, DC, April 1968.

59. Creedon, J.; A Quasi-Parapotential Model for the High ν/γ Diode, PIIR-19-70, Physics International Company, San Leandro, CA, May 1970.

60. Uglum, J.; et al.; Research on Beam Stopping Due to Self-Magnetic Compression, DASA 2167, Ion Physics Corporation, Burlington, MA, November 1968.

61. Graybill, S. E.; et al.; Diagnostics and Applications of Pulsed Self-Focused Relativistic Electron Beams, DASA 2477, Ion Physics Corporation, Burlington, MA, June 1970.

278

62. Ecker, B.; et al.; "Intense Beam Generation at Megampere Currents and Beam Transport in Pulsed External Magnetic Field Configurations," in Record of the 11th Symposium on Electron, Ion, and Laser Beam Technology (R. F. M. Thornley, ed.), San Francisco Press, CA, 1971.

63. Ecker, B.; et al.; Intense Beam Generation at Megampere Currents and Beam Transport in Pulsed External Magnetic Field Configurations, PIIR-27-71, Physics International Company, San Leandro, CA, May 1971.

64. Ecker, B.; Self-Focused 500-GW Electron Flow in an Applied Longitudinal Electric Field, PIIR-13-72, Physics International Company, San Leandro, CA, April 1972.

65. Yonas, G.; Smith, I.; et al.; "Development and Application of a 1-MV, 1-MA Mylar Dielectric Pulsed Electron Accelerator and Concepts for Higher Energy Modular Generator Systems,: in Record of the 11th Symposium on Electron, Ion, and Laser Beam Technology (R. F. M. Thornley, ed.), San Francisco Press, CA, 1971.

66. Trolan, J. k.; Charbonnier, F. M.; Collins, F. M.; Guenther, A. H.; Exploding Wires, Plenum Press, New York, 3, 1964.

67. Trolan, J. K.; Development of an Ultrafast Moderate Energy Pulse Power System, AFWL-TR-65-1, Air Force Weapons Laboratory, Kirtland AFB, NM, January 1966.

68. Collins, F. M.; Design Study of a Photoelectrical Trigger System, AFWL-TR-65-157, Air Force Weapons Laboratory, Kirtland AFB, NM, December 1965.

69. Smith, I. D.; "Pulse Breakdown of Insulator Surfaces in Poor Vacuum," paper presented at the First International Symposium on the Insulation of High Voltage in Vacuum, unpublished, October 1964.

70. Alston, L. L.; High-Voltage Technology, Oxford University Press, London, 1968.

71. Rogers, R. R.; private communication.

72. Boers, J. N.; "Digital-Computer Solution of Laplace's Equation Including Dielectric Interfaces and Small Floating Electrodes," in Record of the 11th Symposium of Electron, Ion, and Laser Beam Technology (R. F. M. Thornley, ed.), San Francisco Press, CA, 1971.

73. Smith, I. D.; private communication.

74. Grover, F. W.; Inductance Calculations: Working Formulas and Tables, Dover Publications, Inc., New York, 1962.

REFERENCES (cont'd)

75. Link, W. T.; private communication.

76. Bradley, L. P.; Parker, R. K.; Martin, T. H.; "Characteristics of Relativistic Field-Emission High-Current Diodes," paper presented at the Fifth International Symposium on Discharges and Electrical Insulation in Vacuum, unpublished, 1972.

77. Toepfer, A. J.; Bradley, L. P.; Bulletin of the American Physical Society, 16, 12218, 1971.

78. Spencer, L. V.; Energy Dissipation by Fast Electrons, NBS Monograph 1, National Bureau of Standards, US Department of Commerce, Washington, DC, September 1959.